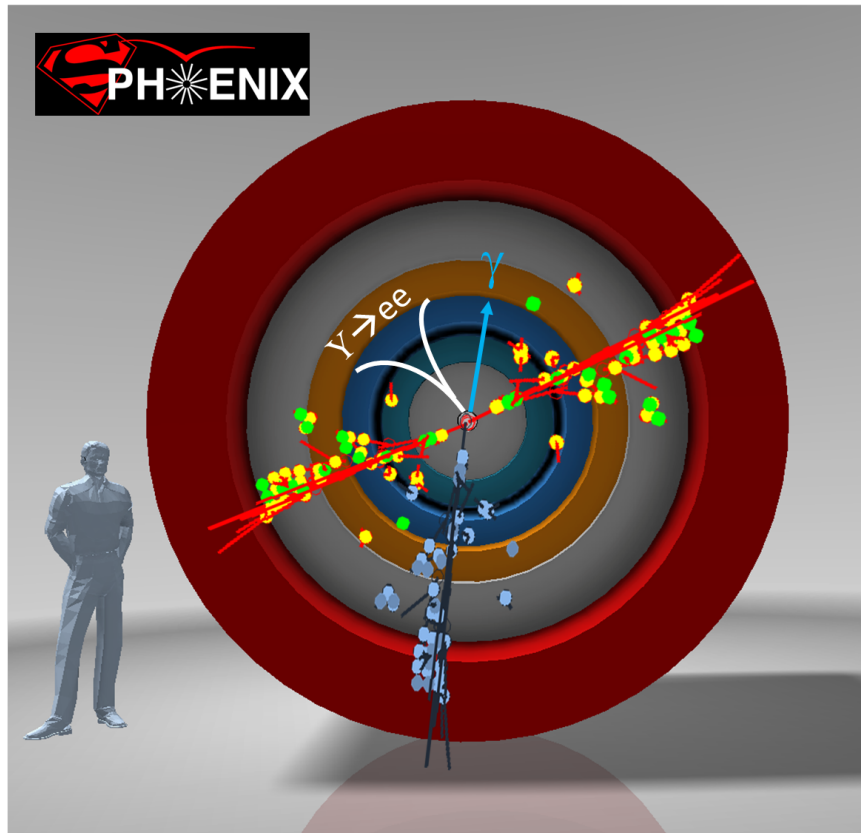




*An Upgrade Proposal from the PHENIX Collaboration*

November 19, 2014





# Executive Summary

In this document the PHENIX collaboration proposes a major upgrade to the PHENIX detector at the Relativistic Heavy Ion Collider. This upgrade, sPHENIX, enables an extremely rich jet and beauty quarkonia physics program addressing fundamental questions about the nature of the strongly coupled quark-gluon plasma, discovered experimentally at RHIC to be a perfect fluid. The startling dynamics of the QGP on fluid-like length scales is an emergent property of QCD, seemingly implicit in the Lagrangian but stubbornly hidden from view. QCD is an asymptotically free theory, but how QCD manifests as a strongly coupled fluid with specific shear viscosity near  $T_C$  as low as allowed by the uncertainty principle is as fundamental an issue as that of how confinement itself arises.

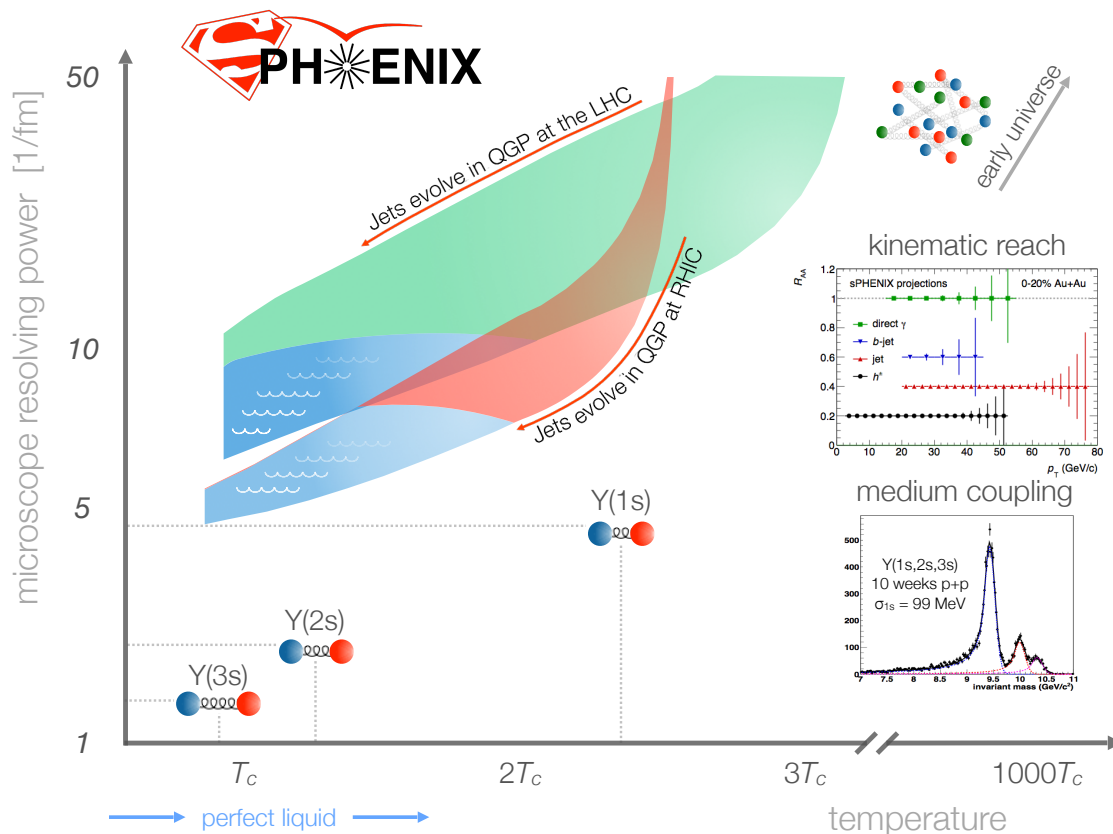
Questions such as this can only be fully addressed with jet, dijet,  $\gamma$ -jet, fragmentation function, and Upsilon observables at RHIC energies, which probe the medium over a variety of length scales. Comparing these measurements with ones at the Large Hadron Collider will yield important insights into the thermodynamics of QCD, and these issues have acquired fresh new importance as recent analyses of data from  $p(d)+A$  collisions have raised questions regarding the minimum size, shape, and temperature needed for the formation of droplets of quark-gluon plasma. Finally, beyond the physics program described here, sPHENIX provides an excellent foundation for a possible future detector able to exploit the novel physics opportunities of an electron-ion collider at RHIC.

The sPHENIX upgrade addresses specific questions whose answers are necessary to advance our understanding of the quark-gluon plasma:

- How does a partonic shower develop and propagate in the quark-gluon plasma?
- How does one reconcile the observed strongly coupled quark-gluon plasma with the asymptotically free theory of quarks and gluons?
- What are the dynamical changes in the quark-gluon plasma in terms of quasiparticles and excitations as a function of temperature?
- How sharp is the transition of the quark-gluon plasma from the most strongly coupled regime near  $T_c$  to a weakly coupled system of partons known to emerge at asymptotically high temperatures?

The development of the sPHENIX physics program has benefited from very active engagement with the theory community. For current-day questions regarding the perfect fluidity of the quark-gluon plasma, engagement between theorists and experimentalists, fed by increasingly

comprehensive data from RHIC and the LHC, has moved the physics discussion beyond merely constraining  $\eta/s$  to exploring its temperature dependence and other properties. In an analogous manner, there is great progress in the theoretical understanding of jet quenching — see Ref. [1] from the JET Collaboration, for example. We foresee that truly comprehensive jet data from RHIC and the LHC — to which sPHENIX contributes crucially — will move the physics discussion beyond merely constraining the single transport property  $\hat{q}$  to a deeper understanding of the dynamics of the quark-gluon plasma.



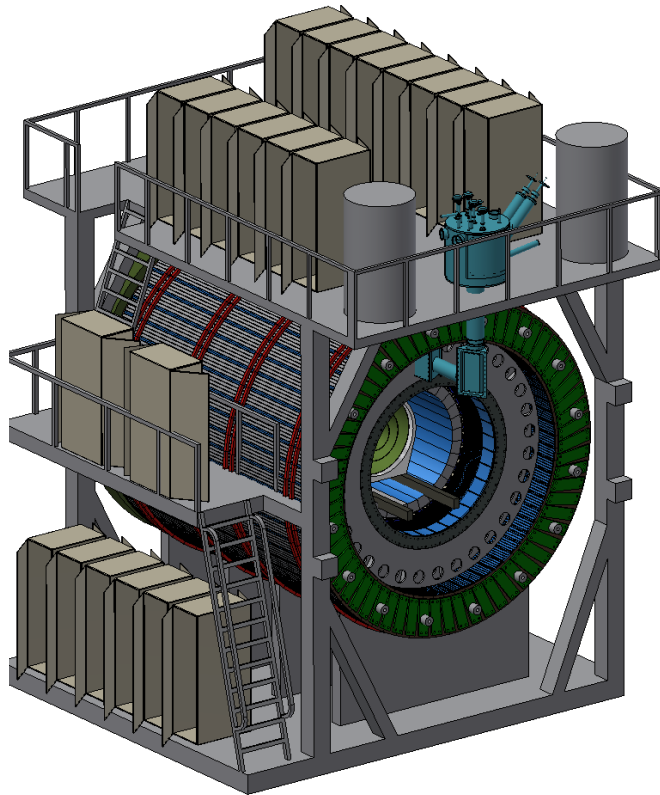
**Figure 1:** The physics goals of sPHENIX, graphically. Hard scattered partons at the LHC and at RHIC evolve through splittings and interaction with the medium, providing sensitivity to QGP dynamics over a wide range of length scales. The heavy quarkonia states are well-localized in this space and provide uniquely valuable probes of the coupling strength of the medium. Shown as inserts are projections of the capabilities of sPHENIX for measuring these key probes.

Figure 1 depicts the physics goals of sPHENIX. Hard scattered partons at both the LHC and at RHIC begin with a very large virtuality at the earliest, hottest stage of the collision. These highly virtual partons have very fine resolving power and probe the medium on extremely small length scales. The scattered partons initially shed their virtuality, evolving downward in scale, through splittings as though they were in vacuum. At later times the momentum scale of the developing partonic shower becomes comparable to that of the hot QCD medium and the nascent jet becomes



more and more sensitive to mesoscopic, fluid-scale excitations in the medium. At the same time, the medium is populated with heavy quarkonia whose physical size and temperature sensitive coupling to the medium provide precisely locatable probes of the medium in this space. At the longest scales, one sees the well-established hydrodynamic behavior of the medium with minimal specific shear viscosity, the so-called perfect liquid. The sPHENIX detector will be able to measure jets,  $b$ -tagged jets, photons, charged hadrons and their correlations over a wide range of energies, and it will also have mass resolution sufficient to separately distinguish the three states of the Upsilon family. These capabilities will enable us to map out the dynamics of the QGP across this space and address the fundamental questions posed above.

To pursue these physics questions we are proposing an upgrade consisting of a 1.5 T superconducting magnetic solenoid of inner radius 140 cm with silicon tracking, electromagnetic calorimetry, and hadronic calorimetry providing uniform coverage for  $|\eta| < 1$ . The sPHENIX solenoid is an existing magnet developed for the BaBar experiment at SLAC, and recently ownership of this key component was officially transferred to BNL. An engineering drawing of the sPHENIX detector and its incorporation into the PHENIX interaction region are shown in Figure 2.



**Figure 2:** An engineering drawing of sPHENIX, showing the superconducting solenoid containing the electromagnetic calorimeter and surrounded by the hadronic calorimeter, with a model of the associated support structure, as it would sit in the PHENIX IR.

The sPHENIX plan has been developed in conjunction with the official timeline from BNL management. The expectation is for RHIC running through 2016, a shutdown in 2017, RHIC running for the increased luminosity beam energy scan in 2018–2019, a shutdown in 2020, and RHIC running

in 2021 and 2022. We anticipate installing the magnet, the hadronic calorimeter and portions of the tracking system to enable significant commissioning of sPHENIX during the 2019 running period. The sPHENIX detector will be completely integrated during the 2020 shutdown and would be available for physics at the start of the 2021 run. With the high luminosity available at RHIC and the high sPHENIX data acquisition bandwidth, sPHENIX will record 100 billion and sample over 2/3 of a trillion Au+Au collisions at  $\sqrt{s_{NN}} = 200$  GeV in a 22 week physics run period. The high rate capability of sPHENIX will enable the recording of over 10 million dijet events with  $E_T > 20$  GeV, along with a correspondingly large  $\gamma$ +jet sample. We envision a run plan for 2021–2022 consisting of two 30 week physics runs allowing a period for final commissioning, 22 weeks of Au+Au running, and extended periods of  $p+p$  and  $p(d)+Au$  running.

The design of sPHENIX takes advantage of a number of technological advances to enable a significantly lower cost per unit solid angle than has been previously possible, and we have obtained budgetary guidance from well-regarded vendors for the major components of sPHENIX. Further cost savings are achieved by reusing significant elements of the existing PHENIX mechanical and electrical infrastructure. Thus sPHENIX physics will be delivered in a very cost effective way.

We have designed sPHENIX so that it could serve as the foundation for a detector intended to make physics measurements at a future electron ion collider (EIC) at RHIC. The BNL implementation of the EIC, eRHIC, adds a 5–15 GeV electron beam to the current hadron and nuclear beam capabilities of RHIC. The sPHENIX detector, when combined with future upgrades in the backward ( $\eta < -1$ ) and forward ( $\eta > 1$ ) regions enables a full suite of EIC physics measurements as described in Appendix B. There is also the potential, if one can realize appropriate instrumentation in the hadron-going direction while polarized  $p+p$  and  $p+A$  collisions are available at RHIC, to pursue a rich program of forward physics measurements [2].

In Chapter 1, we detail the physics accessible via jet, dijet,  $\gamma$ +jet, fragmentation function, and Upsilon measurements at RHIC to demonstrate mission need. In Chapter 2, we detail the sPHENIX detector and subsystem requirements needed to achieve the physics goals. In Chapter 3, we detail the specific detector design and GEANT4 simulation results. In Chapter 4, we detail the physics performance with full detector simulations. In Appendix A we describe two possible augmentations of the baseline sPHENIX detector: one, a preshower for the electromagnetic calorimeter to extend the reach of direct photon measurements; and two, a forward calorimeter to extend the acceptance of sPHENIX and to provide access to additional physics. Lastly, in Appendix B we include a copy of a Letter of Intent for an EIC detector built around the BaBar magnet and the sPHENIX calorimetry.

# Contents

<b>1 The Physics Case for sPHENIX</b>	<b>1</b>
1.1 Pushing and probing the QGP.	3
1.2 What is the temperature dependence of the QGP?	5
1.3 What are the inner workings of the QGP?	13
1.4 How does the QGP evolve along with the parton shower?	17
1.5 Current jet probe measurements.	21
1.6 Theoretical calculations of jets at RHIC	26
1.7 Direct Photons and Fragmentation Functions	35
1.8 Heavy Quark Jets	39
1.9 Beauty Quarkonia in the QGP.	43
1.10 Beauty Quarkonia in proton-nucleus collisions	46
1.11 Rates and Physics Reach	48
<b>2 Physics-Driven Detector Requirements</b>	<b>53</b>
2.1 Acceptance.	55
2.2 Segmentation.	57
2.3 Energy Resolution	57
2.4 Tracking	58
2.5 Triggering	59
<b>3 Detector Concept</b>	<b>61</b>
3.1 Magnet	62
3.2 The Electromagnetic Calorimeter	64
3.3 The Hadronic Calorimeter	66
3.4 Calorimeter Simulations	71
3.5 Electronics	76
3.6 Charged Particle Tracking	81

3.7	Electron Identification . . . . .	86
3.8	Rates and DAQ . . . . .	88
3.9	sPHENIX Triggering . . . . .	89
3.10	Mechanical Design and Infrastructure Concept . . . . .	95
3.11	Detector Development and Testing . . . . .	97
<b>4</b>	<b>Physics Performance . . . . .</b>	<b>101</b>
4.1	Jet simulations . . . . .	101
4.2	Jet finding algorithms . . . . .	102
4.3	Jet performance in $p+p$ collisions . . . . .	106
4.4	Jet performance in Au+Au collisions . . . . .	109
4.5	Extended kinematics and surface bias engineering . . . . .	122
4.6	Fragmentation Function and Photon-Jet Observables . . . . .	125
4.7	Heavy Quark Jets . . . . .	132
4.8	Proton-Nucleus Collision Jet Physics . . . . .	138
4.9	Jet physics at lower RHIC energies . . . . .	143
4.10	Jet Physics Summary . . . . .	144
4.11	Beauty Quarkonia Performance . . . . .	146
<b>A</b>	<b>Forward Hadronic Calorimeter and Barrel Preshower Options . . . . .</b>	<b>153</b>
A.1	Forward Hadronic Calorimeter . . . . .	153
A.2	Preshower . . . . .	157
<b>B</b>	<b>Evolution to an EIC Detector . . . . .</b>	<b>159</b>
B.1	EIC Physics . . . . .	160
B.2	eRHIC: realizing the Electron-Ion Collider . . . . .	162
B.3	Physics Deliverables . . . . .	162
B.4	Detector Requirements . . . . .	170
B.5	Detector Concept . . . . .	182
	<b>List of Tables . . . . .</b>	<b>201</b>
	<b>List of Figures . . . . .</b>	<b>203</b>
	<b>References . . . . .</b>	<b>215</b>

# Chapter 1

## The Physics Case for sPHENIX

Hadronic matter under conditions of extreme temperature or net baryon density transitions to a new state of matter called the quark-gluon plasma. Lattice QCD calculations at zero net baryon density indicate a smooth crossover transition at  $T_c \approx 170$  MeV, though with a rapid change in properties at that temperature as shown in the left panel of Figure 1.1 [3]. This quark-gluon plasma dominated the early universe for the first six microseconds of its existence. Collisions of heavy nuclei at the Relativistic Heavy Ion Collider (RHIC) have sufficient initial kinetic energy that is then converted into heat to create quark-gluon plasma with an initial temperature—measured via the spectrum of directly emitted photons—of greater than 300 MeV [4]. The higher energy collisions at the Large Hadron Collider (LHC) produce an even higher initial temperature  $T > 420$  MeV [5].

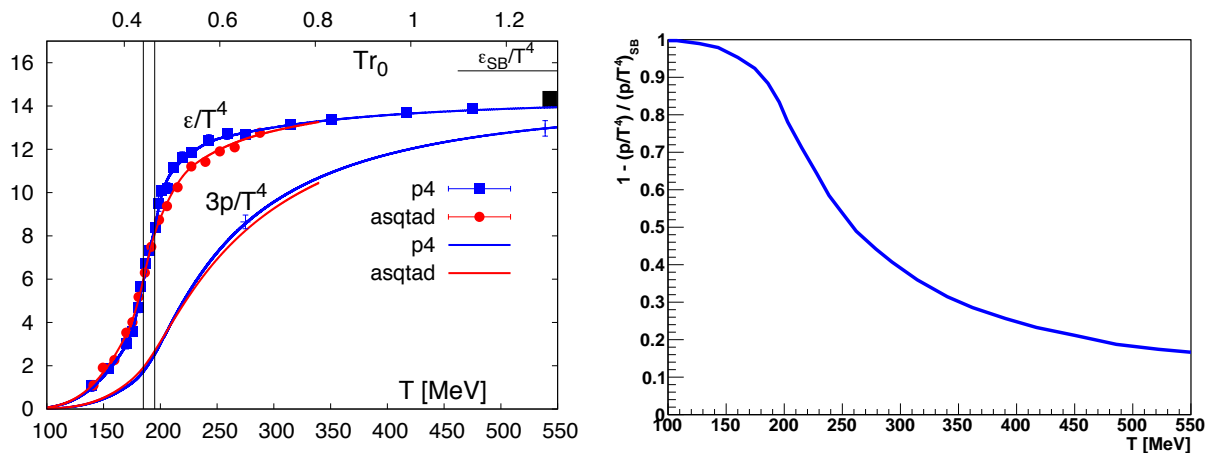


**Figure 1.1:** (left) The energy density and three times the pressure normalized by  $1/T^4$  as a function of temperature [3]. (right) Deviation in  $p/T^4$  relative to the Stefan-Boltzmann value as a function of temperature. The deviation from the Stefan-Boltzmann value is 23%, 39%, 53%, and 80% at temperatures of 420, 300, 250, and 200 MeV, respectively.

In materials where the dominant forces are electromagnetic, the coupling  $\alpha_{em}$  is always much less than one. Even so, many-body collective effects can render perturbative calculations non-convergent and result in systems with very strong effective coupling [6]. In cases where the

nuclear force is dominant, and at temperature scales of order  $1-3 T_c$ , the coupling constant  $\alpha_s$  is not much less than one and the system is intrinsically non-perturbative. In addition, the many-body collective effects in the quark-gluon plasma and their temperature dependence near  $T_c$  are not yet well understood.

The right panel of Figure 1.1 shows the deviation from the Stefan-Boltzmann limit of Lattice QCD results for the pressure normalized by  $1/T^4$ . The Stefan-Boltzmann limit holds for a non-interacting gas of massless particles (i.e., the extreme of the weakly coupled limit), and as attractive inter-particle interactions grow stronger the pressure decreases. Thus, one might expect that the quark-gluon plasma would transition from a weakly coupled system at high temperature to a more strongly coupled system near  $T_c$ . However, a direct quantitative extraction of the coupling strength warrants caution as string theory calculations provide an example where the coupling is very strong and yet the deviation from the Stefan-Boltzmann limit is only 25% [7, 8]. The change in initial temperature between RHIC and LHC collisions is thus expected to be associated with important changes in the nature of the quark-gluon plasma [9]. If not, the question is why not.

The collisions at RHIC and the LHC involve a time evolution during which the temperature drops as the quark-gluon plasma expands. The real constraint on the temperature dependence of the quark-gluon plasma properties will come from calculations which simultaneously describe observables measured at both energies. Since we are studying a phase transition, it is crucial to do experiments near the phase transition and compare them with experiments done further above  $T_c$ . Typically, all the non-scaling behavior is found near the transition.

For many systems the change in coupling strength is related to quasiparticle excitations or strong coherent fields, and to study these phenomena one needs to probe the medium at a variety of length scales. For example, in a superconductor probed at long length scales, one scatters from Cooper pairs; in a superconductor probed at short distance scales one observes the individual electrons. Hard scattered partons generated in heavy ion collisions that traverse the quark-gluon plasma serve as the probes of the medium. Utilizing these partonic probes, measured as reconstructed jets, over the broadest possible energy scale is a key part of unraveling the quasiparticle puzzle in the quark-gluon plasma. Jets at the LHC reach the highest energies, the largest initial virtualities, and large total energy loss to probe the shortest distance scales. The lower underlying event activity at RHIC will push the jet probes to lower energies and lower initial virtualities thus probing the important longer distance scales in the medium. Measurements of the three Upsilon states that span a large range in binding energy and size are an excellent complement to the jet program, with precision required at both RHIC and the LHC.

Continued developments in techniques for jet reconstruction in the environment of a heavy ion collision have allowed the LHC experiments to reliably recover jets down to 40 GeV [10, 11], which is well within the range of reconstructed jet energies at RHIC. This overlap opens the possibility of studying the quark-gluon plasma at the same scale but under different conditions of temperature and coupling strength.

Apart from the temperature and coupling strength differences in the medium created at RHIC and the LHC, the difference in the steepness of the hard scattering  $p_T$  spectrum plays an important role. The less steeply falling spectrum at the LHC has the benefit of giving the larger reach in  $p_T$  with reconstructed jets expected up to 1 TeV. At RHIC, the advantage of the more steeply falling spectrum is the greater sensitivity to the medium coupling and quark-gluon plasma modifications of the parton shower. This greater sensitivity may enable true tomography in particular with

engineering selections for quarks and/or gluons with longer path length through the medium. In addition, for correlations, once a clean direct photon or jet tag is made, the underlying event is 2.5 times smaller at RHIC compared to the LHC thus giving cleaner access to the low energy remnants of the parton shower and possible medium response.

This Chapter is organized into Sections as follows. We first describe the key ways of ‘pushing’ and ‘probing’ the quark-gluon plasma to understand its properties. We then discuss three different aspects in which the RHIC jet results are crucial in terms of (1) the temperature dependence of the QGP, (2) the microscopic inner workings of the QGP, and (3) the QGP time evolution along with the parton shower evolution. We relate each of these three aspects to specific observables measurable with sPHENIX. We then discuss the current state of jet probe measurements from RHIC and LHC experiments, followed by a review of theoretical calculations for RHIC jet observables. We discuss the specific physics of heavy quark jets and open heavy flavor in terms of Upsilon observables. Finally, we review the rates available that enable precision measurements across this comprehensive program.

## 1.1 Pushing and probing the QGP

Results from RHIC and LHC heavy ion experiments have provided a wealth of data for understanding the physics of the quark-gluon plasma. One very surprising result discovered at RHIC was the fluid-like flow of the quark-gluon plasma [12], in stark contrast to some expectations that the quark-gluon plasma would behave as a weakly coupled gas of quarks and gluons. It was originally thought that even at temperatures as low as  $2-5 T_c$ , the quark-gluon plasma could be described with a weakly coupled perturbative approach despite being quite far from energy scales typically associated with asymptotic freedom.

The quark-gluon plasma created in heavy ion collisions expands and cools, eventually passing through the phase transition to a state of hadrons, which are then measured by experiment. Extensive measurements of the radial and flow coefficients of various hadrons, when compared to hydrodynamics calculations, imply a very small ratio of shear viscosity to entropy density,  $\eta/s$  [13]. In the limit of very weak coupling (i.e., a non-interacting gas), the shear viscosity is quite large as particles can easily diffuse across a velocity gradient in the medium. Stronger inter-particle interactions inhibit diffusion to the limit where the strongest interactions result in a very short mean free path and thus almost no momentum transfer across a velocity gradient, resulting in almost no shear viscosity.

The shortest possible mean free path is of order the de Broglie wavelength, which sets a lower limit on  $\eta/s$  [14]. A more rigorous derivation of the limit  $\eta/s \geq 1/4\pi$  has been calculated within string theory for a broad class of strongly coupled gauge theories by Kovtun, Son, and Starinets (KSS) [15]. Viscous hydrodynamic calculations assuming  $\eta/s$  to be temperature independent through the heavy ion collision time evolution are consistent with the experimental data where  $\eta/s$  is within 50% of this lower bound for strongly coupled matter [13, 16, 17, 18, 19, 20]. Even heavy quarks (i.e., charm and beauty) are swept up in the fluid flow and theoretical extractions of the implied  $\eta/s$  are equally small [21].

Other key measures of the coupling strength to the medium are found in the passage of a hard scattered parton through the quark-gluon plasma. As the parton traverses the medium it accu-

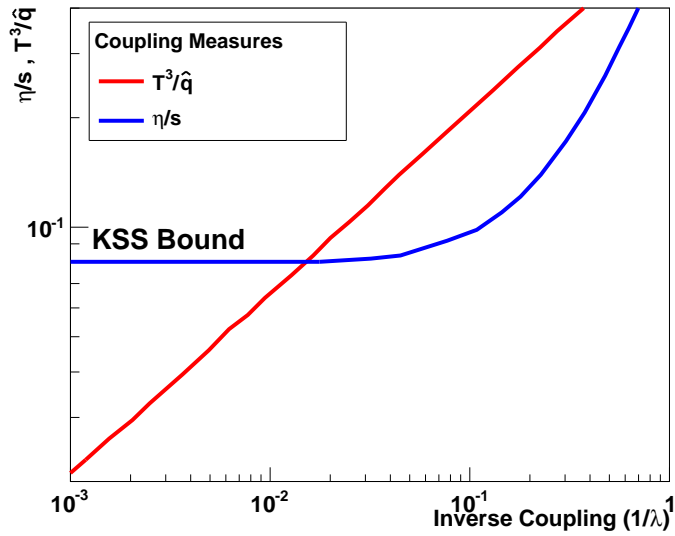


**Figure 1.2:**  $\eta/s$  (blue) and  $T^3/\hat{q}$  (red) as a function of the inverse of the 't Hooft coupling[22]. For large  $\lambda$  (i.e., small  $1/\lambda$ ),  $\eta/s$  approaches the quantum lower bound asymptotically, losing its sensitivity to further changes in the coupling strength.

mulates transverse momentum as characterized by  $\hat{q} = d(\Delta p_T^2)/dt$  and transfers energy to the medium via collisions as characterized by  $\hat{e} = dE/dt$ . Ref. [23] has calculated  $\hat{q}/T^3$  in  $\mathcal{N} = 4$  supersymmetric Yang-Mills theory to be proportional to the square root of the coupling strength whereas  $\eta/s$  asymptotically approaches the quantum lower bound as the coupling increases. Both of these ratios are shown as a function of the inverse coupling in Figure 1.2. For large 't Hooft coupling ( $\lambda$ ),  $\eta/s$  is already quite close to  $1/4\pi$ , whereas  $T^3/\hat{q}$  is still changing. This behavior has caused the authors of Ref. [22] to comment: “The ratio  $T^3/\hat{q}$  is a more broadly valid measure of the coupling strength of the medium than  $\eta/s$ .”

In vacuum, the hard scattered parton creates a shower of particles that eventually form a cone of hadrons, referred to as a jet. In the quark-gluon plasma, the lower energy portion of the shower may eventually be equilibrated into the medium, thus giving a window on the rapid thermalization process in heavy ion collisions. This highlights part of the reason for needing to measure the fully reconstructed jet energy and the correlated particle emission with respect to the jet at all energy scales. In particular, coupling parameters such as  $\hat{q}$  and  $\hat{e}$  are scale dependent and must take on weak coupling values at high enough energies and strong coupling values at thermal energies.

The focus of this proposal is the measurement of jet probes of the medium as a way of understanding the coupling of the medium, the origin of this coupling, and the mechanism of rapid equilibration. The quark-gluon plasma is one form of the “condensed matter” of QCD and in any rigorous investigation of condensed matter of any type, it is critical to make measurements as one pushes the system closer to and further from a phase transition and with probes at different length scales. Substantially extending these scales with measurements at RHIC, particularly closer to the transition temperature and at longer distance scales, is the unique ability provided by this proposal.



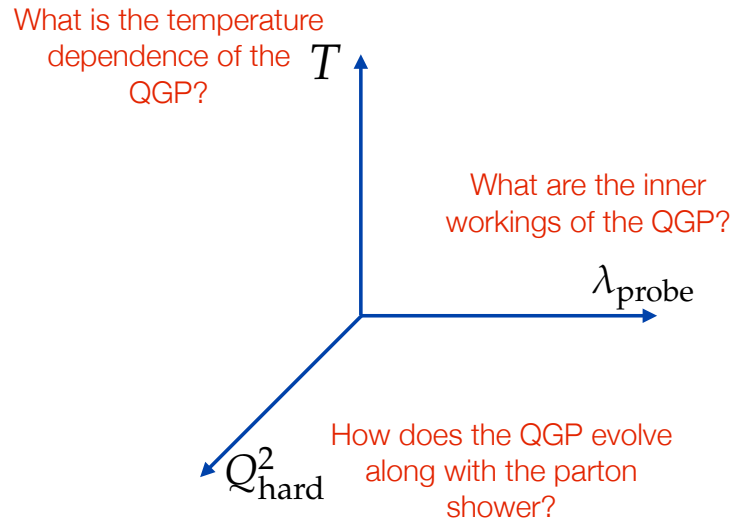


**Figure 1.3:** Pushing Three illustrative axes along which the quark-gluon plasma may be pushed and probed. The axes are the temperature of the quark-gluon plasma, the  $Q_{\text{hard}}^2$  of the hard process that sets of the scale for the virtuality evolution of the probe, and the wavelength with which the parton probes the medium  $\lambda_{\text{probe}}$ .

The critical variables to manipulate for this program are the temperature of the quark-gluon plasma, the length scale probed in the medium, and the virtuality of the hard process as shown schematically in Figure 1.3. In the following three sections we detail the physics of each axis.

## 1.2 What is the temperature dependence of the QGP?

The internal dynamics of more familiar substances—the subjects of study in conventional condensed matter and material physics—are governed by quantum electrodynamics. It is well known that near a phase boundary they demonstrate interesting behaviors, such as the rapid change in the shear viscosity to entropy density ratio,  $\eta/s$ , near the critical temperature,  $T_c$ . This is shown in Figure 1.4 for water, nitrogen, and helium [24]. Despite the eventual transition to superfluidity at temperatures below  $T_c$ ,  $\eta/s$  for these materials remains an order of magnitude above the conjectured quantum bound of Kovtun, Son, and Starinets (KSS) derived from string theory [15]. These observations provide a deeper understanding of the nature of these materials: for example the coupling between the fundamental constituents, the degree to which a description in terms of quasiparticles is important, and the description in terms of normal and superfluid components.

The dynamics of the QGP are dominated by Quantum Chromodynamics and the experimental characterization of the dependence of  $\eta/s$  on temperature will lead to a deeper understanding of strongly coupled QCD near this fundamental phase transition. Theoretically, perturbative calculations in the weakly coupled limit indicate that  $\eta/s$  decreases slowly as one approaches  $T_c$  from above, but with a minimum still a factor of 20 above the KSS bound [25] (as shown in the right panel of Figure 1.4). However, as indicated by the dashed lines in the figure, the perturbative

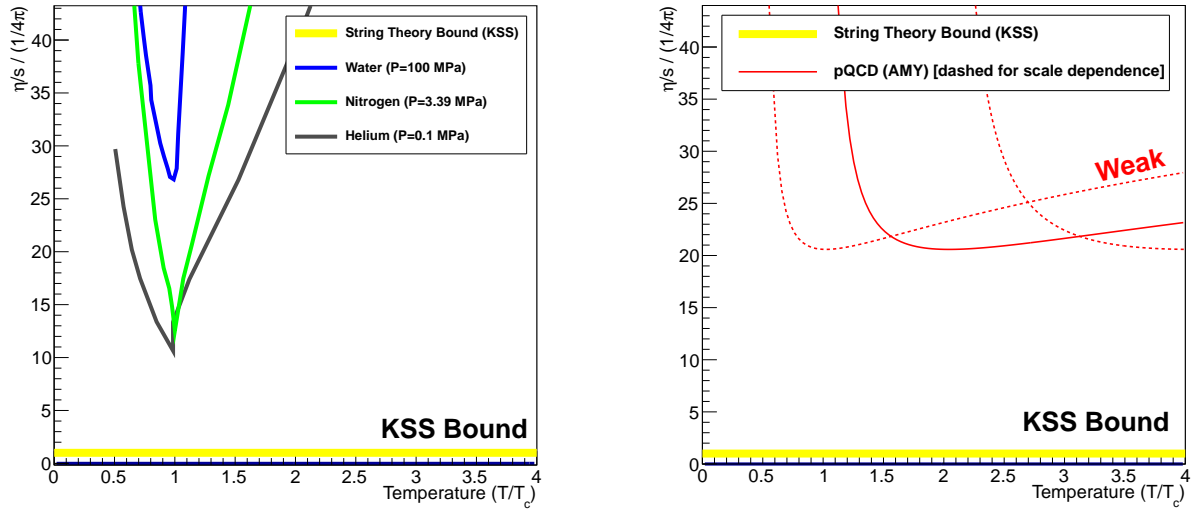


**Figure 1.4:** (left) The ratio of shear viscosity to entropy density,  $\eta/s$ , normalized by the conjectured KSS bound as a function of the reduced temperature,  $T/T_c$ , for water, nitrogen, and helium. The cusp for Helium corresponds to the case at the critical pressure. (right) Calculation of hot QCD matter (quark-gluon plasma) for a weakly coupled system. Dashed lines show the scale dependence of the perturbative calculation.

calculation has a large renormalization scale dependence and results for different values of the scale parameter ( $\mu, \mu/2, 2\mu$ ) diverge from each other near  $T_c$ .

Figure 1.5 (left panel) shows several state-of-the-art calculations for  $\eta/s$  as a function of temperature. Hadron gas calculations show a steep increase in  $\eta/s$  below  $T_c$  [26], and similar results using the UrQMD model have also been obtained [27]. Above  $T_c$  there is a lattice calculation in the SU(3) pure gauge theory [28] resulting in a value near the KSS bound at  $T = 1.65 T_c$ . Calculations in the semi-QGP model [29], in which color is not completely ionized, have a factor of five increase in  $\eta/s$  in the region of  $1-2 T_c$ . Also shown are calculations from a quasiparticle model (QPM) with finite  $\mu_B$  [30] indicating little change in  $\eta/s$  up to  $2 T_c$ . There is also an update on the lower limit on  $\eta/s$  from second order relativistic viscous hydrodynamics [31], with values remaining near  $1/4\pi$ . It is safe to say that little is known in a theoretically reliable way about the nature of this transition or the approach to weak-coupling.

Hydrodynamic modeling of the bulk medium does provide constraints on  $\eta/s$ , and recent work has been done to understand the combined constraints on  $\eta/s$  as a function of temperature utilizing both RHIC and LHC flow data sets [32, 33, 34, 35]. The results from [35] as constrained by RHIC and LHC data on hadron transverse momentum spectra and elliptic flow are shown in Figure 1.5 (left panel). These reach the pQCD weak coupled value at  $20 \times 1/4\pi$  for  $T = 3.4 T_c$ . Also shown are two scenarios, labeled “Song-a” and “Song-b”, for  $\eta/s(T)$  in [33] from which the authors conclude that “one cannot unambiguously determine the functional form of  $\eta/s(T)$  and whether the QGP fluid is more viscous or more perfect at LHC energy.”

Shown in Figure 1.5 (right panel) are three possible scenarios for a more or less rapid modification

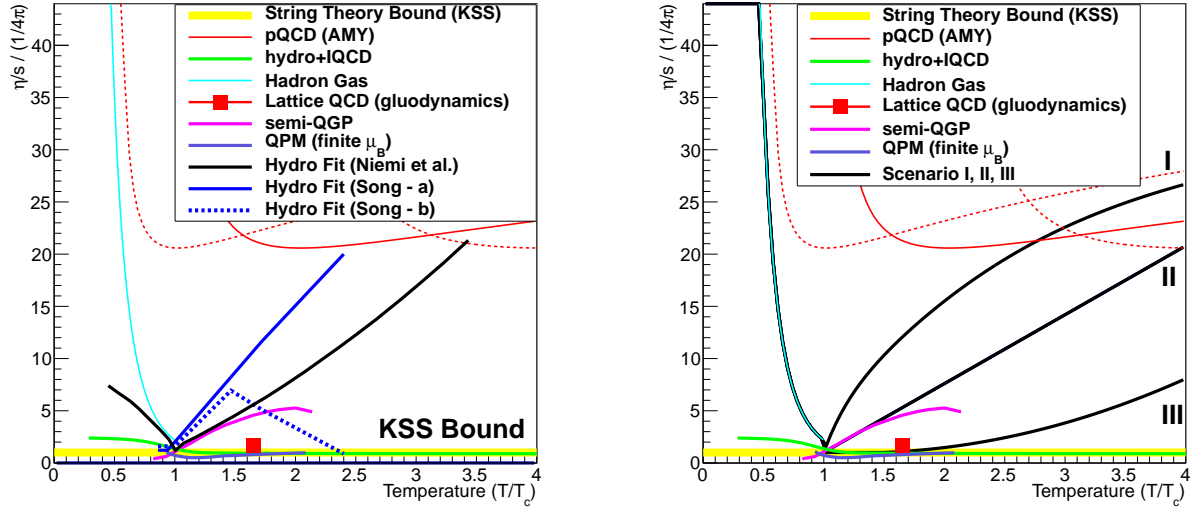


**Figure 1.5:** (left) Shear viscosity divided by entropy density,  $\eta/s$ , renormalized by the conjectured KSS bound as a function of the reduced temperature,  $T/T_c$ , with various calculations for the quark-gluon plasma case. See text for discussion. (right) Figure with three conjectured scenarios for the quark-gluon plasma transitioning from the strongly coupled bound (as a near-perfect fluid) to the weakly coupled case.

of the medium from the strong to the weak coupling limit. Scenario I has the most rapid change in  $\eta/s(T)$  following the “Song-a” parametrization and Scenario III has the least rapid change going through the lattice QCD pure glue result [28]. It is imperative to map out this region in the ‘condensed matter’ physics of QCD and extract the underlying reason for the change.

The above discussion has focused on  $\eta/s$  as the measure of the coupling strength of the quark-gluon plasma. However, both  $\eta/s$  and jet probe parameters such as  $\hat{q}$  and  $\hat{e}$  are sensitive to the underlying coupling of the matter, but in distinct ways. Establishing for example the behavior of  $\hat{q}$  around the critical temperature is therefore essential to a deep understanding of the quark-gluon plasma. Hydrodynamic modeling may eventually constrain  $\eta/s(T)$  very precisely, though it will not provide an answer to the question of the microscopic origin of the strong coupling (something naturally available with jet probes).

The authors of Ref [22] propose a test of the strong coupling hypothesis by measuring both  $\eta/s$  and  $\hat{q}$ . They derive a relation between the two quantities expected to hold in the weak coupling limit:

$$\hat{q} \stackrel{?}{=} \frac{1.25T^3}{\eta/s}. \quad (1.1)$$

The authors conclude that “an unambiguous determination of both sides of [the equation] from experimental data would thus permit a model independent, quantitative assessment of the strongly coupled nature of the quark-gluon plasma produced in heavy ion collisions.” For the three scenarios of  $\eta/s(T)$  shown in Figure 1.5 (right panel), we calculate  $\hat{q}$  as a function of temperature assuming the equivalence case in Eqn. 1.1 and the result is shown in Figure 1.6 (left panel). The inset in Figure 1.6 shows a magnified view of the region around  $T_c$  and a significant local maximum in  $\hat{q}$  is

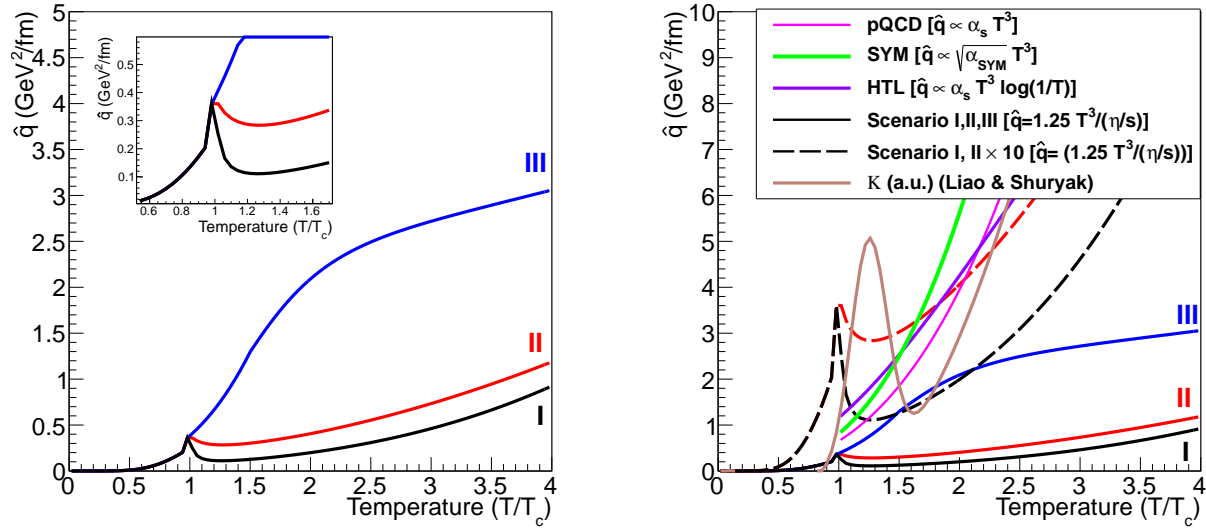


**Figure 1.6:** (left)  $\hat{q}$  as a function of  $T/T_c$  in the three scenarios as related with the weak-coupling calculation. (right) Different calculations for the scaling of  $\hat{q}$  under weak and strong coupling assumptions.

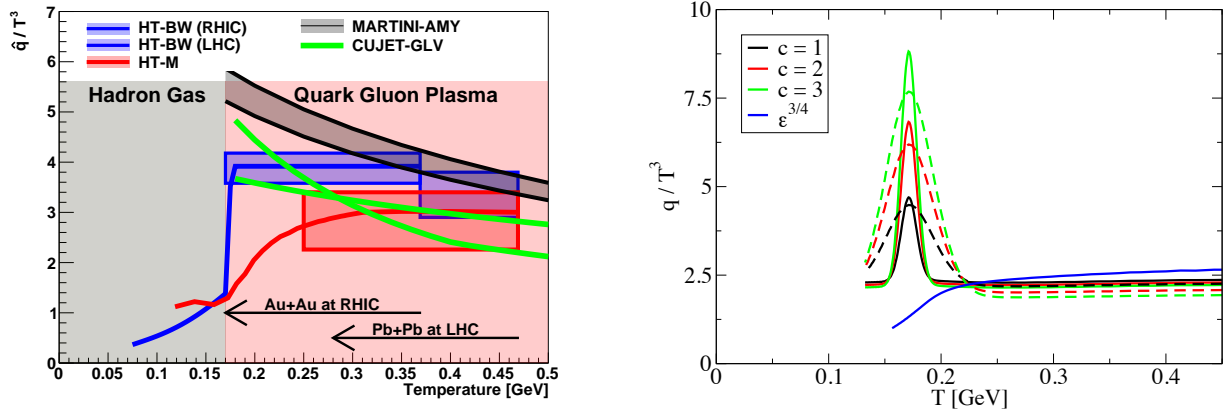
observed in scenarios I and II.

Figure 1.6 (right panel) shows that for the equivalence relation of Eqn. 1.1, all three scenarios have a result that differs significantly from the simple perturbative expectation of  $\alpha_s T^3$  [36]. Also shown in Figure 1.6 are the predicted temperature dependence of  $\hat{q}$  in the strongly coupled AdS/CFT (supersymmetric Yang-Mills) case [23] and the Hard Thermal Loop (HTL) case [37].

Since the expected scaling of  $\hat{q}$  with temperature is such a strong function of temperature, jet quenching measurements should be dominated by the earliest times and highest temperatures. In order to have sensitivity to temperatures around  $1-2 T_c$ , measurements at RHIC are needed in contrast to the LHC where larger initial temperatures are produced. In addition, the ability of RHIC to provide high luminosity heavy-ion collisions at a variety of center of mass energies can be exploited to probe the detailed temperature dependence of quenching right in the vicinity of  $T_c$ .

Theoretical developments constrained simultaneously by data from RHIC and the LHC have been important in discriminating against some models with very large  $\hat{q}$  – see Figure 1.16 from Ref. [38] and theory references therein. Models such as PQM and ASW with very large values of  $\hat{q}$  have been ruled out by the combined constraint. Shown in the left panel of Figure 1.7 is a recent compilation of four theoretical calculations with a directly comparable extraction of  $\hat{q}$ . Developments on the theory and experimental fronts have significantly narrowed the range of  $\hat{q}$  [1]. This theoretical progress lends strength to the case that the tools will be available on the same time scale as sPHENIX data to have precision determinations of  $\hat{q}$  and then ask deeper additional questions about the quark-gluon plasma and its underlying properties.

It is notable that a number of calculations favor an increased coupling strength near the transition temperature. Shown in the right panel of Figure 1.7 are a set of scenarios considered by Renk in Ref. [39]. This paper states that “Comparing weak coupling scenarios with data, NTC [near  $T_c$



**Figure 1.7:** (left) Calculations from four jet quenching frameworks constrained by RHIC and LHC  $R_{AA}$  data with results for  $\hat{q}/T^3$  as a function of temperature. Details of the calculation are given in Ref. [1]. (right) Near  $T_C$  enhancement scenarios of  $\hat{q}/T^3$  considered in Ref. [39].

enhancement] is favored. An answer to this question will require a systematic picture across several different high  $p_T$  observables.”

In Ref. [40], Liao and Shuryak use RHIC measurements of single hadron suppression and azimuthal anisotropy to infer that “the jet quenching is a few times stronger near  $T_c$  relative to the quark-gluon plasma at  $T > T_c$ .” This enhancement of  $\hat{q}$  is shown in Figure 1.6 (right panel) and is the result of color magnetic monopole excitations in the plasma near  $T_c$ .

Most recently this strong coupling picture with color magnetic monopole excitations has been implemented within CUJET 3.0 for a broader comparison with experimental observables and previous theory calculations [41]. Shown in Figure 1.8 are results from their constrained RHIC and LHC data fit for the temperature dependence of the scaled quenching power  $\hat{q}/T^3$ .

Within the jet quenching model WHDG [42], the authors constrain  $\hat{q}$  by the PHENIX  $\pi^0$  nuclear modification factor. They find the prediction scaled by the expected increase in the color charge density created in higher energy LHC collisions when compared to the ALICE results [43] over-predicts the suppression. This over-prediction based on the assumption of an unchanging probe-medium coupling strength led to title of Ref. [42]: “The surprisingly transparent sQGP at the LHC.” They state that “one possibility is the sQGP produced at the LHC is in fact more transparent than predicted.” Similar conclusions have been reached by other authors [44, 45, 46]. Recently work has been done to incorporate the running of the QCD coupling constant [47].

It is important to note that most all calculations predict a stronger coupling near the transition, even if just from the running of the coupling constant  $\alpha_s$ , and the goal is to experimentally determine the degree of the effect. Lower energy data at RHIC also provides important constraints – see for example Refs. [48, 49]. The full set of experimental observables need to be considered spanning the largest range of collision energy, system size, and engineering path length.

One observable that has been particularly challenging for energy loss models to reproduce is the azimuthal anisotropy of  $\pi^0$  production with respect to the reaction plane. A weak dependence on the path length in the medium is expected from radiative energy loss. This translates into a small

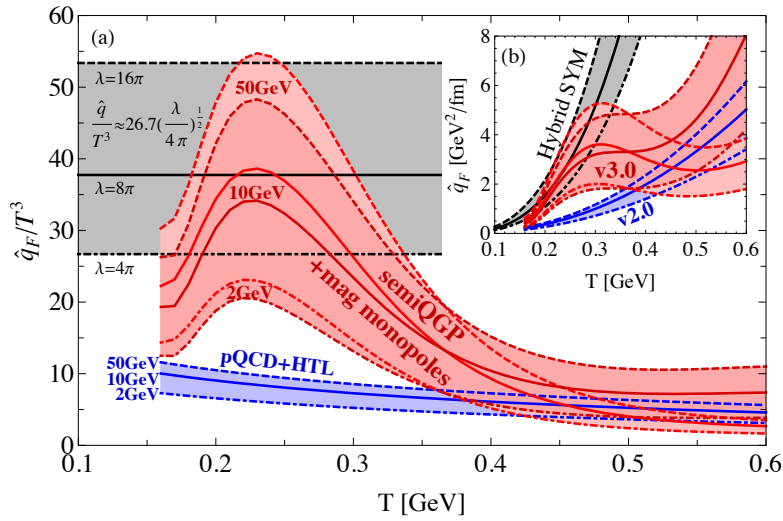


**Figure 1.8:** Results from calculations within CUJET 3.0 with magnetic monopole excitations that result in enhanced coupling near  $T_c$ . Plotted are the constraints on  $\hat{q}/T^3$  as a function of temperature as shown in Ref. [41].

$v_2$  for high  $p_T$  particles (i.e., only a modest difference in parton energy loss when going through a short versus long path through the QGP). Results of  $\pi^0 v_2$  are shown in Figure 1.9 [50]. Weakly coupled radiative energy loss models are compared to the  $R_{AA}$  (bottom panels) and  $v_2$  (top panels) data. These models reproduce the  $R_{AA}$ , but they fall far short of the  $v_2$  data in both  $p_T$  ranges measured (6–9 GeV/c and  $> 9$  GeV/c). This large path length dependence is naturally described by strongly coupled energy loss models [51, 50]. Note that one can match the  $v_2$  by using a stronger coupling, larger  $\hat{q}$ , but at the expense of over-predicting the average level of suppression. New strong coupling models [52, 53] also need to confront the full data set available at RHIC.

The measurement of jet quenching observables as a detailed function of orientation with respect to the reaction plane is directly sensitive to the coupling strength and the path length dependence of the modification to the parton shower. In addition, medium response may be optimally measured in mid-central collisions with a lower underlying event and where the medium excitations are not damped out over a longer time evolution. Shown in Figure 1.10 are projected uncertainties from sPHENIX — detailed in the chapter on physics performance — for the direct photon and reconstructed jet observables in three orientation selections. One expects no orientation dependence for the direct photons and the question is whether the unexpectedly large dependence for charged hadrons persists in reconstructed jets up to the highest  $p_T$ . Note that the same measurements can be made for beauty tagged jets, charged hadrons up to 50 GeV/c, and a full suite of correlation measurements including jet-jet, hadron-jet,  $\gamma$ -jet.

All measurements in heavy ion collisions are the result of emitted particles integrated over the entire time evolution of the reaction, covering a range of temperatures. Similar to the hydrodynamic model constraints, the theory modeling for jet probes requires a consistent temperature and scale dependent model of the quark-gluon plasma and is only well constrained by precision data through different temperature evolutions, as measured at RHIC and the LHC.

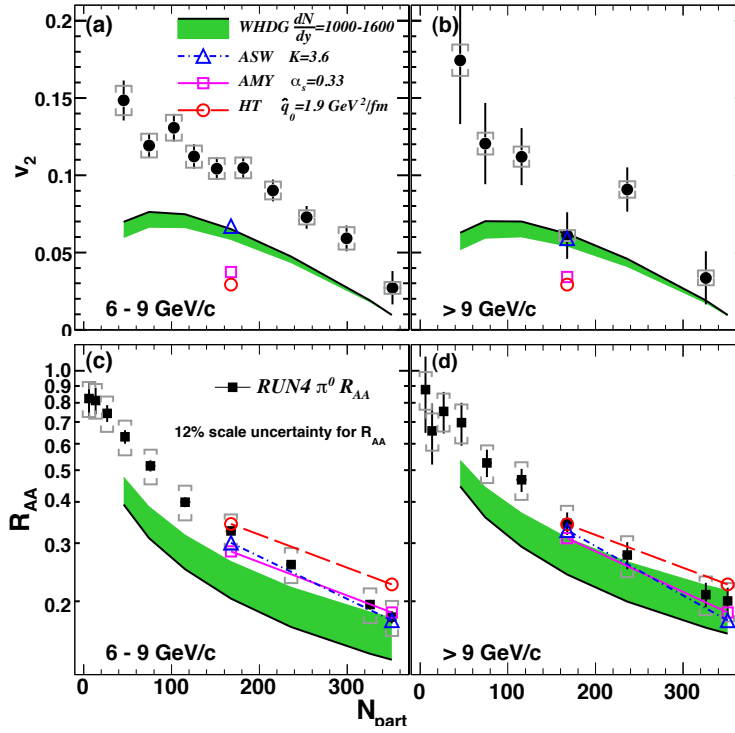


**Figure 1.9:**  $\pi^0$   $v_2$  (top panels) and  $R_{AA}$  (bottom panels) for  $6 < p_T < 9$  GeV/c (left panels) and  $p_T > 9$  GeV/c (right panels). Calculations from four weakly coupled energy loss models are shown as well [54, 55]. From Ref. [50].

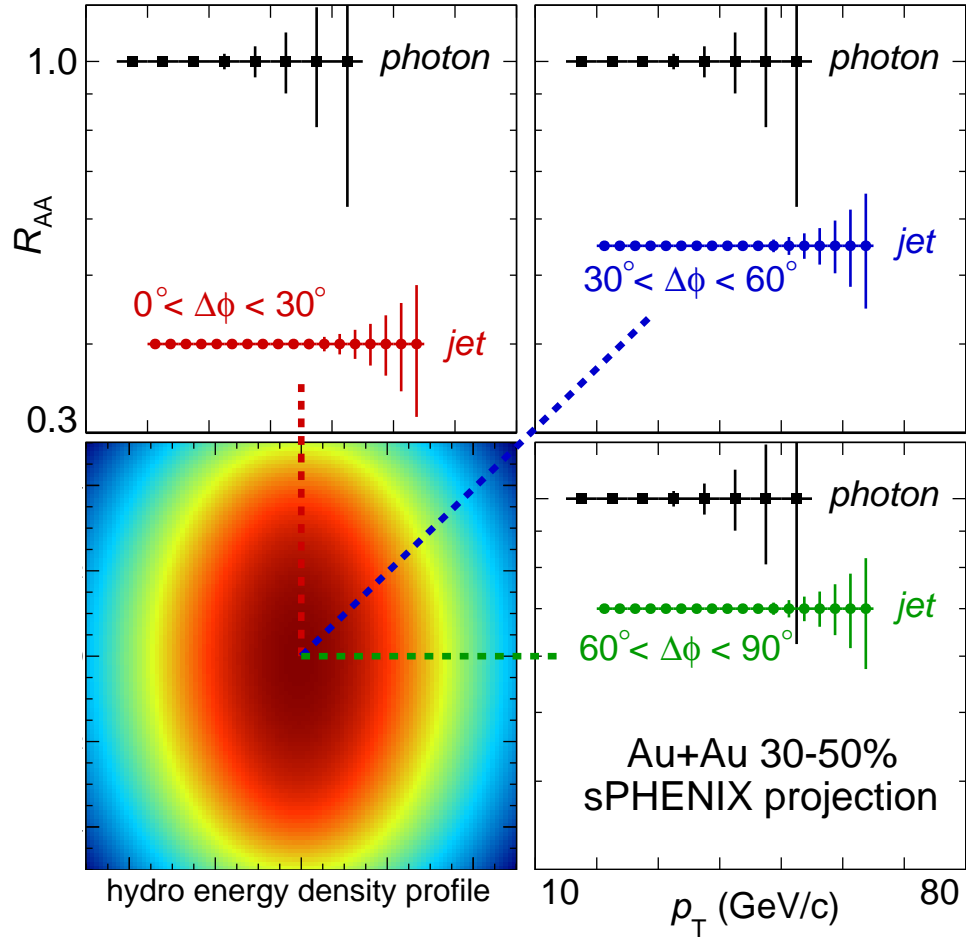


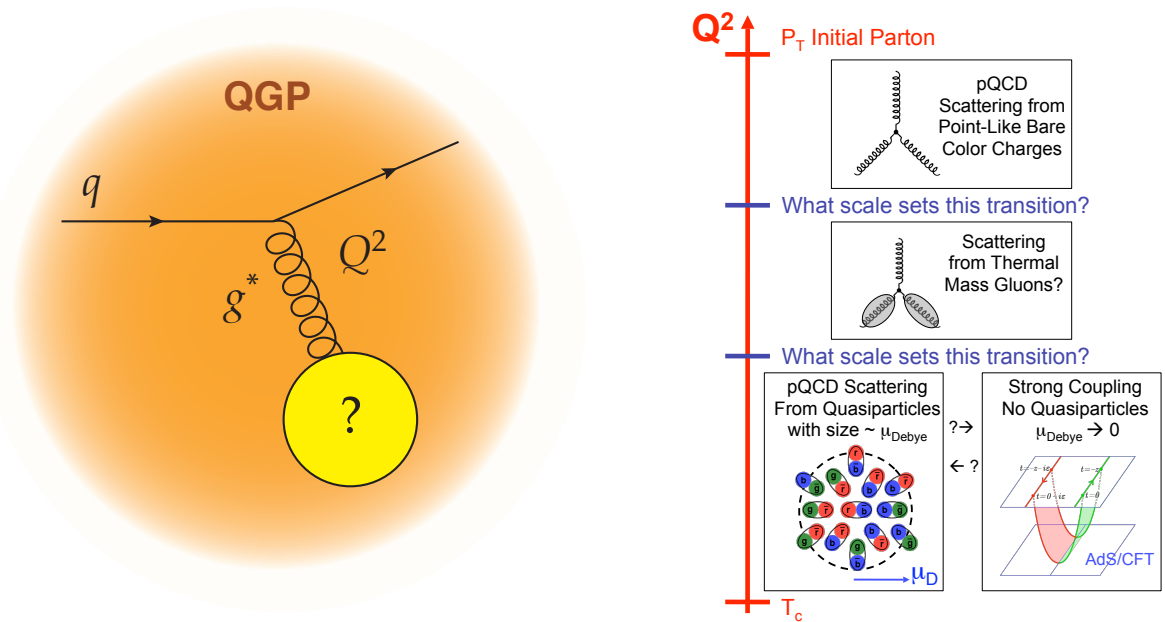
**Figure 1.10:** Demonstration of the statistical reach for azimuthally-sensitive hard probes measurements in sPHENIX. Each panel shows the projected statistical uncertainty for the  $R_{AA}$  of inclusive jets and photons, with each a panel a different  $\Delta\phi$  range with respect to the reaction plane in 30–50% Au+Au events. sPHENIX would additionally have tremendous statistical reach in the analogous charged hadron  $R_{AA}$ .



### 1.3 What are the inner workings of the QGP?

A second axis along which one can investigate the underlying structure of the quark-gluon plasma concerns the question of what length scale of the medium is being probed by jet quenching processes. In electron scattering, the scale is set by the virtuality of the exchanged photon,  $Q^2$ . By varying this virtuality one can obtain information over an enormous range of scales: from pictures of viruses at length scales of  $10^{-5}$  meters, to the partonic make-up of the proton in deep inelastic electron scattering at length scales of less than  $10^{-18}$  meters.

For the case of hard scattered partons in the quark-gluon plasma, the length scale probed is initially set by the virtuality of the hard scattering process. Thus, at the highest LHC jet energies, the parton initially probes a very short length scale. Then as the evolution proceeds, the length scale is set by the virtuality of the gluon exchanged with the color charges in the medium, as shown in the left panel of Figure 1.11. However, if the exchanges are coherent, the total coherent energy loss through the medium may set the length scale.



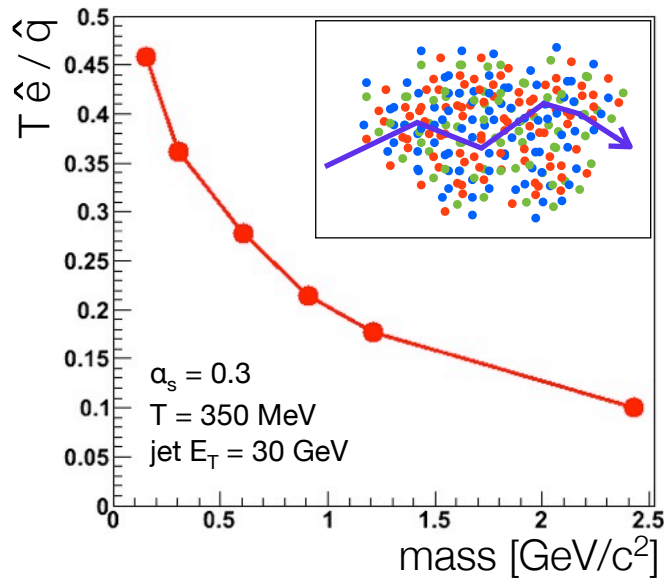
**Figure 1.11:** (left) Diagram of a quark exchanging a virtual gluon with an unknown object in the QGP. This highlights the uncertainty for what sets the scale of the interaction and what objects or quasiparticles are recoiling. (right) Diagram as a function of the  $Q^2$  for the net interaction of the parton with the medium and the range of possibilities for the recoil objects.

Figure 1.11 (right panel) shows that if the length scale probed is very small then one expects scattering directly from point-like bare color charges, most likely without any influence from quasiparticles or deconfinement. As one probes longer length scales, the scattering may be from thermal mass gluons and eventually from possible quasiparticles with size of order the Debye screening length. In Ref. [56], Rajagopal states that “at some length scale, a quasiparticle picture of the QGP must be valid, even though on its natural length scale it is a strongly coupled fluid. It will be a challenge to see and understand how the liquid QGP emerges from short-distance quark

and gluon quasiparticles.”

The extension of jet measurements over a wide range of energies and with different medium temperatures again gives one the largest span along this axis. What the parton is scattering from in the medium is tied directly to the balance between radiative energy loss and inelastic collisional energy loss in the medium (encoded in  $\hat{q}$  and  $\hat{e}$ ). In the limit that the scattering centers in the medium are infinitely massive, one only has radiative energy loss—as was assumed for nearly 10 years to be the dominant parton energy loss effect. In the model of Liao and Shuryak [40], the strong coupling near the quark-gluon plasma transition is due to the excitation of color magnetic monopoles, and this should have a significant influence on the collisional energy loss and equilibration of soft partons into the medium.

In a model by Coleman-Smith [57, 58] consisting of parton showers propagating in a medium of deconfined quarks and gluons, one can directly vary the mass of the effective scattering centers and extract the resulting values for  $\hat{e}$  and  $\hat{q}$ . Figure 1.12 shows  $T\hat{e}/\hat{q}$  as a function of the mass of the effective scattering centers in this model. In the limit of infinitely massive scattering centers, the interactions are elastic and no energy is transferred to the medium.



**Figure 1.12:**  $T\hat{e}/\hat{q}$  as a function of the mass of the effective scattering centers in the medium. As the mass increases, the parton is less able to transfer energy to the medium and the ratio drops.

Many observables are sensitive to the balance of  $\hat{e}$  and  $\hat{q}$ , and thus sensitive to what is being scattered from in the medium. For example, in the same calculation by Coleman-Smith [59], the transverse radial jet energy profile is significantly modified by the balance of collisional and radiative energy loss. Shown in the left panels Figure 1.13 are the vacuum and medium modified fractional energy distribution as a function of distance  $R$  from the jet axis. The upper left panel is including both elastic and inelastic processes and the lower left panel with only elastic processes. In the right panel we show the ratio of the profiles and for three different effective medium coupling parameters. The sub-leading jet profiles are dramatically modified compared to the vacuum and leading jet profiles. The elastic and radiative profiles clearly separate, the radiative sub-leading jets become

broader and softer than the elastic only. Both sets of sub-leading jets become much broader and softer compared to the leading jets.

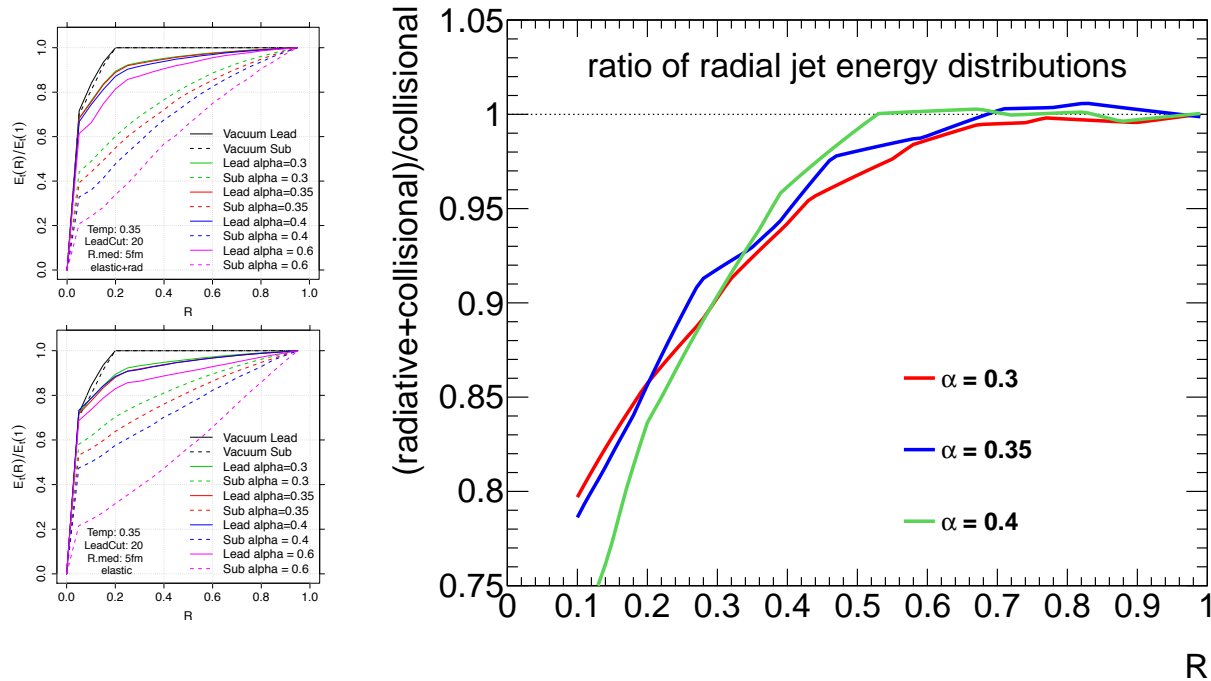


**Figure 1.13:** (left) Calculations from Coleman-Smith [59] showing the jet energy profile as a function of radius for leading (solid lines) and sub-leading (dashed lines) jets. Leading jets have  $E_T > 20$  GeV and sub-leading jets have  $E_T > 5$  GeV. The medium temperature is 350 MeV. (right) Ratio the radial distribution of energy in sub-leading jets in a medium with radiative and elastic energy loss to the distribution in a medium with elastic energy loss only. In these calculations,  $\alpha$  serves as a proxy for the effective medium coupling.

In the calculation by Vitev et al. [60, 61, 62], the inclusion of collisional energy loss results in a substantial shift in the dijet asymmetry as shown comparing the top left and the bottom left of Figure 1.14. The right panel of Figure 1.14 shows the  $A_J$  ratio with and without collisional energy loss. There is a significant additional suppression of back-to-back matched jets at low  $A_J$  and a much larger number of very asymmetric jet pairs. Detailed measurements as a function of jet energy, jet radius, and collision geometry are needed to map out the magnitude of the collisional component, and thus  $\hat{e}$  and its related effective mass of the scattering centers.

One of the most sensitive observables to collisional energy loss is the modification of high  $p_T$  charm and beauty heavy quarks in the medium. We detail this physics in the later section specifically on heavy quarks – Section 1.8.

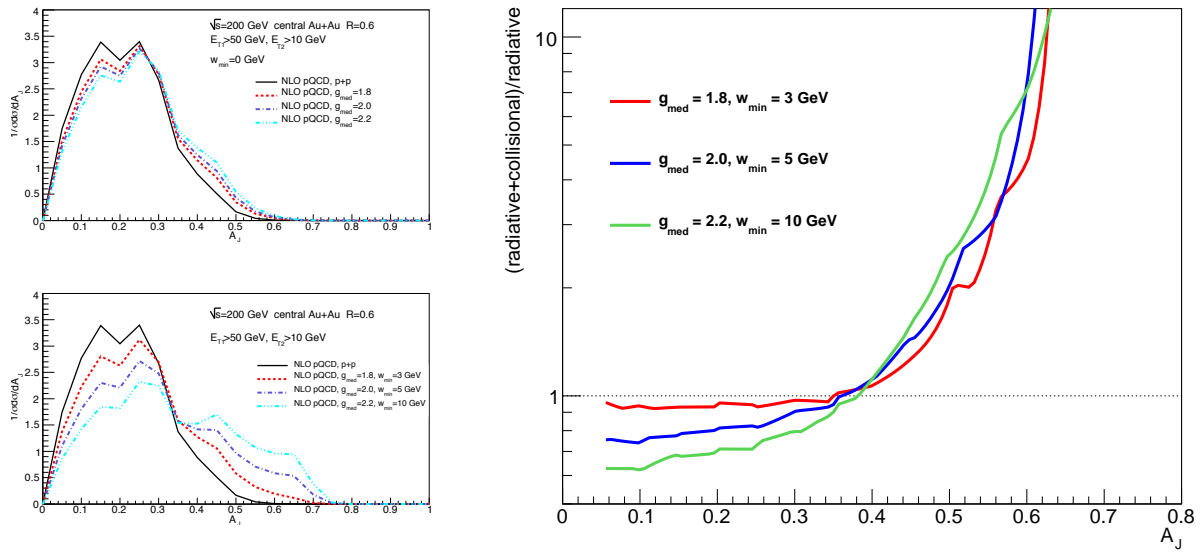


**Figure 1.14:** (left)  $A_J$  distributions calculated by Vitev et al. [60, 61, 62] for leading jet  $E_T > 50$  GeV, jet cone radius,  $R = 0.6$  and different medium coupling strengths. The upper plot shows results for radiative energy loss only, and the lower plot includes collisional energy loss as well. (right) Ratio of  $A_J$  distributions with radiative and collisional energy loss to those with radiative energy loss only.

## 1.4 How does the QGP evolve along with the parton shower?

The initial hard scattered parton starts out very far off-shell and in  $e^+e^-$ ,  $p+p$  or  $p+\bar{p}$  collisions the virtuality evolves in vacuum through gluon splitting down to the scale of hadronization. In heavy ion collisions, the vacuum virtuality evolution is interrupted at some scale by scattering with the medium partons which increase the virtuality with respect to the vacuum evolution. Figure 1.15 shows the expected evolution of virtuality in vacuum, from medium contributions, and combined for a quark-gluon plasma at  $T_0 = 300$  MeV with the traversal of a 30 GeV parton (left) and at  $T_0 = 390$  MeV with the traversal of a 200 GeV parton (right) [63, 64]. If this picture is borne out, it “means that the very energetic parton [in the right picture] hardly notices the medium for the first 3–4 fm of its path length [64].” Spanning the largest possible range of virtuality (initial hard process  $Q^2$ ) is very important, but complementary measurements at both RHIC and LHC of produced jets at the same virtuality (around 50 GeV) will test the interplay between the vacuum shower and medium scattering contributions.

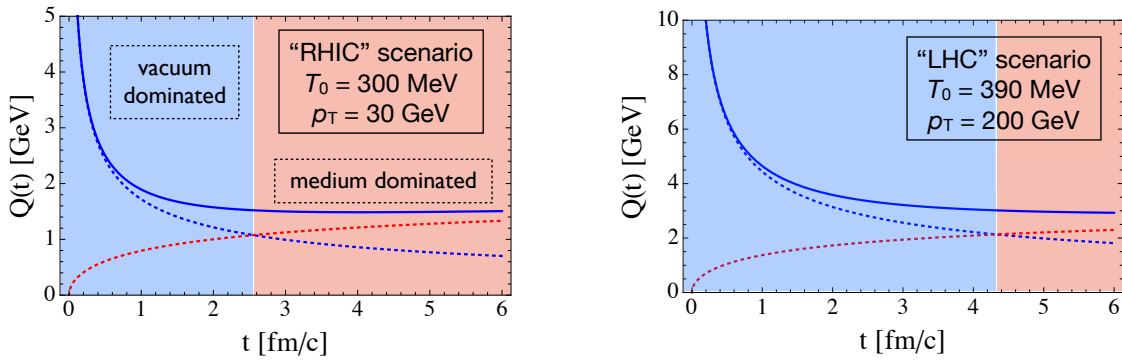


**Figure 1.15:** Jet virtuality evolution in medium at RHIC (left) and LHC (right). Vacuum contributions to virtuality (blue dashed lines) decrease with time and medium induced contributions (red dashed lines) increase as the parton scatters in the medium. The total virtuality (blue solid lines) is the quadrature sum of the two contributions. At RHIC the medium induced virtuality dominates by 2.5 fm/c while at the LHC the medium term does not dominate until 4.5 fm/c. From Ref. [63].

In some theoretical frameworks — for example Refs [65, 66, 67] — the parton splitting is simply dictated by the virtuality and in vacuum this evolves relatively quickly from large to small scales as shown above. The  $Q$  evolution means that the jet starts out being considerably off mass shell when produced, and this off-shellness is reduced by successive splits to less virtual partons. In these calculations, the scattering with the medium modifies this process of parton splitting. The scale of the medium as it relates to a particular parton is  $\hat{q}$  times the parton lifetime (this is the mean transverse momentum that the medium may impart to the parent and daughter partons during the splitting process). When the parton’s off-shellness is much larger than this scale, the effect of the medium on this splitting process is minimal. As the parton drops down to a lower scale, the medium begins to affect the parton splitting more strongly.

Shown in Figure 1.16 is the single hadron  $R_{AA}$  in central Au+Au collisions at 200 GeV along side measurements at other beam energies. One specifically notes that for the YAJEM calculation, inclusion of the virtuality evolution leads to a factor of 50% rise in  $R_{AA}$  from 20–40 GeV/c, and in the HT-M calculation a 100% rise. A strong rise in  $R_{AA}$  measured at higher  $p_T$  at the LHC has

been observed, and measurement of the consistent effect within the same framework at RHIC is a key test of this virtuality evolution description. It is notable that the JEWEL calculation which describes the rising  $R_{AA}$  at the LHC [68], results in a nearly flat  $R_{AA}$  over the entire  $p_T$  range at RHIC. sPHENIX can perform precision measurements of charged hadrons over this  $p_T$  range.

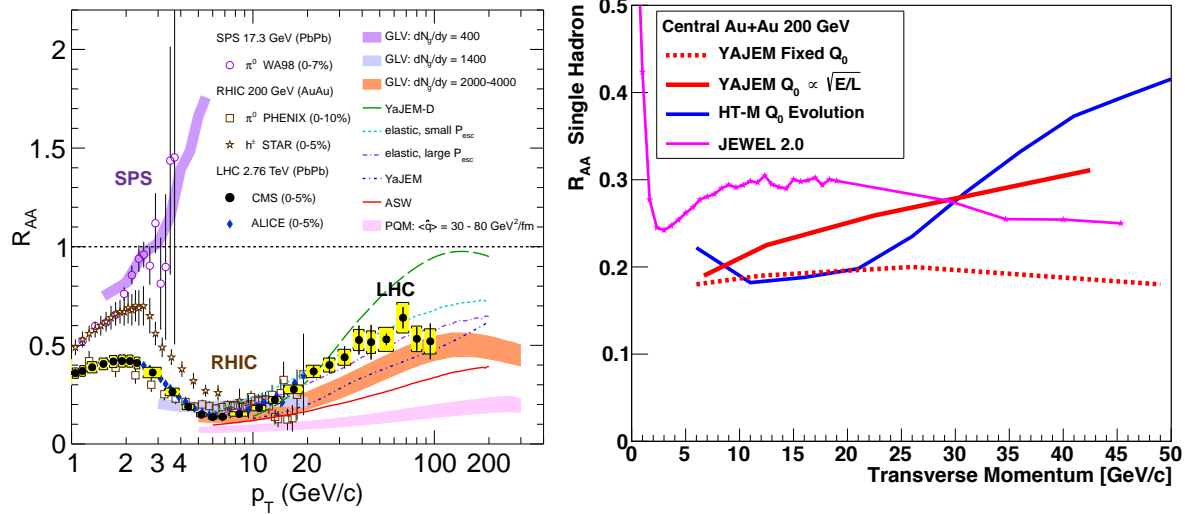


**Figure 1.16:** (left) The nuclear modification factor  $R_{AA}$  as a function of transverse momentum in A+A collisions at the SPS, RHIC, and LHC. Comparisons with various jet quenching calculations as detailed in Ref. [38] and references therein are shown. The simultaneous constraint of RHIC and LHC data is a powerful discriminator. (right) Predictions for single hadrons  $R_{AA}$  to  $p_T \sim 50$  GeV/c in central Au+Au at 200 GeV.

Further emphasizing the importance of having such measurements over the maximum kinematic reach at RHIC and the LHC are the recent jet and charged hadron  $R_{pA}$  measurements shown in Figure 1.17. It is quite striking that the flat reconstructed jet  $R_{AA}$  and rising charged hadron  $R_{AA}$  are mimicked already in proton-nucleus collisions. This may hint that all the physics of the rising hadron  $R_{AA}$  does not fully constrain the virtuality evolution and various calculations thus predict quite different effects at RHIC.

To convey the scale probed and virtuality evolution differences at RHIC and the LHC, we show the off-shellness of the initial hard scattered parton virtuality in units of  $1/\text{fm}$  as a function of the local temperature of the QGP medium where the parton resides in Figure 1.18. The calculation incorporates the vacuum virtuality evolution which falls off quickly with time and the medium scattering contribution that kicks the virtuality back up. We incorporate the full time evolution of pre-equilibrium dynamics, viscous hydrodynamics, and hadron cascade from Ref. [69] to map the time of the parton evolution to the local temperature. The medium virtuality contribution also scales with the local temperature. The red (black) curves are for different initial parton energies in the RHIC (LHC) medium. The thicker line regions highlight where the medium virtuality has a substantial influence on the parton splitting. It is notable that highest energy partons at the LHC, of order 1 TeV, are always dominated by the initial vacuum virtuality evolution (for more than 10 fm/c). In contrast, the lower energy jets and the RHIC medium evolution have the largest

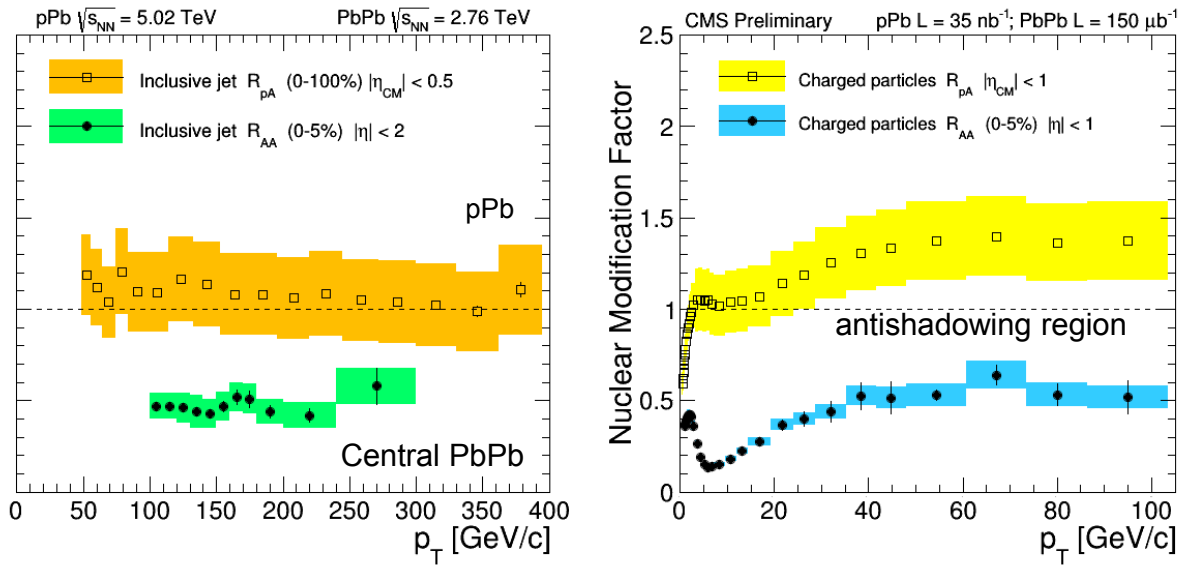


**Figure 1.17:** (left) Preliminary results from CMS showing the jet  $R_{AA}$  in  $p+A$  near 1 and in Pb+Pb near 0.2. (right) Preliminary results from CMS showing the charged particle  $R_{AA}$  in  $p+A$  and in Pb+Pb. In contrast to the jet  $R_{AA}$  results which are essentially flat with  $p_T$ , the charged particle  $R_{AA}$  shows a rise with  $p_T$ .

influence and map out a unique part of this microscope resolving power and temperature of the quark-gluon plasma.

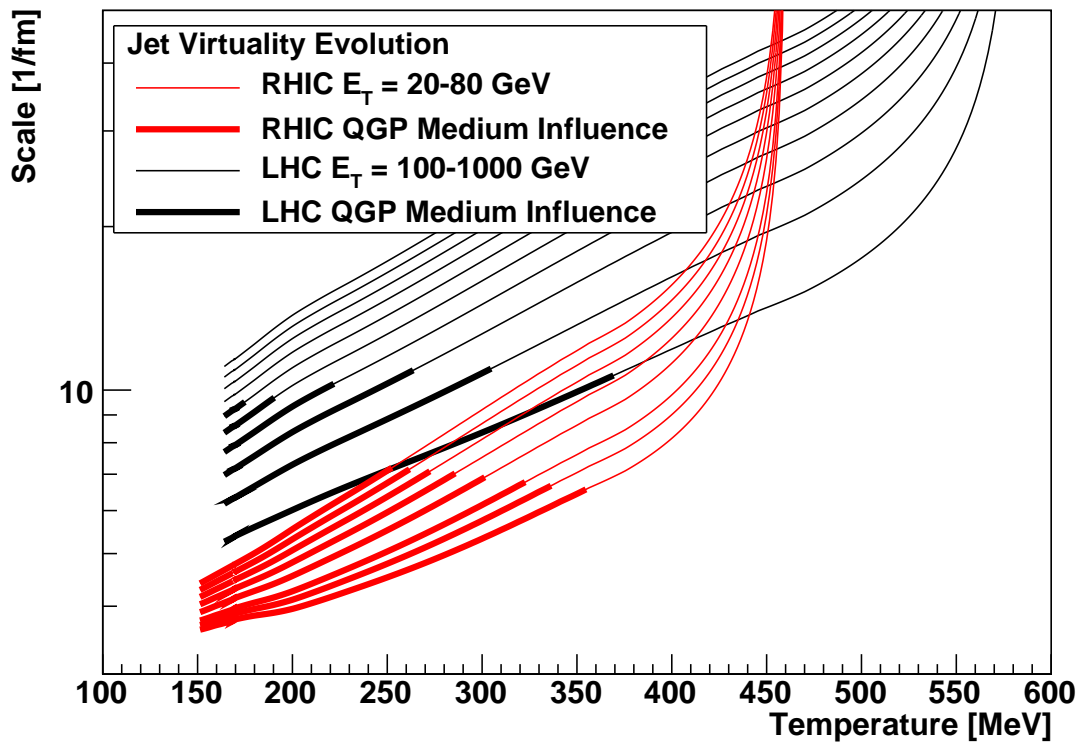


**Figure 1.18:** Scale probed in the medium in [1/fm] via high energy partons as a function of the local temperature in the medium. The red (black) curves are for different initial parton energies in the RHIC (LHC) medium.



## 1.5 Current jet probe measurements

Jet quenching (i.e., the significant loss of energy for partons traversing the QGP) was discovered via measurements at RHIC of the suppression of single hadron yields compared to expectations from  $p+p$  collisions [70, 71]. Since the time of that discovery there has been an enormous growth in jet quenching observables that have also pushed forward a next generation of analytic and Monte Carlo theoretical calculation to confront the data.

As detailed in Ref. [72, 54], many formalisms assuming weakly coupled parton probes are able to achieve an equally good description of the single inclusive hadron data at RHIC and the LHC. The single high  $p_T$  hadron suppression constrains the  $\hat{q}$  value within a model, but is not able to discriminate between different energy loss mechanisms and formalisms for the calculation. Two-hadron correlations measure the correlated fragmentation between hadrons from within the shower of one parton and also between the hadrons from opposing scattered partons. These measurements, often quantified in terms of a nuclear modification  $I_{AA}$  [73, 74, 75], are a challenge for models to describe simultaneously [76].

The total energy loss of the leading parton provides information on one part of the parton-medium interaction. Key information on the nature of the particles in the medium being scattered from is contained in how the soft (lower momentum) part of the parton shower approaches equilibrium in the quark-gluon plasma. This information is accessible through full jet reconstruction, jet-hadron correlation, and  $\gamma$ -jet correlation observables.

The measurements of fully reconstructed jets and the particles correlated with the jet (both inside the jet and outside) are crucial to testing these pictures. Not only does the strong coupling influence the induced radiation from the hard parton (gluon bremsstrahlung) and its inelastic collisions with the medium, but it also influences the way soft partons are transported by the medium outside of the jet cone as they fall into equilibrium with the medium. Thus, the jet observables combined with correlations get directly at the coupling of the hard parton to the medium and the parton-parton coupling for the medium partons themselves.

These jet observables are now available at the LHC. The first results based on reconstructed jets in heavy ion collisions were the centrality dependent dijet asymmetries measured by ATLAS [77]. These results, shown in Figure 1.19, indicate a substantial broadening of dijet asymmetry  $A_J = (E_1 - E_2)/(E_1 + E_2)$  distribution for increasingly central Pb+Pb collisions and the lack of modification to the dijet azimuthal correlations. The broadening of the  $A_J$  distribution points to substantial energy loss for jets and the unmodified azimuthal distribution shows that the opposing jet  $\Delta\phi$  distribution is not broadened as it traverses the matter. Figure 1.20 shows CMS results [78] quantifying the fraction of dijets which are balanced (with  $A_J < 0.15$ ) decreases with increasing centrality.

Direct photon-jet measurements are also a powerful tool to study jet quenching. Unlike dijet measurements the photon passes through the matter without losing energy, providing a cleaner handle on the expected jet  $p_T$  [79]. CMS has results for photons with  $p_T > 60$  GeV/c correlated with jets with  $p_T > 30$  GeV/c [80]. Though with modest statistical precision, the measurements indicate energy transported outside the  $R = 0.3$  jet cone through medium interactions. Similar results from the ATLAS experiment are shown in the left panel of Figure 1.21, again indicating a shifting of energy outside the opposing jet radius.

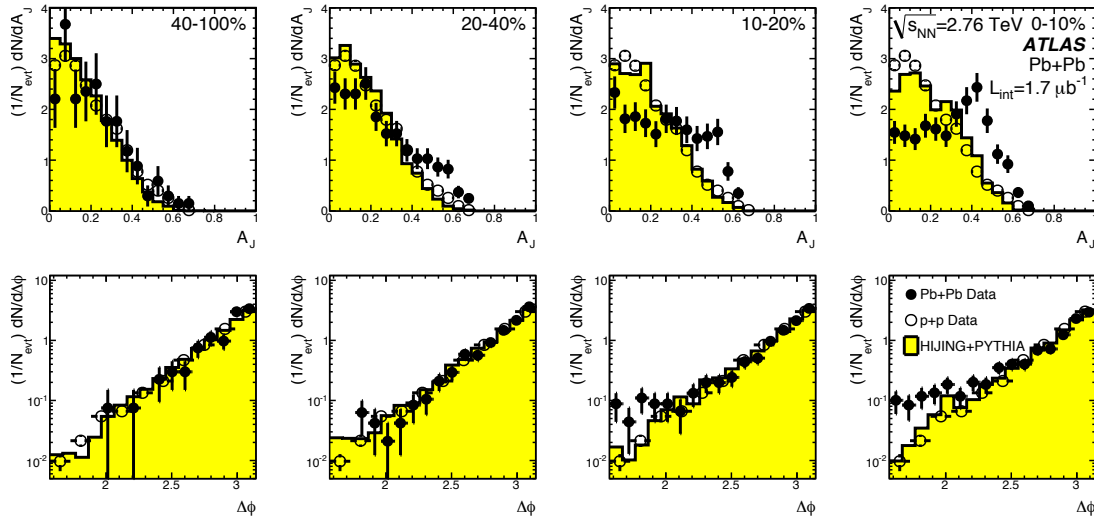


**Figure 1.19:**  $A_J$  (top row) and dijet  $\Delta\phi$  distribution from ATLAS [77]. Jets are reconstructed with the anti- $k_T$  algorithm with  $R = 0.4$ . The leading jet has  $E_T > 100$  GeV and the associated jet has  $E_T > 25$  GeV. Pb+Pb data (solid points),  $p+p$  data at 7 TeV (open points) and PYTHIA embedded in HIJING events and run through the ATLAS Monte Carlo (yellow histograms) are shown. From Ref. [77].

Reconstructed jets have significantly extended the kinematic range for jet quenching studies at the LHC, and quenching effects are observed up to the highest reconstructed jet energies ( $> 300$  GeV) [81]. They also provide constraints on the jet modification that are not possible with particle based measurements. For example, measurements from ATLAS constrain jet fragmentation modification from vacuum fragmentation to be small [82] and CMS results on jet-hadron correlations have shown that the lost energy is recovered in low  $p_T$  particles far from the jet cone [78]. The lost energy is transported to very large angles and the remaining jet fragments as it would in the vacuum.

Detector upgrades to PHENIX and STAR at RHIC with micro-vertex detectors will allow the separate study of  $c$  and  $b$  quark probes of the medium, as tagged via displaced vertex single electrons and reconstructed  $D$  and  $\Lambda_c$  hadrons. Similar measurements at the LHC provide tagging of heavy flavor probes as well – initial results on beauty tagged jets from CMS are shown in the right panel of Figure 1.21. These measurements also provide insight on the different energy loss mechanisms, in particular because initial measurements of non-photonic electrons from RHIC challenge the radiative energy loss models.

There are other preliminary results on fully reconstructed jets from both STAR [83, 84, 85, 86] and PHENIX experiments [87, 88]. However, these results have not yet proceeded to publication in part due to limitations in the measurement capabilities. In this proposal we demonstrate that a comprehensive jet detector (sPHENIX) with large, uniform acceptance and high rate capability, combined with the now completed RHIC luminosity upgrade can perform these measurements to access this key physics.

Figure 1.22 shows results from the STAR collaboration [89] on correlations between reconstructed

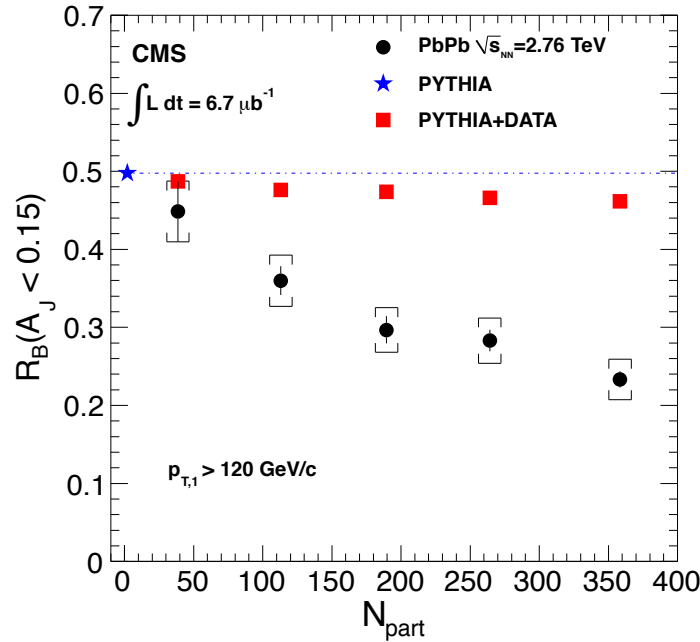


**Figure 1.20:** Fraction of dijets which have  $A_J < 0.15$  in Pb+Pb collisions as a function of centrality. Jets are reconstructed with an iterative cone algorithm with a radius of 0.5. The leading jet is required to have an  $E_T > 120$  GeV and the associated jet has  $E_T > 50$  GeV. Results are shown for Pb+Pb data (circles), PYTHIA (star) and PYTHIA jets embedded into real data (squares). From Ref. [78].

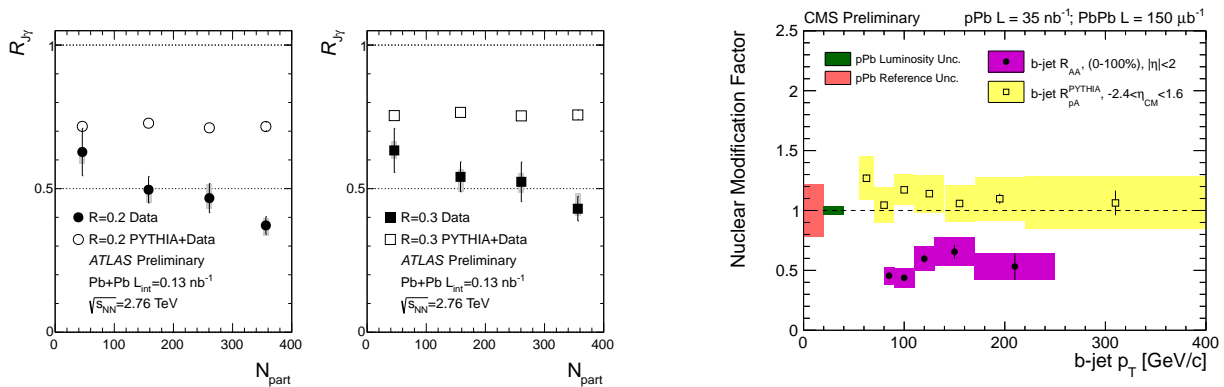


**Figure 1.21:** (left) ATLAS results on the change in balance of direct photons and jets in Pb+Pb collisions at the LHC. (right) CMS results on the  $R_{AA}$  for beauty tagged jets in Pb+Pb collisions at the LHC.

trigger jets and single charged hadrons. The experimental results show the difference in the away-side momentum of hadrons between Au+Au and  $p+p$  events. The extent to which this value differs from zero is an indication of the strength of the medium modification of the fragmentation process. The figure also compares these results to calculations obtained using the YAJEM-DE model that qualitatively reproduces the data.

Figure 1.23 shows a compilation panel with results from RHIC preliminary jet results and LHC

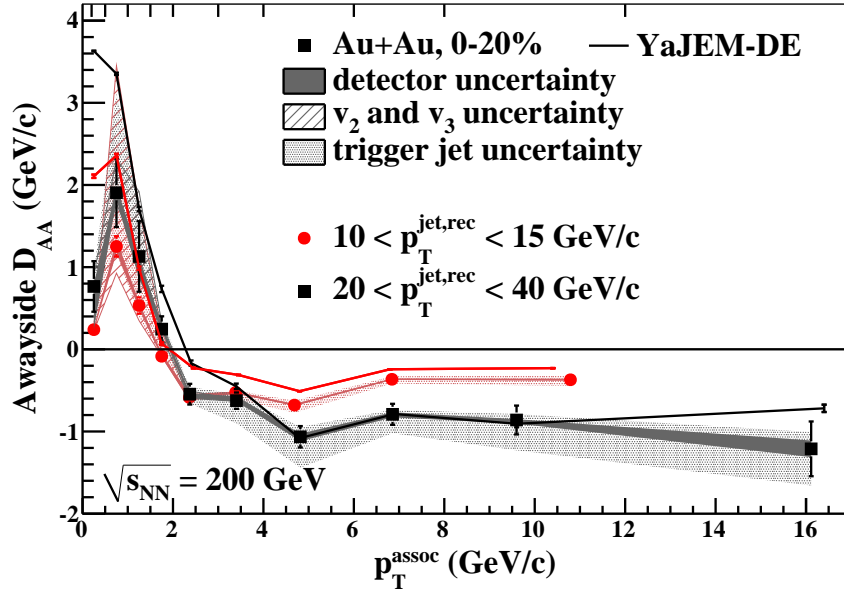


**Figure 1.22:** The away-side momentum difference,  $D_{AA}$ , of hadrons between Au+Au and  $p+p$  events, as measured by STAR [89], showing medium modification of jet fragmentation.

jet results. They indicate that with this set of observables, the behavior is quite different at RHIC and the LHC. Whether the significant radius  $R$  dependence of jet suppression  $R_{AA}$  at RHIC, not observed at the LHC, is the result of engineered bias selections on the STAR results remains to be tested. In addition, the recovery of most energy within  $R = 0.4$  is an exciting result from STAR which could potentially indicate a different redistribution of energy in the RHIC created quark-gluon plasma.

It is clear that in addition to extending the RHIC observables to include fully reconstructed jets and  $\gamma$ -jet correlations, theoretical development work is required for converging to a coherent 'standard model' of the medium coupling strength and the nature of the probe-medium interaction. In the next section, we detail positive steps in this direction.

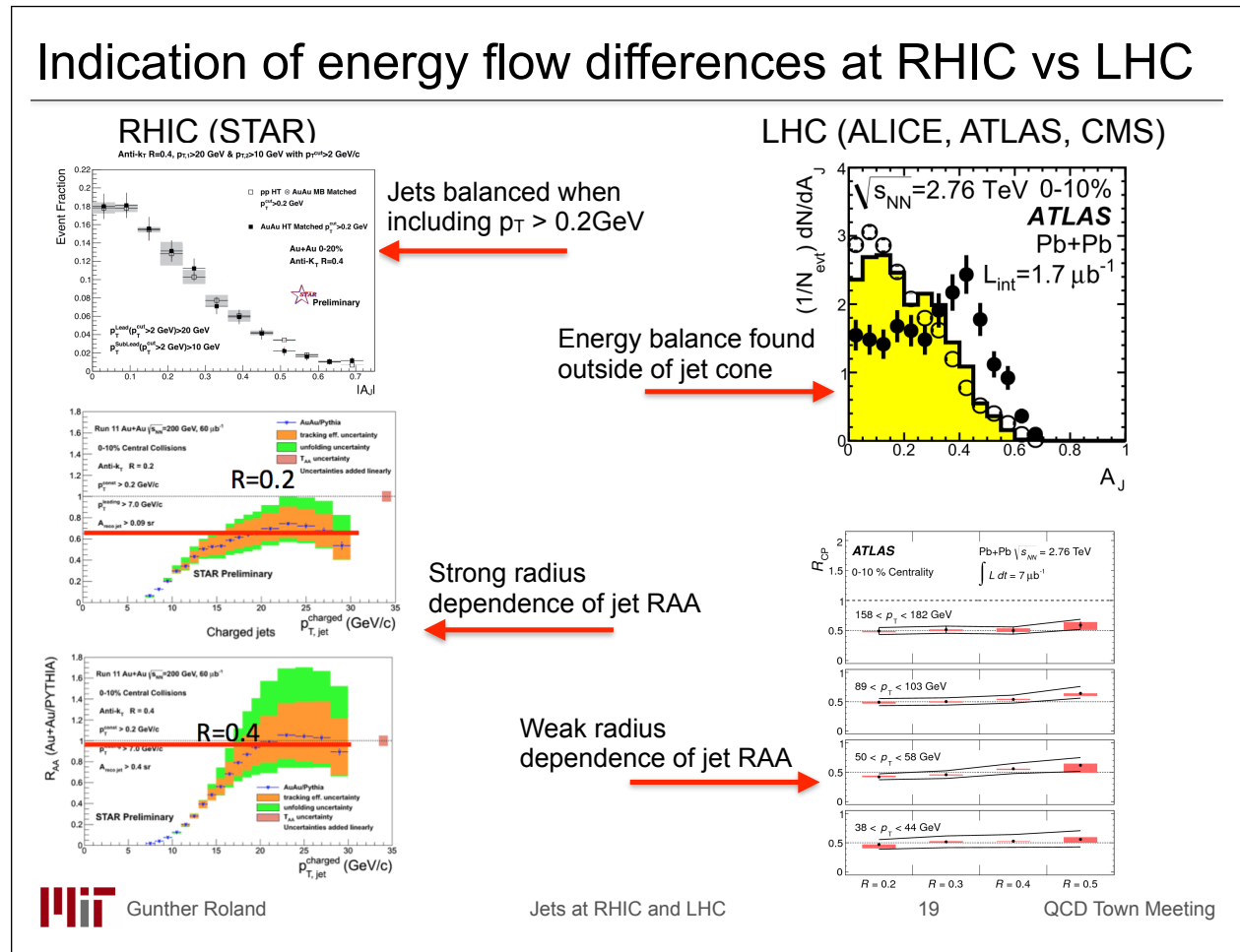


**Figure 1.23:** Slide from G. Roland’s talk at the QCD Town Meeting (September 2014). Shown are preliminary RHIC results from STAR for jet  $R_{AA}$  and dijet asymmetry  $A_J$  in comparison with LHC results. The initial observation is for quite different trends. Data with overlapping energy ranges and comparable jet algorithms and jet bias selections from sPHENIX will shed significant light on the underlying physics differences.

## 1.6 Theoretical calculations of jets at RHIC

Motivated in part by the new information provided by LHC jet results and the comparison of RHIC and LHC single and di-hadron results, the theoretical community is actively working to understand the detailed probe-medium interactions. The challenge is to understand not only the energy loss of the leading parton, but how the parton shower evolves in medium and how much of the lost energy is re-distributed in the quark-gluon plasma. Theoretical calculations attempting to describe the wealth of new data from RHIC and the LHC have not yet reconciled some of the basic features, with some models including large energy transfer to the medium as heat (for example [90]) and others with mostly radiative energy loss (for example [91, 92]). None of the current calculations available has been confronted with the full set of jet probe observables from RHIC and the LHC. Measurements of jets at RHIC energies and with jets over a different kinematic range allow for specific tests of these varying pictures. In this section, we give a brief review of a subset of calculations for jet observables at RHIC enabled by the sPHENIX upgrade and highlight the sensitivity of these observables to the underlying physics.

Much of this work has been carried out under the auspices of the Department of Energy Topical Collaboration on Jet and Electromagnetic Tomography of Extreme Phases of Matter in Heavy-ion Collisions [93]. Workshops held by the JET Collaboration at Duke University in March 2012 and Wayne State University in August 2013 and 2014 have been dedicated to the topic of jet measurements at RHIC. These workshops were attended by theorists as well as experimentalists from both RHIC and the LHC. This is an active collaborative effort.

In order to overcome specific theoretical hurdles regarding analytic parton energy loss calculations and to couple these calculations with realistic models of the QGP space-time evolution, Monte Carlo approaches have been developed (as examples [94, 95, 96, 58, 97, 98]). Here we describe RHIC energy jet probe results from specific theory groups utilizing different techniques for calculating the jet-medium interactions. These efforts indicate a strong theoretical interest and the potential constraining power of a comprehensive jet physics program at RHIC.

Jets provide a very rich spectrum of physics observables, ranging from single jet observables such as  $R_{AA}$ , to correlations of jets with single particles, to correlations of trigger jets with other jets in the event. An example of how one can exploit this variety can be found in recent calculations by Renk [99]. Figure 1.24 is based on calculations using the YaJEM model to illustrate what could be called “jet surface engineering”. Triggers ranging from single hadrons on up to ideally reconstructed jets are used to form correlations with another jet in the event. The different triggers demonstrate different degrees of surface bias in the production point of the “dijet” and this bias itself can be used as a lever to investigate properties of the medium.

We show results are from Coleman-Smith and collaborators [57, 58] where they extract jet parton showers from PYTHIA (turning off hadronization) and then embed the partons into a deconfined quark-gluon plasma, modeled with the VNI parton cascade [100]. For the calculations shown here, the background medium consists of a cylinder of deconfined quarks and gluons at a uniform temperature. One excellent feature of the calculation is that it provides the ability to track each individual parton and thus not only look at the full time evolution of scattered partons from the shower, but also medium partons that are kicked up and can contribute particles to the reconstructed jets.

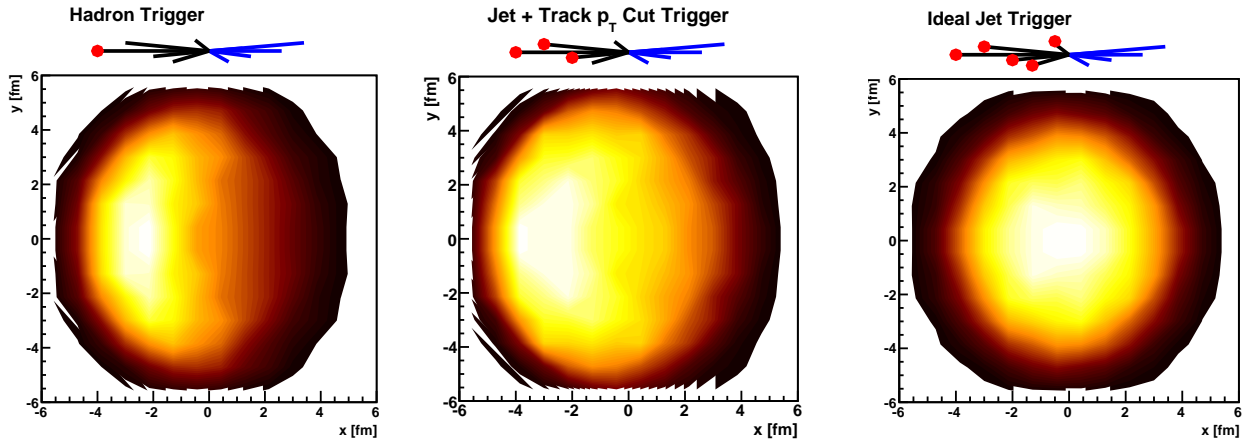


**Figure 1.24:** Dijet surface bias in YaJEM for various trigger definitions. As the trigger is changed from a single hadron (left) to a reconstructed jet with a minimum  $p_T$  selection on charged tracks and electromagnetic clusters (middle) to an ideally reconstructed jet (right), the surface bias in the production point becomes less pronounced. sPHENIX is capable of all three types of measurements. (Based on figure taken from [99].)

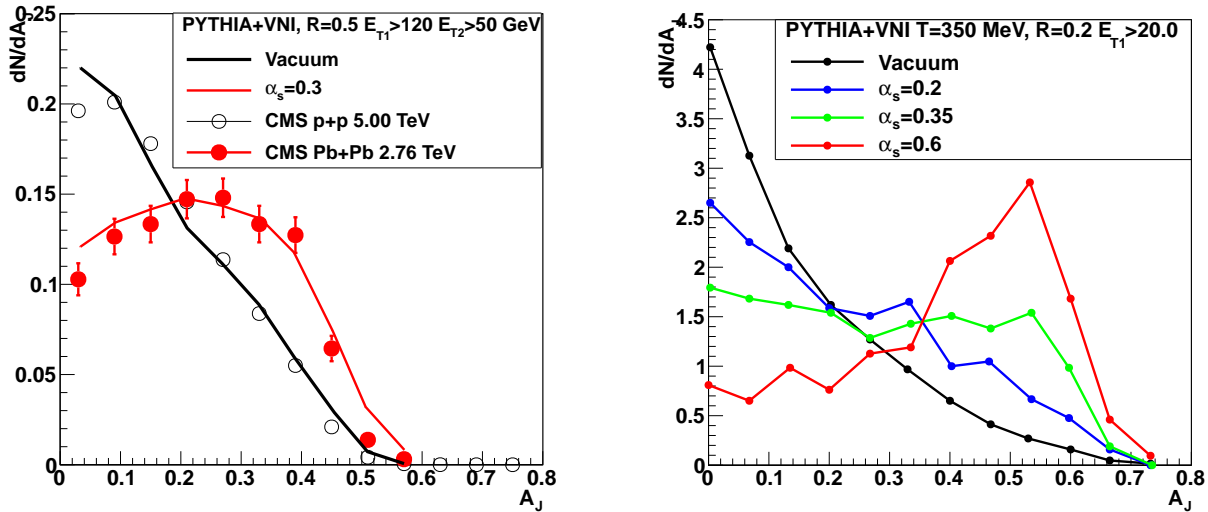


**Figure 1.25:** (left) Calculation in VNI parton cascade of dijet  $A_J$  with  $T = 0.35$  GeV and  $\alpha_s = 0.3$  compared to the CMS data [57]. (right) Calculation for RHIC jet energies,  $E_{T,1} > 20$  GeV, for a circular geometry of radius 5 fm of  $A_J$  for different values of  $\alpha_s$  increasing to  $\alpha_s = 0.6$  (red line) [59].

Calculation results for the dijet asymmetry  $A_J = (E_1 - E_2)/(E_1 + E_2)$  in a QGP with a temperature appropriate for LHC collisions and fixed  $\alpha_s = 0.3$  are shown in Figure 1.25 (left panel) [57]. The jets in the calculation are reconstructed with the anti- $k_T$  algorithm with radius parameter  $R = 0.5$  and then smeared by a simulated jet resolution of  $100\%/\sqrt{E}$ , and with requirements of  $E_{T1} > 120$  GeV and  $E_{T2} > 50$  GeV on the leading and sub-leading jet, respectively. The calculated  $A_J$  distributions reproduce the CMS experimental data [78].

In Figure 1.25 (right panel) the calculation is repeated with a medium temperature appropriate for RHIC collisions and with RHIC observable jet energies,  $E_{T1} > 20$  GeV and  $R = 0.2$ . The calculation is carried out for different coupling strengths  $\alpha_s$  between partons in the medium themselves and the parton probe and medium partons. The variation in the value of  $\alpha_s$  should be viewed as changing the effective coupling in the many-body environment of the QGP. It is interesting to note that in the parton cascade BAMPS, the authors find a coupling of  $\alpha_s \approx 0.6$  is required to describe the bulk medium flow [101]. These results indicate sizable modification to the dijet asymmetry and thus excellent sensitivity to the effective coupling to the medium at RHIC energies.

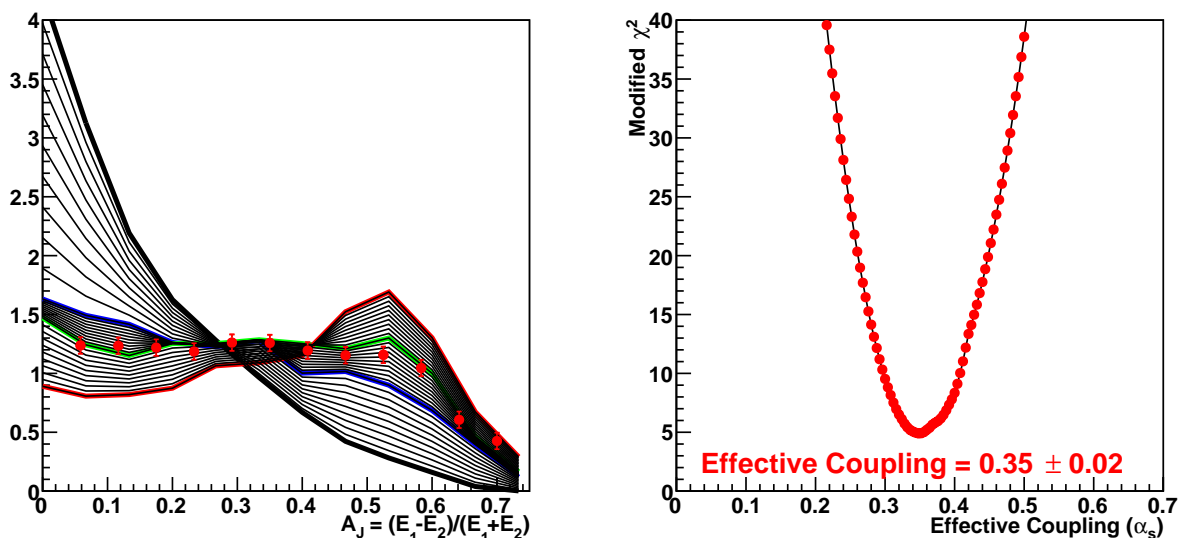
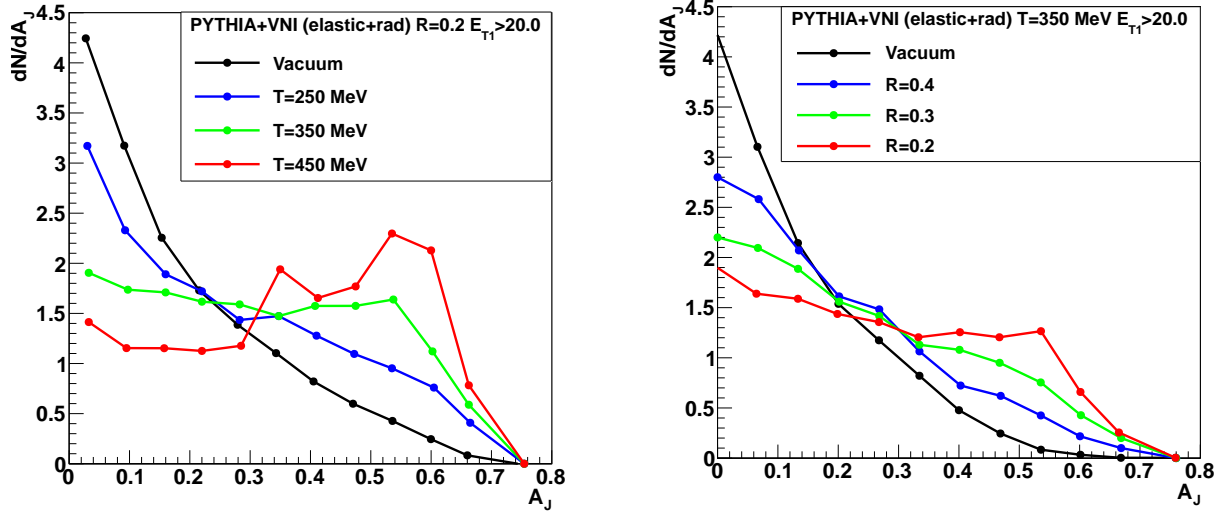


**Figure 1.26:** Determination of effective coupling strength in the model of Coleman-Smith.

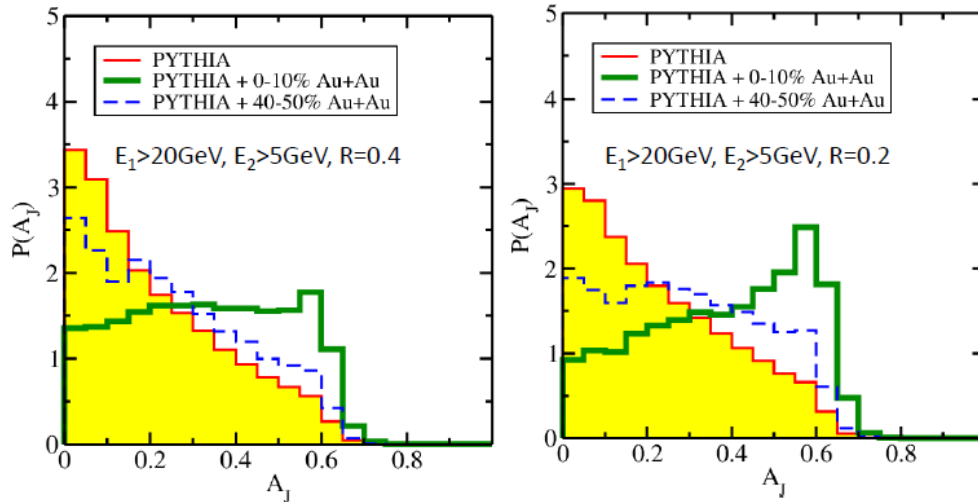
Figure 1.26 demonstrates the determination of the effective coupling in the model of Coleman-Smith. The different curves in the left panel show the distribution of dijet asymmetry for different values of the effective coupling. The data points are generated for a particular value of the coupling strength and the uncertainties are representative of those that sPHENIX would record. By performing a modified  $\chi^2$  comparison of the model to the data, one obtains the curve in the right panel. From that curve, one is able to determine the coupling with an uncertainty of about 5%.

Figure 1.27 (left panel) shows the temperature dependence of the dijet asymmetry, now keeping the coupling  $\alpha_s$  fixed. One observes a similar sharp drop in the fraction of energy balanced dijets with increasing temperature to that seen for increasing the effective coupling, and so combining these observations with constrained hydrodynamic models and direct photon emission measurements is important. Given that the initial temperatures of the QGP formed at RHIC and the LHC should be significantly different, this plot shows that if RHIC and LHC measure the  $A_J$  distribution at the same jet energy there should still be a sensitivity to the temperature which will lead to an observable difference. Thus, having overlap in the measured jet energy range at RHIC and the LHC is important, and this should be available for jet energies of 40–70 GeV. Figure 1.27 (right panel) shows the jet cone size,  $R$ , dependence of  $A_J$  at a fixed temperature. The narrowest jet cone  $R = 0.2$  has the most modified  $A_J$  distribution, as partons are being scattered away by the medium to larger angles.





**Figure 1.27:** Calculations from Coleman-Smith [59] for dijets embedded into the VNI parton cascade. The dijet asymmetry  $A_J$  for leading jets with  $E_T > 20$  GeV is shown as the medium temperature is varied (left panel) and as the jet cone radius is varied with fixed temperature  $T = 350$  MeV (right panel).



**Figure 1.28:** Calculations from Qin et al. [102] of dijet  $A_J$  for  $E_{T,1} > 20$  GeV and  $E_{T,2} > 5$  GeV for  $R = 0.4$  jets (left) and  $R = 0.2$  jets (right). Central (green) and mid-central (blue) distributions are shown along with the initial PYTHIA distributions (red).

The second results are from Qin and collaborators [103, 102] where they solve a differential equation that governs the evolution of the radiated gluon distribution as the jet propagates through the medium. Energy contained inside the jet cone is lost by dissipation through elastic collisions and by scattering of shower partons to larger angles. Their calculation is able to describe the LHC measured dijet asymmetry [103]. Figure 1.28 shows the predicted dijet asymmetry at RHIC for

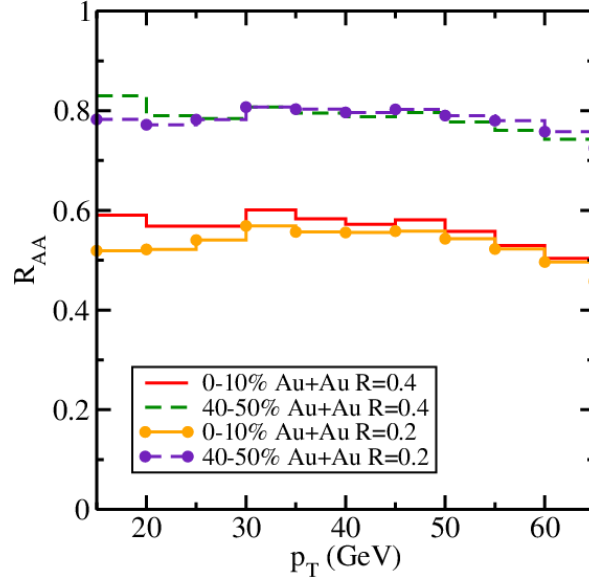


**Figure 1.29:** Calculations from Qin et al. [102] for jet  $R_{AA}$  for central (solid lines) and mid-central collisions (dashed lines) for  $R = 0.2$  and  $0.4$  jets.

mid-central and central Au+Au collisions for leading jets  $E_{T1} > 20$  GeV and jet radius parameter  $R = 0.4$  and  $R = 0.2$  in the left and right panels, respectively. Despite the calculation including a rather modest value of  $\hat{q}$  and  $\hat{e}$ , the modification for  $R = 0.2$  is as strong as the result with  $\alpha_s = 0.6$  from Coleman-Smith and collaborators shown above in the right panel of Figure 1.25. Calculations of  $\gamma$ -jet correlations indicate similar level modifications. It is also notable that Qin and collaborators have calculated the reaction plane dependence of the dijet  $A_J$  distribution and find negligible differences. This observable will be particularly interesting to measure at RHIC since these calculations have difficulty reproducing the high  $p_T$   $\pi^0$  reaction plane dependence ( $v_2$ ) as discussed in the previous section.

Figure 1.29 shows results for the inclusive jet  $R_{AA}$  as a function of  $p_T$  for jet radius parameters  $R = 0.2$  and  $R = 0.4$ . It is striking that the modification is almost independent of  $p_T$  of the jet and there is very little jet radius dependence. The modest suppression, of order 20%, in mid-central Au+Au collisions is of great interest as previous measurements indicate modification of single hadrons and dihadron correlations for this centrality category. Measurements of jets with a broad range of radius parameters are easier in the lower multiplicity mid-central collisions.

The third results are from Young and Schenke and collaborators [96]. These calculations utilize a jet shower Monte Carlo, referred to as MARTINI [104], and embed the shower on top of a hydrodynamic space-time background, using the model referred to as MUSIC [105]. Figure 1.30 shows the jet energy dependence of  $A_J$  for RHIC energy dijets,  $E_{T1} > 25$  GeV and  $E_{T1} > 35$  GeV in the left and right panels, respectively. These results are directly compared to the calculations from Qin and collaborators and indicate a substantially different modification for the higher energy dijets. Interestingly, both of these approaches, when applied at the higher collision energies of the LHC, each reproduce the measured data quite well [106, 103].

Our next set of illustrative theory calculations come from Vitev and collaborators [60, 61, 62] where

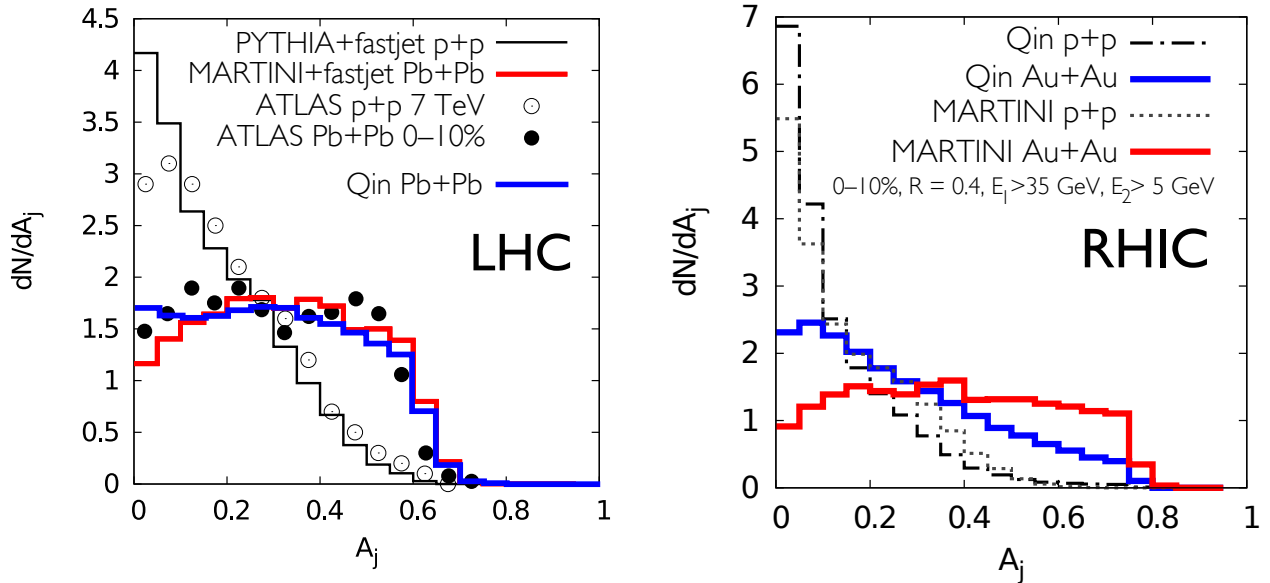


**Figure 1.30:**  $A_j$  distributions in MARTINI+MUSIC [107] and the model of Qin et al. [102]. (left) Comparison of  $A_j$  calculations in MARTINI+MUSIC and by Qin et al for Pb+Pb collisions at 2.76 TeV (red line, Qin et al; blue line, MARTINI+MUSIC). Both calculations show a similar broad  $A_j$  distribution. (right) Same as left panel, but for Au+Au collisions at 200 GeV (with leading jet  $E_T > 35$  GeV). Here a difference in shape is observed between the two models with the Qin et al. model developing a peak at small  $A_j$  while the MARTINI+MUSIC calculation retains a shape in the calculation at the higher energy.

they utilize a Next-to-Leading-Order (NLO) calculation and consider not only final-state inelastic parton interactions in the QGP, but also initial-state cold nuclear matter effects. Figure 1.14 shown earlier plots the dijet asymmetry  $A_j$  for jets with  $E_{T1} > 50$  GeV and  $R = 0.6$ . The plots are for cases of radiative energy loss only and including collisional energy loss as well, and then the different colors are varying the probe-medium coupling by  $\pm 10\%$ . There is sensitivity even to these 10% coupling modifications, and for the higher energy jets there is a dramatic difference predicted from the inclusion of collisional energy loss.

For the inclusive jet suppression, these calculations predict a significant jet radius  $R$  dependence to the modification, in contrast to the result from Qin and collaborators. Figure 1.31 shows the significant radius dependence. In addition, Vitev and collaborators hypothesize a substantial cold nuclear matter effect of initial state parton energy loss. Because the high energy jets originate from hard scattering of high Bjorken  $x$  partons, a modest energy loss of these partons results in a reduction in the inclusive jet yields. At RHIC with  $d+Au$  running we will make cold nuclear matter measurements at the same collision energy and determine the strength of these effects as a baseline to heavy ion measurements.

Recently a framework with a hybrid strong coupling approach has been implemented with initial success at describing specific jet quenching observables [52, 53]. Shown in Figure 1.32 are the predicted  $R_{AA}$  for reconstructed jets at the LHC (left) and at RHIC (right). The jet  $R_{AA}$  shows a rise as a function of  $p_T$  at both energies, in contrast to calculations as shown in Figure 1.29 for example. This framework enables an alternate set of predictions for a host of observables sensitive to the

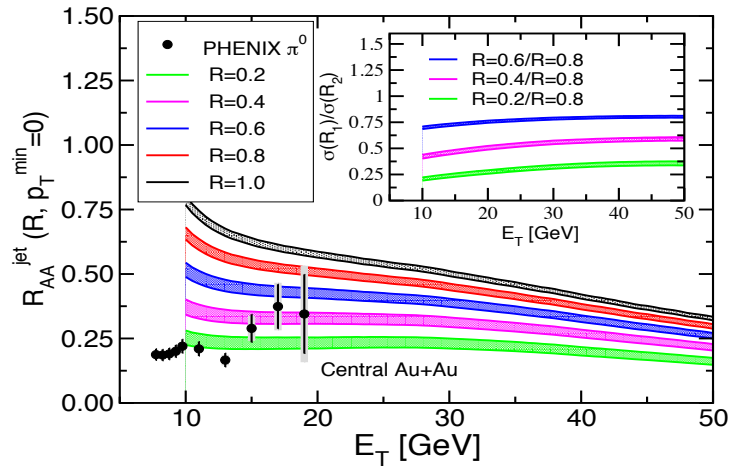


**Figure 1.31:** Calculations from Vitev et al. for the inclusive jet  $R_{AA}$  as a function of the jet energy and radius.

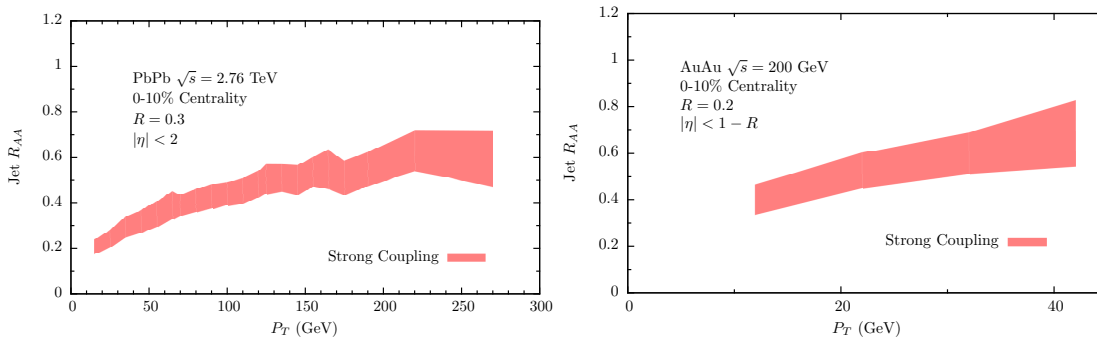


**Figure 1.32:** Calculations from a hybrid strong coupling approach with predictions for reconstructed jet  $R_{AA}$  as a function of  $p_T$  appropriate for central collisions at the LHC (left) and RHIC (right) [52, 53].

redistribution of energy within the parton shower at RHIC and the LHC. The steeper spectrum at RHIC and the lower energy jets should make them more sensitive to the details of the hybrid calculations.

The simultaneous development of parton shower Monte Carlo codes – for example see Refs. [94, 95, 96, 58, 97, 98] – and in some cases their public availability allows the community to explore a full range of experimental observables. We have run the JEWEL 2.0 code [68] at both RHIC and LHC kinematics and medium parameters and then run the HEPMC output through the FASTJET reconstruction code. Results of a suite of observables for both energies are shown in Figure 1.33. The top panel shows the jet  $R_{AA}$  for different jet radii and charged hadron  $R_{AA}$ . It is striking as pointed out earlier that the charged hadron  $R_{AA}$  is quite flat at RHIC and at the same time has the characteristic rise at the LHC as observed in data. The next panel shows the modified fragmentation function from inclusive jets, where the observable reflects both the modification in the parton shower and the potentially reduced fraction of energy captured within the reconstructed

jet. The next panel shows the dijet azimuthal asymmetry with the dashed lines in  $p+p$  collisions and the solid lines in central heavy ion collisions. The RHIC predictions show a measurable broadening of the azimuthal distribution. The next panel shows the  $A_J$  dijet asymmetry distribution. The steeper falling spectrum at RHIC leads to a more significant depletion of balanced jets (i.e.  $A_J \approx 0$ ) and a larger shifts in the  $\langle A_J \rangle$ . The bottom panel shows the related  $I_{AA}$  for dijets, in this case with a narrow trigger jet with  $R = 0.2$  and varying the away-side jet radius. Again, a dramatic modification is expected at RHIC from the interplay of both larger surface bias from the trigger jet and a bias for the away-side parton to be a gluon opposed a quark trigger parton. sPHENIX will have excellent statistics across this breadth of observables and more.

It is notable that in the recommended running mode for JEWEL, one retains recoil partons for hadron reconstruction and not for jet reconstruction. JEWEL treats the medium partons as a gas of nearly free quarks and gluons and thus it is relatively easy to transfer energy to these partons, which then recoil. In the case where recoil partons are included in the jet reconstruction they have also their initial thermal energy and thus one gets large jet  $R_{AA}$  enhancements. When excluding them, some energy is lost and  $R_{AA}$  for large radius jets appears smaller than expected. We are working on a running mode to only include the transferred energy and thus test the sensitivity to the model of the medium partons. We continue to directly engage the theory community for development of these Monte Carlo codes for optimal comparison between data and theory.

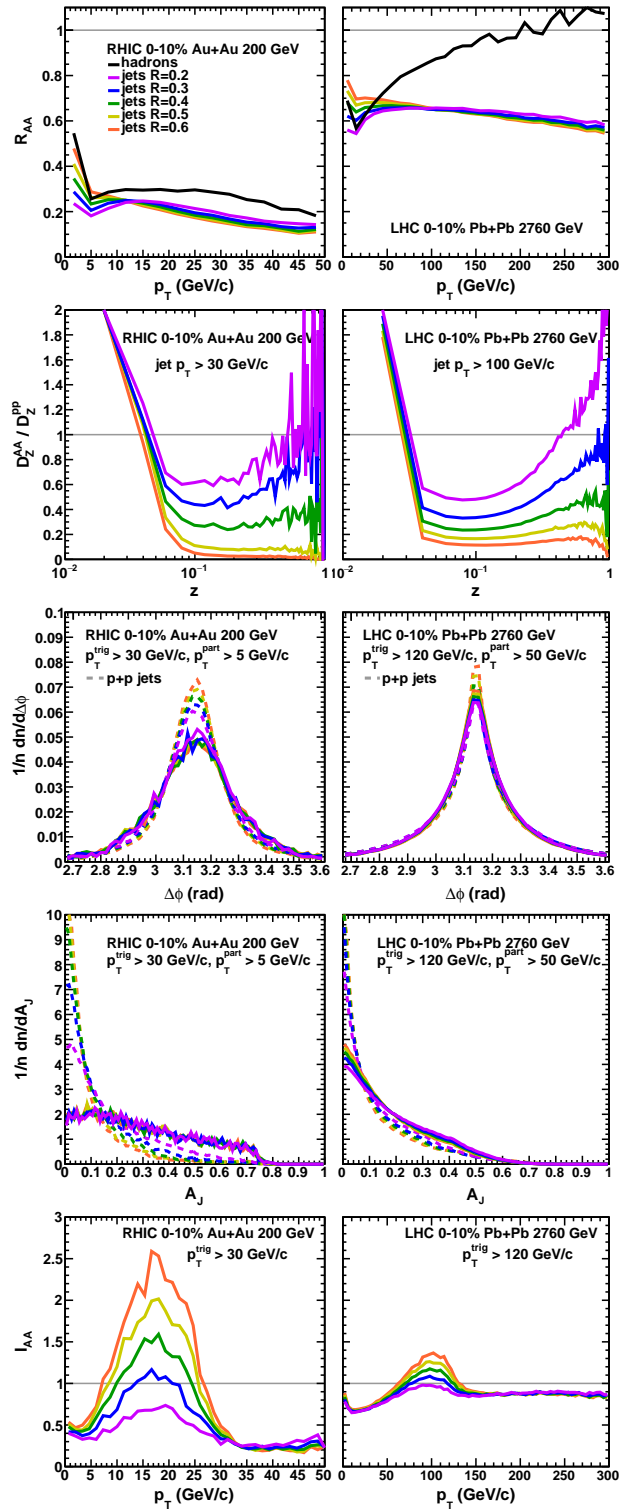
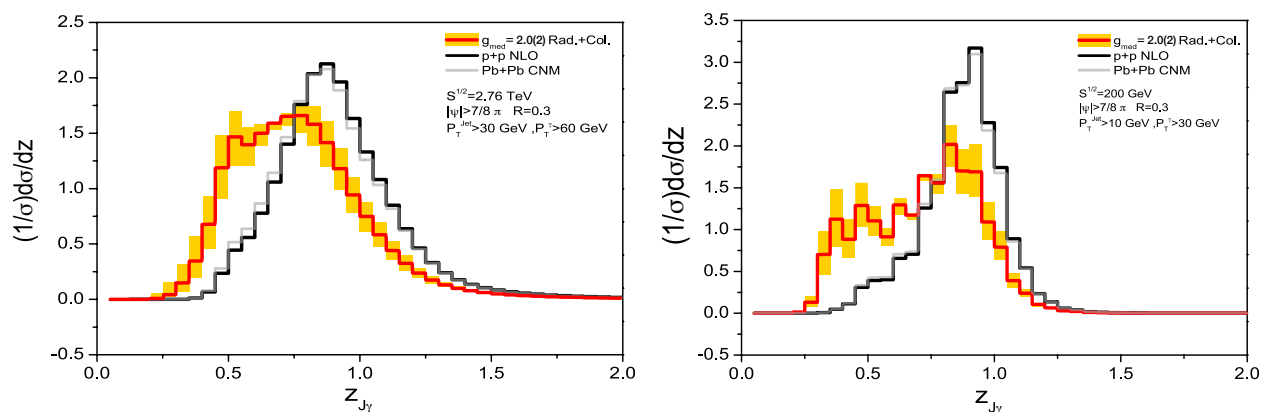


**Figure 1.33:** JEWEL 2.0 parton shower Monte Carlo results for jet and hadron observables at RHIC and the LHC using the publicly available code [68, 108]. See text for the detailed description of the panels.

## 1.7 Direct Photons and Fragmentation Functions

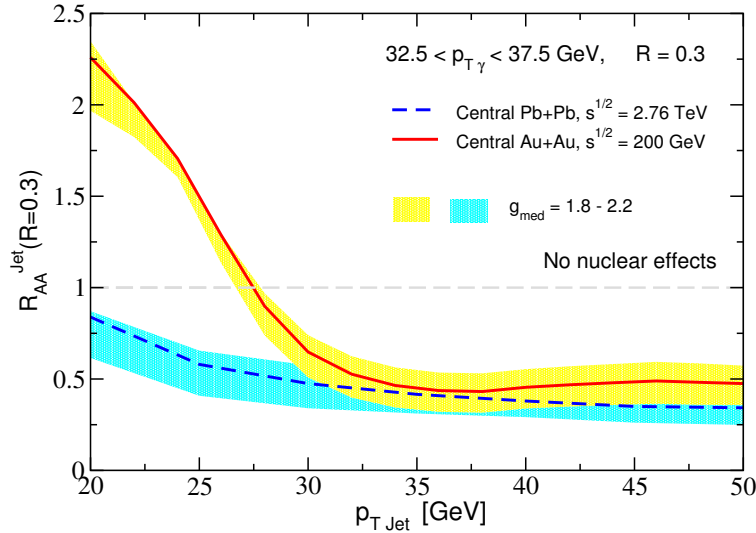
Ideally, one would like to understand how a quark or gluon of perfectly known energy interacts traversing the quark-gluon plasma and the redistribution of energy and particles both longitudinal and transverse to the initial parton direction. The *golden channel* for the calibration of initial quark energy is to tag them via an opposing direct photon [79]. One can measure fully reconstructed jets opposite the photon with different jet radii to parse out the transverse energy redistribution.

Figure 1.34 shows the event distribution for the ratio of the reconstructed jet energy with  $R = 0.3$  relative to the direct photon energy [109]. As the authors note, “The steeper falling cross sections at RHIC energies lead not only to a narrow  $z_{J_\gamma}$  distribution in  $p+p$  collisions but also to a larger broadening end shift in  $\langle z_{J_\gamma} \rangle$  in A+A collisions.” This results in a greater sensitivity to the redistribution of energy, which is again sensitive to the balance of processes including radiative and collisional energy loss. Figure 1.35 shows the jet  $R_{AA}$  opposite a 35 GeV direct photon [109]. There is a dramatic difference between the RHIC and LHC result, where one expects a factor of two enhancement in jets near 20 GeV in these collision systems. As detailed in the sPHENIX performance section in Figure 4.26, with an underlying event energy a factor of 2.5 lower at RHIC compared to the LHC, sPHENIX can reconstruct jets over a very broad range of radii and energies opposite these direct photons.



**Figure 1.34:** Calculation results for the vacuum and medium modified distribution for direct photon — reconstructed jet events at LHC collision energy (left) and RHIC collision energy (right) [109].

With charged particle tracking one can also measure the longitudinal redistribution of hadrons opposite the direct photon. sPHENIX will have excellent statistical reach for such direct photon measurements. At the same time, it is advantageous to measure modified fragmentation functions within inclusive reconstructed jets and via correlations as well. The original predictions of jet quenching in terms of induced forward radiation had the strongest modification in the longitudinal distribution of hadrons from the shower (i.e., a substantial softening of the fragmentation function). One may infer from the nuclear suppression of  $\pi^0$  in central Au+Au collisions  $R_{AA} \approx 0.2$  that the high  $z$  (large momentum fraction carried by the hadron) showers are suppressed. Shown in Figure 1.36 is the fragmentation function for 40 GeV jets in vacuum (PYTHIA) compared with the case of substantial jet quenching (Q-PYTHIA with a quenching factor used to match RHIC single hadron suppression observables). In the sPHENIX upgrade, fragmentation functions via



**Figure 1.35:** Calculation results for the jet  $R_{AA}$  opposite to a tagged direct photon in Au+Au collisions at 200 GeV and Pb+Pb collisions at 2.76 TeV [109].

precision charged track measurements are available from high- $z$  where the effects are predicted to be largest to low- $z$  where medium response and equilibration effects are relevant. The independent measurement of jet energy (via calorimetry) and the hadron  $p_T$  via tracking is crucial. This independent determination also dramatically reduces the fake track contribution by the required coincidence with a high energy jet.

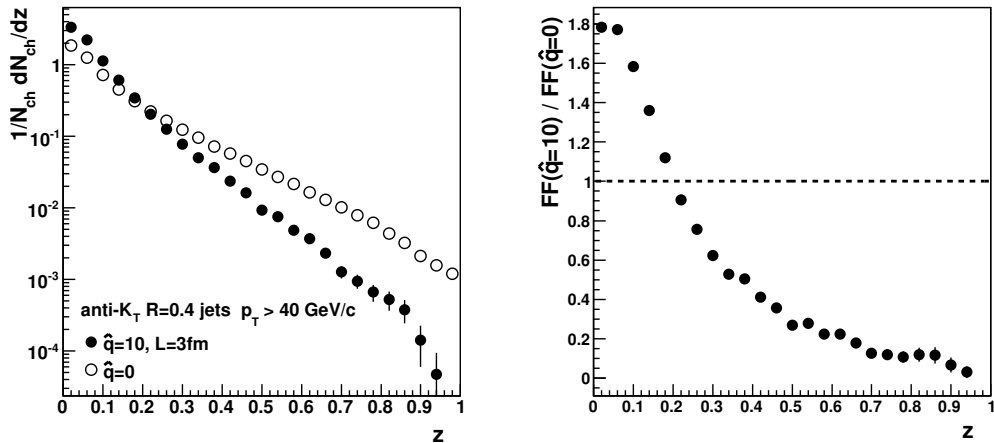


**Figure 1.36:** Q-PYTHIA simulation with quenching parameter  $\hat{q} = 0$  (i.e., in vacuum) and  $\hat{q} = 10 \text{ GeV}/c^2$  for the fragmentation function of light quark and gluon jets as a function of  $z$ .

Measurements at the LHC reveal a very different behavior as shown in Figure 1.37 where a slight enhancement is hinted at for large  $z$ , rather than a large suppression. Measurements of fragmentation functions within reconstructed jets from the CMS and ATLAS experiments in



Pb+Pb collisions show very modest modification within uncertainties. Although one explanation is that the jets that are reconstructed are from near the surface and thus not modified, with a nuclear modification factor for inclusive jets  $R_{AA} \approx 0.5$  that explanation is challenged. Similar measurements at RHIC energies are crucial to fully map out the re-distribution of energy in the shower and medium response. An example of the sPHENIX precision for such measurements is shown later in Figure 4.24.

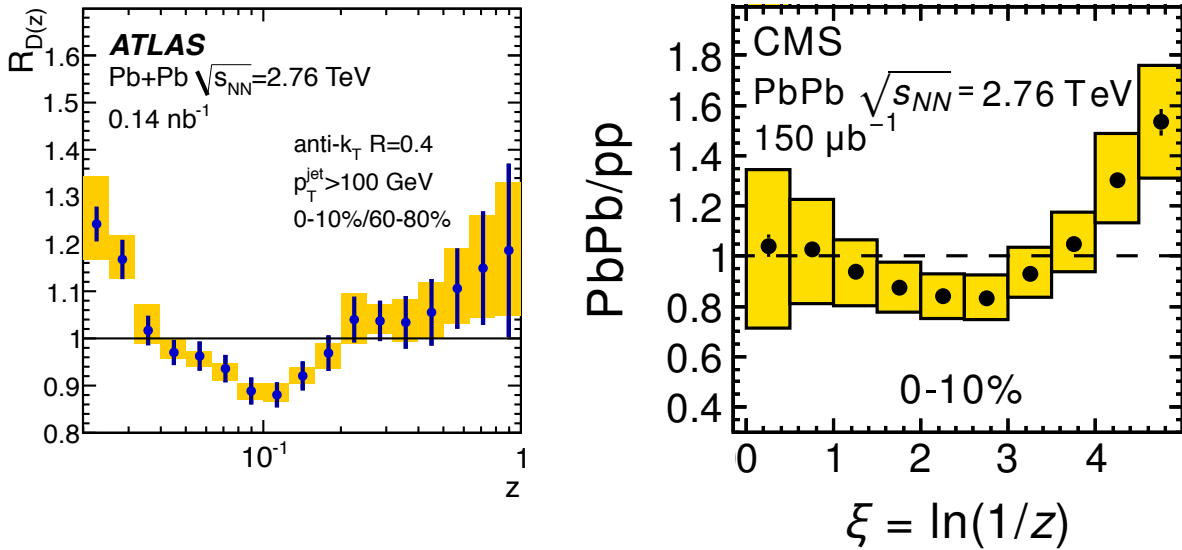


**Figure 1.37:** Measurements of the modified fragmentation function for  $p_T > 100$  GeV jets in central Pb+Pb collisions from ATLAS [110] (left plot, as a function of  $z = \vec{p}_T^{\text{hadron}} \cdot \vec{p}_T^{\text{jet}} / |\vec{p}_T^{\text{jet}}|^2$ ) and CMS [111] (right plot, as a function of  $\xi = \ln(1/z)$ ).

One can also access less directly this transverse and longitudinal redistribution of energy and particles via trigger high  $p_T$  hadrons and narrow reconstructed jets. Similar measurements have been carried out by the STAR experiments, as discussed earlier in the context of Figure 1.22. With the large kinematic reach of sPHENIX, one can have very high statistics observables that span a reach where the opposing parton is mostly a gluon near 20 GeV and then increases in quark fraction for higher energy triggers. This is another complement between the kinematics at RHIC and the LHC as shown in Figure 1.38 comparing the quark-quark, quark-gluon, gluon-gluon relative contributions as a function of  $p_T$ .

Combining high statistics results on this full set of observables from RHIC and the LHC can lead to a detailed description of the quark and gluon interaction in the quark-gluon plasma as a function of parton energy analogous to that from the Particle Data Group for the muon in copper as shown in Figure 1.39.

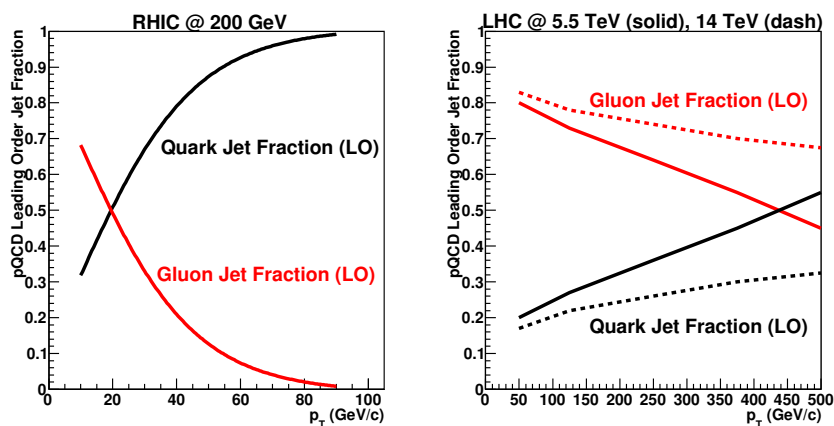


**Figure 1.38:** Comparison of the fraction of quark and gluon jets from leading order pQCD calculations for RHIC and LHC energies.

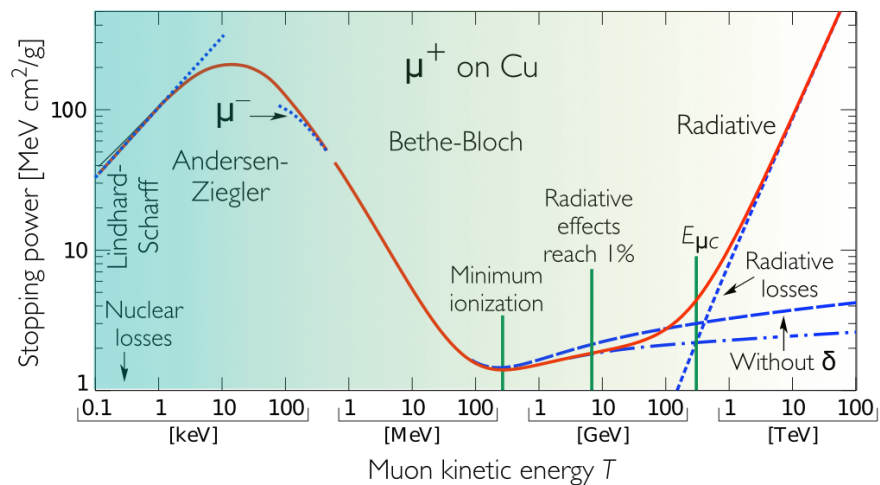


**Figure 1.39:** The muon stopping power in copper demonstrates a comprehensive understanding of the interaction of a fundamental particle with matter over an enormous range of scales.

## 1.8 Heavy Quark Jets

A main motivation for studying heavy flavor jets in heavy ion collisions is to understand the mechanism for parton-medium interactions and to further explore the issue of *strong versus weak* coupling [112]. As detailed in Section 1.3, a major goal is understanding the constituents of the medium and how fast partons transfer energy to the medium. Heavy quarks have gathered special attention as they are particularly sensitive to the contribution of collisional energy loss, due to suppressed radiative energy loss from the “dead cone” effect [113]. Measurements of beauty-tagged jets and reconstructed  $D$  mesons over the broadest kinematic reach will enable the disentangling of  $\hat{q}$  and  $\hat{e}$ .

There are important measurements currently being made of single electrons from semileptonic  $D$  and  $B$  decays and direct  $D$  meson reconstruction with the current PHENIX VTX and STAR Heavy Flavor Tracker (HFT). The sPHENIX program can significantly expand the experimental acceptance and physics reach by having the ability to reconstruct full jets with a heavy flavor tag. The rates for heavy flavor production from perturbative QCD calculations [114] are shown in Figure 1.40.

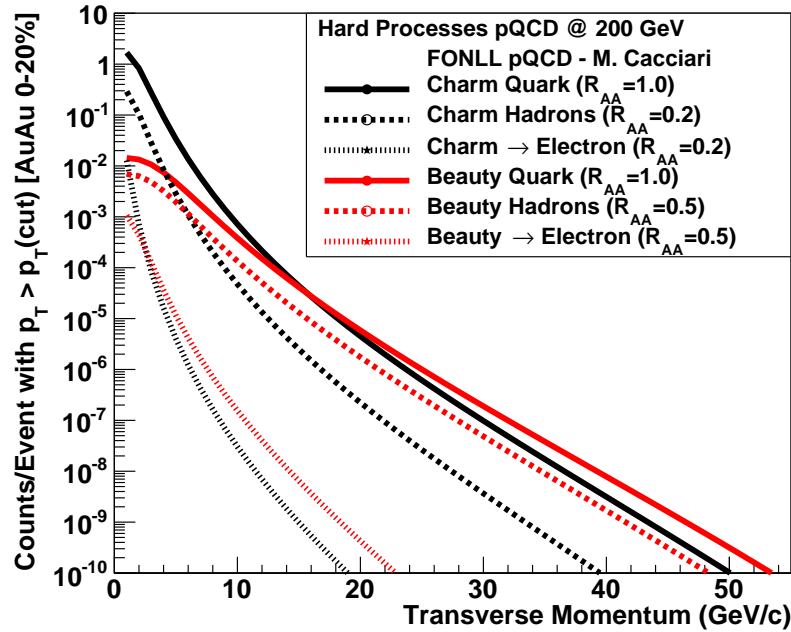


**Figure 1.40:** FONLL calculations [114] for heavy flavor (charm and beauty) jets, fragmentation hadrons ( $D$ ,  $B$  mesons primarily), and decay electrons as a function of transverse momentum. The rates have been scaled to correspond to counts with  $p_T > p_T(\text{cut})$  for Au+Au 0–20% central collisions.

Calculations including both radiative and collisional energy loss for light quark and gluon jets, charm jets, and beauty jets have been carried out within the CUJET 2.0 framework [115]. The resulting  $R_{AA}$  values in central Au+Au at RHIC and Pb+Pb at the LHC for  $\pi$ ,  $D$ ,  $B$  mesons are shown as a function of  $p_T$  in Figure 1.41. The mass orderings are a convolution of different initial spectra steepness, different energy loss mechanisms, and final fragmentation. Measurements of  $D$

mesons to high  $p_T$  and reconstructed beauty-tagged jets at RHIC will provide particularly sensitive constraints in a range where, due to their large masses, the charm and beauty quark velocities are not near the speed of light.

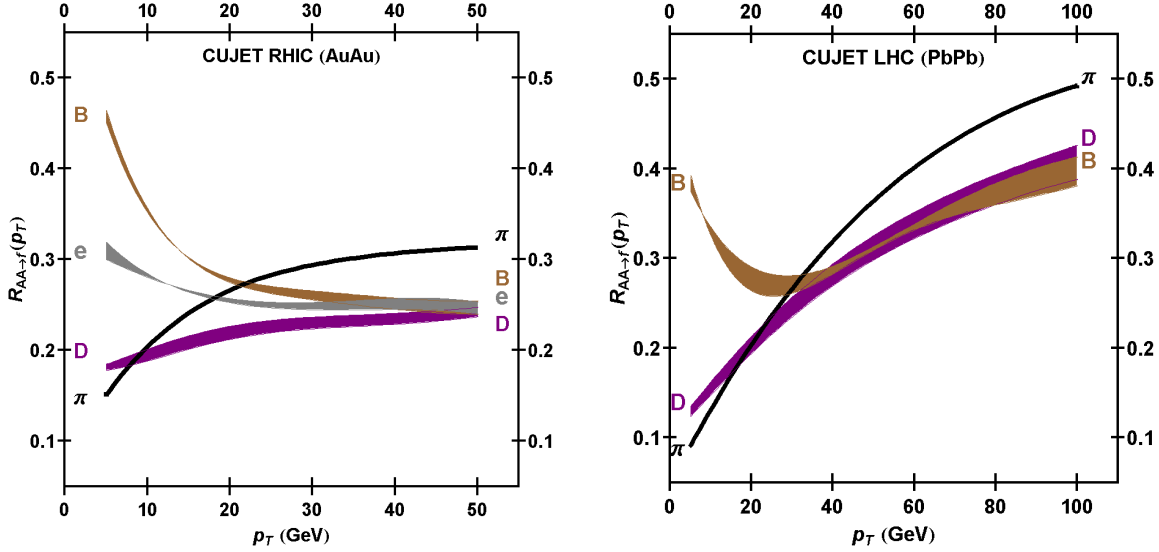


**Figure 1.41:** Calculations within the CUJET 2.0 [115] framework of the  $R_{AA}$  in central Au+Au collisions at RHIC (left panel) and Pb+Pb collisions at the LHC (right panel), with light, charm and beauty hadrons and electrons shown as separate curves.

Shown in Figure 1.42 are calculations from Ref. [116] that highlight the sensitivity of beauty quark jets to collisional energy loss mechanisms. Initial measurements from the LHC show first indications of this mass ordering, and precision data from higher statistics in future LHC running and at RHIC are needed. One expects larger effects at RHIC where radiative energy loss contributions for the lower  $p_T$  beauty quarks are suppressed. Another promising tool is the study of heavy flavor jet-shape modification in Au+Au relative to  $p+p$  collisions. Different mechanisms of energy loss (radiative versus collisional) predict different re-distributions of the jet fragments both inside and outside the jet cone. There are also scenarios where the heavy meson forms inside the medium and is dissociated in the matter [117, 118]. This would lead to a nearly unmodified jet shape relative to  $p+p$  collisions and a much softer fragmentation function for the leading heavy meson.

Figure 1.43 shows the D meson fragmentation function in PYTHIA and Q-PYTHIA for 20 GeV charm jets. The peak of the fragmentation function is shifted in Q-PYTHIA from  $z \approx 0.7$  to  $z \approx 0.5$ . Thus, for a given  $p_T$ , D mesons are more suppressed than charm jets. Measurement of D mesons within a reconstructed jet will provide access to fragmentation function modifications with emphasis on effects at large  $z$ .

The tagging of charm and beauty jets has an extensive history in particle physics experiments. There are multiple ways to tag heavy flavor jets. First is the method of tagging via the selection of a high  $p_T$  electron with a displaced vertex inside the jet. In minimum bias Au+Au collisions at  $\sqrt{s_{NN}} = 200$  GeV, the fraction of inclusive electrons from D and B meson decays is already greater than 50% for  $p_T > 2$  GeV/c. The sPHENIX tracking can confirm the displaced vertex of the electron from the collision point, further enhancing the signal. Since the semileptonic branching fraction

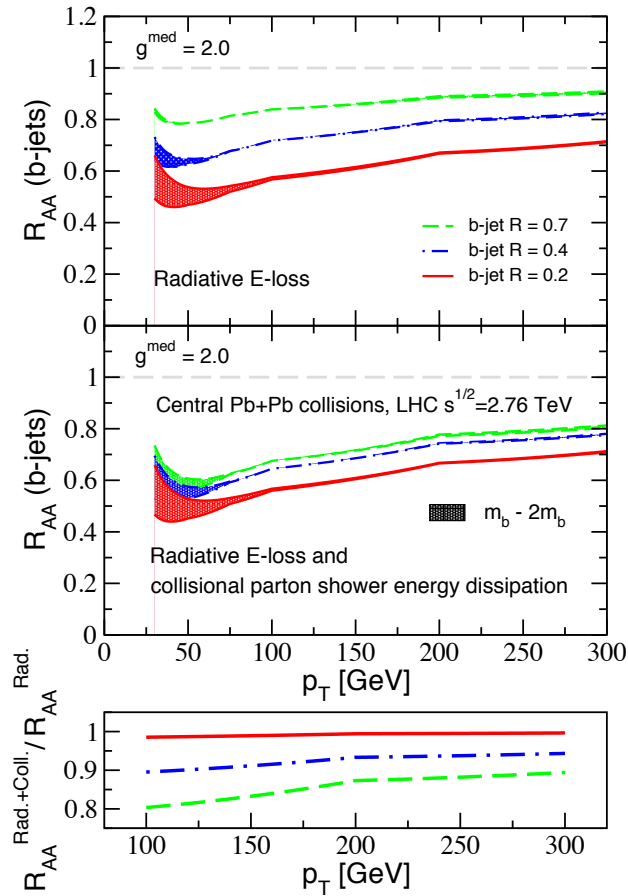


**Figure 1.42:** Calculations from Ref. [116] are shown for beauty tagged jets showing the sensitivity to radiative and collisional energy loss contributions.

of  $D$  and  $B$  mesons is approximately 10%, this method provides a reasonable tagging efficiency. Also, the relative angle of the lepton with respect to the jet axis provides a useful discriminator for beauty jets as well, due to the decay kinematics. Second, the direct reconstruction of  $D$  mesons is possible within sPHENIX as detailed in the performance section. The third method utilizes jets with many tracks that do not point back to the primary vertex. This technique is detailed by the  $D0$  collaboration to identify beauty jets at the Tevatron [119], and employed with variations by ATLAS and CMS at the LHC. This method exploits the fact that most hadrons with a beauty quark decay into multiple charged particles all with a displaced vertex. The detailed performance metrics for tagged beauty jets are given in Section 4.7.

As detailed in Ref. [116], beauty tagged jets at the LHC come from a variety of initial processes. In fact, most often a tagged beauty jet does not have a back-to-back partner beauty jet. As shown in Figure 1.44, at RHIC energies the pair creation process represents  $\sim 35\%$  of the beauty jet cross-section, which is a larger fractional contribution than at the LHC, though flavor excitation still produces  $\sim 50\%$  of all  $b$ -jets at RHIC. Measurements at RHIC offer a different mixture of initial processes, and thus kinematics, when looking at correlated back-to-back jets including heavy flavor tags.

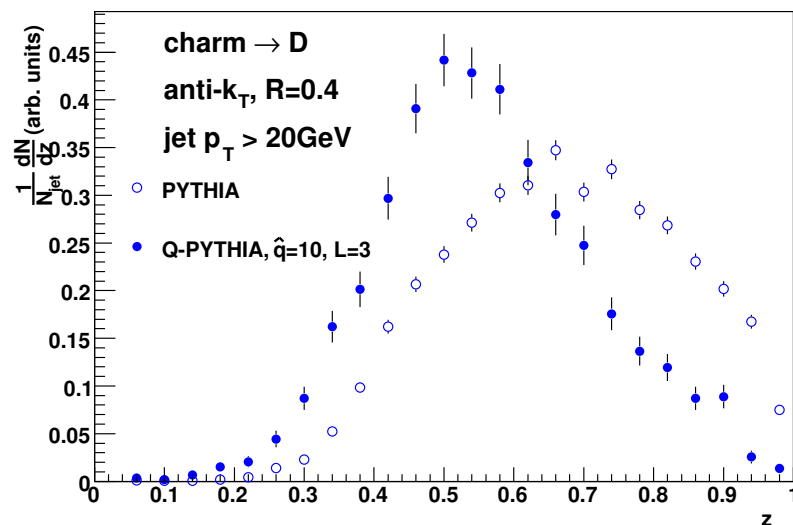


**Figure 1.43:**  $D$  meson fragmentation function in PYTHIA (open points) and Q-PYTHIA (solid points) for anti- $k_T$  jets with  $R = 0.4$  and  $E_T(\text{jet}) > 20$  GeV as a function of  $z$ , the fractional momentum of the  $D$  meson relative to the charm quark.

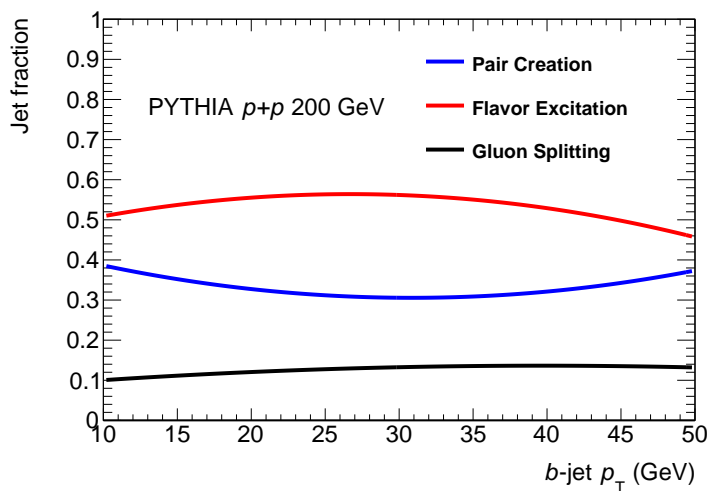


**Figure 1.44:** Fraction of inclusive  $b$ -jets, as a function of jet  $p_T$ , originating from the pair creation (black), flavor excitation (red) and gluon splitting (blue) modes in  $\sqrt{s} = 200$  GeV PYTHIA events.

## 1.9 Beauty Quarkonia in the QGP

An extensive program of  $J/\psi$  measurements in A+A collisions has been carried out at the SPS ( $\sqrt{s_{NN}} = 17.3$  GeV) and RHIC ( $\sqrt{s_{NN}} = 200$  GeV) and the LHC ( $\sqrt{s_{NN}} = 2.76$  TeV). These measurements were motivated by a desire to observe the suppression of  $J/\psi$  production by color screening in the QGP. In fact, strong suppression is observed at all three energies, but it has become clear that the contribution of color screening to the observed modification can not be uniquely determined without a good understanding of two strong competing effects.

The first of these, the modification of the  $J/\psi$  production cross section in a nuclear target, has been addressed at RHIC using  $d$ +Au collisions and at the SPS using  $p$ +Pb collisions, and is being addressed at the LHC using  $p$ +Pb collisions. The second complicating effect arises from the possibility that previously unbound heavy quark pairs could coalesce into bound states due to interactions with the medium. This opens up the possibility that if a high enough density of heavy quark pairs is produced in a single collision, coalescence of heavy quarks formed in different hard interactions might actually increase the production cross section beyond the initial population of bound pairs [120].

Using  $p$ +Pb and  $d$ +Au data as a baseline, and under the assumption that cold nuclear matter (CNM) effects can be factorized from hot matter effects, the suppression in central collisions due to the presence of hot matter in the final state has been estimated to be about 25% for Pb+Pb at the SPS [121], and about 50% for Au+Au at RHIC [122], both measured at midrapidity. The first  $J/\psi$  data in Pb+Pb collisions at  $\sqrt{s_{NN}} = 2.76$  TeV from ALICE [123], measured at forward rapidity, are shown alongside PHENIX data in Figure 1.45. Interestingly, the suppression in central collisions is far greater at RHIC than at the LHC. This is qualitatively consistent with a predicted [120] strong coalescence component due to the very high  $c\bar{c}$  production rate in a central collision at LHC. There is great promise that, with CNM effects estimated from  $p$ +Pb data, comparison of these data at widely spaced collision energies will lead to an understanding of the role of coalescence.

Upsilon measurements have a distinct advantage over charmonium measurements as a probe of deconfinement in the quark-gluon plasma. The  $Y(1S)$ ,  $Y(2S)$  and  $Y(3S)$  states can all be observed with comparable yields via their dilepton decays. Therefore it is possible to compare the effect of the medium simultaneously on three bottomonium states—all of which have quite different radii and binding energies.

At the LHC, CMS has measured Upsilon modification data at midrapidity in Pb+Pb collisions at 2.76 GeV that show strong differential suppression of the 2S and 3S states relative to the 1S state [124]. ALICE has measured the  $Y(1S)$  modification at forward rapidity in Pb+Pb collisions at 2.76 GeV [125], and in  $p$ +Pb collisions at 5.02 TeV [126]. With longer Pb+Pb runs, and corresponding  $p$ +Pb modification data to establish a CNM baseline, the LHC measurements will provide an excellent data set within which the suppression of the three upsilon states relative to  $p$ +Pb can be measured simultaneously at LHC energies.

At RHIC, upsilon measurements have been hampered by a combination of low cross sections and acceptance, and insufficient momentum resolution to resolve the three states. So far, there are measurements of the modification of the three states combined in Au+Au by PHENIX [127] and STAR [128]. However a mass-resolved measurement of the modifications of the three upsilon states at  $\sqrt{s_{NN}} = 200$  GeV would be extremely valuable for several reasons.

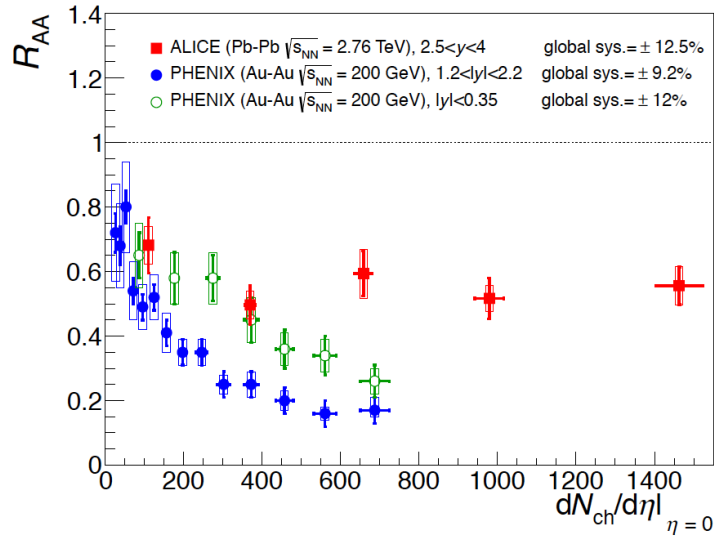


**Figure 1.45:** Comparison of nuclear modification measured by PHENIX and ALICE, showing that suppression is much stronger at the lower energy [123]. The modification measured by NA50 at low energy is similar to the PHENIX midrapidity result.

First, the core QGP temperature is approximately  $2T_c$  at RHIC at 1 fm/ $c$  and is at least 30% higher at the LHC (not including the fact that the system may thermalize faster) [129]. This temperature difference results in a different color screening environment. Figure 1.46 shows the temperature as a function of time for the central cell in Au+Au and Al+Al collisions at 200 GeV and Pb+Pb collisions at 2.76 TeV from hydrodynamic simulations that include earlier pre-equilibrium dynamics and post hadronic cascade [69]. Superimposed are the lattice expected dissociation temperatures with uncertainties for the three upsilon states. The significant lever arm in temperature between RHIC and LHC, and the use of either centrality or system size, allow one to bracket the expected screening behavior.

Second, the bottomonium production rate at RHIC is lower than that at the LHC by  $\sim 100$  [122]. As a result, the average number of  $b\bar{b}$  pairs in a central Au+Au collision at RHIC is  $\sim 0.05$  versus  $\sim 5$  in central Pb+Pb at the LHC. Qualitatively, one would expect this to effectively remove at RHIC any contributions from coalescence of bottom quarks from different hard processes, making the upsilon suppression at RHIC dependent primarily on color screening and CNM effects. This seems to be supported by recent theoretical calculations [130] where, in the favored scenario, coalescence for the upsilon is predicted to be significant at the LHC and small at RHIC.

Finally, it is of interest at RHIC energy to directly compare the modifications of the  $J/\psi$  and the  $Y(2S)$  states as a way of constraining the effects of coalescence by studying two states - in the same temperature environment - that have very similar binding energies and radii, but quite different underlying heavy quark populations.

An example theoretical calculation for both RHIC and the LHC is shown in Figure 1.47 indicating the need for substantially improved precision and separation of states in the temperature range probed at RHIC.



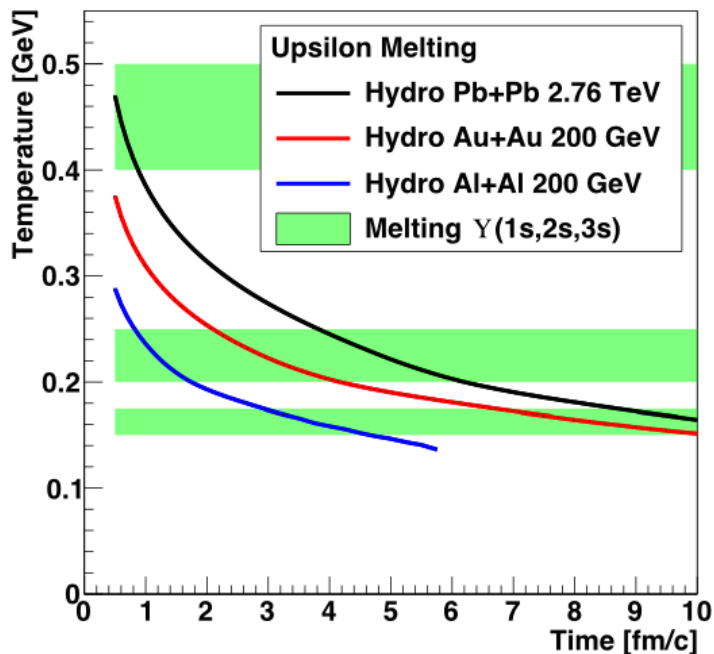


**Figure 1.46:** Temperature as a function of time for the central cell in Au+Au and Al+Al collisions at 200 GeV and Pb+Pb collisions at 2.76 TeV from hydrodynamic simulations that include earlier pre-equilibrium dynamics and post hadronic cascade [69]. Superimposed are the lattice expected dissociation temperatures with uncertainties for the three upsilon states.

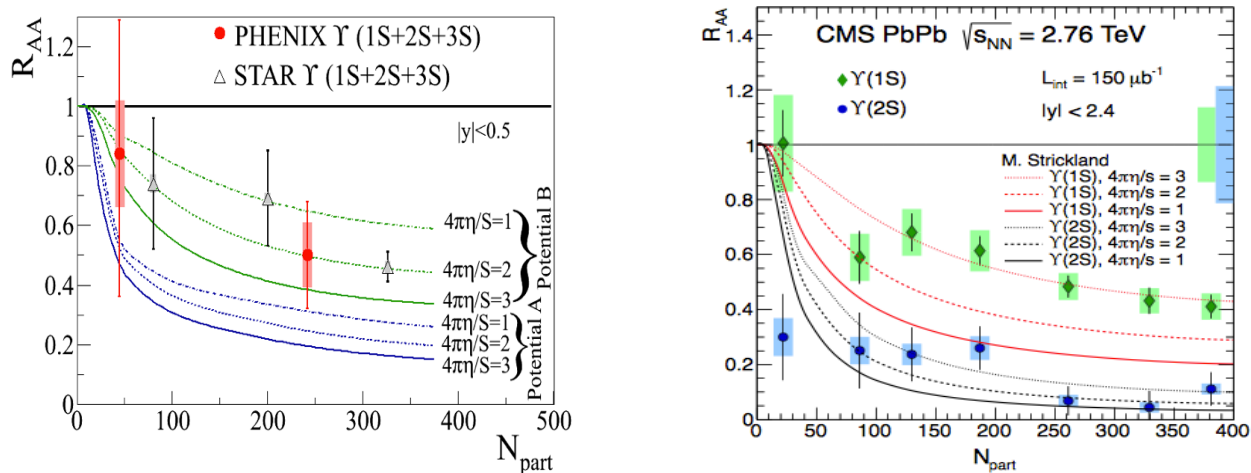


**Figure 1.47:** Calculations for Upsilon state suppression at RHIC and LHC energies as a function of collision centrality. The current state of measurements are also shown from PHENIX and CMS.

STAR has constructed a Muon Telescope Detector (MTD) to measure muons at midrapidity [131]. The MTD has coverage over  $|\eta| < 0.5$ , with about 45% effective azimuthal coverage. The MTD will have a muon to pion enhancement factor of 50–100, and the mass resolution will provide a clean separation of the  $Y(1S)$  from the  $Y(2S+3S)$ , and likely the ability to separate the  $Y(2S)$  and  $Y(3S)$  by fitting. While STAR has already taken data in the 2014 run with the MTD installed, the upgrade to sPHENIX will provide better mass resolution and approximately 10 times higher yields per run for upsilon measurements. In concert with the expected higher statistics results from the LHC experiments, sPHENIX data will provide the required precision to discriminate models of breakup in the dense matter and the length scale probed in the medium.

## 1.10 Beauty Quarkonia in proton-nucleus collisions

Measurements of quarkonia production in proton-nucleus collisions have long been considered necessary to establish a cold nuclear matter baseline for trying to understand hot matter effects in nuclear collisions. It has become clear, however, that the physics of  $p+A$  collisions is interesting in its own right [122]. Modification of quarkonia production in a nuclear target has been described by models that include gluon saturation effects (see for example [132]), breakup of the forming quarkonia by collisions with nucleons in the target [133, 134], and partonic energy loss in cold nuclear matter [135]. These mechanisms, which are all strongly rapidity and collision energy dependent, have been used, in combination, to successfully describe  $J/\psi$  and  $Y(1S)$  data in  $p(d)+A$  collisions.

The observation of what appears to be hydrodynamic effects in  $p+Pb$  collisions at the LHC [136, 137, 138] and  $d+Au$  collisions at RHIC [139] has raised questions about the longstanding assumption that  $p(d)+A$  collisions are dominated by cold nuclear matter effects. For quarkonia, it raises the obvious question: does the small hot spot produced in the  $p(d)+A$  collision affect the quarkonia yield?

Recent measurements of the modification of quarkonia excited states in  $p(d)+A$  collisions have produced unexpected and puzzling results. An example is shown in Figure 1.48, where the centrality dependence of the  $\psi'$  modification in  $p(d)+A$  collisions is shown for data measured at midrapidity at  $\sqrt{s_{NN}} = 200$  GeV by PHENIX [140], and preliminary data at forward and backward rapidity at  $\sqrt{s_{NN}} = 5.02$  TeV from ALICE. The suppression versus  $N_{\text{coll}}$  is strikingly similar in all three cases, despite the large difference in collision energy between the PHENIX and ALICE data, and the large range of rapidities spanned by the three data sets. In two of the cases — PHENIX at midrapidity and ALICE at backward rapidity — the  $\psi'$  is much more strongly suppressed than the  $J/\psi$ . In the third case — ALICE at forward rapidity — the  $J/\psi$  and  $\psi'$  suppressions are much closer to each other.

The strong differential suppression between the  $\psi'$  and  $J/\psi$  can not be understood as an effect of breakup by collisions with nucleons in the target, because the time scale of the nuclear crossing in all of these collisions is too short for the size difference between the fully formed mesons to become important. Similarly, shadowing and current models of energy loss in cold nuclear matter lead to the expectation of similar modification in  $p(d)+A$  collisions for the  $J/\psi$  and  $\psi'$  (see for example the detailed discussion in [141]). So despite the fact that models which combine those effects have been reasonably successful in describing  $J/\psi$  data, one must look elsewhere for an explanation of

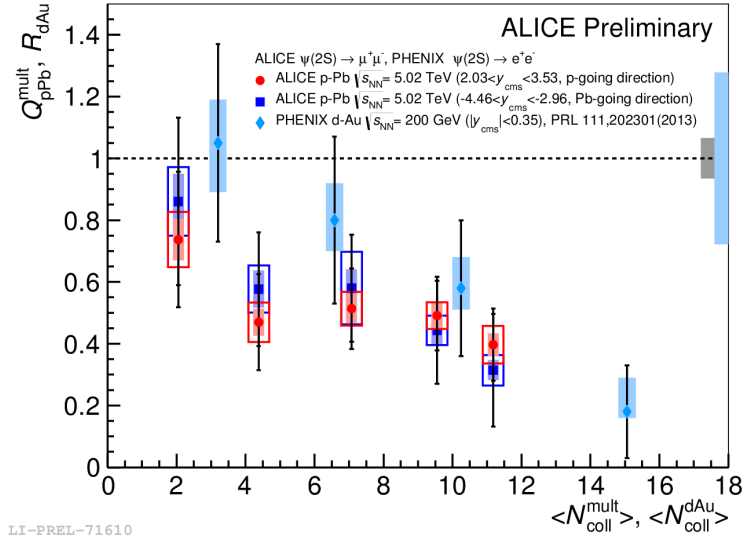


**Figure 1.48:** Comparison of  $\psi'$  nuclear modification measured by PHENIX and ALICE, showing very similar suppression at RHIC and LHC energies.

the strong  $\psi'$  suppression. A possibility is breakup of the mesons by interactions with comoving matter (which could be partonic or hadronic) produced in the collision [142]. Since the time scale for interactions with comoving matter is longer than the meson formation time, this might produce stronger suppression of larger, more weakly bound states.

The situation has become more interesting with the release of data from CMS on production of Upsilon excited states in  $p$ +Pb collisions. They find that the  $Y(2S)$  to  $Y(1S)$  ratio is suppressed by about 20% in minimum bias  $p$ +Pb collisions, while for the  $Y(3S)$  the differential suppression in minimum bias collisions is about 30%. The effect will be considerably larger in the most central collisions, but data showing the centrality dependence are not released yet.

A comprehensive  $p$ +A collision program with sPHENIX will provide Upsilon measurements in  $p$ +Au collisions at RHIC energy with all three states resolved from each other. This data set will constrain theoretical efforts to understand the physics of  $p$ +A collisions in the following ways:

- Provide very precise measurements of the  $Y(1S)$  modification at RHIC energies over 2 units of rapidity and a broad  $p_T$  range that would complement the very precise data at LHC energies that will be available by 2023. These data for the  $Y(1S)$  (binding energy 1.1 GeV) will, with the LHC data, constrain models of shadowing and partonic energy loss in cold nuclear matter.
- Provide precise measurements at RHIC energies of the modification for the  $Y(2S)$  and  $Y(3S)$  states (binding energies of 540 and 200 MeV, respectively). Combined with precise data at LHC energies, these data will constrain models that attempt to explain the differential suppression of these excited states, as well as that of the  $\psi'$ .

## 1.11 Rates and Physics Reach

Detailed information about the quark-gluon plasma properties, dynamics, time evolution, and structure at  $1-2 T_c$  is accessible at RHIC through the extensive set of reconstructed jet measurements proposed here. The theoretical bridgework needed to connect these measurements to the interesting and unknown medium characteristics of deconfined color charges is under active construction by many theorists. Combining this work with the flexible and high luminosity RHIC accelerator facility can produce new discoveries in heavy ion collisions with an appropriate set of baseline measurements provided a suitable detector apparatus is constructed. Our proposed design for a jet detector at RHIC that is best able to make use of these opportunities is given in the following chapter. Here we highlight the large rate of such events available at RHIC energies.

In order to realize this comprehensive program of jet probes, direct photon tagged jets, Upsilon and more, one requires very high luminosities and the ability to sample that full physics without selection biases.

The inclusive jet yield within  $|\eta| < 1.0$  in 0–20% central Au+Au collisions at 200 GeV has been calculated for  $p+p$  collisions by Vogelsang in a Next-to-Leading-Order (NLO) perturbative QCD formalism [143] and then scaled up by the expected number of binary collisions, as shown in Figure 1.49. Also shown are calculation results for  $\pi^0$  and direct and fragmentation photon yields. The bands correspond to the renormalization scale uncertainty in the calculation (i.e.,  $\mu, \mu/2, 2\mu$ ).

The effect of the completed stochastic cooling upgrade to the RHIC accelerator [144] has been incorporated into the RHIC beam projections [145]. Utilizing these numbers and accounting for accelerator and experiment uptime and the fraction of collisions within  $|z| < 10$  cm, the nominal full acceptance range for the detector, the sPHENIX detector can record 100 billion Au+Au minimum bias collisions in a one-year 22 week run. In fact, with the latest luminosity projections, for the purely calorimetric jet and  $\gamma$ -jet observables with modest trigger requirements, one can sample 0.6 trillion Au+Au minimum bias collisions – see details in Section 3.8. Note that the PHENIX experiment has a nearly dead-timeless high-speed data acquisition and trigger system that has already sampled tens of billions of Au+Au minimum bias collisions, and maintaining this high rate performance with the additional sPHENIX components is an essential design feature.

Figure 1.49 shows the counts per event with  $p_T$  larger than the value on the x-axis for the most central 20% Au+Au collisions at  $\sqrt{s_{NN}} = 200$  GeV. With 20 billion events per RHIC year for this centrality selection, this translates into jet samples from 20–80 GeV and direct photon statistics out beyond 40 GeV. It is notable that within the acceptance of the sPHENIX detector, over 80% of the inclusive jets will also be accepted dijet events. The necessary comparable statistics are available with 10 weeks of  $p+p$  and 10 weeks of  $p+Au$  running.

Measurement of direct photons requires them to be separated from the other sources of inclusive photons, largely those from  $\pi^0$  and  $\eta$  meson decay. The left panel of Figure 1.50 shows the direct photon and  $\pi^0$  spectra as a function of transverse momentum for both  $\sqrt{s} = 200$  GeV and 2.76 TeV  $p+p$  collisions. The right panels show the  $\gamma/\pi^0$  ratio as a function of  $p_T$  for these energies with comparison PHENIX measurements at RHIC. At the LHC, the ratio remains below 10% for  $p_T < 50$  GeV while at RHIC the ratio rises sharply and exceeds one at  $p_T \approx 30$  GeV/c. In heavy ion collisions the ratio is further enhanced because the  $\pi^0$ s are significantly suppressed. Taking the suppression into account, the  $\gamma/\pi^0$  ratio at RHIC exceeds one for  $p_T > 15$  GeV/c. The large

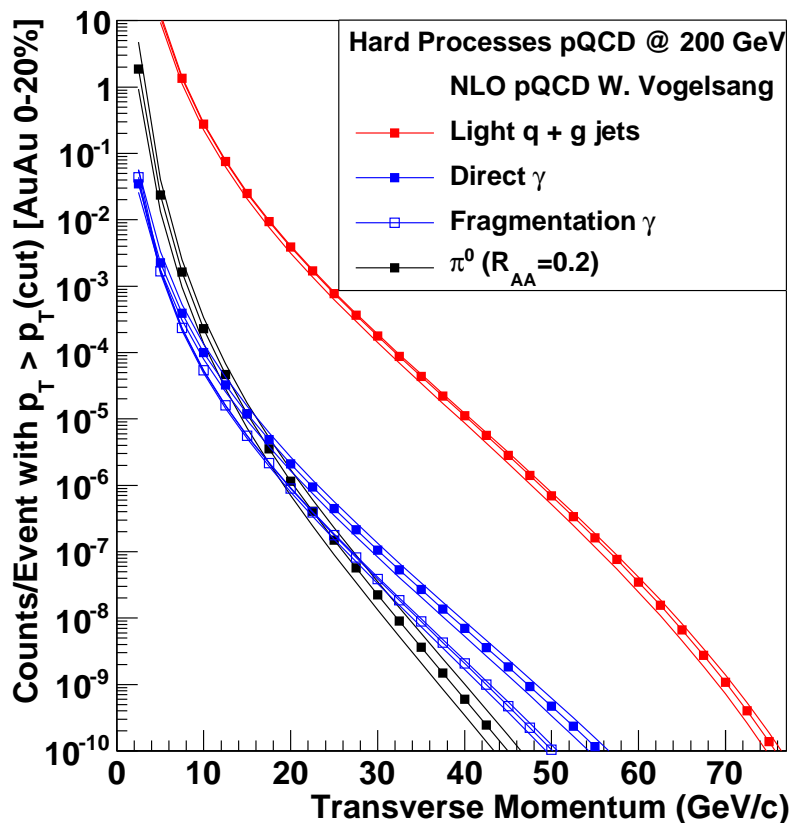


**Figure 1.49:** Jet, photon and  $\pi^0$  rates for  $|\eta| < 1.0$  from NLO pQCD [143] calculations scaled to Au+Au central collisions for  $\sqrt{s_{NN}} = 200$  GeV. The scale uncertainties on the pQCD calculations are shown as additional lines. Ten billion Au+Au central collisions correspond to one count at  $10^{-10}$  at the bottom of the y-axis range. A nominal 22 week RHIC run corresponds to 20 billion central Au+Au events.

signal to background means that it will be possible to measure direct photons with the sPHENIX calorimeter alone, even before applying isolation cuts. Beyond measurements of inclusive direct photons, this enables measurements of  $\gamma$ -jet correlations and  $\gamma$ -hadron correlations.

Figure 1.51 summarizes the current and future state of hard probes measurements in A+A collisions in terms of their statistical reach. The top panel shows the most up to date  $R_{AA}$  measurements of hard probes in central Au+Au events by the PHENIX Collaboration (sometimes called the “T-shirt plot”) plotted against statistical projections for sPHENIX channels measured after the first two years of data-taking. While these existing measurements have greatly expanded our knowledge of the QGP created at RHIC, the overall kinematic reach is constrained to  $< 20$  GeV even for the highest statistics measurements. Due to the superior acceptance, detector capability and collider performance, sPHENIX will greatly expand the previous kinematic range studied at RHIC energies (in the case of inclusive jets, the data could extend to 80 GeV/c, four times the range of the current PHENIX  $\pi^0$  measurements) and will allow access to new measurements entirely (such as fully

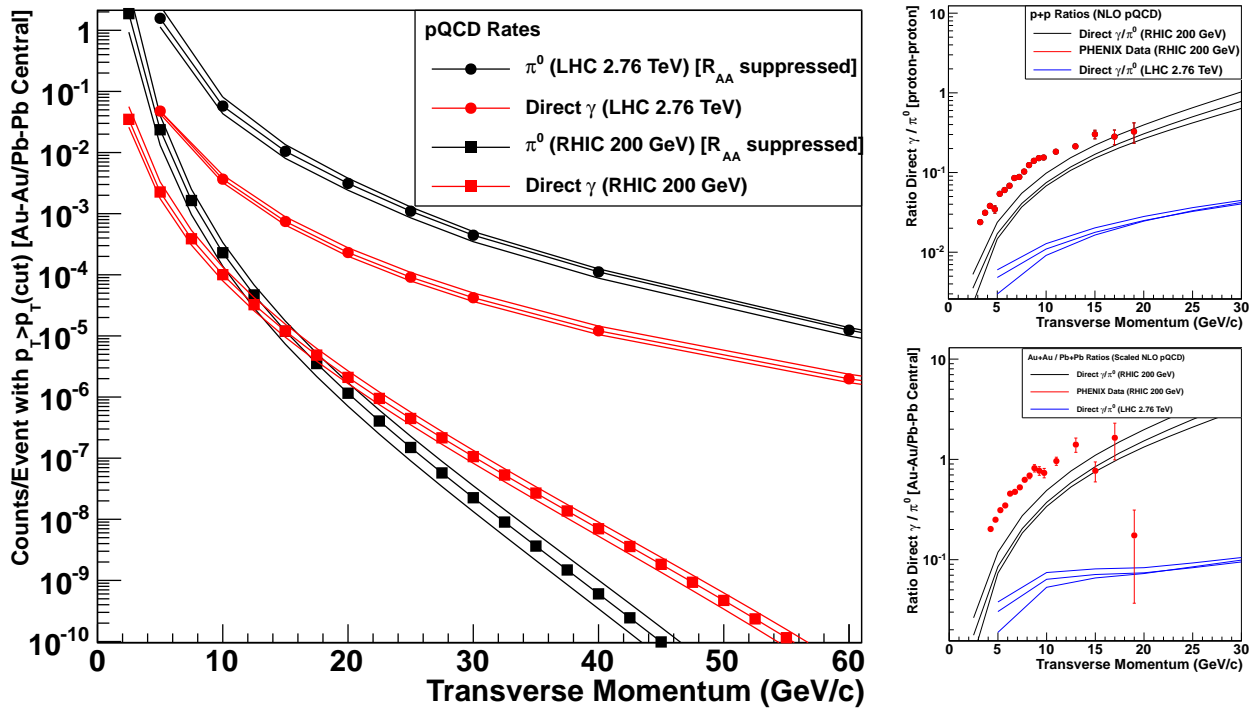


**Figure 1.50:** NLO pQCD calculations of direct photons and  $\pi^0$  for RHIC and LHC. The plot on the left shows the counts per event in Au+Au or Pb+Pb collisions (including the measured  $R_{AA}$  suppression factor for  $\pi^0$ ). The upper (lower) panel on the right shows the direct  $\gamma$  to  $\pi^0$  ratio in  $p+p$  (Au+Au or Pb+Pb) collisions, in comparison with measurements from the PHENIX experiment at RHIC [146, 147].

reconstructed  $b$ -tagged jets).

The bottom panel of Figure 1.51, adapted from slides shown by G. Roland at the QCD Town Meeting in September 2014, shows the statistical reach in  $p_T$  for single inclusive measurements (i.e. the  $R_{AA}$ ) and for “jet+X” correlation measurements. Although there are some  $p_T$  ranges in common between present day measurements at RHIC and the LHC, it can be seen that the higher kinematic ranges accessed by sPHENIX (referred to in the figure as “RHIC Tomorrow”) will have substantially more overlap with current and future LHC data in a wide variety of channels. Thus sPHENIX in tandem with the LHC experiments will allow for a detailed set of measurements of the same observables within the same kinematic ranges.

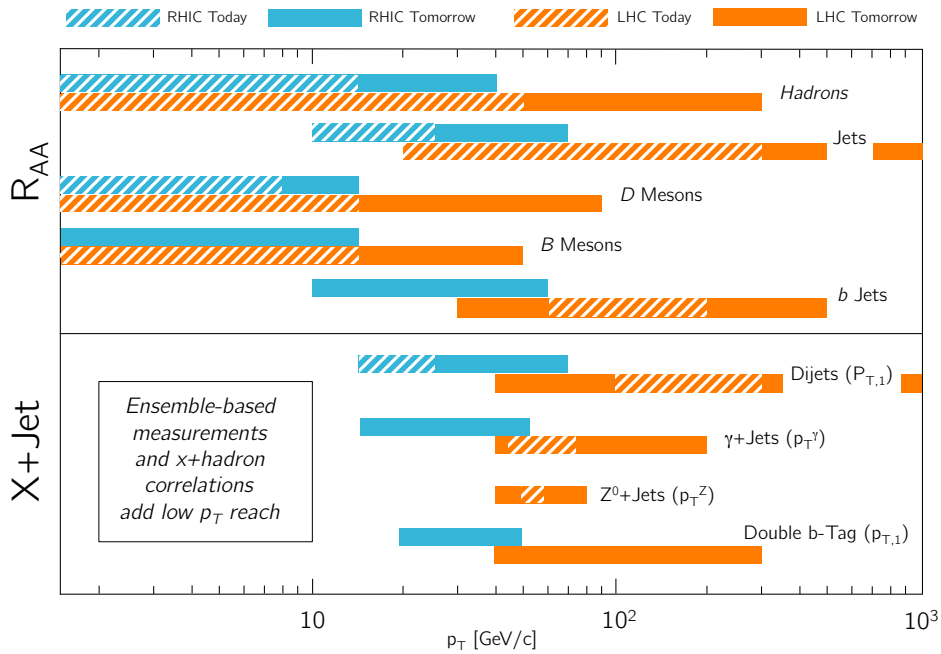
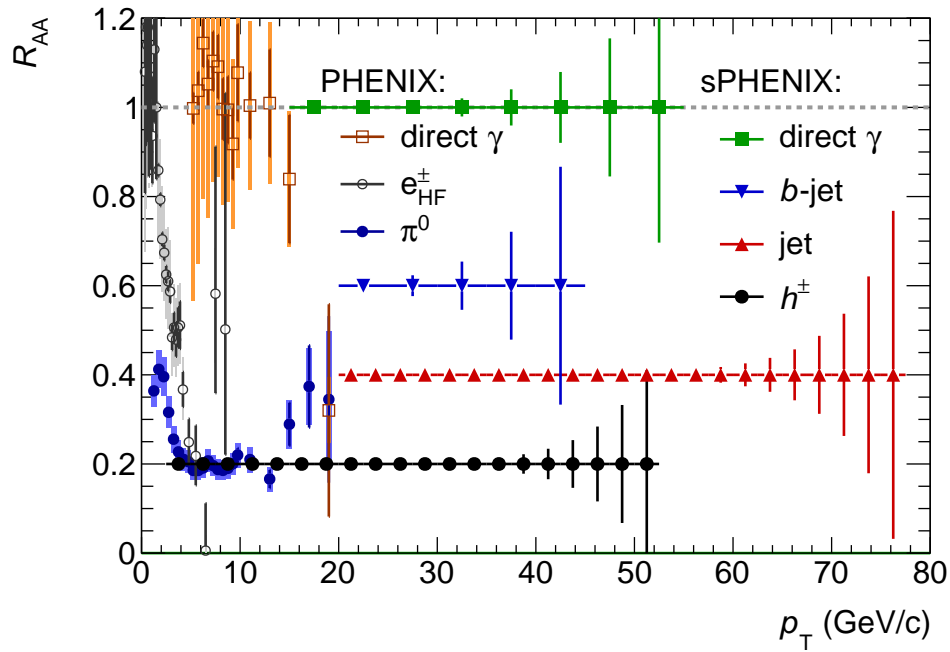


**Figure 1.51:** (Top) Statistical projections for the  $R_{AA}$  of various hard probes vs  $p_T$  in 0–20% Au+Au events with the sPHENIX detector after two years of data-taking, compared with a selection of current hard probes data from PHENIX. (Bottom) Kinematic reach of various jet quenching observables from previous and future RHIC and LHC data-taking. Adapted from slides by G. Roland at the QCD Town Meeting at Temple University.





## Chapter 2

# Physics-Driven Detector Requirements

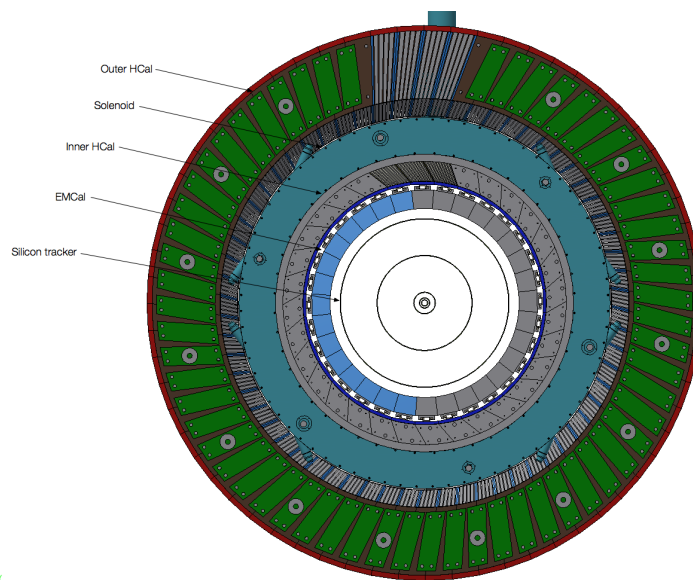


**Figure 2.1:** End view of the sPHENIX detector with its component subdetectors.

In order to perform the physics measurements outlined in Chapter 1, sPHENIX must satisfy a set of detector requirements. In this Chapter we discuss the physics-driven requirements on the performance of the sPHENIX detector. In addition, as outlined in the Executive Summary, this sPHENIX upgrade serves as the foundation for a future upgrade to a world class Electron-Ion Collider (EIC) detector built around the BaBar magnet and sPHENIX calorimetry, and those requirements are taken into account. The details of specific detector and GEANT4 simulations regarding the physics capability of the sPHENIX reference design are given in Chapter 4. The sPHENIX physics program rests on several key measurements, and the requirements that drive any particular aspect of the detector performance come from a broad range of considerations related to those measurements. A consideration of the physics requirements has led to the development of the reference design shown in Figure 2.1 and this will be described in detail in Chapter 3.

The primary components of the sPHENIX reference design are as follows.

**Magnetic Solenoid** solenoid built for the BaBar experiment at SLAC which became available after the termination of the BaBar program. The cryostat has an inner radius of 140 cm and is 33 cm thick, and can produce a central field of 1.5 T.

**Silicon Tracking** seven layers of silicon tracking for charged track reconstruction and momentum determination.

**Electromagnetic Calorimeter** tungsten-scintillating fiber sampling calorimeter inside the magnet bore read out with silicon photo-multipliers. The calorimeter has a small Molière radius and short radiation length, allowing for a compact design.

**Inner Hadronic Calorimeter** sampling calorimeter of non-magnetic metal and scintillator located inside the magnet bore.

**Outer Hadronic Calorimeter** sampling calorimeter of steel scintillator located outside the cryostat which doubles as the flux return for the solenoid.

In the following list we provide a high-level mapping between physics aims and various detector requirements. The justification for these requirements is then discussed in more detail in subsequent sections.

**Upsilon** The key to the physics is high statistics  $p+p$ ,  $p+A$ , and  $A+A$  data sets, with mass resolution and signal-to-background sufficient to separate the three states of the  $Y$  family.

- large acceptance ( $\Delta\phi = 2\pi$  and  $|\eta| < 1$ )
- high rate data acquisition (15 kHz)
- trigger for electrons from  $Y \rightarrow e^+e^-$  ( $> 90\%$  efficiency) in  $p+p$  and  $p+A$
- track reconstruction efficiency  $> 90\%$  and purity  $> 90\%$  for  $p_T > 3$  GeV/c
- momentum resolution of 1.2% for  $p_T$  in the range 4-10 GeV/c.
- electron identification with efficiency  $> 70\%$  and charged pion rejection of 90:1 or better in central Au+Au at  $p_T = 4$  GeV/c.

**Jets** The key to the physics is to cover jet energies of 20–70 GeV, for all centralities, for a range of jet sizes, with high statistics and performance insensitive to the details of jet fragmentation.

- energy resolution  $< 120\% / \sqrt{E_{\text{jet}}}$  in  $p+p$  for  $R = 0.2-0.4$  jets
- energy resolution  $< 150\% / \sqrt{E_{\text{jet}}}$  in central Au+Au for  $R = 0.2$  jets
- energy scale uncertainty  $< 3\%$  for inclusive jets
- energy resolution, including effect of underlying event, such that scale of unfolding on raw yields is less than a factor of three
- measure jets down to  $R = 0.2$  (segmentation no coarser than  $\Delta\eta \times \Delta\phi \sim 0.1 \times 0.1$ )
- underlying event influence event-by-event (large coverage HCal/EMCal) (ATLAS method)

- energy measurement insensitive to softness of fragmentation (quarks or gluons) — HCal + EMCal
- jet trigger capability in  $p+p$  and  $p+A$  without jet bias (HCal and EMCal)
- rejection ( $> 95\%$ ) of high  $p_T$  charged track backgrounds (HCal)

**Dijets** The key to the physics is large acceptance in conjunction with the general requirements for jets as above

- $> 80\%$  containment of opposing jet axis
- $> 70\%$  full containment for  $R = 0.2$  dijets
- $R_{AA}$  and  $A_J$  measured with  $< 10\%$  systematic uncertainty (also key in  $p+A$ , onset of effects)

**Fragmentation functions** The key to the physics is unbiased measurement of jet energy

- excellent tracking resolution out to  $> 40 \text{ GeV}/c$  ( $dp/p < 0.2\% \times p$ )
- independent measurement of  $p$  and  $E$  ( $z = p/E$ )

**Heavy quark jets** The key to the physics is tagging identified jets containing a displaced secondary vertex

- precision DCA ( $< 100$  microns) for electron  $p_T > 4 \text{ GeV}/c$
- electron identification for high  $p_T > 4 \text{ GeV}/c$

**Direct photon** The key to the physics is identifying photons

- EMCal resolution for photon ID ( $< 15\%/\sqrt{E}$ )
- EMCal cluster trigger capability in  $p+p$  and  $p+A$  with rejections  $> 100$  for  $E_\gamma > 10 \text{ GeV}$

**High statistics** Ability to sample high statistics for  $p+p$ ,  $p+A$ ,  $A+A$  at all centralities — requires high rate, high throughput DAQ (10 kHz).

In the following sections, we detail the origin of key requirements.

## 2.1 Acceptance

The total acceptance of the detector is determined by the requirement of high statistics jet measurements and the need to fully contain both single jets and dijets. To fully contain hadronic showers in the detector requires both large solid angle coverage and a calorimeter deep enough to fully absorb the energy of hadrons up to 70 GeV.

The PYTHIA event generator has been used to generate a sample of  $p+p$  at 200 GeV events which can be used to demonstrate the pseudorapidity distribution of jets. The left panel in Figure 2.2 shows the pseudorapidity distribution of jets with  $E_T$  above 20, 30, and 40 GeV. The right panel in Figure 2.2 shows the fraction of events where a trigger jet with  $E_T$  greater than a given value within

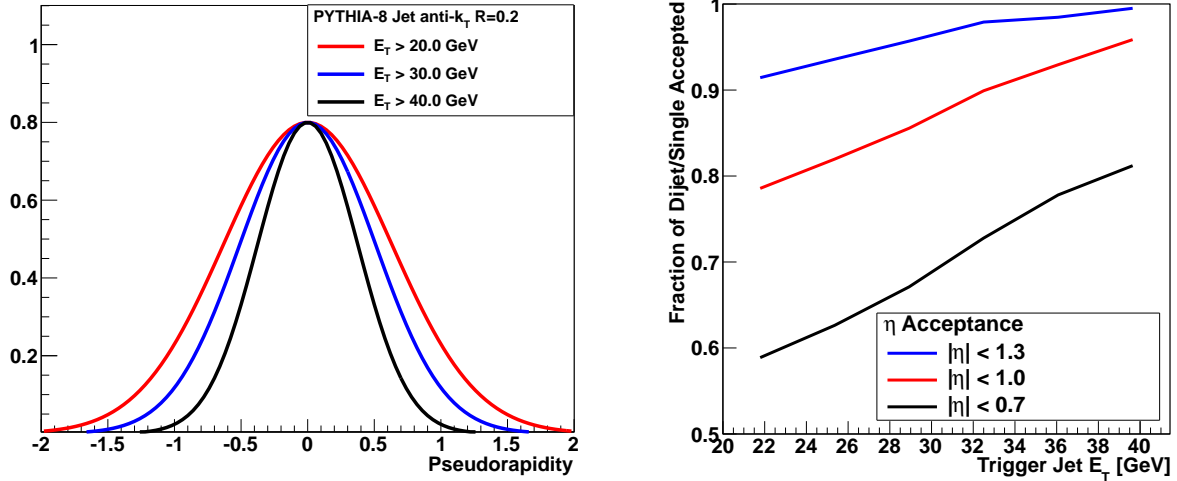


**Figure 2.2:** (Left) Pseudorapidity distribution of PYTHIA jets reconstructed with the FASTJET anti- $k_T$  and  $R=0.2$  for different transverse energy selections. (Right) The fraction of PYTHIA events where the leading jet is accepted into a given pseudorapidity range where the opposite side jet is also within the acceptance. Note that the current PHENIX acceptance of  $|\eta| < 0.35$  corresponds to a fraction below 30%.

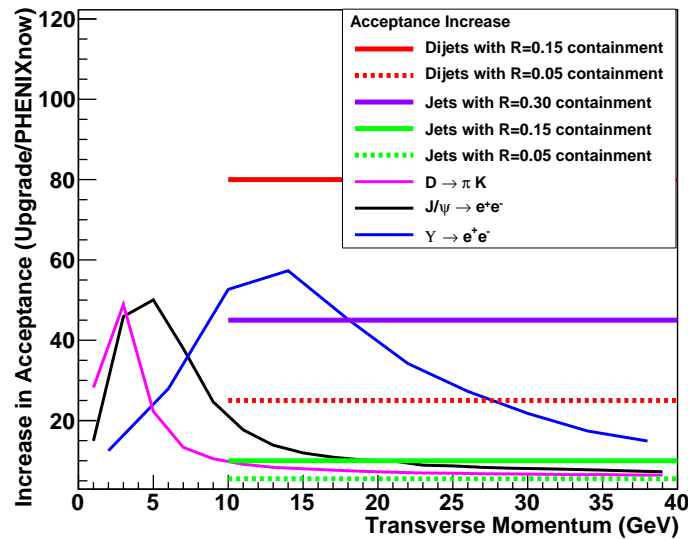


**Figure 2.3:** Acceptance increase for various processes (as modeled using the PYTHIA event generator) for the proposed sPHENIX barrel detector compared with the current PHENIX central arm spectrometers.

a pseudorapidity range has an away side jet with  $E_T > 5$  GeV accepted within the same coverage. In order to efficiently capture the away side jet, the detector should cover  $|\eta| < 1$ , and in order to

fully contain hadronic showers within this fiducial volume, the calorimetry should cover slightly more than that. Given the segmentation to be discussed below, the calorimeters are required to cover  $|\eta| < 1.1$ .

It should be noted that reduced acceptance for the away-side jet relative to the trigger suffers not only a reduction in statistics for the dijet asymmetry and  $\gamma$ -jet measurements but also results in a higher contribution of low energy fake jets (upward fluctuations in the background) in those events where the away side jet is out of the acceptance. For the latter effect, the key is that both jet axes are contained within the acceptance, and then events can be rejected where the jets are at the edge of the detector and might have partial energy capture.

Compared to the current PHENIX acceptance (the central arms cover  $|\eta| < 0.35$  and  $\Delta\phi = \pi$ ), full azimuthal coverage with  $|\eta| < 1.1$  results in a very substantial increase in the acceptance of single jets and an even larger increase in the acceptance of dijets for other observables including heavy quarkonia states, as shown in Figure 2.3. The large acceptance and high rate are key enablers of the physics program detailed in Chapter 1.

## 2.2 Segmentation

Jets are reconstructed from the four-vectors of the particles or measured energies in the event via different algorithms (as described in Chapter 4), and with a typical size  $R = \sqrt{\Delta\phi^2 + \Delta\eta^2}$ . In order to reconstruct jets down to radius parameters of  $R = 0.2$  a segmentation in the hadronic calorimeter of  $\Delta\eta \times \Delta\phi = 0.1 \times 0.1$  is required. The electromagnetic calorimeter segmentation should be finer as driven by the measurement of direct photons for  $\gamma$ -jet correlation observables. The compact electromagnetic calorimeter design being considered for sPHENIX has a Molière radius of  $\sim 15$  mm, and with a calorimeter at a radius of about 100 cm, this leads to an optimal segmentation of  $\Delta\eta \times \Delta\phi = 0.024 \times 0.024$  in the electromagnetic section.

## 2.3 Energy Resolution

The requirements on the jet energy resolution are driven by considerations of the ability to reconstruct the inclusive jet spectra and dijet asymmetries and the fluctuations on the fake jet background (as detailed in Chapter 4). The total jet energy resolution is typically driven by the hadronic calorimeter resolution and many other effects including the bending of charged particles in the magnetic field out of the jet radius. Expectations of jet resolutions approximately 1.2 times worse than the hadronic calorimeter resolution alone are typical (see a more detailed discussion in Chapter 4).

In a central Au+Au event, the average energy within a jet cone of radius  $R = 0.2$  ( $R = 0.4$ ) is approximately 10 GeV (40 GeV) resulting in an typical RMS fluctuation of 3.5 GeV (7 GeV). This sets the scale for the required reconstructed jet energy resolution, as a much better resolution would be dominated by the underlying event fluctuations regardless. A measurement of the jet energy for  $E = 20$  GeV with  $\sigma_E = 120\% \times \sqrt{E} = 5.4$  GeV gives a comparable contribution to the underlying event fluctuation. A full study of the jet energy resolution with a GEANT4 simulation of the detector configuration is required and is presented in Chapter 4.

Different considerations set the scale of the energy resolution requirement for the EMCal. The jet physics requirement is easily met by many EMCal designs. For the direct  $\gamma$ -jet physics, the photon energies being considered are  $E_\gamma > 10$  GeV where even a modest  $\sigma_E/E = 12\%/\sqrt{E}$  represents only a blurring of 400 MeV. In Au+Au central events, the typical energy in a  $3 \times 3$  tower array is also approximately 400 MeV. These values represent a negligible performance degradation for these rather clean photon showers even in central Au+Au events.

Most of these physics measurements require complete coverage over a large range of rapidity and azimuthal angle ( $\Delta\eta \leq 1.1$  and  $\Delta\phi = 2\pi$ ) with good uniformity and minimal dead area. The calorimeter should be projective (at least approximately) in  $\eta$ . For a compact detector design there is a trade-off in terms of thickness of the calorimeter and Molière radius versus the sampling fraction and, therefore, the energy resolution of the device. Further optimization if these effects will be required as we work towards a final design.

## 2.4 Tracking

The requirements on tracking capabilities are tied to three particular elements of the sPHENIX physics program: fragmentation functions at high and at low  $z$ , heavy flavor tagged jets, and the measurement of the upsilon family of quarkonia states.

In order to utilize the available luminosity fully, the tracking systems should have large, uniform acceptance and be capable of fast readout. Measuring fragmentation functions at low  $z$  means looking for possibly wide angle correlations between a trigger jet and a charged hadron. This places only moderate requirements on the momentum resolution ( $\Delta p/p \simeq 1\% \cdot p$ ), but reinforces the requirement of large acceptance.

Fragmentation functions at high  $z$  place more stringent requirements on momentum resolution. In order to unfold the full fragmentation function,  $f(z)$ , the smearing due to momentum uncertainty should be very small compared to the corresponding smearing due to the calorimetric jet measurement for a cleanly identified jet. For a 40 GeV jet this condition is satisfied by a tracking momentum resolution of  $\Delta p/p \simeq 0.2\% \cdot p$  or better.

The measurement of the Y family places the most stringent requirement on momentum resolution. The large mass of the upsilon means that one can focus primarily on electrons with momenta of  $\sim 4 - 10$  GeV/c. The Y(3S) has about 3% higher mass than the Y(2S) state; to distinguish them clearly one needs invariant mass resolution of  $\sim 100$  MeV, or  $\sim 1\%$ . This translates into a momentum resolution for the daughter  $e^\pm$  of  $\sim 1.2\%$  in the range  $4 - 10$  GeV/c.

The Y measurement also generates requirements on the purity and efficiency of electron identification. The identification needs to be efficient because of the low cross section for Y production at RHIC, and it needs to have high purity against the charged pion background to maintain a good signal to background ratio. Generally speaking, this requires minimizing track ambiguities by optimizing the number of tracking layers, their spacing, and the segmentation of the strip layers. Translating this need into a detector requirement can be done only by performing detailed simulations with a specific tracking configuration, followed by evaluation of the tracking performance. This will be discussed in detail in Section 3.6.

Tagging heavy-flavor jets introduces the additional tracking requirement of being able to measure the displaced vertex of a D or B meson decay, as described in Section 4.7. The  $c\tau$  for D and B decays is  $123 \mu\text{m}$  and  $457 \mu\text{m}$ , respectively, and the displaced vertex would need to be identified with a resolution sufficient to distinguish these decays against backgrounds.

## 2.5 Triggering

The jet energy should be available at the Level-1 trigger as a standard part of the PHENIX dead-timeless Data Acquisition and Trigger system. This triggering ability is important as one requires high statistics measurements in proton-proton, proton-nucleus, light nucleus-light nucleus, and heavy nucleus-heavy nucleus collisions with a wide range of luminosities. It is important to have combined EMCal and HCal information available so as to avoid a specific bias on the triggered jet sample.





## Chapter 3

# Detector Concept

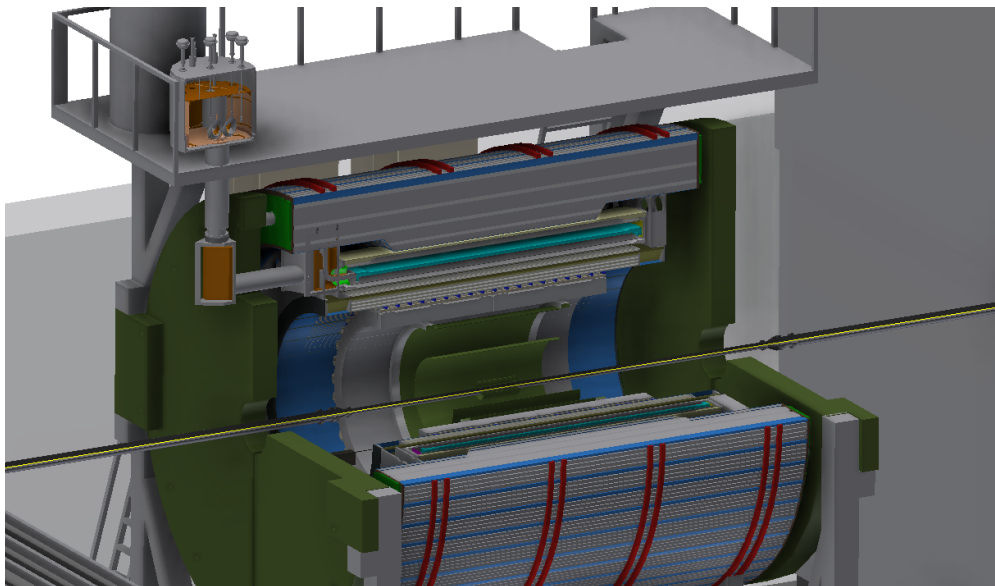


**Figure 3.1:** An engineering drawing of sPHENIX, showing the superconducting solenoid containing the electromagnetic calorimeter and surrounded by the hadronic calorimeter, with a model of the associated support structure, as it would sit in the PHENIX IR.

In this Chapter we detail the sPHENIX detector design including the magnetic solenoid, electromagnetic and hadronic calorimeters, silicon tracking, and readout electronics. Detector performance specifications are checked using a full GEANT4 simulation of the detector. Full physics performance measures are detailed in Chapter 4.

The sPHENIX detector concept takes advantage of technological developments to enable a compact design with excellent performance. A tungsten-scintillator electromagnetic calorimeter read out with silicon photomultipliers (SiPMs) or avalanche photodiodes (APDs) allows for a physically thin device which can operate in a magnetic field, without the bulk of photomultiplier tubes and the need for high voltage distribution. The thinner electromagnetic calorimeter allows space for the first longitudinal segment of the hadronic calorimeter to sit inside the bore of the solenoid, with positive implications for electron identification and reducing the overall size of the calorimeter

system. The use of solid-state sensors for the hadronic calorimeter allows for nearly identical electronic readout for the two major systems. A superconducting magnet coupled with high resolution tracking detectors provides excellent momentum resolution inside the solenoid. The detector has been designed from the beginning to minimize the number of distinct parts to be simpler to manufacture and assemble. The use of components insensitive to magnetic fields enables the hadronic calorimeter to double as the flux return for the solenoid, reducing both mass and cost. Adapting existing electronic designs for the readout allows for reduced development cost and risk, and leverages a decade and a half of experience at PHENIX. We now detail each subsystem in the following Sections.

A number of alternative designs of both the electromagnetic and hadronic calorimeter have been investigated by means of simulation as well as construction of prototype devices which have demonstrated the feasibility of the approach. Work continues to optimize and simplify the design and manufacture of the calorimeter, but we have chosen a reference design of the technologies used in the calorimeters which has been used to confirm that the design can achieve the physics goals of the experiment. The design discussed in this chapter is identical to the concept used in the simulations shown in this proposal.

### 3.1 Magnet

The magnet and tracking system should ultimately be capable of order 1% momentum resolution at 10 GeV/c, cover the full  $2\pi$  in azimuth and  $|\eta| < 1.1$ . The BaBar solenoid is a good match to the requirements, became available in late 2012, and measures were taken to transfer ownership of the coil and related equipment to Brookhaven in early 2013.

**Table 3.1:** Key characteristics of the BaBar solenoid and cryostat.

Central field in BaBar	1.5 T
Cryostat inner radius	140 cm
Cryostat outer radius	173 cm
Cryostat length	385 cm
Mean radius of windings	153 cm
Coil length	351 cm
Material thickness at normal incidence	$\sim 126$ mm Al
Operating current	4596 A
Manufacturer	Ansaldo Energia (now ASG)

The main features of the BaBar solenoid are shown in Table 3.1. The solenoid fits well into the mechanical infrastructure of the existing PHENIX interaction region (IR). The RHIC beamline is 444.8 cm above the tracks that are used to move detectors into the collision hall and 523.2 cm above the floor, and we propose to keep the track system in place for maneuvering detectors in and out. The hadron calorimeter which serves as the flux return for the magnet is about 100 cm thick, so the outer radius of the hadronic calorimeter is about 150 cm above the tracks which provides adequate clearance for support. Instrumentation in the forward and backward direction is not part of this proposal but the space available is approximately the same as the present muon tracker systems.

The BaBar magnet and related equipment, including the power supply, the quench protection electronics, the dump resistor, rigging fixtures, and some cryogenic components have been removed from the decommissioned BaBar detector and are in staging areas at SLAC. The coil in its transfer frame have been surveyed for residual radiation and have been found to be acceptable to move to Brookhaven. The BaBar solenoid has been prepared for shipping, and is shown in its transfer



**Figure 3.2:** The BaBar solenoid in its transfer frame for shipping at SLAC in May, 2013.

frame in Figure 3.2.

### 3.1.1 Magnetic Field Calculations

Magnetic field calculations of the solenoid coil and a model of the return steel were carried out with the OPERA magnetic field simulation software package. A field map is shown in Figure 3.3. Tools are under development for complete three dimensional field calculations and calculations of the forces on the detector and flux return.

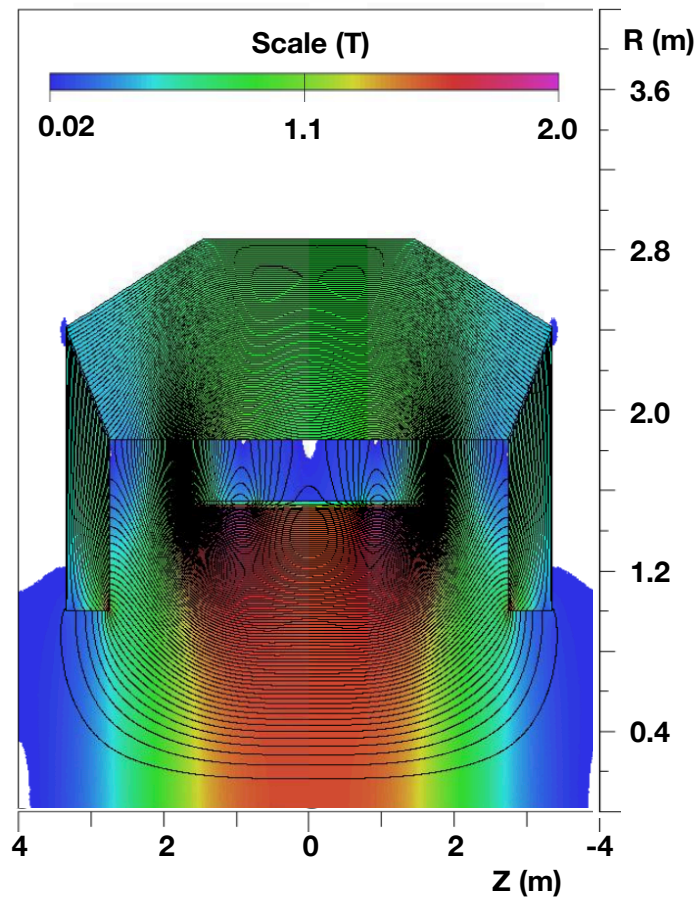


**Figure 3.3:** Calculation of the magnetic field from the solenoid with the flux returned by the hadronic calorimeter.

## 3.2 The Electromagnetic Calorimeter

The concept for the sPHENIX electromagnetic calorimeter follows from the physics requirements outlined earlier in this proposal. These requirements lead to a calorimeter design that is compact (i.e. has a small Molière radius and short radiation length), has a high degree of segmentation ( $0.024 \times 0.024$  in  $\eta$  and  $\phi$ ), has small dead area, and can be built at a reasonable cost. Since the calorimeter will be located inside the solenoid cryostat, it will also have to operate in a high magnetic field. A number of alternative designs have been investigated and work continues to optimize and simplify the design and manufacture of the calorimeter, but we have chosen a reference design.

### 3.2.1 Segmentation and readout

The segmentation of the calorimeter is determined by a number of different requirements. One primary factor is the occupancy of the individual readout towers in heavy ion collisions, which determines the ability to resolve neighboring showers and to measure the energy in the underlying event. In addition, the degree of segmentation also determines the ability to measure the transverse shower shape, which is used in separating electrons from hadrons ( $e/\pi$  rejection). The segmentation chosen for the reference design of the detector will provide the capability to perform the physics program of this proposal.

The calorimeter will be divided into individual towers corresponding to a segmentation in  $\eta$  and  $\phi$  of approximately  $0.024 \times 0.024$  and would result in about 25,000 readout channels (256 in  $\phi \times 96$  in  $\eta$ ). The light can be collected at the front or the back of the calorimeter with short light guides forming towers measuring  $\sim 2 \times 2$  cm. A design goal is to minimize the radial space required by the light guide, SiPM, readout electronics, and cables.



**Figure 3.4:** View of a prototype calorimeter module with fibers embedded before light guides are installed. (Figure courtesy of Oleg Tsai, EIC-RD1)

The reference design for the electromagnetic calorimeter, which satisfies the physics requirements of sPHENIX and the requirements of an experiment at an electron-ion collider is a sampling calorimeter with tungsten powder absorber and scintillating fibers constructed with techniques developed at UCLA [148]. A calorimeter with 0.47 mm diameter fibers on 1 mm centers has a final density of  $10.2 \text{ g/cm}^3$  and a radiation length of 7 mm which implies a Molière radius of about 2.3 cm. A calorimeter 18 radiation lengths thick occupies 12.6 cm in radius, and with light collection, sensors, preamps, and cables, the calorimeter is expected to occupy radial space of about 25 cm. Figure 3.4 shows an end view of  $4 \times 4$  towers with the end of the scintillating fibers visible, before light guides are installed.

A key element of the design of the calorimeter is the light output of the scintillator available to the photodetectors. There must be sufficient light produced by the scintillator at all energies of interest so that photostatistics do not degrade the resolution of the calorimeter. Measured light yields of  $\sim$

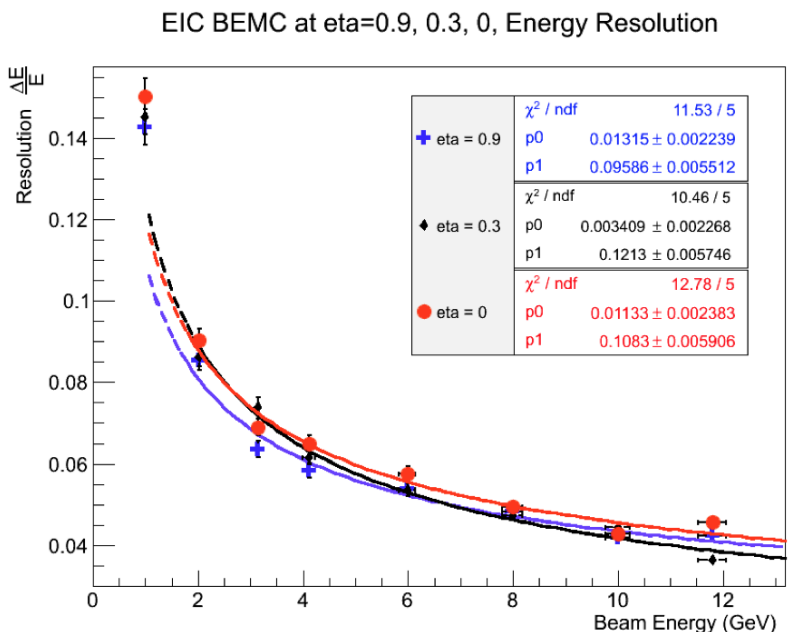


**Figure 3.5:** Energy resolution achieved in beam tests of a prototype electromagnetic calorimeter compared with GEANT4 simulation. (Figure courtesy of Oleg Tsai, EIC-RD1)

500 photoelectrons/GeV of incident energy have been demonstrated with SiPM readout in beam tests. The resulting energy resolution is less than about  $12\% / \sqrt{E}$  at the energies and angles relevant to the calorimeter. Figure 3.5 shows the measured resolution of a prototype calorimeter compared with simulation at three incident angles.

The reference design of the electromagnetic calorimeter is projective only in the azimuthal direction; the calorimeter modules are expected to be wedges in  $\phi$ . There are ongoing Monte Carlo simulations in conjunction with manufacturing feasibility studies to study the costs and benefits of projectivity at large pseudorapidity in jet reconstruction.

The PHENIX collaboration has worked with the company Tungsten Heavy Powder [149] on the design and fabrication of actual calorimeter components with funding from a Phase I Small Business Innovation Research (SBIR) grant to study and develop materials and components for compact tungsten based calorimeters for nuclear physics applications. Research and development, as part of a broader collaboration, has also been supported by a “Joint Proposal to Develop Calorimeters for the Electron Ion Collider” for EIC research and development funds (EIC-RD1).

### 3.3 The Hadronic Calorimeter

The hadronic calorimeter is a key element of sPHENIX and many of the overall performance requirements are directly tied to performance requirements of the HCal itself. The focus on measuring jets and dijets in sPHENIX leads to a requirement on the energy resolution of the



calorimeter system as a whole—the particular requirement on the HCal is that it have a single particle energy resolution better than  $\sigma_E/E = 100\%/\sqrt{E}$ .

The jet measurement requirements also lead to a transverse segmentation requirement of  $\Delta\eta \times \Delta\phi \approx 0.1 \times 0.1$  over a rapidity range of  $|\eta| < 1.1$  with minimal dead area and a longitudinal segmentation satisfactory for electron identification and measurements of the structure of energy flow in the underlying event.

The combination of the EMCal and the HCal needs to be at least  $\sim 6\lambda_{\text{int}}$  deep—sufficient to absorb  $\sim 97\%$  of the energy of impinging hadrons with momenta below 50 GeV/c, as shown in Figure 3.6. The electromagnetic calorimeter is  $\sim 1\lambda_{\text{int}}$  thick, so the hadronic calorimeter should be  $\sim 5\lambda_{\text{int}}$  deep. Although the thickness of the HCal is driven by physics needs, building it of iron plates and scintillating tiles insures that the hadronic calorimeter can also serve as the return yoke for the solenoid.

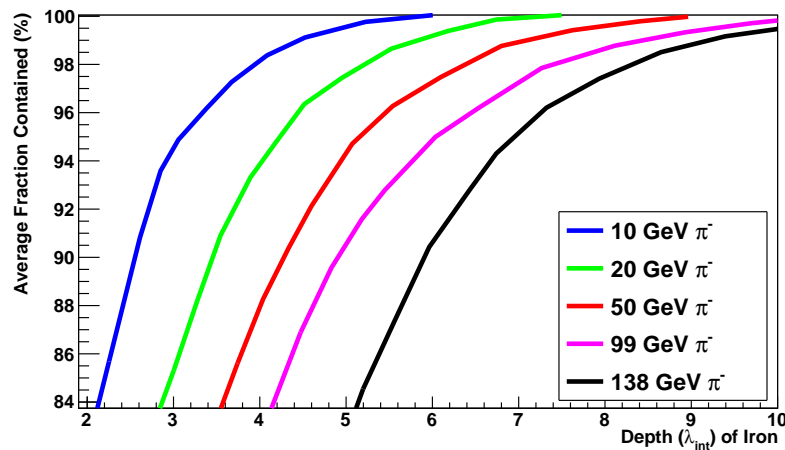


**Figure 3.6:** Average energy fraction contained in a block of iron with infinite transverse dimensions, as a function of the thickness of the block. Figure adapted from Ref. [150].

The HCal is divided into electromagnetic leakage section integrated with the EMCal inside the solenoid with the bulk of the hadronic calorimeter per se outside of the magnet. This design minimizes the overall size of the detector and minimizes the spread of the hadronic shower in the radial space occupied by the cryostat. A detailed mechanical design is needed to determine exactly how much absorber fits in the available space, but about one interaction length is expected to be feasible with the space needed for support, light collection, electronics, and cables.

The outer hadronic calorimeter as shown in Figure 3.7 surrounds the cryostat in an envelope which extends from just outside the cryostat at a radius of about 180 cm to 264.5 cm.

Both the inner and outer longitudinal segments of the calorimeter are constructed of tapered absorber plates, creating a finned structure, with each fin oriented at an angle of  $\sim \pm 10^\circ$  with respect to a radius vector perpendicular to the beam axis, with the angle chosen so that a radial ray from the interaction point crosses four scintillator layers. There are 384 tapered plates in each of the inner and outer segments. The plates in the inner and outer segments are radially tilted in opposite directions resulting in a  $\sim 20^\circ$  angle with respect to each other. They are also staggered by half a

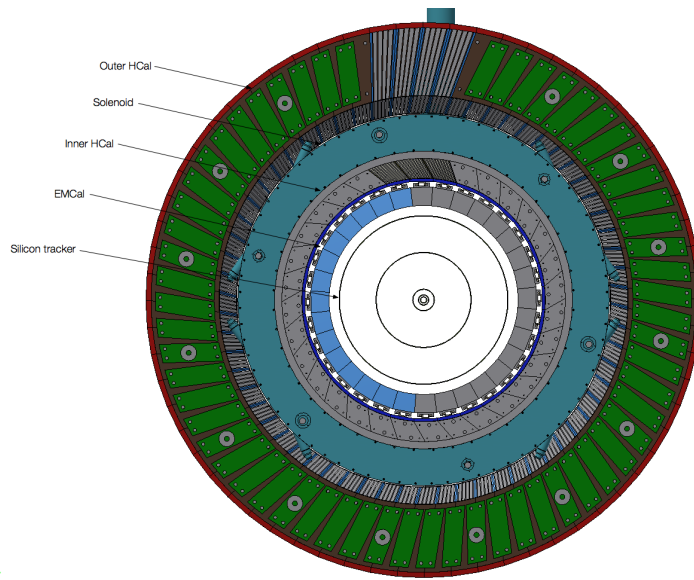


**Figure 3.7:** Cross section of sPHENIX. The outer hadronic calorimeter surrounds the solenoid cryostat.

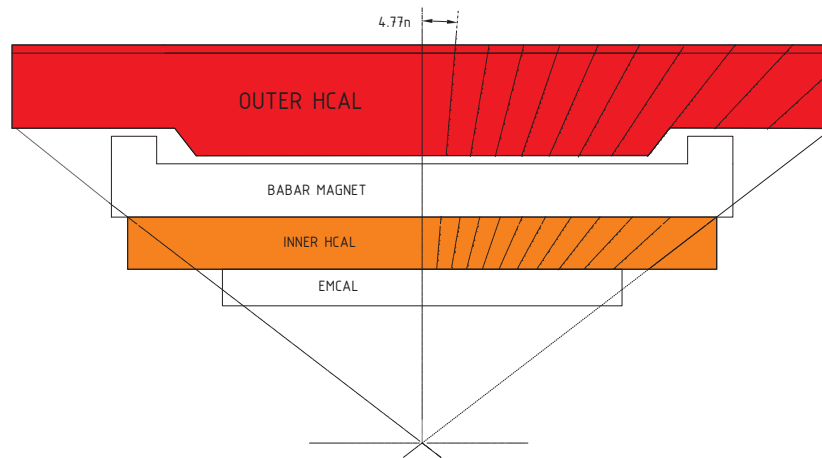


**Figure 3.8:** Scintillating tiles in the sampling gap of sPHENIX hadronic calorimeter, showing the transverse segmentation into elements 0.1 units of pseudorapidity wide.

fin thickness. The gaps between the iron plates are 8 mm wide and contain individually wrapped 7 mm thick scintillating tiles with a diffuse reflective coating and an embedded wavelength shifting fiber which traverses the entire tile, entering and exiting on the same edge. The slight tilt and



the azimuthal staggering of steel fins and scintillating tiles prevents particles from traversing the depth of the calorimeter without encountering the steel absorber (channeling). The benefits of two longitudinal segments include a further reduction in the channeling of particles in the scintillator, shorter scintillators with embedded fibers for collecting the light, shower depth information, more symmetric response for particles of opposite charge, and less variation in sampling fraction with depth.

With plates oriented as described, particles striking the calorimeter at normal incidence will, on average, traverse about 90 cm of absorber resulting in a probability for the punch through of particles with momenta above  $\sim 2$  GeV/c of only 1%. This design has a very small number of distinct components which makes it simple to fabricate, assemble, and to model.

Within each gap, there are 22 separately wrapped scintillator tiles of 11 different shapes, corresponding to a detector segmentation in pseudorapidity of  $\Delta\eta \sim 0.1$  (see Figure 3.8). Azimuthally, the hadronic calorimeter is divided into 64 wedges ( $\Delta\phi \simeq 0.1$ ). Each wedge is composed of six sampling cells (steel plate and scintillating tile) with the scintillating tile edges pointing towards the origin. The 22 pseudorapidity slices result in towers about  $10 \text{ cm} \times 10 \text{ cm}$  in size at the inner surface of the calorimeter. The total channel count in the calorimeter is  $1408 \times 2$ .

The light from the scintillating tiles between the steel fins is collected using wavelength shifting fibers laid along a path as shown in Figure 3.9. This arrangement provides relatively uniform light collection efficiency over the whole tile. We have considered two fiber manufacturers: (1) Saint-Gobain (formerly BICRON), product brand name BCF91A [151] and (2) Kuraray, product name Y11 [152]. Both vendors offer single and double clad fibers.

The calorimeter performance is determined by the sampling fraction and the light collection and readout efficiency. The readout contributes mostly to the stochastic term in calorimeter resolution through Poisson fluctuations in the number of photoelectrons on the input to the analog signal processing. Factors contributing to those fluctuations are luminous properties of the scintillator, efficiency of the light collection and transmission, and the photon detection efficiency of the photon detector.

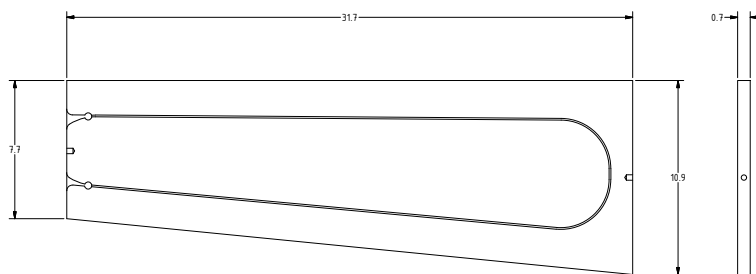


**Figure 3.9:** Grooved scintillating tiles for inner HCal section, showing the path of the fiber and the uniform thickness of the tiles. This was the design of the tile used in the prototype.

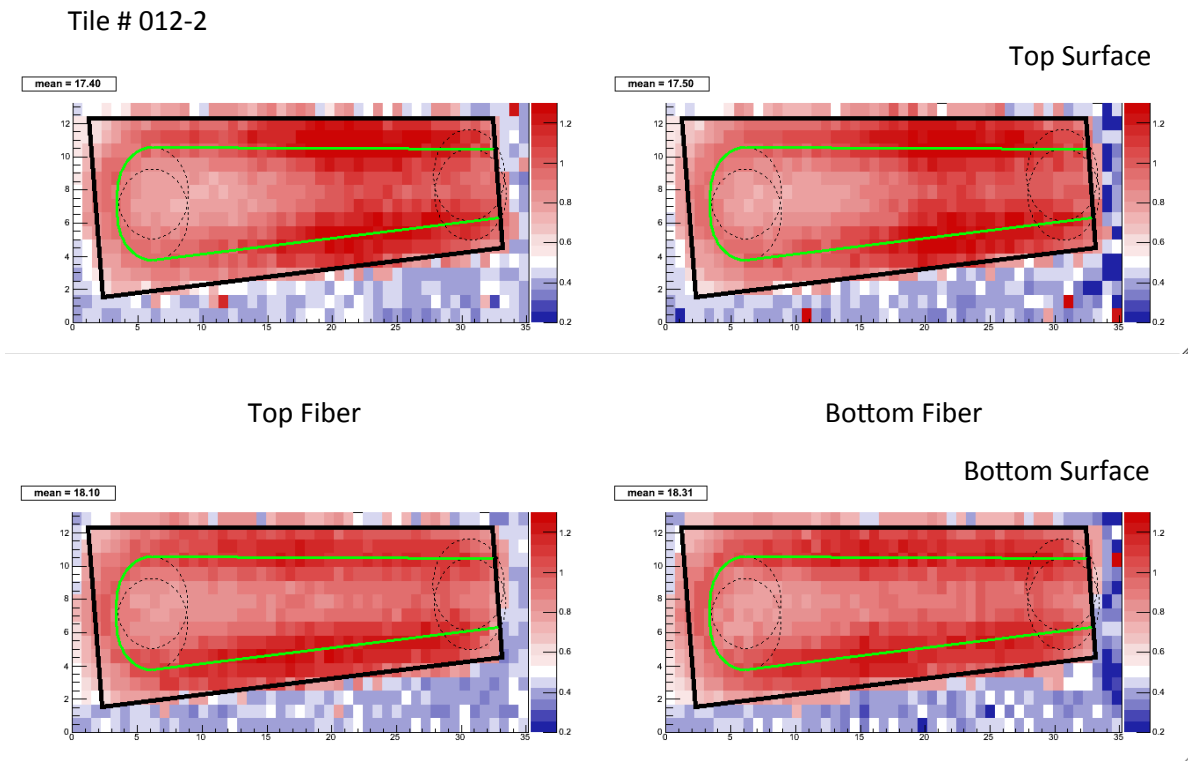


**Figure 3.10:** Measurement of uniformity of light collection in an sPHENIX prototype tile measured with a  $^{90}\text{Sr}$  source at the University of Colorado.

The scintillating tiles are based on the design of scintillators for the T2K experiment by the INR group (Troitzk, Russia) who designed and built 875 mm long scintillation tiles with a serpentine wavelength shifting fiber readout [153]. The T2K tiles are injection molded polystyrene tiles of a geometry similar to those envisioned for sPHENIX, read out with a single serpentine fiber, with each fiber viewed by an SiPM on each end. The measured light yield value was 12 to 20 photoelectrons/MIP at 20°C [154]. With 12 p.e./MIP measured by T2K for 7 mm thick tiles (deposited energy  $\sim 1.4$  MeV) and an average sampling fraction of 4% estimated for the sPHENIX HCal we expect the light yield from the HCal to be about 400 p.e./GeV. A 40 GeV hadron will share its energy nearly equally between the inner and outer HCal segments so the upper limit of the dynamic range of the HCal can be safely set to  $\sim 30$  GeV which corresponds to a yield of 12000 p.e. on the SiPM. To avoid signal saturation and ensure uniform light collection, care will be required to both calibrate the light yield (possibly requiring some attenuation) and randomize it.

The uniformity of light collection from prototype tiles constructed for the sPHENIX prototype arrangement can be judged from Figure 3.10 with measurements made by scanning a  $^{90}\text{Sr}$  source over the surface of a tile. The largest drop in the light yield is along the tile edges and in the corners farthest from the fibers.

We note that this design is optimized for simplicity of manufacturing, good light yield, and to serve as the flux return for the magnet. As such, it has a manifestly non-uniform sampling fraction as a function of depth and is not highly compensated. However, the performance specifications are quite different from particle physics hadronic calorimeters, particularly with a limited energy measurement range (0–60 GeV). GEANT4 simulations described in the next section indicate a performance better than the physics requirements, and test beam results which validate the design.

## 3.4 Calorimeter Simulations

We have employed the GEANT4 simulation toolkit [155] for our full detector simulations. It provides collections of physics processes suitable for different applications. We selected the QGSP\_BERT list which is recommended for high energy detector simulations like the LHC experiments. We have also run additional tests with different physics lists in detailed comparison with test beam data. We have integrated the sPHENIX simulations with the PHENIX software framework, enabling us to use other analysis tools we have developed for PHENIX.

The detectors and readout electronics and support structures are highly configurable in our GEANT4 framework, making it easy to test various geometries and detector concepts. Magnetic field maps for the BaBar magnet have been imported from OPERA calculations. We keep track of each particle and its descendants so every energy deposition can be traced back to the original particle from the event generator. The detector geometry can be easily configured when events are generated from a number of libraries which simulate concentric cylinders (the simplest idealized geometry), tilted plates, and spaghetti fiber geometries for the electromagnetic and hadronic calorimeters.

The superconducting magnet is simulated with the proper location of the material thickness in the cryostat.

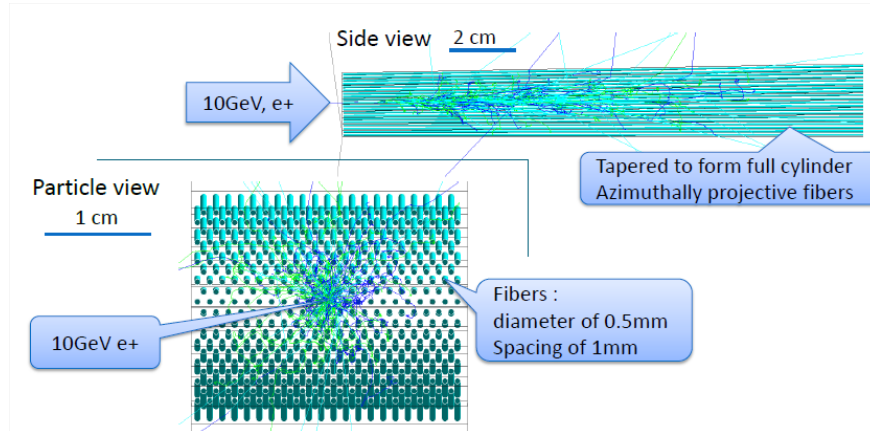
All tracks which reach a layer 10 cm behind the HCal are aborted to prevent particles which are curled up by the field from re-entering the detector. Adding up the energy of those aborted tracks yields an estimate of the energy which leaks from the back of the hadronic calorimeter.

### 3.4.1 Electromagnetic Calorimeter Simulation

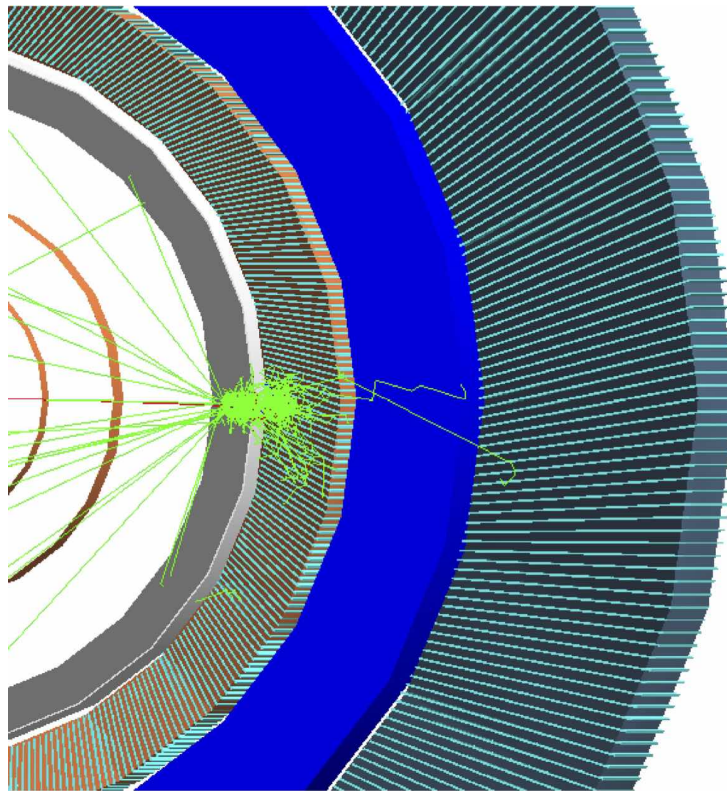
The electromagnetic calorimeter has been simulated using the GEANT4 tools described above. A detailed description of the SPACAL design is included with fiber locations and orientations as shown in Figure 3.11. This geometry is based on the GEANT4 description developed by Alexander Kiselev for the EIC research and development calorimeter project.

Figure 3.12 shows a typical GEANT4 event in which a 10 GeV/ $c$  electron hits the calorimeter. Most of the shower develops in the EMCal. The resolution of the electromagnetic calorimeter for electrons at normal incidence was shown earlier in comparison with the test beam data in Figure 3.5.

The energy deposited in the electromagnetic calorimeter in central HIJING events is shown in Figure 3.13. The mean energy deposited in any single tower is estimated to be approximately 50 MeV. The existing PHENIX electromagnetic calorimeter cluster finding algorithm has been adapted for the sPHENIX EMCal specifications. Initial results indicate that for a 10 GeV photon



**Figure 3.11:** GEANT4 event display showing the fiber matrix and an electron shower development in the calorimeter.



**Figure 3.12:** Transverse view of a 10 GeV/ $c$  electron in sPHENIX, showing it showering mainly in the ECal.

there is an extra 4% of underlying event energy in the cluster and a degradation of less than 10% in the energy resolution when embedded in a central Au+Au event (simulated with the HIJING event generator).

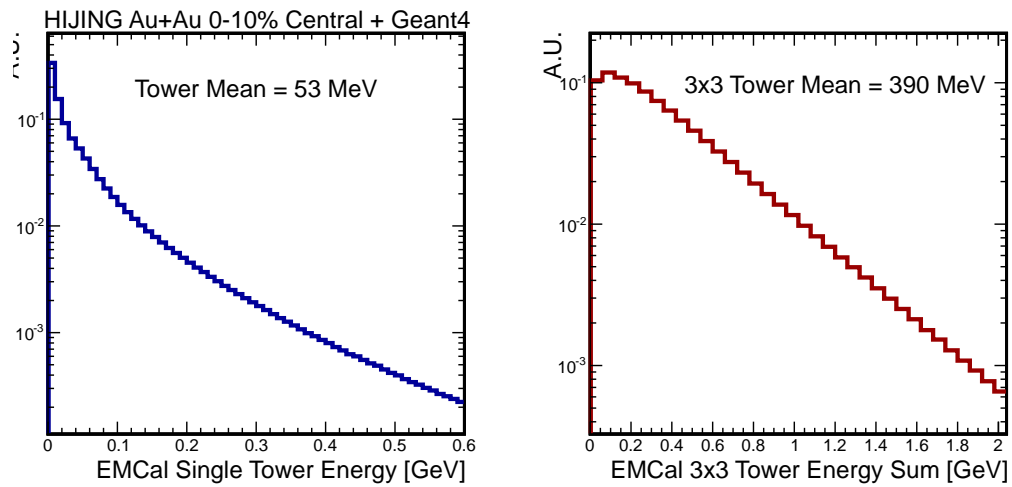


**Figure 3.13:** Distribution of energy deposited in the electromagnetic calorimeter for single towers (left panel) and in  $3 \times 3$  arrays of towers (right panel) in central HIJING events.

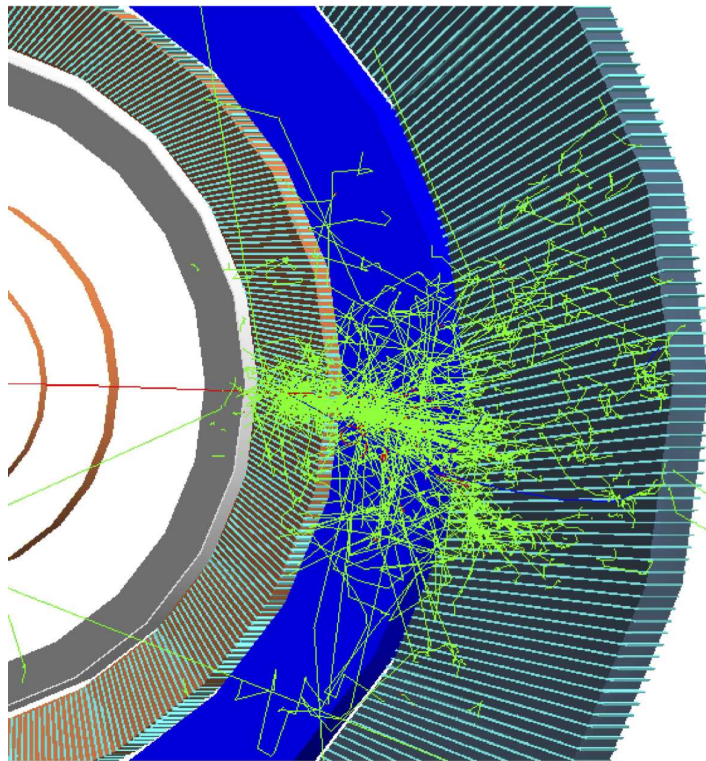


**Figure 3.14:** Transverse view of a  $10 \text{ GeV}/c \pi^-$  in sPHENIX. It penetrates the EMCal and magnet and showers in the first segment of the HCal.

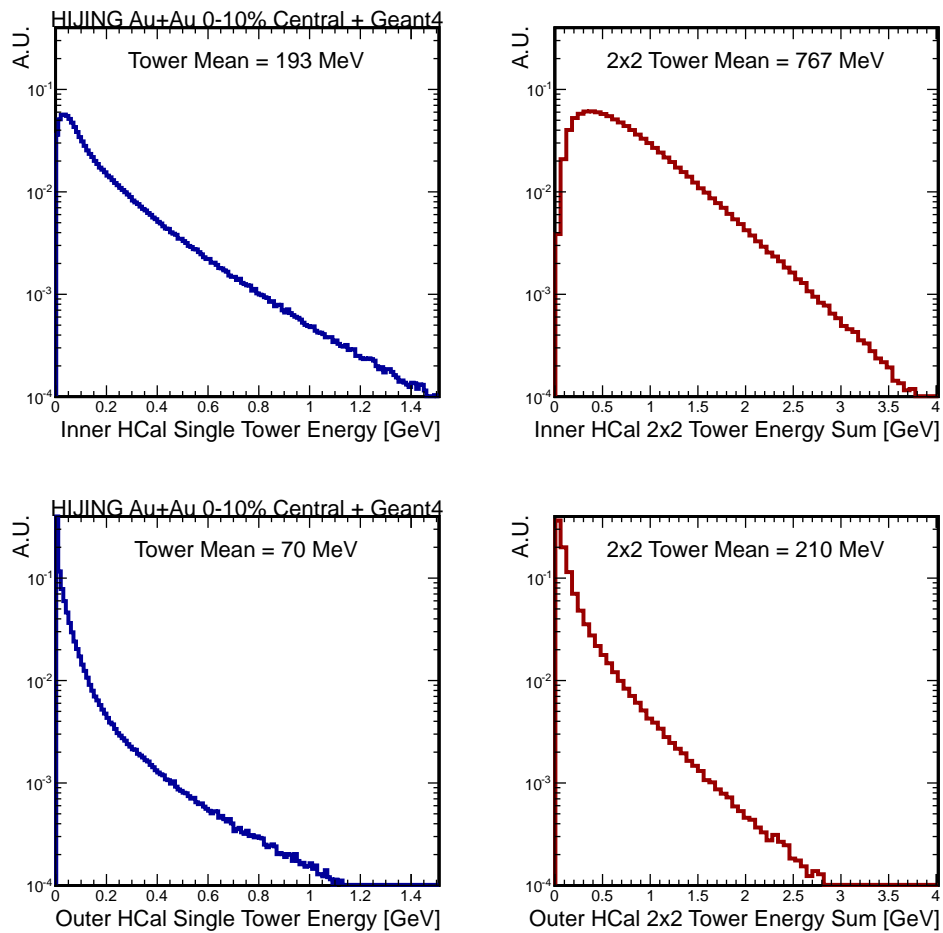


**Figure 3.15:** Energy occupancy distribution for the inner and outer hadronic calorimeter sections in 10% central Au+Au HIJING events run through the full GEANT4 simulation.

### 3.4.2 Hadronic Calorimeter Simulation

The hadronic calorimeter has been simulated using the GEANT4 tools described above. The simulation includes the detailed geometry of the steel plates and interleaved scintillator tiles. Figure 3.14 shows a typical GEANT4 event in which a 10 GeV/ $c$   $\pi^+$  incident on the calorimeter showers in the Hcal.

The average energy deposition in the hadronic calorimeter inner and outer longitudinal segments in a HIJING 10% central Au+Au event is shown in Figure 3.15.

The single particle energy resolution in the HCal has been determined using a full GEANT4 description of the calorimeters. The energy deposition in the scintillator is corrected for the average sampling fraction of the inner and outer sections and electromagnetic calorimeter separately.

The full calorimeter response to single protons and charged pions is shown in Figure 3.16. The mean and standard deviation from a Gaussian fit to the measured energy distribution are used to



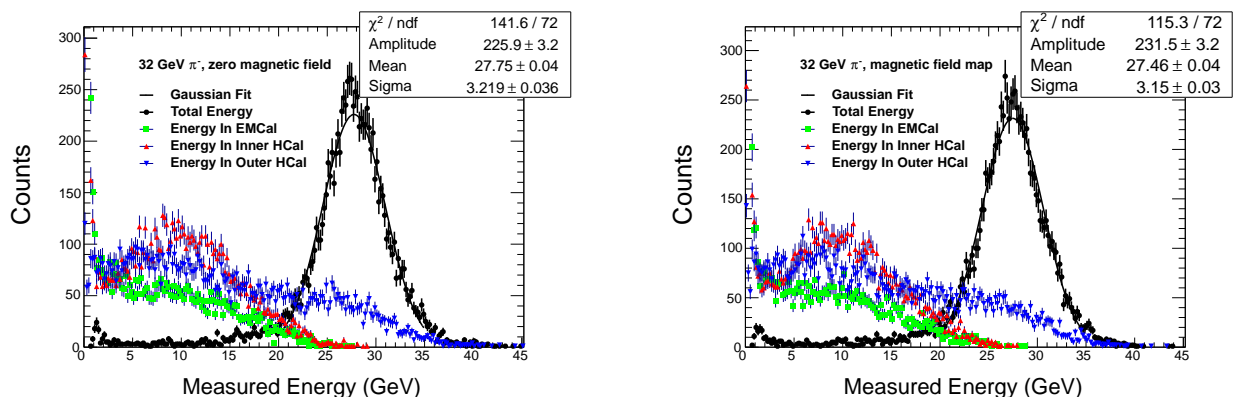


**Figure 3.16:** Energy deposited in the three longitudinal segments of the calorimetry by 32 GeV/c charged pions, showing the good containment and Gaussian response of the calorimeter (shown with and without the magnetic field turned on).

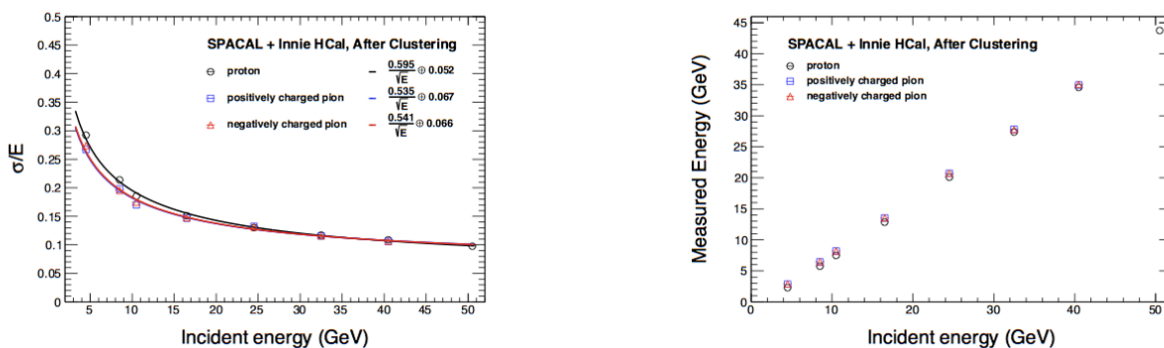


**Figure 3.17:** Energy resolution of the full calorimeter as a function of incident hadron energy. The left panel shows the Gaussian resolution width and the right panel shows the linearity of the energy response.

calculate the nominal detector resolution. These indicate a GEANT4 performance level better than the physics requirements. Note that for jets in the energy range 20–70 GeV, the constant term is not a dominant effect. Detailed comparisons with test beam data are necessary for final optimization of the design.

As mentioned above, the proposed sPHENIX calorimeter system is about  $6\lambda_{int}$  deep, and one expects some leakage of energy out of calorimeter. The amount of this leakage and its energy dependence can be estimated from literature, Figure 3.6 above, or from simulation which is tuned to available experimental data. The probability for a proton to go through the whole depth of the calorimeter without an hadronic interaction is about 0.6% (verified with full GEANT4 simulations). Therefore, energy leakage out the back of the calorimeter is not expected to be a serious problem.

## 3.5 Electronics

For the readout of both the EMCal and HCal a common electronics design will be used to reduce the overall cost and minimize the design time. The reference design approach is based on electronics developed for the PHENIX Hadron Blind Detector (HBD) and Resistive Plate Chambers (RPC), and uses the current PHENIX DAQ as the backend readout, although there are alternatives which have been examined and could still be viable.

### 3.5.1 Sensors

For both the electromagnetic and hadronic calorimeters, we are currently considering as sensors 3 mm×3 mm silicon photomultipliers (SiPMs), such as the Hamamatsu S10362-33-25C MultiPixel Photon Counters (MPPC). These devices have 14,400 pixels, each 25 μm×25 μm. Any SiPM device will have an intrinsic limitation on its dynamic range due to the finite number of pixels, and with over 14K pixels, this device has a useful dynamic range of over 10<sup>4</sup>. The saturation at the upper end of the range is correctable up to the point where all pixels have fired. The photon detection efficiency is ~ 36% and it should therefore be possible to adjust the light level to the SiPM using a mixer to place the full energy range for each tower (~ 5 MeV–50 GeV) in its useful operating range. For example, if the light levels were adjusted to give 10,000 photoelectrons for 50 GeV, this would require only 200 photoelectrons/GeV, which should be easily achieved given the light level from the fibers entering the mixer.

A number of sample devices, all 3 mm×3 mm, from AdvansID, Excelitas, SensL, and R&D devices from RMD have been characterized for use in sPHENIX, in addition to a suite of new sensors from Hamamatsu. Cost, photon detection efficiency, gain, number of micro-pixels, and dark current have been compared for a wide variety of devices. Concern about radiation damage to SiPMs resulted in a test in PHENIX in Run 14 in which two Hamamatsu SiPMs were placed at approximately the location of the sPHENIX EMCal, and while the leakage current was monitored during Au+Au operation, the thermal neutron flux was measured with a <sup>3</sup>He proportional counter. The devices are thought to be damaged by neutrons with an energy of a few MeV which result from secondary neutrons produced by collision products, and so simulation of the neutron background in sPHENIX will be necessary. Radiation damage has also been measured on a variety of devices with a 14.1 MeV neutron generator at the BNL Instrumentation Solid State Gamma Irradiation Facility, and these studies will allow selection of the most rad-hard device. KETEK, working with the CMS experiment, has been working on devices which may be more immune to radiation, and samples of those devices will be tested as well. The result of these and future studies should allow us to select the most appropriate readout device for sPHENIX that will meet all of its requirements.

While we believe that the SiPMs are likely the most suitable sensor for the calorimeters, we are also considering avalanche photodiodes (APDs) as an alternative. They have much lower gain (~50–100 compared to ~ 10<sup>5</sup> for SiPMs), and therefore would require lower noise and more demanding readout electronics, but they do provide better linearity over a larger dynamic range. In addition, while the gain of both SiPMs and APDs depend on temperature, SiPMs have a stronger gain variation than APDs (typically 10%/°C for SiPMs vs 2%/°C for APDs). Thus, we are considering APDs as an alternative solution as readout devices pending further tests with SiPMs and our light mixing scheme.



### 3.5.2 Digital and Analog Electronics

#### SiPM Preamplifier Circuitry

The requirements of the sPHENIX calorimeter preamplifier circuit board are to provide localized bias/gain control, temperature compensation, signal wave shaping and differential drive of the SiPM signal to an ADC for acquisition. Gain adjustment and temperature compensation are performed as part of the same control circuit. Signal wave shaping is performed by the differential driver to satisfy the sampling requirements of the ADC.

#### Temperature Compensation

The reverse breakdown voltage  $V_{br}$  for the Hamamatsu S10362-33-25C device is nominally 70 Volts. As the bias is increased over the value of  $V_{br}$  the SiPM begins to operate in Geiger mode with a gain of up to  $2.75 \times 10^5$ . The range of this over-voltage ( $V_{ov}$ ) is typically 1–2 Volts and represents the useful gain range of the device. The  $V_{br}$  increases by  $56 \text{ mV}/^\circ\text{C}$  linearly with temperature and must be compensated to achieve stable gain. This compensation is achieved using a closed feedback loop circuit consisting of a thermistor, ADC, logic and DAC voltage control as shown in Figure 3.18.

The thermistor is fixed to the back of the SiPM and provides a significant voltage variation over temperature when used as part of a voltage divider, thereby easing temperature measurement over a length of cable. The bias supply for an array of SiPMs is fixed nominally at  $V_{br} + 2.5\text{V}$ . The DAC in each SiPM circuit then outputs a subtraction voltage of 0 V to 5 V to provide a full range of gain control over the device temperature range. The SiPM gain may then be adjusted externally through an interface to the logic.

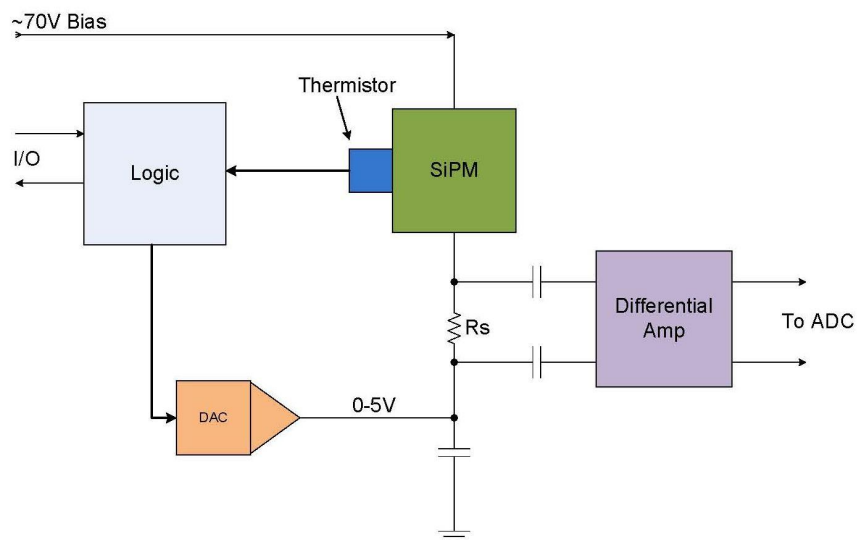


**Figure 3.18:** Block diagram of a temperature compensating circuit for SiPMs

## Preamplifier-Shaper-Driver

The SiPM current develops a voltage across the load resistor  $R_s$  proportional to the number of pixels fired. To avoid the region of greatest non-linearity due to saturation of the SiPM, the maximum signal level is optically adjusted to 10K out of 14.4K pixels fired. Simulations of the SiPM indicate that the current could be as much as several tenths of an ampere at this maximum level. Results of a SPICE simulation are shown in Figure 3.19. Such a large current affords the use of a small value for  $R_s$  which virtually eliminates the contribution of  $R_s$  to non-linearity. This signal voltage is sensed differentially, amplified and filtered by a low power, fully differential amplifier. For sampling by a 65MSPS ADC, a peaking time of approximately 35 ns is achieved through the use of a second order Butterworth filter implemented in the differential driver circuit.

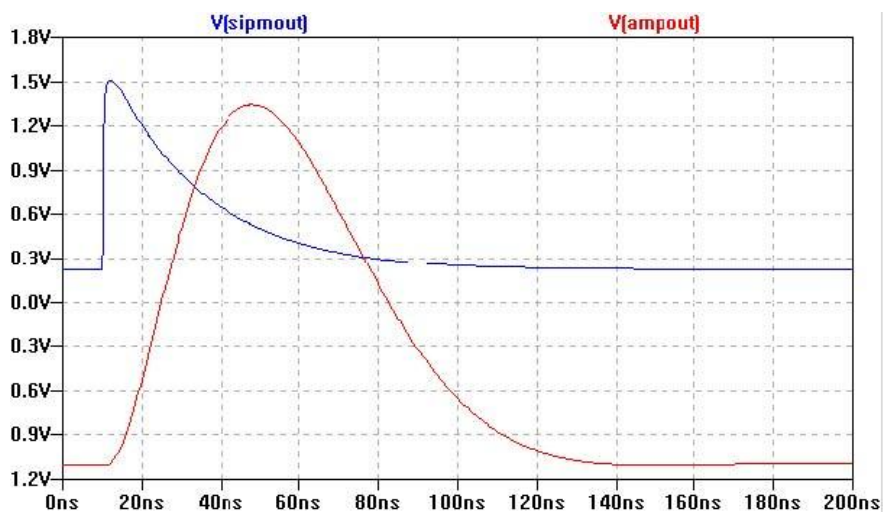


**Figure 3.19:** SPICE simulation of a prototype temperature compensating circuit for SiPM readout of the sPHENIX EMCAL and HCal.

## Signal Digitization

One solution for the readout of the EMCAL and HCal detectors for sPHENIX is the direct digitization of the SiPM signal. The signals from the SiPM are shaped to match the sampling frequency, and digitized using a flash ADC. The data are stored in local memory pending a Level-1 (L1) trigger decision. After receiving an L1 trigger decision, the data are read out to PHENIX Data Collection Modules (DCM II). These second generation Data Collection Modules would be the identical design as those developed and implemented for reading out the current PHENIX silicon detectors. One advantage of direct digitization is the ability to do data processing prior to sending trigger primitives to the L1 trigger system. The data processing can include channel by channel gain and offset corrections, tower sums, etc. This provides trigger primitives that will have near offline quality, improved trigger efficiency, and provide better trigger selection.

A readout system based on this concept was implemented for the Hadron Blind Detector (HBD) for the PHENIX experiment as shown in Figure 3.20 and subsequently modified for the PHENIX Resistive Plate Chamber (RPC) system. The block diagram of the Front-End Module (FEM) is

showed in Figure 3.21. In the HBD system, the discrete preamplifier-shaper is mounted on the detector and the signals are driven out differentially on a 10 meter Hard Metric cable. The signals are received by Analog Device AD8031 differential receivers which also serves as the ADC drivers. Texas Instruments ADS5272 8 channel 12 bit ADCs receive the differential signals from 8 channels and digitize them at 6x the beam crossing clock. The 8 channels of digitized data are received differentially by an Altera Stratix II 60 FPGA which provides a 40 beam crossing L1 delay and a 5 event L1 triggered event buffer.

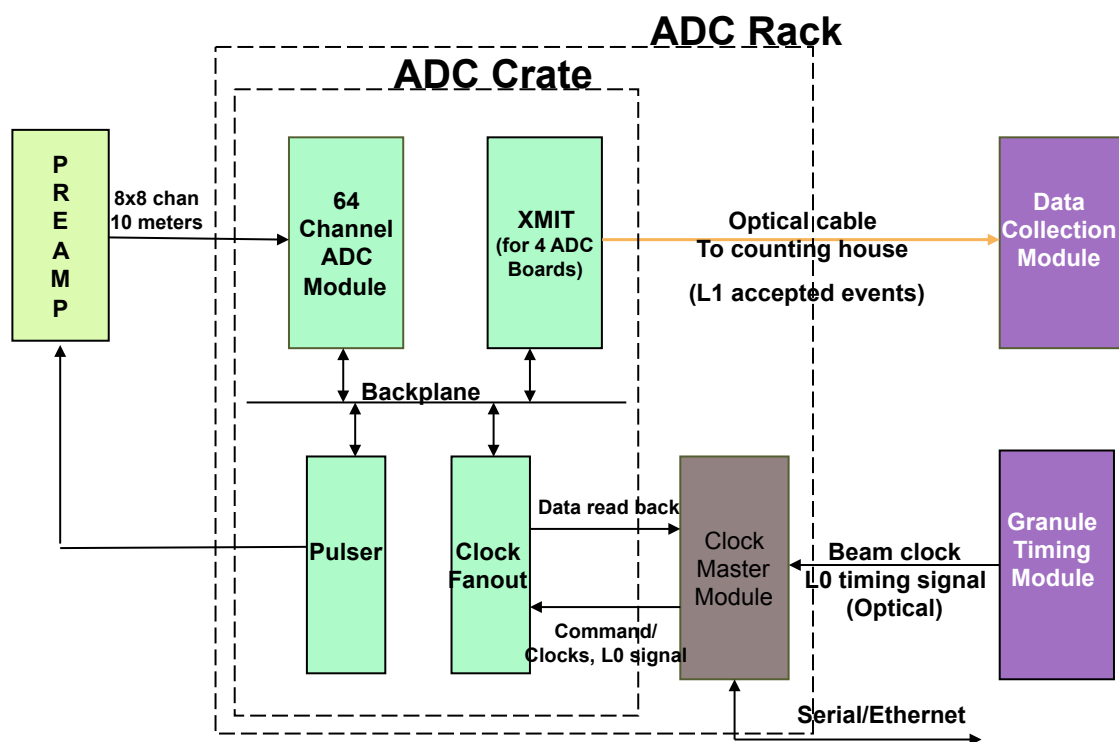


Figure 3.20: Block diagram of read out electronics based on electronics designed for the HBD.

The L1 triggered data from 4 FEMs is received by an XMIT board using token passing to control the readout of the FEMs. The data is then sent by 1.6 GBit optical links to the PHENIX DAQ. A ClockMaster module interfaces to the PHENIX Granule Timing Manager (GTM) system and fans out the clocks, L1 triggers and test enable signals to the FEMs and XMIT modules. The ClockMaster module also receives slow control signals for configuring the readout.

Although not shown in the block diagram, the FEM has 4 LVDS outputs that can be used to bring out L1 trigger primitives at 800 Mbits/sec. This feature was not used for the HBD readout, however it has been implemented for the RPC detector. A trigger module for the RPC system based on the Altera Arria FPGA receives the trigger primitives from the FEMs, combines them and sends them to the PHENIX L1 trigger system through two 3.125 GBit optical links.

Distributing the analog and digital electronics directly on the detector in close proximity to the sensors with all control and data connections transmitted via high-speed optical fiber has been considered, and has not been found to be feasible considering cost, cooling, development time, and serviceability. The approach chosen for the reference design has the temperature compensating preamplifier mounted on the detector which distributes the bias voltage to the sensors and the

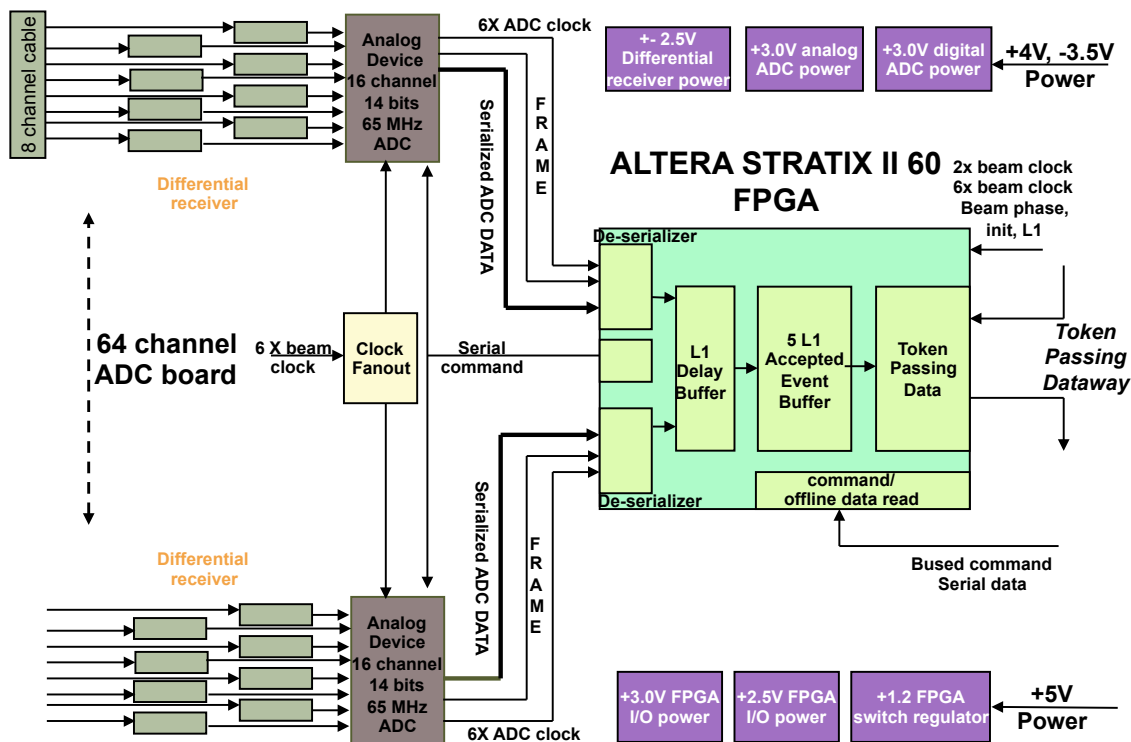
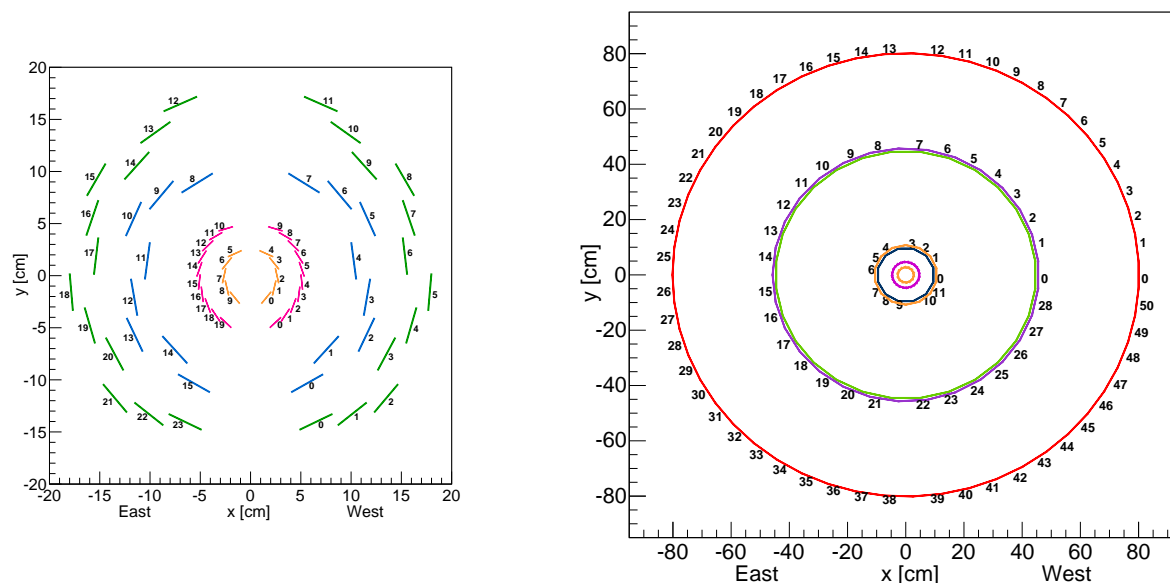


Figure 3.21: Block diagram of 64 channel ADC board based on design of the HBD system.

drives the shaped and amplified signals differentially to the digital modules located in racks near the detector using shielded cables. High speed fiber optic cables bring in all control and clock signals to the digitizers and transmit Level 1 trigger primitives and triggered data to the PHENIX DAQ.

### 3.6 Charged Particle Tracking

As discussed in Chapter 2, the key design requirements of the tracking system are precise momentum resolution, high track reconstruction efficiency for the signals of interest, good purity of the reconstructed tracks in central Au+Au collisions, and precise measurement of displaced vertices. After detailed GEANT4 studies and extensive work on the tracking and pattern recognition software, a reference design has been adopted that is capable of meeting all of the key design requirements for the tracking system. The reference design, which incorporates seven planes of silicon detectors, is described and its performance detailed in this section.



**Figure 3.22:** (left) Present configuration of silicon tracking layers in the PHENIX VTX detector. (right) Reconfiguration of the VTX inner two layers and additional tracking layers as described in the text.

The current PHENIX silicon vertex tracker (VTX) consists of two inner layers (pixels) at radii 2.5 and 5 cm from the beamline and two outer layers (strip-pixels) at radii of 11.8 and 16.7 cm. The ladders comprising the current PHENIX VTX are shown in the left panel of Figure 3.22. The VTX, combined with the outer PHENIX drift chambers (DC) and pad chambers (PC) provides good track pattern recognition, high efficiency, and excellent displaced vertex resolution with a specification for the distance of closest approach resolution in the transverse plane of better than  $100 \mu\text{m}$  for  $p_T > 1 \text{ GeV}/c$ . This resolution is exceeded even in the high occupancy Au+Au environment.

The reference configuration adds eight additional ladders to the two inner pixel layers, thus completing azimuthal  $2\pi$  coverage with the existing  $|\eta| < 1.0$  coverage. In addition to the two inner pixel layers, there will be five planes of strip detectors designed for precise momentum measurement and pattern recognition in a high multiplicity environment. Three of those layers will use strips of  $60 \mu\text{m}$  pitch and 8 mm length, and two will use strips of  $240 \mu\text{m}$  pitch and 2 mm length. The primary purpose of the latter two strip layers is pattern recognition. Each of the two pattern recognition layers is mounted on the same support and cooling structure as one of the longer strip layers. The lengths of the strips in the five outer layers represent a compromise between cost and

pattern recognition performance. Table 3.2 summarizes the reference configuration tracker layout.

**Table 3.2:** The parameters of the reference configuration tracking layers.

Layer	radius (cm)	sensor pitch ( $\mu\text{m}$ )	sensor length (mm)	sensor depth ( $\mu\text{m}$ )	total thickness % $X_0$	area $m^2$
1	2.7	50	0.425	200	1.3	0.034
2	4.6	50	0.425	200	1.3	0.059
3	9.5	60	8	320	1.35	0.152
4	10.5	240	2	320	1.35	0.185
5	44.5	60	8	320	1	3.3
6	45.5	240	2	320	1	3.5
7	80.0	60	8	320	2	10.8

Charged particle tracks are reconstructed as follows. Modest thresholds are applied on struck silicon cells. These thresholds eliminate small energy deposits that are produced by low energy spallation from passing particles, while preserving deposits from lower momentum signal tracks that pass through the outer silicon layers with large angles away from radial. Adjacent hits are then clustered, and the clusters are passed into the track pattern recognition algorithm as a set of spatial points averaged from the clustered hits. We employ a 5-dimensional Hough transform to locate the helical hit patterns from tracks bending through the solenoid field. The large 5-d parameter space is spanned efficiently with low memory overhead in the high occupancy of central heavy ion collisions by a recursive search. The discovered track candidates are then passed into a Kalman fitter assuming a constant magnetic field, and smoothing is applied to measure the distance of closest approach (DCA) with respect to the primary vertex. Some iterations are performed to simultaneously determine the primary vertex position and the track DCAs. Finally, a 1.6% momentum recalibration is applied to account for the small differences between the true field map of the BaBar solenoid and the assumption of a constant field. We then select from tracks sharing more than 3 hits the track with the best  $\chi^2$  and reject the others. This final rejection has minimal impact on the track population for the reference design.

To evaluate how well the reference design and tracking software meet the key requirements of the physics program, a full GEANT4 simulation of the tracking performance has been carried out using single particle events and central HIJING Au+Au events — with and without embedded single particles.

The  $p_T$  resolution for single pions is shown as a function of  $p_T$  in Figure 3.23. The constant term, which is due to multiple scattering in the material of the tracker, is found to be 1.1%. The linear term, determined by the position resolution of the tracker, is  $2.7 \times 10^{-4}(\text{GeV}/c)^{-1}$ . This momentum

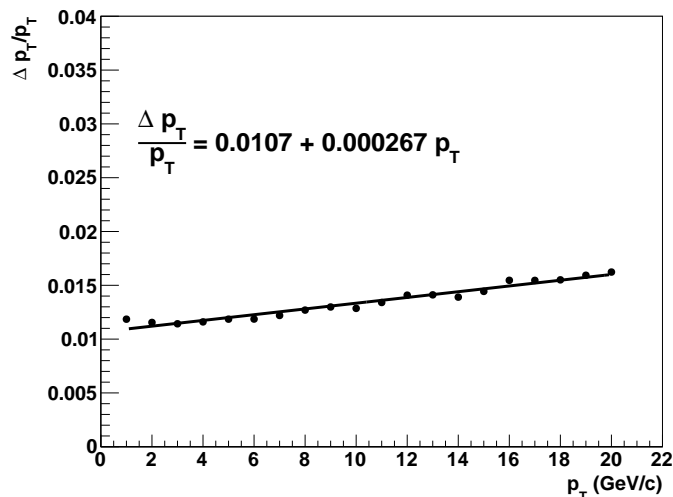


**Figure 3.23:** GEANT4 and track model evaluation of single particle (pion) transverse momentum resolution. The fit consists of a term that is constant in  $p_T$ , and a term that is linear in  $p_T$ . The best fit parameters are shown on the plot.

resolution leads to a mass resolution of just under 100 MeV for the  $Y(1S)$  state, which is sufficient to deliver the physics of separate measurements of the Upsilon states. The momentum resolution of the reference design is more than adequate for the less demanding (in terms of momentum resolution) tasks of measuring heavy flavor tagged jets and high- $z$  fragmentation functions.

The performance of the tracking system in high multiplicity events has been investigated using a full GEANT4 simulation of the tracker response for 5000 HIJING Au+Au events with impact parameters in the range 0-4 fm. This impact parameter range corresponds to about 0-10% collision centrality. For these studies only tracks that hit all seven layers of the tracker were reconstructed. To eliminate fake tracks, cuts were made on the track quality ( $\chi^2$  per degree of freedom) and on the track distance of closest approach to the event vertex (DCA). The track quality was required to satisfy quality < 3, and the track DCA was required to satisfy DCA < 1 mm.

To define the track reconstruction efficiency we start by counting all truth tracks that originated at the primary vertex and deposited energy in all seven layers. This is the denominator. The numerator is then the number of reconstructed tracks that pass track cuts of quality < 3 and DCA < 1 mm, and whose momentum lies within  $3\sigma$  of the truth momentum for the associated GEANT4 track. The resulting efficiency for 5000 HIJING events is shown in the left panel of Figure 3.24. The efficiency is found to be 88% at 500 MeV/c, 92% at 1 GeV/c and 97% at high  $p_T$ .

Another way to look at the pattern recognition performance is to start with all reconstructed tracks that have quality < 3 and DCA < 1 mm, and see what fraction of them satisfy the additional requirement that their reconstructed momentum is within  $3\sigma$  of the truth momentum for the associated GEANT4 track. The result from 5000 central Au+Au HIJING events is shown in the right panel of Figure 3.24.

Heavy flavor tagged jet measurements rely critically on the DCA resolution performance of the

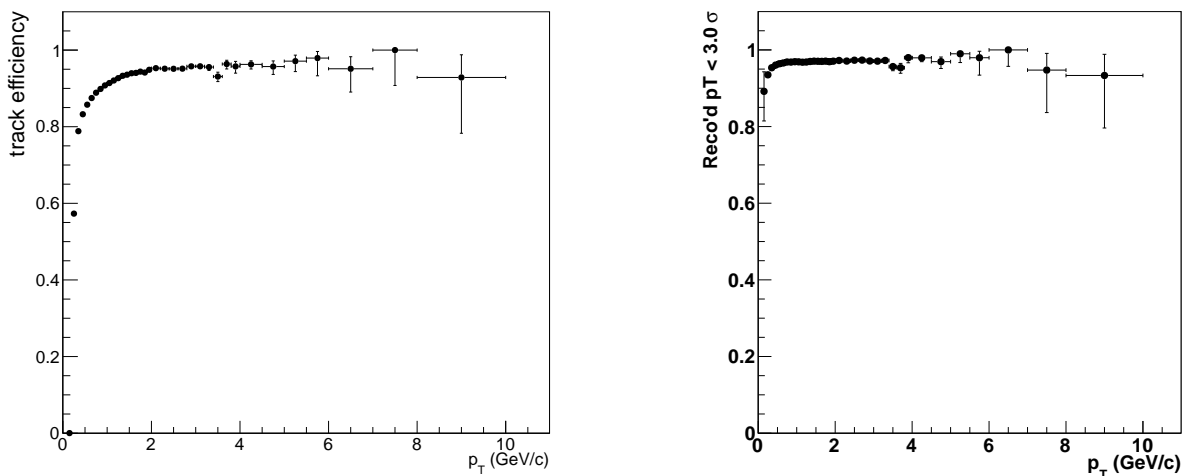


**Figure 3.24:** (left) The fraction of GEANT4 tracks from the primary vertex with hits in all seven tracking layers that are reconstructed with quality  $< 3$  and DCA  $< 1$  mm, and whose momentum lies within  $3\sigma$  of the truth momentum. Only tracks that hit all seven layers were considered. (right) The fraction of all reconstructed tracks (passing cuts of quality  $< 3$  and DCA  $< 1$  mm) that also have reconstructed momentum within  $3\sigma$  of the truth momentum for the associated GEANT4 track.

tracking system. Figure 3.25 shows the DCA distribution obtained from 5000 central Au+Au HIJING events in three  $p_T$  bins. The distributions were made using all reconstructed tracks, with the only track cut being quality  $< 3$ .

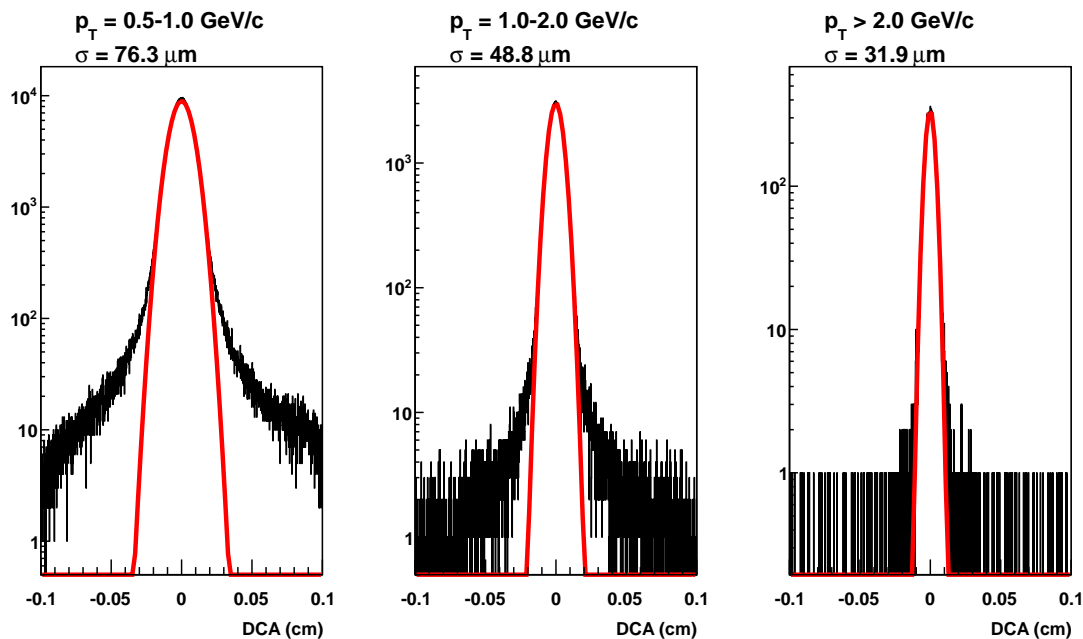


**Figure 3.25:** DCA distributions in three  $p_T$  bins from reconstruction of 5000 central HIJING events.



We have also extracted the DCA resolution as a function of  $p_T$  for single pions embedded in central HIJING events. The result is shown in Figure 3.26. The standard track cuts of quality  $< 3$  and DCA  $< 1$  mm were applied. Because the embedded pions were placed at the event vertex, this directly measures the DCA resolution in each  $p_T$  bin.

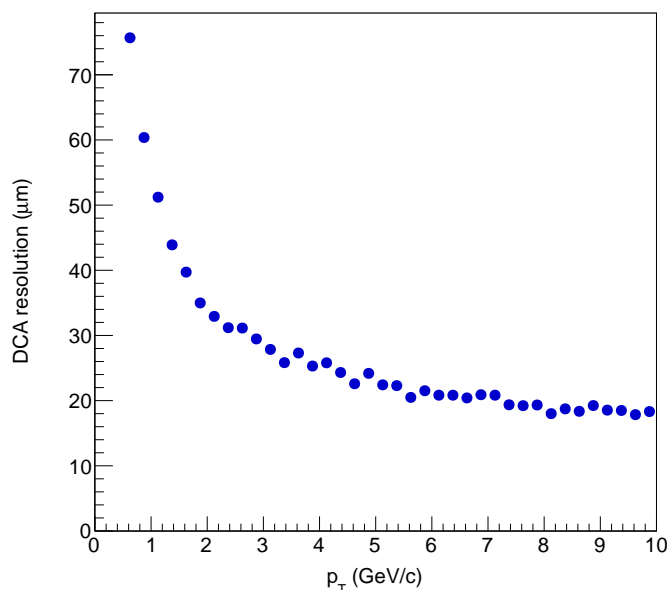


**Figure 3.26:** DCA resolution versus  $p_T$  from simulations with pions embedded in central HIJING events.

These simulation results show that the reference design is capable of delivering the momentum resolution, tracking efficiency, track purity and displaced vertex resolution needed for the sPHENIX physics program. We are considering possible modifications to the reference design that would maintain the same performance but may reduce cost or add redundancy. For example we are evaluating the possibility of using pairs of stereo strips, inclined at a small angle, for layers 3/4 and 5/6. This would maintain the same tracking and pattern recognition performance, but may preserve good track efficiency even if some channels are lost. We are also looking critically at whether the material budget can be reduced. Because the momentum resolution in the range relevant for the Upsilon measurement is dominated by multiple scattering in the tracker, reducing the tracker thickness would allow us to reduce the radius of the outer tracking layer, translating to lower cost for the same performance. There is ongoing tracking R&D, particularly driven by interest in future use in an EIC detector, that may inform our particular design choices. We are also weighing the cost and performance balance of other possible tracking options, such as a potential time-projection chamber in place of the outer silicon tracking layers in the reference design.

### 3.7 Electron Identification

For the beauty quarkonia measurements (further discussed in Section 4.11), the electron track candidates from the decayed Upsilon are identified using a combination of the electromagnetic calorimeter (EMCal) and the inner hadron calorimeter (Inner HCal). The main backgrounds to reject are the hadron tracks, which produces a continuous background under the Upsilon invariant mass peaks (as simulated in Figure 4.45). To reject this background, an EMCal energy matching with the track momentum and a leaked energy veto in the Inner HCal are used. By simulating the full calorimeter system in GEANT4, the electron identification (eID) efficiency was studied against pion rejection for  $p+p$  and central Au+Au events.

In  $p+p$  collisions, the underlying event activity is low within the shower size in the calorimeter. Therefore, the eID performance is studied using single track simulations as shown in Figure 3.27. In this study, single events containing an electron or negatively charged pion shower are simulated in the full calorimeter system using GEANT4. The cluster is built around the initial track projection for each layer of the calorimeters, which roughly corresponding to the size of  $3 \times 3$  towers in that layer.

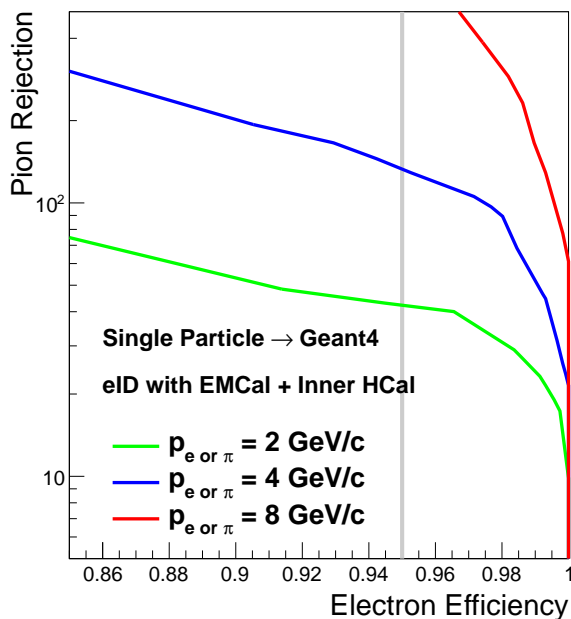


**Figure 3.27:** Electron ID efficiency versus pion rejection near central rapidity ( $|\eta| < 0.2$ ) for a GEANT4 simulation of single particles of 2 (green), 4 (blue) and 8 (Red)  $\text{GeV}/c$  in the total momentum. The vertical gray band highlights the proposed eID cut for  $p+p$  events, which corresponds to 95% single electron ID efficiency.

The electron track candidate is identified using a two-dimensional likelihood analysis based on both EMCal and Inner HCal cluster energies. The usage of the Inner HCal information improves the rejection by roughly a factor of two and the cut value is around the level of 250 MeV (about 1 MIP) at 90% eID efficiency. The average momentum for Upsilon-decayed electron is between the blue ( $p = 4 \text{ GeV}/c$ ) and red curve ( $p = 8 \text{ GeV}/c$ ), which corresponds to better than 100:1 pion

rejection for 95% electron efficiency.

In central Au+Au collisions, the underlying event fluctuation is quite significant within the electron shower clusters. Therefore, eID becomes more challenging. Nevertheless, the eID performance is quantified for the most challenging environment of the central 0–10% Au+Au collisions, by embedding the above single-track candidates into the full event HIJING and GEANT4 simulations. Comparing to the EMCal, the Inner HCal picks up significant amount of background energy due to its large cluster area size. Therefore, eID in this study is based on the EMCal cluster energy only, which is matched against the sum of the expected electron track and the average background energy.

The efficiency-rejection curves for three typical momentum are calculated again based on momentum-dependent likelihood analysis of EMCal cluster energies, as shown in Figure 3.28. For  $p = 4 \text{ GeV}/c$  tracks (blue curves), as a conservative estimation for the average momentum tracks for Upsilon-decayed electron candidates, the pion rejection is roughly 100:1 at 70% of electron efficiency as highlighted by the gray vertical line.

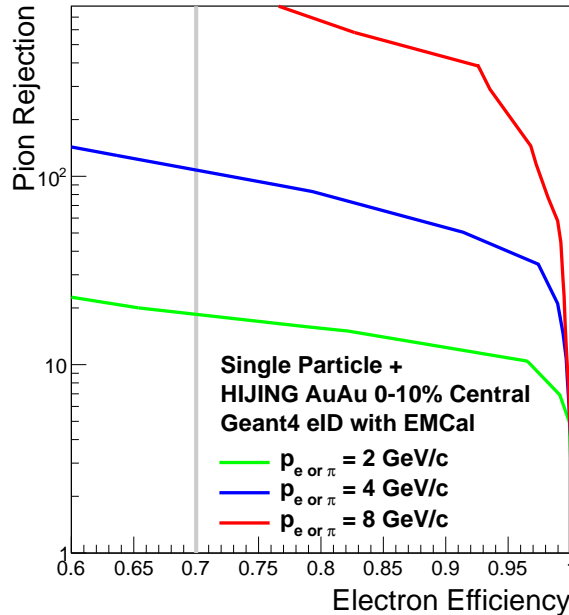


**Figure 3.28:** After embedding into 0–10% central HIJING event, the electron ID efficiency versus pion rejection in the central rapidity ( $|\eta| < 0.2$ ) for particles of 2 (green), 4 (blue) and 8 (Red)  $\text{GeV}/c$  in the total momentum. The vertical gray band highlights the proposed cut for the central Au+Au events, which corresponding to 70% single electron ID efficiency.

Our studies indicate that the electron ID performance is sufficient for the beauty quarkonia measurements described in Section 4.11. Meanwhile, the forward pseudo-rapidity electron ID is still being optimized, as the details for the calorimeter towering structure are being developed.

### 3.8 Rates and DAQ

A critical aspect of the sPHENIX detector is the ability to collect large data samples for high statistics jet and upsilon measurements. The Collider-Accelerator Division (C-AD) has updated their RHIC Collider Projections as documented in Ref. [145]. For Au+Au collisions at 200 GeV, in the years 2021-2022, store luminosities in excess of  $150 \times 10^{26} \text{ cm}^2\text{s}^{-1}$  are expected. They project that 35% of those interactions will take place within the select z-vertex range  $|z| < 10 \text{ cm}$ . These projections represent an increase in delivered luminosity more than a factor of two above the 2014 Au+Au achieved average numbers. The interaction rate as a function of time-in-store from these projections is shown in Figure 3.29.

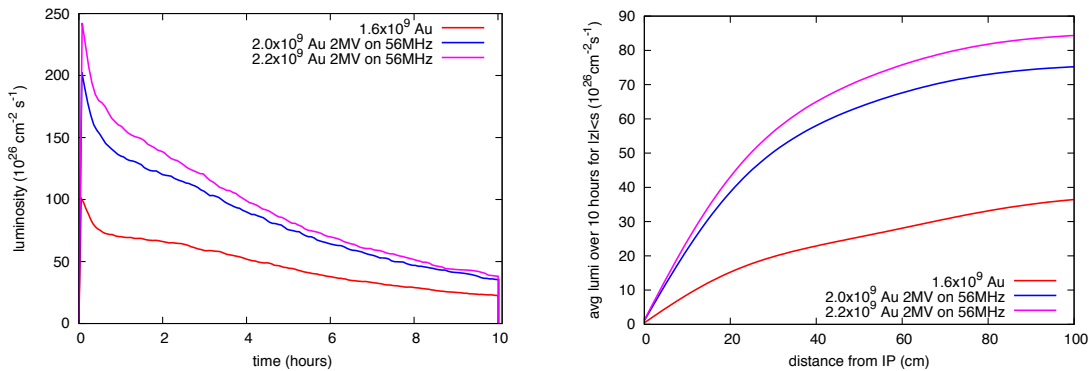


**Figure 3.29:** (Left) Projections of instantaneous luminosity versus time in store for Au+Au at 200 GeV. (Right) Projections of average luminosity, as a function of the integration range around the nominal interaction point. In both plots, the effect of the 56 MHz RF system is apparent.

The backbone of the PHENIX data acquisition system, which is the basis of the sPHENIX system, is the fully pipelined and so-called “dead-timeless” Global Level-1 Trigger system and Granule Timing architecture. The design limits the maximum Level-1 Trigger accept rate to 25 kHz. Currently the PHENIX silicon pixel layers (VTX) are planned for re-use in the inner sPHENIX tracker. Tests show that rate above 15 kHz are achievable with the current VTX electronics with data transmission to the Data Collection Module II boards with a modest growth in occupancy at higher luminosity. A Level-1 Trigger accept rate of 15 kHz for the reference design of the entire system is a good match to the delivered luminosities from the C-AD projections. This would allow the recording without any additional trigger bias of more than half of all collisions within  $|z| < 10 \text{ cm}$  at the very highest luminosities. At these highest luminosities, many of the rarest probes can be sampled with more selective Level-1 triggers, as detailed in Section 3.9.

Thus, for a 22 week physics running period of Au+Au at 200 GeV, sPHENIX with an uptime of 80%, would record 100 billion minimum bias events with  $|z| < 10 \text{ cm}$ . More selective triggers could sample slightly less than a factor of two more events again within  $|z| < 10 \text{ cm}$ . For observables not requiring the inner silicon tracking which has the more restrictive coverage, one would utilize collisions over the much larger range  $|z| < 30 \text{ cm}$ , and sample with selective Level-1 triggers 0.6 trillion events. As detailed in Section 3.9, direct photons and purely calorimetric high energy jets would be able to utilize the full 0.6 trillion events.

The luminosity in  $p+p$  collisions is limited by the beam-beam tune shift, which will be reduced by

fully operational electron lenses. This will bring the average store luminosity to  $1.7 \times 10^{32} \text{ cm}^2\text{s}^{-1}$  at 200 GeV and  $7.1 \times 10^{32} \text{ cm}^2\text{s}^{-1}$  at 510 GeV, a factor of two to three times the projected 2015 and 2016 average luminosity. C-AD projects for  $p+p$  collisions at 200 GeV delivering  $63 \text{ pb}^{-1}$  per week over all vertices. They project 35% of these collisions to be within  $|z| < 10 \text{ cm}$ . Accounting for sPHENIX uptime and projecting a 10 week physics data taking period, one can effectively sample  $500 \text{ pb}^{-1}$  over all z-vertices and  $175 \text{ pb}^{-1}$  over  $|z| < 10 \text{ cm}$ .

For the  $p+Au$  at 200 GeV case, the C-AD projection is delivering  $400 \text{ nb}^{-1}$  per week over all vertices. They project 30% of these collisions within  $|z| < 10 \text{ cm}$ . Again, accounting for sPHENIX uptime and projecting a 10 week physics data taking period, one can effectively sample  $3200 \text{ nb}^{-1}$  over all z-vertices and  $960 \text{ nb}^{-1}$  over  $|z| < 10 \text{ cm}$ . As detailed in the Physics Performance Chapter, the  $p+p$  and  $p+Au$  data sets provide very robust baseline and cold-nuclear matter statistics.

### 3.9 sPHENIX Triggering

Collider experiments typically require rather sophisticated trigger capabilities to sample the rare physics of interest from the large number of “uninteresting” collisions. In the case of sPHENIX, for many jet observables, selective triggering biases the physics of interest and results in covering only a partial phase space of jets (e.g. jets originating from partons emitted near the surface of the medium). For Au+Au collisions, the high bandwidth and deadtimeless nature of the sPHENIX data acquisition system allows us to record (with only a global Au+Au interaction or minimum bias trigger) a data sample of 100 billion events within a z-vertex  $|z| < 10 \text{ cm}$ , corresponding to the optimal acceptance of the silicon tracking system. During that same time period, a total of 0.6 trillion Au+Au interactions over a wider z-vertex range will have taken place that can be sampled with modestly selective triggering. In addition, critical trigger requirements are relevant for  $p+p$  and  $p(d)+Au$  running, and the lower occupancy environment simplifies the task at hand.

There are three systems where we plan for inputs to the sPHENIX Level-1 trigger system. The current requirement is a modest 4.0 microsecond (i.e. 40 beam clock) latency on the trigger decision. The first two systems with trigger inputs are the electromagnetic and hadronic calorimeters. Both systems utilize a common electronics that digitized the signals at full clock speed, thus removing any need for having separate trigger thresholds applied to split analog signals. The reference design has a set of full digitized energy values with a modest bit number reduction collected into one module from the entire calorimeter systems (of order 25,000 channels). Thus, one has full information in a set of FPGAs to apply a variety of trigger selections:

- Total electromagnetic energy, hadronic energy, and both
- Jet patch energy sums including with average underlying event subtraction
- Cluster energy in the electromagnetic calorimeter, or cluster pairs with geometric configurations

The third detector with input is envisioned utilizing the current PHENIX Beam-Beam Counters (BBC), described in detail in Ref. [156]. The BBC consists of 128 channels of quartz radiators with PMTs on each side in the z-direction of the collision point. The detectors would be moved

further back just outside the current design for the magnet flux return. They would thus be moved about one unit further forward in pseudorapidity from their current configuration. In Au+Au collisions, these would provide a precision  $\sigma < 1$  cm z-vertex resolution for Level-1 triggering and an independent centrality and event plane determination.

For the jet physics program with observables for single jets, high momentum photons, and high momentum hadrons, the electromagnetic calorimeter cluster trigger inputs and jet patch capabilities are sufficient for sampling the full 600 billion events for the highest energies where the increase in Au+Au statistics is particularly beneficially. This triggering also works well in  $p+p$  and  $p(d)+Au$  collisions, with the interaction rates projected.

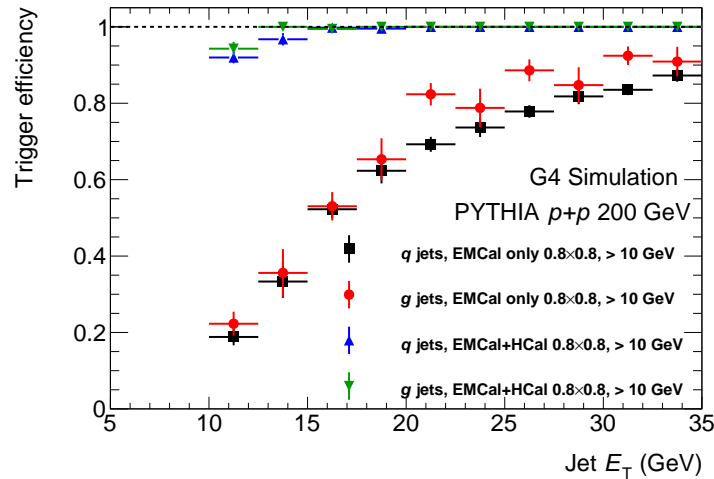


**Figure 3.30:** Trigger efficiency for jets using GEANT4 simulated calorimeter-based triggers as a function of  $R = 0.4$  truth-level jet  $E_T$ , with results for quark- and gluon-initiated jets shown separately. Results are shown for triggers requiring at least  $E_T > 10$  GeV in a  $\Delta\eta \times \Delta\phi = 0.8 \times 0.8$  calorimeter region. The efficiency using the electromagnetic calorimeter (EMCal) only is shown in black and red for quark- and gluon jets, respectively, and the efficiency using both calorimeters (EMCal+HCal) is shown in blue and green for quark- and gluon-jets, respectively.

We have benchmarked the performance of possible “jet patch” triggers in high-luminosity  $p+p$  collisions implemented by examining the sum of tower energies in the electromagnetic and hadronic calorimeters. In this study, PYTHIA jet events with a hard scattering parameter chosen to sample a wide kinematic range and minimum bias PYTHIA events are examined under a GEANT4 simulation of the calorimeter response. The calorimeters are towerized into towers of size  $\Delta\eta \times \Delta\phi = 0.1 \times 0.1$ , and the total transverse energy from both calorimeters is analyzed in sliding tower windows of various sizes. For jet events, the highest energy window within  $\Delta R < 0.4$  of the jet is considered for the purposes of determining whether the jet fired the trigger. For minimum bias events, the highest energy window anywhere in the event is considered.

Figure 3.30 illustrates the relevant results for window sizes of  $0.8 \times 0.8$ , with a minimum transverse energy requirement of 10 GeV. When both calorimeters are used for triggering, the efficiency for  $E_T > 15$  GeV jets is unity, with no dependence on the flavor of the jet. To demonstrate the importance of using both calorimeters in the trigger, results are also shown for the efficiency of an electromagnetic calorimeter-based trigger only. In that case, it can be seen that the efficiency has a

non-trivial jet  $E_T$  dependence and reaches only  $\epsilon \approx 85\text{--}90\%$  even for  $E_T = 35$  GeV jets. Furthermore, a systematic difference can be observed between quark- and gluon-initiated jets. Thus, wide-area jet patch triggers utilizing both calorimeters can most efficiently select an unbiased set of jets.

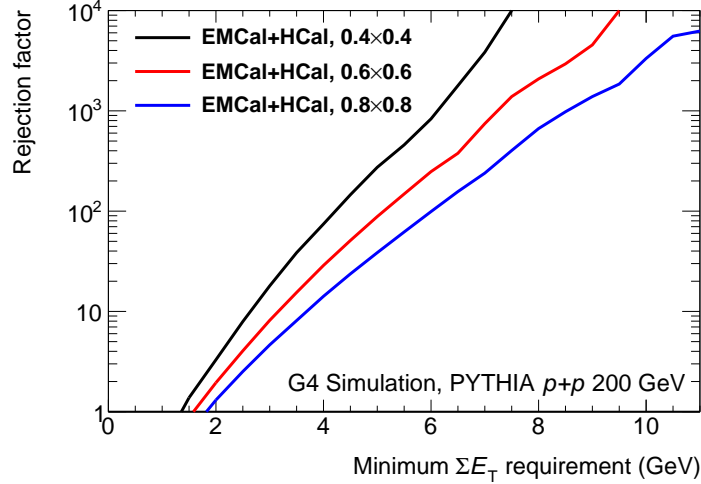


**Figure 3.31:** Rejection factor for minimum bias  $p+p$  events using GEANT4 simulated calorimeter-based triggers, as a function of the minimum  $E_T$  trigger requirement. Results are shown for requiring this amount of energy in  $\Delta\eta \times \Delta\phi = 0.4 \times 0.4$  (black line),  $0.6 \times 0.6$  (red line) and  $0.8 \times 0.8$  (blue line) calorimeter regions.

Figure 3.31 shows the rejection factor (the inverse of the fraction of events which fire the trigger) for minimum bias  $p+p$  events of various electromagnetic and hadronic calorimeter jet patch trigger schemes. The rejection factor is shown for three choices of sliding window size and as a function of the minimum required transverse energy. The figure demonstrates that a minimum energy can be chosen to give rejection factors larger than  $10^3$ , which will be necessary in high-luminosity  $p+p$  and  $p(d)+\text{Au}$  running.

Taken together, the results in Figures 3.30 and 3.31 demonstrate that jet patch style triggers in sPHENIX will be sufficient to sample an unbiased set of jets down to low  $E_T$  while still providing the large rejections needed for high-luminosity running.

The performance of possible electron triggers for selecting di-electron  $Y$  decays in high-luminosity  $p+p$  running in sPHENIX has also been investigated. These triggers are based on energy sums in the electromagnetic calorimeter, and have been examined with a GEANT4 simulation of the calorimeter response. For this study, electrons with an energy equal to half the nominal  $Y(1S)$  mass,  $E_{e\pm} = 4.7$  GeV, were generated, since this is the lowest possible energy of the highest-energy electron in the decay of an at rest ( $p_T = 0$ ) Upsilon. Thus, a successful trigger strategy for  $E_{e\pm} = 4.7$  GeV electrons is sufficient for all other  $Y$  decay topologies where both electrons are within the sPHENIX acceptance. The electromagnetic calorimeter towers of size  $\Delta\phi \times \Delta\eta = 0.025 \times 0.025$  were collected into sliding tower windows made from  $2 \times 2$  and  $3 \times 3$  blocks of these towers, and a  $4 \times 4$  block made from sliding windows over the  $2 \times 2$  tower blocks. The total energy (not transverse energy) in the electromagnetic calorimeter was considered. For each window size, the distribution of largest energy sums in minimum bias PYTHIA events were used to determine the

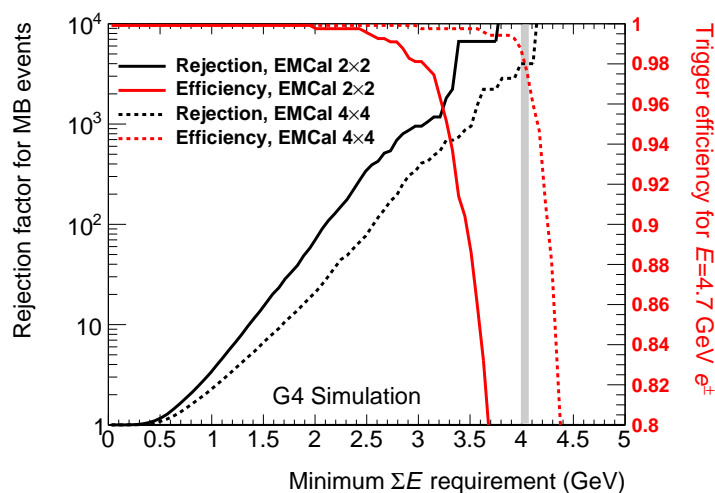


**Figure 3.32:** Rejection factor and efficiency for an electron trigger which requires some minimum amount of energy in a region of the electromagnetic calorimeter ( $\Sigma E$ ). Results are shown for a full GEANT4 simulation of the detector response. The rejection factor for minimum bias  $p+p$  events (black lines) and the efficiency for  $E_{e^\pm} = 4.7$  GeV electrons (red lines) are plotted as a function of the required energy  $\Sigma E$ . The solid and dashed lines show the results for trigger schemes in  $2 \times 2$  and  $4 \times 4$  EMCal windows.

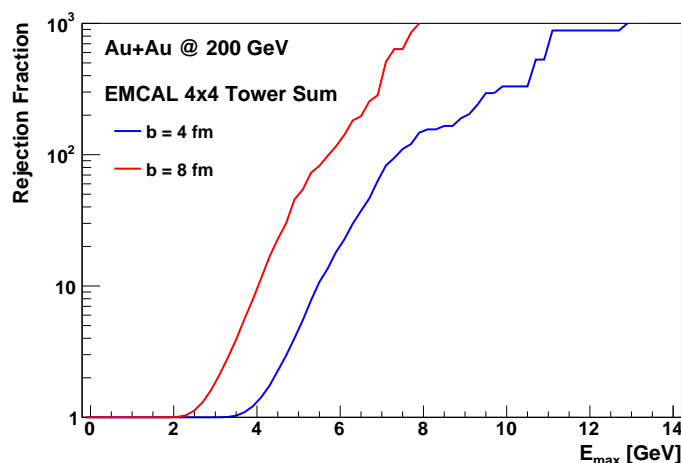
rejection factors for the trigger.

Figure 3.32 summarizes the performance of such an electron trigger by simultaneously plotting the rejection factor for minimum bias events and efficiency for  $E_{e^\pm} = 4.7$  GeV electrons as a function of the minimum energy required in the electromagnetic calorimeter tower windows. In particular, the vertical gray band in the figure at  $\Sigma E = 4$  GeV, gives an example of a choice of minimum threshold energy in  $4 \times 4$  windows for which the rejection factor is  $\approx 5 \times 10^3$  while maintaining an electron efficiency of 98%. This demonstrates the feasibility of an electron trigger for the Upsilon program in high-luminosity  $p+p$  data-taking.

The reference design for the calorimeter digitizers have digitization available on every crossing for triggering, and transmission of data to a Level 1 trigger board capable of making trigger decisions such as shown in 3.33 is being included from the beginning. The digitizer electronics is being designed with the capability of transmitting data from every channel with reduced precision, or  $2 \times 2$  sums as trigger primitives which can be used in more complex trigger algorithms running in FPGA-based trigger boards similar to trigger boards developed for the PHENIX muon trigger. The segmentation of the electronics and the detector matches well the need for  $2 \times 2$  or  $4 \times 4$  digital sums. Cost and complexity, and the need for higher speed encoding and decoding of trigger data are being considered in the overall system design.

We have extended these  $p+p$  trigger studies to minimum bias  $p+Au$  collisions where we also require selective physics based triggers. Shown in Figure 3.34 are the rejection factors as a function of EMCal trigger threshold (left) and the rejection factors as a function of the total calorimeter jet patch trigger threshold (right) for different patch sizes. The calculations are carried out with HIJING simulated minimum bias  $p+Au$  events run through the full GEANT4 response chain. The





**Figure 3.33:** HIJING and GEANT4 calculated EMCAL trigger patch  $4 \times 4$  rejections for central and mid-central events ( $b = 4$  and  $b = 8$  fm) as a function of threshold energy.

rejection factors are quite sufficient for sampling the full luminosity in  $p$ +Au for unbiased jets and Upsilon's as in the  $p$ + $p$  case.

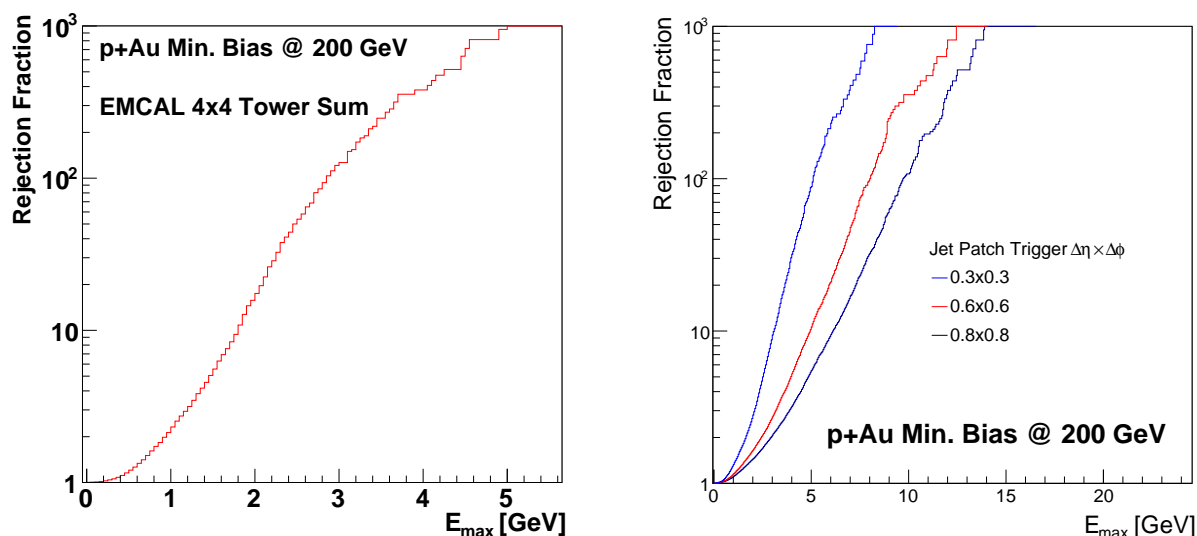


**Figure 3.34:** (Left) HIJING and GEANT4 calculated EMCAL trigger patch  $4 \times 4$  rejections for  $p$ +Au minimum bias collisions. (Right) HIJING and GEANT4 calculated full calorimeter jet patch trigger rejections for  $p$ +Au minimum bias collisions.

We have also explored possibilities for rare probe triggers in Au+Au events, where the high-multiplicity fluctuating background can significantly affect the trigger performance. Though the performance of the analogous  $p$ + $p$  and  $p(d)$ +Au triggers is worse due to the presence of the underlying event, the required rejection factors are smaller. The studies described below were

performed using a full GEANT4 simulation of the electromagnetic and hadronic calorimeter in minimum bias  $b = 4$  fm and  $b = 8$  fm HIJING events.

For triggering on photons, we consider a trigger requiring some minimum energy ( $\Sigma E_T$ ) in a  $4 \times 4$  patch of EMCal towers. Figure 3.33 shows the rejection factor for HIJING events of both  $b$  values as a function of the minimum energy required. It can be seen that for relatively modest requirement of  $\Sigma E_T > 8$  GeV, the rejection factor for minimum bias HIJING events is  $> 1000$ , which is generously higher than the rejection of a few hundred needed to sample the full rare probe rate in the highest luminosity Au+Au data-taking. Thus, in such a scenario, an unbiased sample of high- $p_T$  photon events can be recorded.

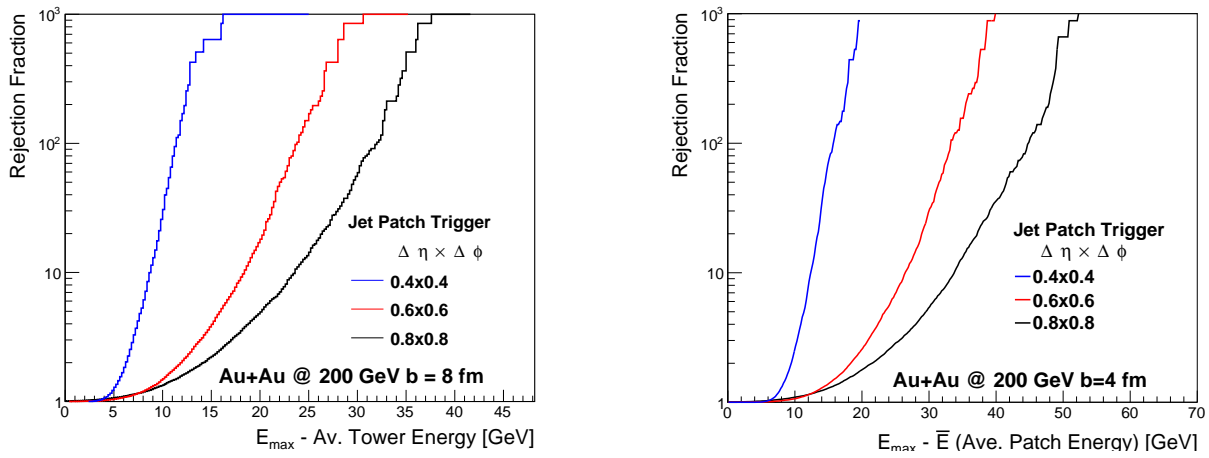


**Figure 3.35:** Full HIJING and GEANT4 calculated calorimeter (EMCal and HCal) trigger patch rejections for central and mid-central events ( $b=4$  and  $b=8$  fm) as a function of threshold energy. The patch sizes considered are  $\Delta\eta \times \Delta\phi = 0.4 \times 0.4$ ,  $0.6 \times 0.6$ , and  $0.8 \times 0.8$ .

For triggering on jets, we consider instead the large area “jet patch” triggers composed of sliding windows of EMCal and HCal towers used above in studies of trigger in  $p+p$  collisions. However, in Au+Au events an underlying event subtraction is necessary at the trigger level so that the jet patch trigger does not fire primarily on the large  $\Sigma E_T$  of the underlying event pedestal. This underlying event subtraction consists of subtracting the mean energy density measured over the entire calorimeter, and is kept simple to approximate what could be performed computationally in a fast online trigger. Figure 3.35 shows the rejection factors for jet patch triggers of various window sizes and for  $b = 4$  fm and  $b = 8$  fm HIJING events, as a function of the minimum window  $\Sigma E_T$ . It can be seen that even in the central HIJING events, it will be possible to trigger on high- $p_T$  in a way that still maintains a rejection factor of 100–200 (for example, requiring  $\Sigma E_T > 30$  GeV in  $0.6 \times 0.6$  windows). Thus, while the jet spectrum below this cutoff would be measured using the minimum bias Au+Au event sample, the full luminosity can be sampled to measure the high- $p_T$  end of the jet spectrum to its statistical limit. Taken together, these figures demonstrate a triggering strategy for rare probes in Au+Au collisions.

### 3.10 Mechanical Design and Infrastructure Concept

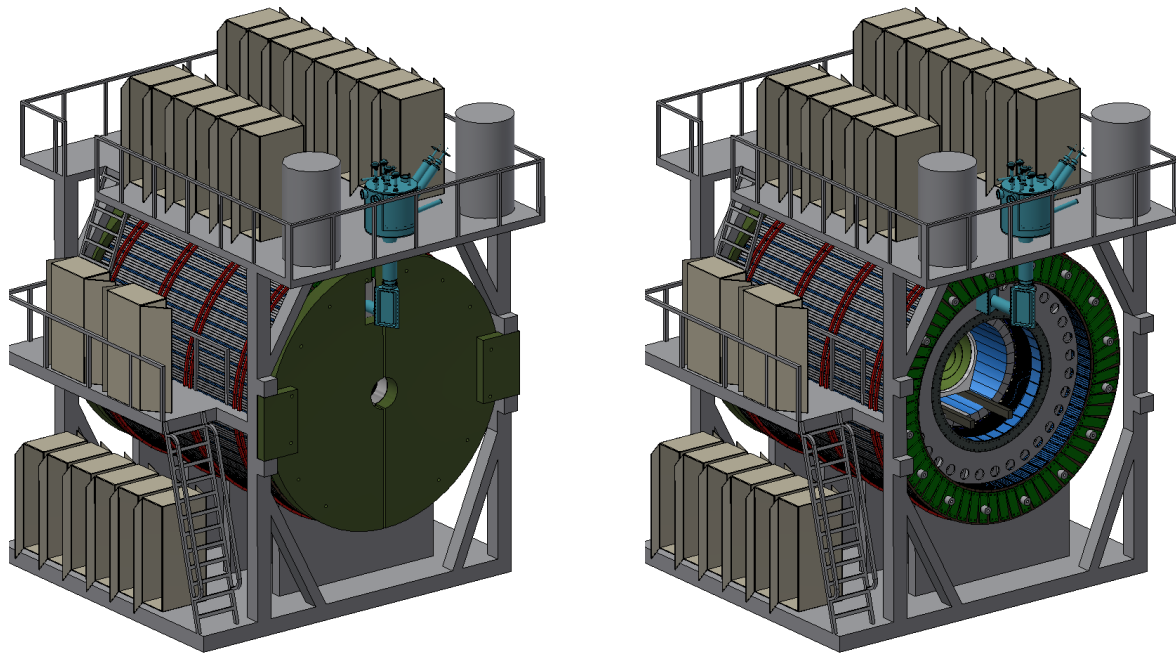


**Figure 3.36:** Illustration of sPHENIX underlying structural support, support equipment, overall assembly and maintenance concepts with and without endcaps.

sPHENIX has been designed to be straightforward to construct and assemble, but it still requires significant infrastructure to support and service it. The overall concept for how sPHENIX will sit in the existing PHENIX IR is shown in Figure 3.36. A set of envelope dimensions for each of the major components of sPHENIX has been established and is discussed below.

#### 3.10.1 Beampipe

The existing PHENIX beampipe will be used with minimal modification. The current beampipe has a 40 mm outside diameter in the central area, and connected on either end with transition pipe sections from 40 mm to 75 mm OD and 75 mm OD to 125 mm OD. A new support structure to support the beampipe inside the superconducting solenoid will need to be designed.

#### 3.10.2 Silicon Tracker

The support structure for the silicon tracker, utilities supply and readout design will be designed to allow the tracker to be inserted into the superconducting solenoid cryostat. Existing VTX and additional silicon layers will be integrated into a new structural support design and mechanisms which will mount onto rails allowing insertion and removal of the detector from within the EMCal central bore. The on-detector electronics and services inside the cryostat will generally not be serviceable during runs.

### 3.10.3 Superconducting solenoid magnet

The BaBar magnet has a 1.5 Tesla solenoid field, 140 cm inner cryostat radius, 173 cm outer cryostat radius, 385 cm cryostat length. The cryostat is not designed to be disassembled. The cryostat will be supported by the hadronic calorimeter which also acts as the flux return. The services stack will be modified to exit outside the acceptance beyond the south end of the HCal detector to carry cryogenic supply lines, power leads and monitoring cables. The existing rigging fixtures from SLAC will be adapted for transport, lifting and installation whenever possible. The Superconducting Magnet Division and Collider-Accelerator Department have the technical expertise to integrate the solenoid into existing RHIC infrastructure.

### 3.10.4 Electromagnetic calorimeter

The EMCAL will have a 13 cm radial thickness with electronics and services on the inner radius and full  $2\pi$  azimuthal coverage. The EMCAL will be supported by the Inner HCal, with provision for maintenance, assembly, disassembly and integration of component sectors. More detailed mechanical and structural design is ongoing, and assembly procedures are being developed.

### 3.10.5 Hadronic calorimeter

The HCal will have full  $2\pi$  azimuthal coverage, and the calorimeter is divided into an inner radial section inside the solenoid and an outer radial section just outside the solenoid. The inner radial section, which occupied 23 cm in radial thickness in the simulation, will be designed to maximize the absorber inside the magnet while allowing sufficient space for readout electronics and services. The inner HCal was simulated with copper absorber, but non-magnetic stainless steel or brass have almost the same interaction length and may be preferable mechanically. The outer HCal was 67 cm thick in the simulation, making the total HCal about 5.5 nuclear interaction lengths thick. The Outer HCal will support the cryostat and the Inner HCal and EMCAL assembly. The HCal will also incorporate provision for support of itself in the fully assembled configuration, any maintenance configuration and for assembly/disassembly and integration of component segments. The HCal will be constructed of 384 segments of 7 mm thick scintillator sections with embedded optical fibers which collect the light. The scintillator sections will be sandwiched between tapered steel plates tilted from the radial direction, with the inner steel plates tilted in the opposite direction from the outer steel and offset by a half a segment thickness.

### 3.10.6 Structural support apparatus

Structural support for the sPHENIX major components will provide structural support for all of the equipment with the following criteria:

- Appropriate structural support will be provided to all components, with integral connections and support interfaces and/or clearances for support structure designed into the comprising detector subassemblies and the superconducting solenoid.

- Components will be able to be completely assembled in the PHENIX Assembly Hall (AH) utilizing existing cranes (40 ton load limit). The assembly will be mounted on the existing PHENIX rail system or a modification of the existing rail system.
- Functional tests including pressure, and magnetic tests will be able to be performed in the AH.
- The sPHENIX detector will be capable of disassembly to allow maintenance of electronics, support services and replaceable components. This capability will be available with the full assembly in the AH or the Interaction Region (IR), with full maintenance capabilities during shutdowns between runs and with as much maintenance capabilities during a run as possible.
- The sPHENIX assembly will be relocatable from the AH to the IR using the existing rail system or a modification to the existing rail system. This relocation may be accomplished fully assembled or disassembled into subdivisions which are reassembled in the IR. Disassembly and re-assembly will use existing AH and IR cranes.
- Support equipment for the above components and the utilities supplied to the above structure including provision for electronics racks, cooling services, cryogenics, power and signal cables, and monitoring and control equipment will be provided.
- The assembled sPHENIX will allow partial disassembly during maintenance periods to provide access to all serviceable components, electronics and services. The assembled sPHENIX will provide for electronics racks and all other support components for operation and monitoring of the sPHENIX active components. Safe and efficient access to all service/monitoring components will be integrated into the design of the underlying structural support.
- Infrastructure used successfully for the past fourteen years of PHENIX operation will be adapted and expanded to support sPHENIX. This includes the chilled water system for electronic cooling, air conditioning, and safety systems.

Figure 3.37 shows a view of the HCal and EMCal inside the solenoid cryostat with power and cryogenic services provided through a modified chimney.

### 3.11 Detector Development and Testing

Prototype electromagnetic and hadronic calorimeters have been developed for beam tests to validate the design concepts and gain experience with the readout and calibration of silicon photomultipliers in an operating detector. The first prototypes were tested at the Fermilab Test Beam Facility as T-1044 February 5–25, 2014. The EMCal prototype was a  $7 \times 7$  device with 1 mm tungsten absorber which can be rotated in the beam to study shower development and energy resolution. A beam test of the SPACAL electromagnetic calorimeter was carried out by the UCLA group and collaborators immediately following T-1044. The HCal prototype consists of inner and outer  $4 \times 4$  sections with machined tapered plates using a mechanical design that is being evaluated for use in building the full detector. Both detectors are read out with Hamamatsu silicon photomultipliers with signal conditioning that allows them to be flash digitized at 60 MHz with existing PHENIX electronics.

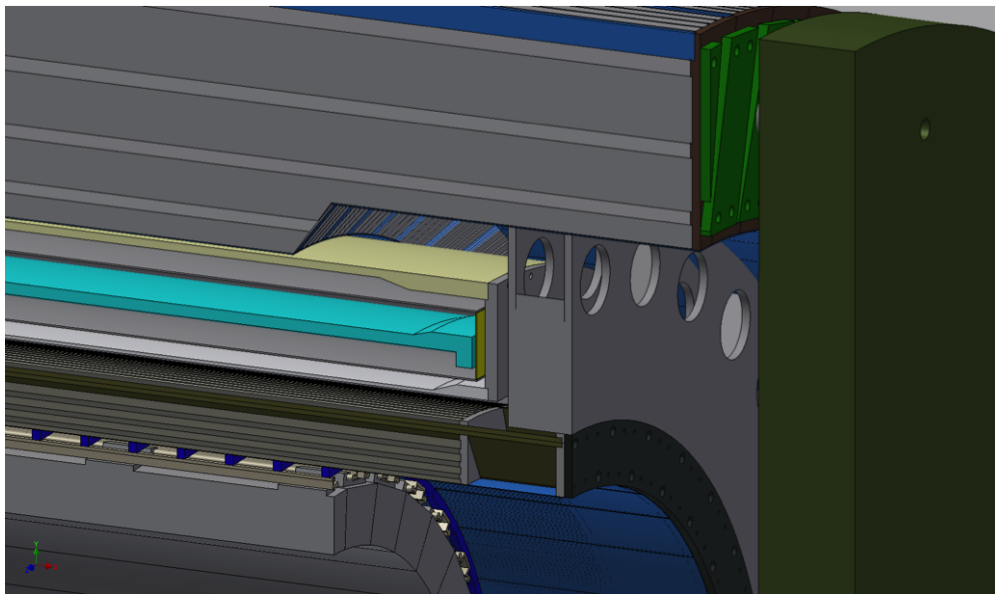


**Figure 3.37:** Closeup view of EMCAL and HCal with the solenoid cryostat and services.





**Figure 3.38:** Top: HCal prototype under construction. The first layers of absorber are being stacked on the lift table for the beam test. Bottom: Calorimeters in MWEST beamline of the Fermilab Test Beam Facility.





## Chapter 4

# Physics Performance

In this Chapter we detail the expected sPHENIX physics performance. The sPHENIX jet, dijet,  $\gamma$ -jet, fragmentation function, and beauty quarkonia performance demonstrates the ability to measure key observables that can test and discriminate different quenching mechanisms, coupling strengths to the medium, and with sensitivity to different length scales in the QGP.

The key aspects of jet performance are the ability to find jets with high efficiency and purity, and to measure the kinematic properties of jet observables with good resolution. It is also necessary to discriminate between jets from parton fragmentation and fake jets caused by fluctuations in the soft underlying event. For the sPHENIX physics program, there are four crucial observables that we have simulated in detail to demonstrate the jet performance: single inclusive jet yields, dijet correlations,  $\gamma$ +jet correlations, and modified fragmentation functions. We also find that the combination of full calorimetric reconstructed jets combined with track and electromagnetic cluster jets allows one to engineer the surface emission of the leading jet and thus the path of the partner jet. Other significant observables such as the participant plane dependence (e.g.,  $v_2$ ,  $v_3$ , etc.) of jets and jet-hadron correlations are also enabled by this upgrade.

For beauty quarkonia decaying to  $e^+e^-$ , the key aspects of performance are electron identification (particularly in being able to discriminate against charged pions), and good momentum resolution to provide sufficient invariant mass resolution to distinguish clearly the  $Y(1s)$ ,  $Y(2s)$ , and  $Y(3s)$  states.

An important focus will be to demonstrate the capabilities of sPHENIX for central Au+Au collisions at  $\sqrt{s_{NN}} = 200$  GeV, where the complications of the underlying event are the most severe. We first detail the physics performance for jet observables and then the performance for the beauty quarkonia physics.

### 4.1 Jet simulations

It is not practical to simulate with GEANT4 [155] a sample of events equivalent to a full year of RHIC running. We therefore perform three different levels of simulations described in detail below.

The most sophisticated and computationally intensive are full GEANT4 simulations with

PYTHIA [157] or HIJING [158] events where all particles are traced through the magnetic field, energy deposits in the calorimeters recorded, clustering applied, and jets are reconstructed via the FASTJET package [159]. We utilize this method to determine the jet resolution in  $p+p$  and Au+Au collisions from the combined electromagnetic and hadronic calorimeter information. We have also performed a full GEANT4 study of the reconstruction of PYTHIA jets embedded in central Au+Au HIJING events to gauge the effect of the underlying event on jet observables.

For studies of fake jets in Au+Au central collisions, one needs to simulate hundreds of millions of events and for this we utilize a fast simulation where the particles from the event generator are parsed by their particle type, smeared by the appropriate detector resolution parametrization from GEANT4 simulations, and segmented into detector cells. As described in detail below, a full underlying event subtraction procedure is applied, and then jets are reconstructed using FASTJET. This method is also utilized for embedding events from PYTHIA or PYQUEN [160] (a jet quenching parton shower model) into Au+Au HIJING events to study dijet and  $\gamma$ +jet observables.

Finally, in order to gain a more intuitive understanding of the various effects, we run a very fast simulation where PYTHIA particles are run directly through FASTJET and then the reconstructed jet energies smeared by the parametrized resolutions and underlying event fluctuations.

This section is organized as follows. First we describe the jet reconstruction and evaluate its performance in  $p+p$  collisions for both an idealized detector as well as a fully simulated version. Then we describe our study of fake jet contamination, which has been published in Physical Review C [161]. We show the expected performance for sPHENIX measurements of inclusive single jet, dijet and  $\gamma$ +jet correlations, and modified fragmentation functions.

## 4.2 Jet finding algorithms

For all of the studies presented here we use the anti- $k_T$  jet algorithm [162] implemented as part of the FASTJET package [159]. The anti- $k_T$  algorithm is well suited to heavy ion collisions and produces cone-like jets in an infrared and collinear safe procedure. The parameter that controls the size of the jet in this algorithm is the jet radius,  $R$ . While this is not strictly a cone size it does specify the typical extent of the jet in  $\eta$ - $\phi$  space. High energy experiments typically use large  $R$  values of 0.4–0.7 in order to come as close as possible to capturing the initial parton energy. In heavy ion collisions, the desire to measure the quenching effects on the jet profile and to minimize the effects of background fluctuations on jets has led to the use of a range of  $R$  values. Values from 0.2 to 0.5 have been used to date in Pb+Pb collisions at 2.76 TeV at the LHC [77, 81]. We note that looking at the jet properties as a function of the radius parameter is very interesting and potentially sensitive to modifications to the jet energy distribution in the medium.

The excellent charged particle tracking capabilities of sPHENIX documented in Section 3.6, there are a number of alternative jet reconstruction inputs that are available. These range from jet reconstruction with tracks only, as utilized recently by the STAR and ALICE experiments. These inputs have the benefit of a well defined energy scale, though with significant fluctuations due to non-charged track energy and track inefficiencies in central Au+Au or Pb+Pb events. There are results from the same experiments with charged tracks combined with electromagnetic energy. There are also hybrid, particle flow type inputs as utilized to great benefit by the CMS experiment [163, 164, 165]. We have implemented all of these algorithms and have initial performance

metrics with full GEANT4 simulations in  $p+p$  PYTHIA reactions.

The particle flow algorithm in CMS results in a substantial improvement in the jet energy resolution, particularly at lower jet energies, with contributions from multiple effects. In  $p+p$  collisions, the benefits include (i) charged tracks can be input to FASTJET with the momentum vector at the collision vertex rather than with calorimeter clusters where the vector is modified as bent in the magnetic field, (ii) the charged tracking resolution is significantly better than the calorimeter resolution for particles up to hundreds of GeV, (iii) charged tracks can be more easily associated with specific collision points in the case of multiple interactions per bunch crossing. The first two items are very significant for CMS since the magnetic field strength at 4 Tesla really pulls the different charged constituents of the jet apart for easier unique association with calorimeter clusters.

We have implemented a first pass particle flow algorithm where charged tracks are associated with energy clusters in the full calorimeter system. If there is a match within the 90% confidence level for the track energy (assuming it is a pion) and the calorimeter energy (as determined with GEANT4 single particle simulations), the cluster is replaced by the track as an input to FASTJET. If the track energy is above this confidence interval, we do not include the track as there is some probability for this to be a poor reconstruction or fake track. If the track energy is below this confidence interval, there is a probability that the cluster has energy from additional sources (neutrals or poor cluster splitting). In this case, the track energy is subtracted from the cluster energy and both are input to FASTJET. Note that for this last scenario, the better tracking resolution does not improve the jet resolution, since one also leaves any residual from the poorer calorimeter resolution in the modified cluster. Figure 4.1 shows four example PYTHIA dijet events reconstructed through the sPHENIX GEANT4 simulation. The circles represent reconstructed calorimeter clusters (white) and reconstructed charged tracks (pink) with the area being proportional to the energy.

In order to gauge the benefit to the jet resolution of the particle flow algorithm, we consider the three effects listed above. Since the luminosities at RHIC result in much lower numbers of collisions per crossing in  $p+p$  and negligible in Au+Au, the third effect of pileup is not a significant consideration. To assess the possible benefit of correcting the energy to the correct vector at the vertex, we first compare the fully calorimetric results with the GEANT4 magnetic field turned off. Shown in the left panel of Figure 4.2 are the GEANT4 jet resolutions from PYTHIA  $p+p$  events with the anti- $k_T$  algorithm and  $R = 0.4$  when using calorimeter towers or calorimeter reconstructed clusters as inputs, with and without the magnetic field turned on. The results all give equivalent jet resolutions, which means that for  $R = 0.4$  jets the moving calorimeter energies to the center of clusters and the bending of soft charged particles in the magnetic field has minimal effect. We do note that for  $R = 0.2$  jets, we observe a modest improvement in the jet resolution with the magnetic field off as expected. The right panel of Figure 4.2 compares the resolution with calorimeter clusters to the first pass particle flow algorithm. There is only a very modest difference in the results. This is not so unexpected as detailed checks indicate that within jets, many of the calorimeter clusters have multiple-particle energy contributions. We are exploring more sophisticated matching criteria that we expect to yield some additional improvement in resolution.

Even with marginal jet resolution improvement, the particle flow algorithm allows one to make more detailed selections on track constituents and individual calorimeter clusters. The same applies for the tracking only or tracking + EMCal jet inputs. The full suite of these algorithms will be further developed as the design of the overall system is optimized. These different algorithms have

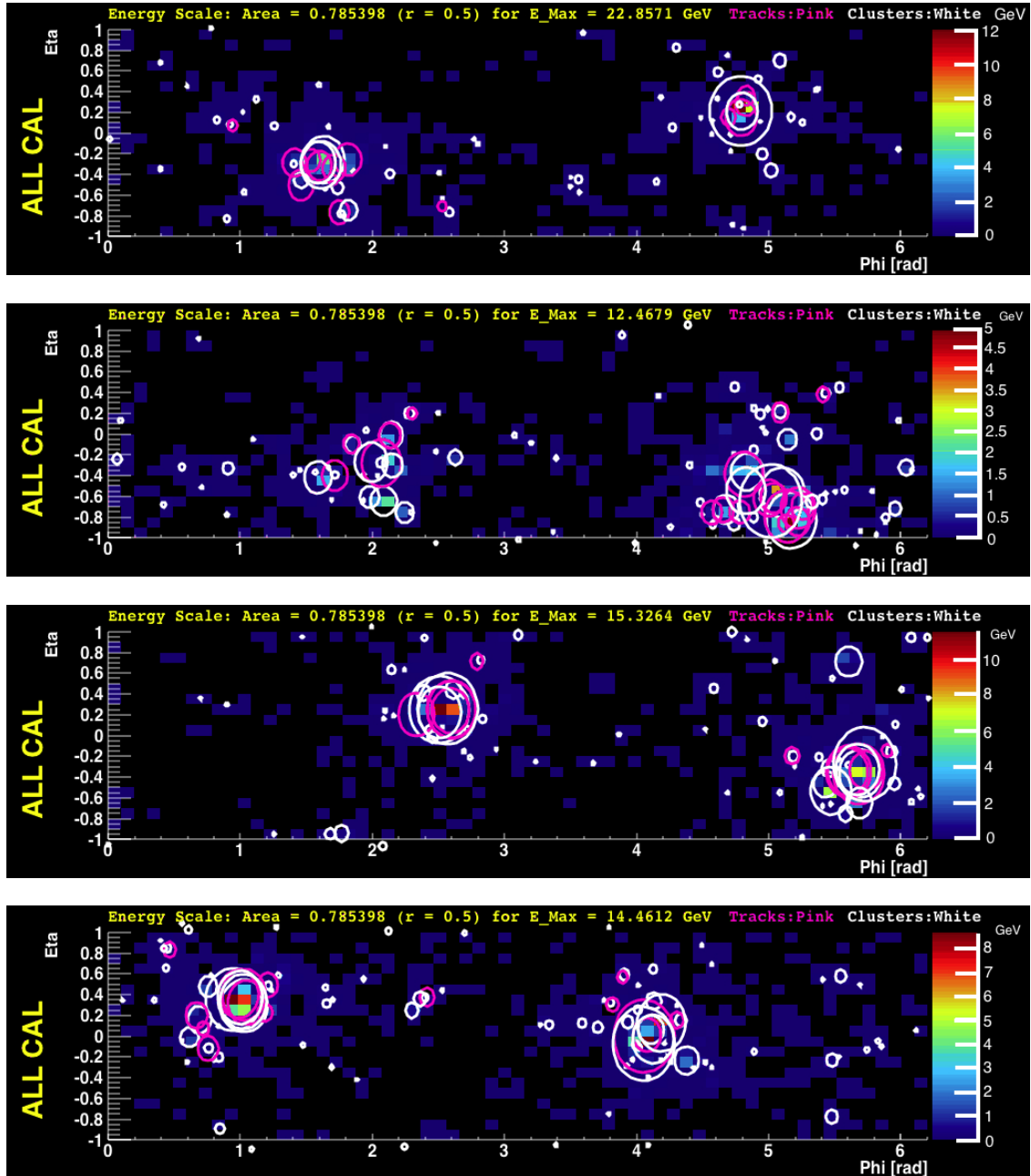


**Figure 4.1:** GEANT4 event display of PYTHIA dijet events. Circles indicate clusters found in the calorimeter (white) and reconstructed charged tracks (pink). The area of all circles is proportional to the energy of the track or calorimeter cluster. Thus, one can visually see closely matched tracks and clusters in position and energy.

multiple benefits including very different systematics, including on the energy scale, and will allow detailed comparisons with other experiments and their results.

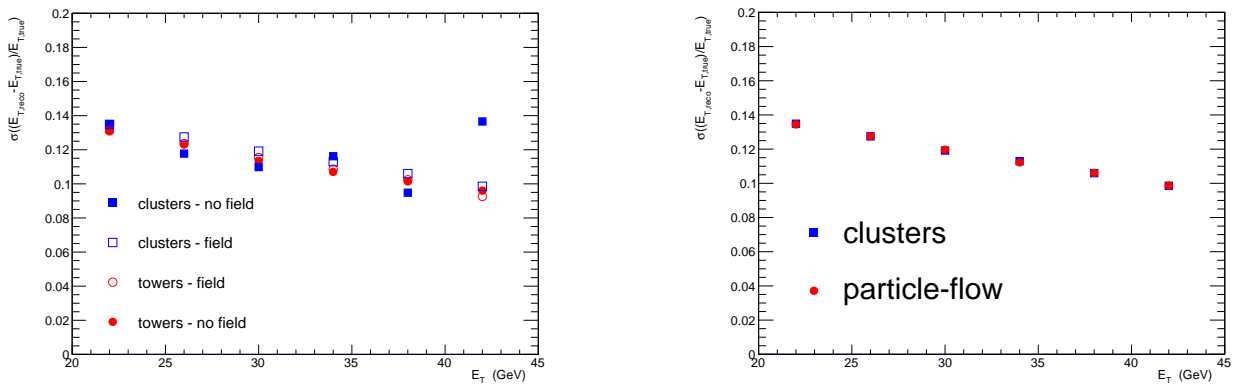


**Figure 4.2:** (left) GEANT4 simulations with PYTHIA dijet events and the resulting jet energy resolution for anti- $k_T$  and  $R = 0.4$  with input calorimeter towers and clusters, with and without the magnetic field turned on. (right) Comparison of the jet energy resolution with pure calorimetric cluster input and the first pass particle flow jet algorithm.

### 4.3 Jet performance in $p+p$ collisions

We begin by exploring the performance of the detector in  $p+p$  collisions. This allows us to investigate the effects of detector resolution and how well the process of unfolding these effects in simpler collisions works before considering the additional effects of the underlying event and jet quenching in heavy-ion collisions.

The most realistic understanding of the sPHENIX jet reconstruction performance comes from a full GEANT4 simulation of the detector response. In this case, PYTHIA particles are run through a GEANT4 description of sPHENIX, the resulting energy deposition is corrected for by the sampling fraction of the relevant calorimeter, binned in cells of  $\eta$ - $\phi$  ( $0.024 \times 0.024$  for the EMCal and  $0.1 \times 0.1$  for the HCal) and the resulting cells are used as input to FASTJET. Particles from PYTHIA events are put through FASTJET to determine the truth jets.

We then calculate the difference between the energy of the reconstructed calorimeter jets,  $E_{\text{reco}}$ , and the particle-level truth jets,  $E_{\text{true}}$ . The width of this distribution,  $\sigma(E)$ , is fit with a functional form:  $\sigma(E)/E = a/\sqrt{E} + b$ .

Full GEANT4 calculations of the energy resolutions for jets in  $p+p$  collisions reconstructed with anti- $k_T$  and  $R = 0.2$  and  $R = 0.4$  are shown in Figure 4.3. The resolutions are relatively independent of  $R$  and in simulation are substantially better than the required specification detailed in Chapter 2.

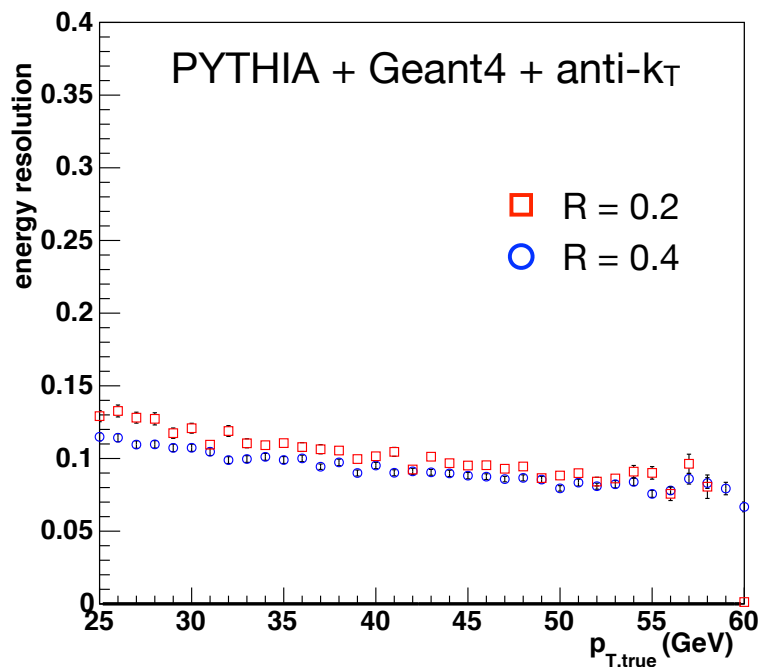


**Figure 4.3:** The GEANT4 calculated energy resolution of single jets in  $p+p$  collisions reconstructed with the FASTJET anti- $k_T$  algorithm with  $R = 0.2$  and  $R = 0.4$ .

The jet energy resolution in collider experiments is often found to be a factor of 1.2–1.3 worse than the quoted single particle resolution of the hadronic calorimeter. This factor is a balance of many effects including the better resolution for the electromagnetic part of the shower, soft particles that deflect out of the jet cone in the magnetic field, some lost energy, etc. The CMS quoted jet resolution

in  $p+p$  collisions at 7.0 TeV is approximately  $120\%/\sqrt{E}$  which is roughly 1.2 times worse than the quoted single particle hadronic calorimeter resolution [166]. The sPHENIX jet energy resolution and hadronic calorimeter resolution from GEANT4 are consistent with this expectation, and both are within our performance specifications.

We also calculate the jet energy scale and resolution where we have tagged from the truth information quark and gluon jets. These results are shown in Figure 4.4 (left) and indicate no significant differences in jet energy scale and resolution despite the significantly different fragmentation function (right).

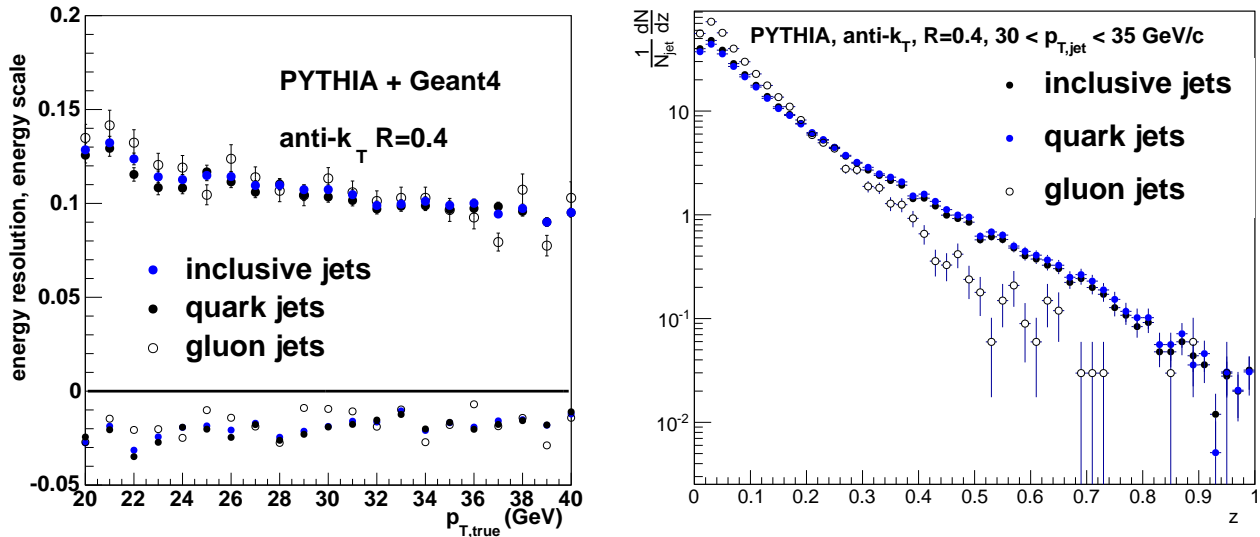


**Figure 4.4:** (left) The GEANT4 calculated energy resolution of single jets in  $p+p$  collisions separated into quark and gluon jets. (right) The PYTHIA calculated fragmentation function of quark and gluon jets separately.

### 4.3.1 $p+p$ Inclusive Jet Spectra

In order to model the jet resolution effects described above on the inclusive jet spectra in  $p+p$  collisions at  $\sqrt{s_{NN}} = 200$  GeV, we have used the very fast simulation. This method entails running PYTHIA, sending the resulting final state particles through FASTJET to find jets, and then blurring the energy of the reconstructed jets with values obtained from the full GEANT4 simulation.

The truth spectrum of jets is obtained by using FASTJET to cluster the PYTHIA [157] event with the anti- $k_T$  algorithm. Figure 4.5 shows the true jet  $p_T$  spectrum as the solid histogram. The convolution of the hard parton-parton scattering cross section and the high- $x$  parton distribution function results in a jet cross section that falls nearly exponentially over the range 20–60 GeV, before turning steeply downward as it approaches the kinematic limit,  $x = 1$ .

Figure 4.5 also shows the very fast simulation result for the measured jet  $E_T$  spectrum. The main effects of the jet resolution on the jet energy spectrum are to shift it to higher energy and stiffen the slope slightly. Both of these effects can be undone reliably by a process of unfolding. We have employed the ROOUNFOLD [167] package and for this demonstration utilize the Iterative Bayes method with 4 iterations. The results of the unfolding are shown in Figure 4.5, along with the ratio

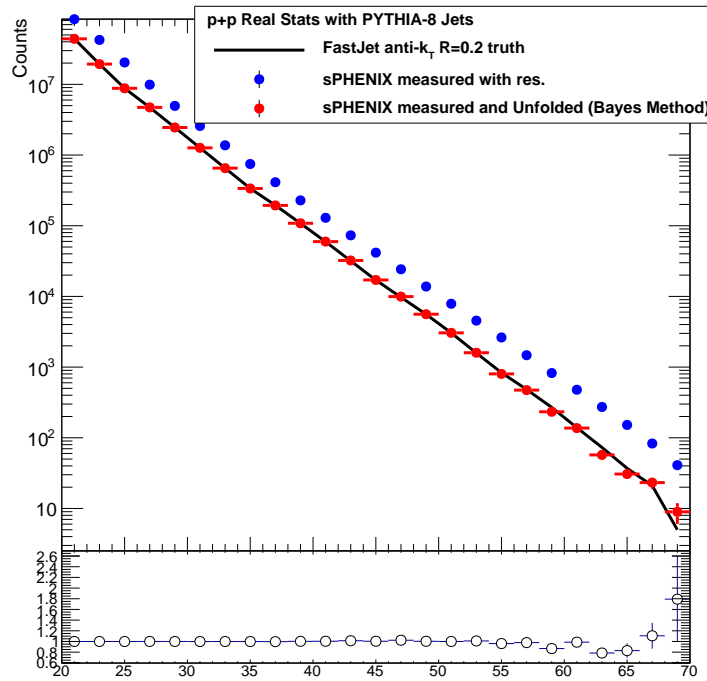


**Figure 4.5:** Unfolding the effect of finite detector resolution on jet reconstruction in  $p+p$  events. The black histogram is the truth spectrum of jets from PYTHIA, the blue dotted histogram is the spectrum after smearing by the jet energy resolution and the red histogram shows the result of using ROOUNFOLD Iterative Bayes method to unfold the detector effects. The lower panel shows the ratio of the unfolded to the true  $E_T$  spectrum.

of the unfolded to the true  $E_T$  spectrum, in the lower panel. The ratio of the two distributions demonstrates that the measurement provides an accurate reproduction of the true jet energy spectrum.

### 4.3.2 $p+p$ Dijet Asymmetry

The very fast simulation is also used to establish expectations for dijet correlations. Figure 4.6 shows the dijet correlation for PYTHIA events reconstructed using the anti- $k_T$  algorithm with  $R = 0.2$ . The highest energy jet in the event is taken as the trigger jet and its transverse energy is compared to the transverse energy of the highest energy jet in the opposite hemisphere.

The jet asymmetry  $A_J = (E_{T1} - E_{T2}) / (E_{T1} + E_{T2})$  for the true jets, reconstructed at the particle level, is shown for leading jets with  $E_{T1} > 30$  GeV in Figure 4.6. Also shown is the simulated measurement with the jet resolution included. The resolution results in a reduction in the fraction of events observed with balanced jet energies (i.e. near  $A_J \approx 0$ ). ATLAS and CMS dijet asymmetries in Pb+Pb collisions [77, 78] are shown without unfolding for these detector or underlying event effects. A simultaneous two-dimensional unfolding of both the jet energies (i.e.,  $E_{T1}(\text{meas}), E_{T2}(\text{meas}) \rightarrow E_{T1}(\text{true}), E_{T2}(\text{true})$ ) is required in this case. Both ATLAS and CMS collaborations are actively working on this two-dimensional unfold, and the sPHENIX group is as well. At RHIC energies, the largest effect is that the trigger jet is being selected from a steeply falling spectrum and is



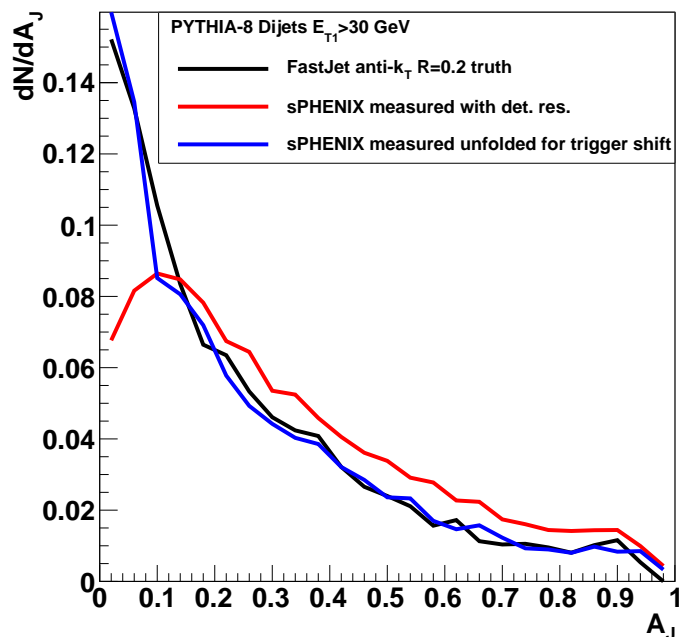


**Figure 4.6:** Dijet asymmetry,  $A_J$ , in  $p+p$  collisions. The truth spectrum is shown in black; the spectrum measured in PYTHIA and smeared by the jet energy resolution is shown in red. The effect of the unfolding of the trigger jet bias is also shown in blue.

biased by the resolution to be reconstructed higher than the true energy. If one simply shifts the trigger jet down by this average bias (and inverts the identity of trigger and associated jet if the trigger jet energy is then below that of the associated jet), the original dijet asymmetry distribution is recovered, as shown in Figure 4.6. This procedure is not a replacement for the eventual two-dimensional unfolding, but demonstrates the dominant effect.

#### 4.4 Jet performance in Au+Au collisions

Here we simulate the performance of inclusive jet and dijet observables in heavy ion collisions. The sPHENIX trigger and data acquisition will sample jets from the full Au+Au minimum bias centrality range, resulting in key measurements of the full centrality dependence of jet quenching effects. Finding jets and dealing with the rate of fake jets becomes much easier as the multiplicity due to the underlying event drops, and so we have concentrated on showing that we have excellent performance in central Au+Au collisions (i.e., in the most challenging case).

The effective jet resolution also has an important contribution from fluctuations in the underlying event in the same angular space as the reconstructed jet. We have carried out a full GEANT4 simulation embedding PYTHIA jets into 0–10% central Au+Au HIJING events. The true PYTHIA reconstructed jets are then compared with the Au+Au extracted jets (as detailed below) to determine the jet energy resolution, as shown in Figure 4.7. Also shown in the figure as dotted lines are the parametrized electromagnetic and hadronic calorimeter resolution contributions used in the fast

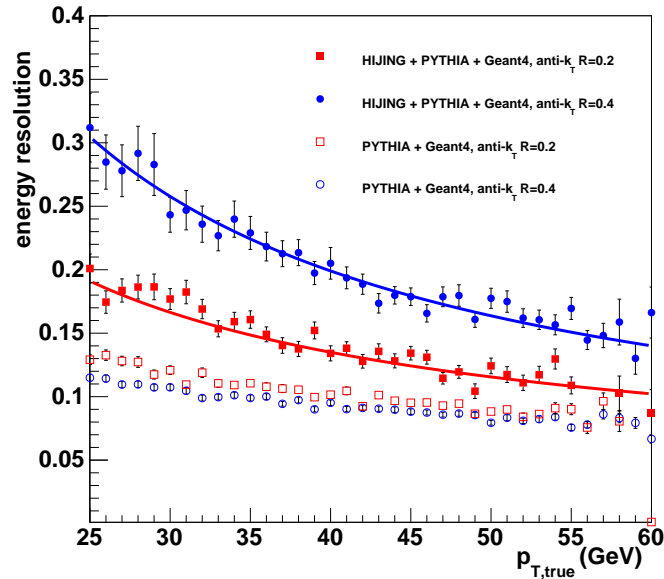


**Figure 4.7:** The GEANT4 calculated energy resolution of PYTHIA jets embedded in a Au+Au HIJING event, reconstructed using the anti- $k_T$  algorithm with  $R = 0.2$  and  $R = 0.4$ . The points, showing the result of the full simulation, are compared to the dotted lines, showing the result obtained using the fast simulation.

simulation. Again, the GEANT4 resolutions are well below our physics performance specifications.

In addition to the resolution effects, fluctuations in the underlying event can create local maxima in energy that mimic jets, and are often referred to as fake jets. While resolution effects can be accounted for in a response matrix and unfolded, significant contributions of fake jets cannot be since they appear only in the measured distribution and not in the distribution of jets from real hard processes. Thus, we first need to establish the range of jet transverse energies and jet radius parameters for which fake jet contributions are minimal. Then within that range one can benchmark measurements of the jet and dijet physics observables.

#### 4.4.1 Jet and Fake Jet Contributions

In this section we discuss both the performance for finding true jets and estimations based on HIJING simulations for determining the contribution from fake jets. It is important to simulate very large event samples in order to evaluate the relative probabilities for reconstructing fake jets compared to the rate of true high  $E_T$  jets. Thus, we employ the fast simulation method and the HIJING simulation model for Au+Au collisions. The ATLAS collaboration has found that the energy fluctuations in the heavy ion data are well matched by HIJING at  $\sqrt{s_{NN}} = 2.76$  TeV [168]. We have also added elliptic flow to the HIJING events used here. The fast simulation takes the particles from the event generator and parses them by their particle type. The calorimeter energies are summed into cells based on the detector segmentation and each tower is considered as a four-vector for input into FASTJET.

Any jet measurements in heavy ion collisions must remove the uncorrelated energy inside the jet cone from the underlying event. The approach developed in our studies is described in detail in Ref. [161]. A schematic diagram of the algorithm (based on the ATLAS heavy ion method) is shown in Figure 4.8. Candidate jets are found and temporarily masked out of the event. The remaining event background is then characterized by the strength of its  $v_2$  and the overall background level in individual slices in pseudorapidity. Higher order flow harmonics were not included in this study. New candidate jets are determined and the background and  $v_2$  are recalculated. The jet finding algorithm is then re-run on the background subtracted event to determine the collection of final reconstructed jets. This process is then run iteratively to a convergent result.

In order to distinguish true jets from fake jets we have augmented the HIJING code to run the FASTJET anti- $k_T$  algorithm with the output of each call to the fragmentation routine (HIJFRG). In this way the true jets are identified from a single parton fragmentation without contamination from the rest of the simulated event. The reconstructed jets can then be compared to these true jets. Reconstructed jets which are within  $\Delta R = \sqrt{\Delta\eta^2 + \Delta\phi^2} < 0.25$  of a true jet with  $E_T > 5$  GeV are considered to be matched and those which are not are classified as fake jets.

Other estimates of fake jet rates in heavy ion collisions have failed to take into account how the structure of the background fluctuations and the detector granularity affects the probability of any particular fluctuation being reconstructed as a jet. Note that simply blurring individual particles by a Gaussian with an underlying event fluctuation energy results in a substantial overestimate of the fake jet rate, and is not a replacement for a complete event simulation incorporating FASTJET reconstruction with a full jet and underlying event algorithm implementation. Thus, we believe these studies provide an accurate assessment of the effect of fake jets.

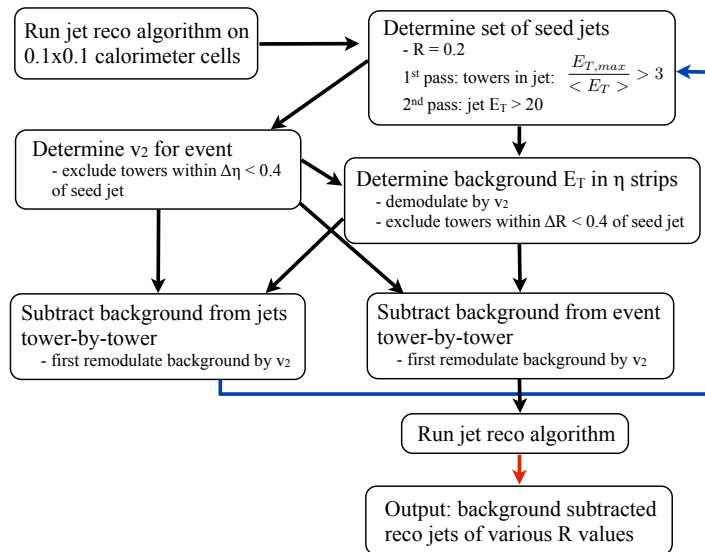


**Figure 4.8:** Schematic diagram for the jet reconstruction algorithm.

As an illustration of true and fake jets we show two calorimeter event displays in Figure 4.9. True jets at high  $E_T$  are a rare occurrence. A large energy background fluctuation at high  $E_T$  that mimics a jet is also a rare occurrence. Thus the only way to quantify the impact of fake jets on the jet performance is to run a large sample of untriggered simulated events and assess the relative

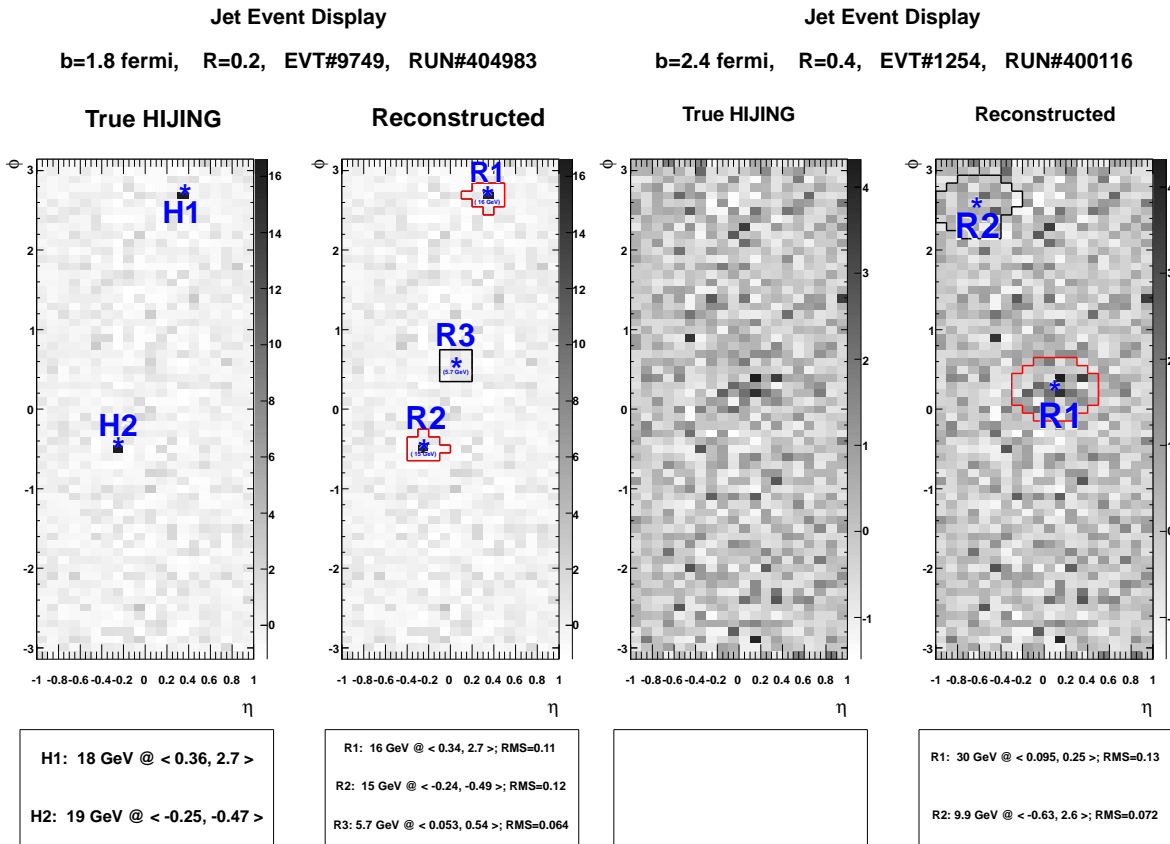


**Figure 4.9:** Event displays of true and reconstructed jets shown overlaid on background subtracted calorimeter towers from fast simulation. The left event shows a HIJING dijet event where both dijets (labeled H1 and H2) are reconstructed and matched (R1 and R2). A third jet, not matched to a true jet, is also reconstructed (R3). The right event shows a HIJING event with no true jets with  $E_T > 5$  GeV. Two fake jets are reconstructed, one with  $E_T = 30$  GeV.

probability of true and fake jets as a function of  $E_T$  and  $R$ .

A sample of over 750 million minimum bias Au+Au HIJING events at  $\sqrt{s_{NN}} = 200$  GeV with quenching turned off was used in these studies. The observable particles are binned in  $\eta$ - $\phi$  cells of size  $\Delta\eta \times \Delta\phi = 0.1 \times 0.1$ . In these studies, we have not included smearing due to detector resolution as it is expected to be a sub-dominant effect and we want to isolate the effects of the underlying event. At the end of this Section we present results including detector resolution that do not change the key conclusions of these studies.

The fast simulation result for  $R = 0.2$  jets without including detector-level smearing of the jet energies is shown in Figure 4.10. The full spectrum is shown on the left as solid points. The spectrum of those jets that are successfully matched to true jets is shown as a blue curve. That curve compares very well with the spectrum of true jets taken directly from HIJING. The fake jet, those not matched with a true jet, spectrum is shown as the dashed curve. For  $R = 0.2$ , real jets begin to dominate over fake jets above 20 GeV. The panels on the right of Figure 4.10 are slices in reconstructed jet energy showing the distribution and make up of the true jet energy. For reconstructed jets with  $E_T = 25$ –30 GeV, a contribution of fake jets can be seen encroaching on

the low energy side of the distribution. For  $E_{\text{reco}} > 25$  GeV fake jets are at the 10% level and for  $E_{\text{reco}} > 30$  GeV fake jets are negligible. Contributions from fake jets for larger jet cones are shown in Figure 4.11. The true jet rate becomes large compared to the fake jet rate at 30 GeV for  $R = 0.3$  and 40 GeV for  $R = 0.4$ . We note that in one year of RHIC running, sPHENIX would measure  $10^5$  jets with  $E_T > 30$  GeV and  $10^4$  jets with  $E_T > 40$  GeV.

There are various algorithms for rejecting fake jets based on the jet profile or the particles within the jet. These methods applied by the ATLAS experiment significantly reduce the fake rate by an order of magnitude or more, increasing the energy and  $R$  values over which it is possible to measure jets [11]. A detailed study of this fake jet rejection method and its utility is enabling new physics is discussed later in Section 4.5.

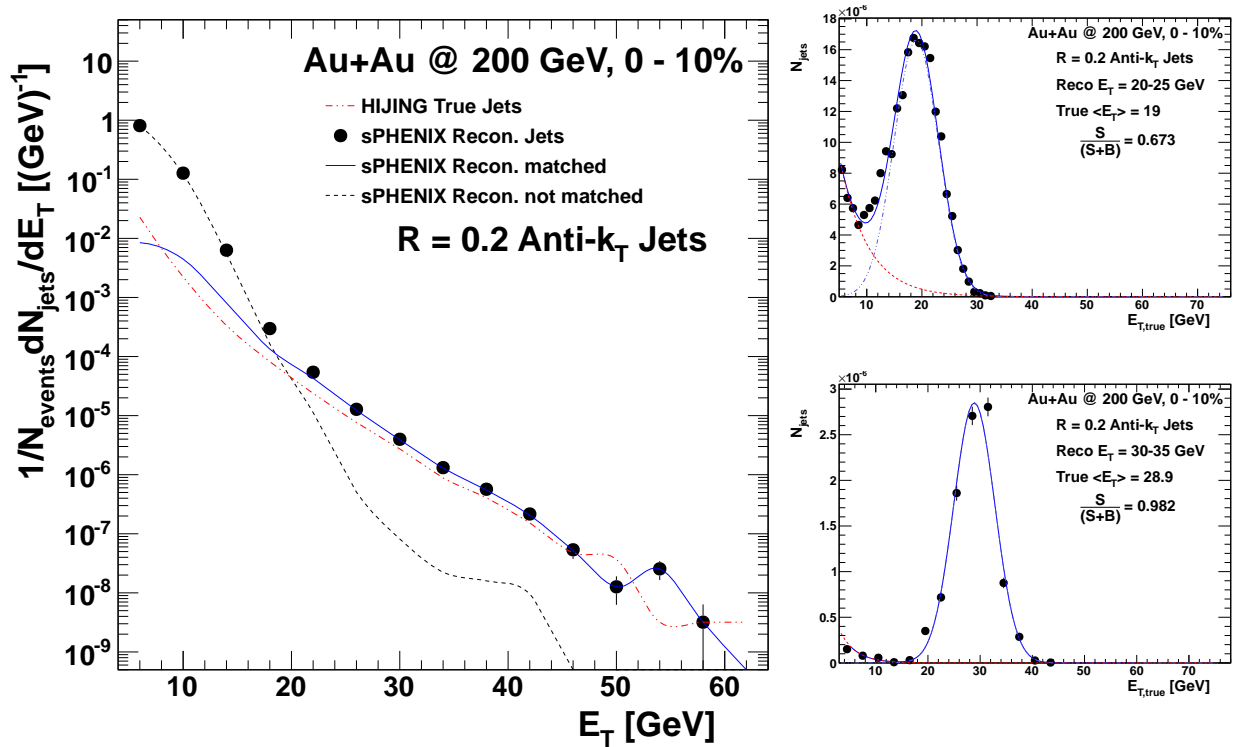


**Figure 4.10:** The composition of the jet spectrum in central 0–10% Au+Au based on 750M HIJING events. The full spectrum is shown in the left plot as solid points. The spectrum of those jets that are successfully matched to known real jets is shown as a blue curve. That curve compares very well with the spectrum of true jets taken directly from HIJING. The jets which are not matched with known jets are the fake jets, and the spectrum of those jets is shown as the dashed curve. For  $R = 0.2$ , real jets begin to dominate over fake jets above 20 GeV. The panels on the right are slices in true jet energy showing the distribution and make up of the reconstructed jet energy. At low  $E_{\text{true}}$ , fake jets can be seen encroaching on the low energy side of the distribution. For higher  $E_{\text{true}}$  the fake jets are negligible.

The efficiency of finding true jets is shown in Figure 4.12. We find  $> 95\%$  efficiency for finding jets above 20 GeV reconstructed with  $R = 0.2$  or 0.3 and above 25 GeV for jets reconstructed using  $R = 0.4$ .

Having found the jets in Au+Au with good efficiency and having established that the rate of fake

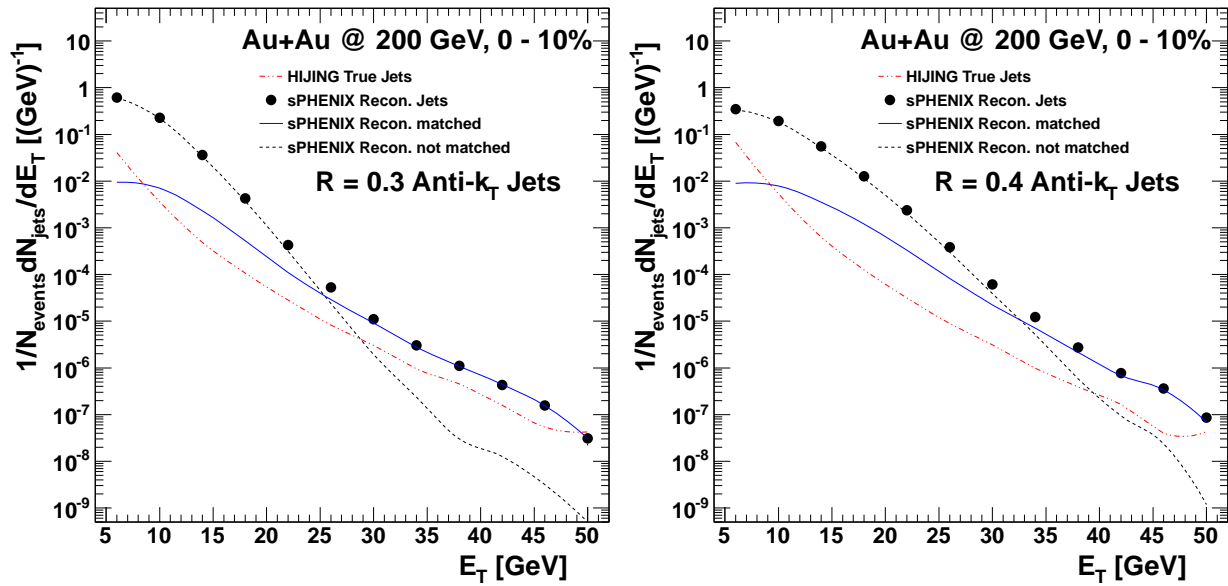


**Figure 4.11:** Composition of the jet spectra in central 0–10% Au+Au based on 750 million HIJING events for  $R = 0.3$  (left) and  $R = 0.4$  (right) jets.

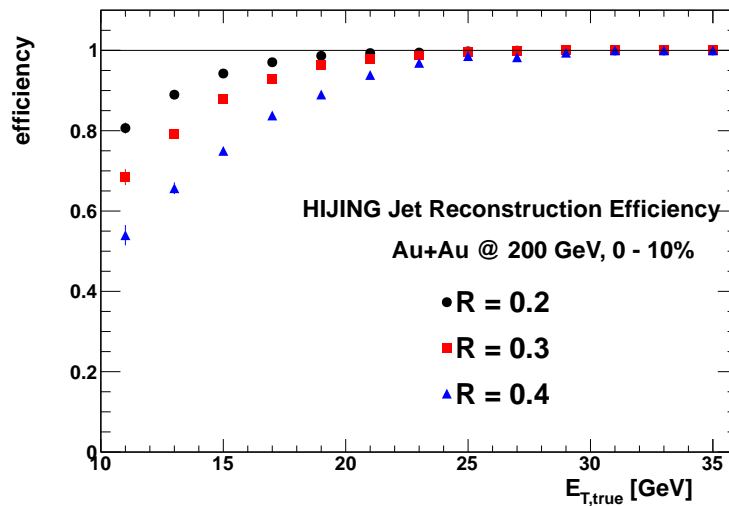


**Figure 4.12:** The efficiency for finding jets in central Au+Au collisions as a function of true jet energy and for  $R = 0.2, 0.3$  and  $0.4$ .

jets coming as a result of background fluctuations are understood and under control, we also need to show that we can reconstruct the kinematics of jets accurately and precisely. This is quantified by the jet energy scale, the average shift of the jet energy between reconstructed and true jets and the jet energy resolution which shows the relative width of the difference between the true and reconstructed jet energies. Results from  $R = 0.2$  and  $0.4$  are shown in Figure 4.13. For both jet radii the jets are reconstructed within 4% of the true energy over the measured range. Note that this is just a first step energy scale determination. The jet energy resolution shown in the right panel only includes effects due to the detector segmentation applied and the underlying event

resolution. In  $p+p$  collisions the resolution for  $R = 0.4$  jets is better than for  $R = 0.2$  jets because the segmentation can cause jet splitting with the smaller jet cones. In Au+Au collisions the order is swapped because the dominant effect is the additional smearing due to the underlying event.

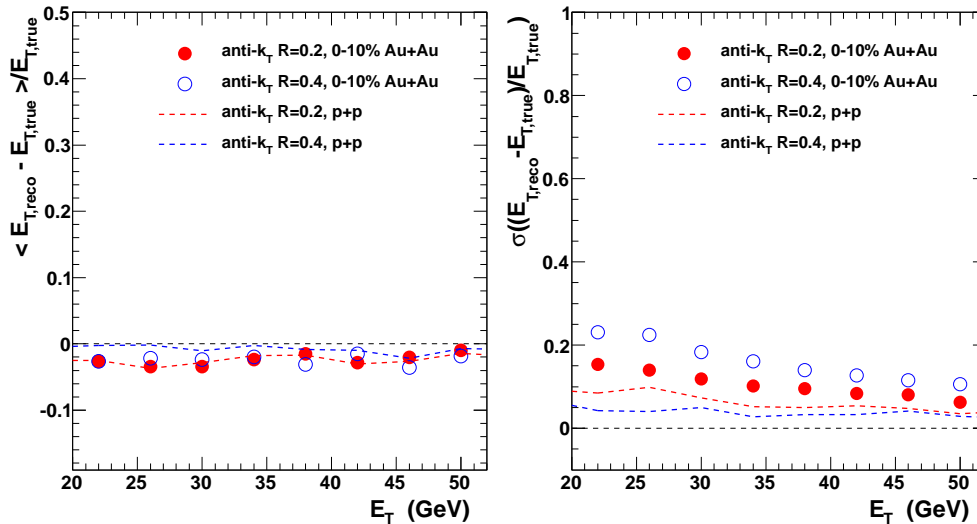


**Figure 4.13:** The jet energy scale and energy resolution of reconstructed jets in Au+Au collisions. The left plot shows the shift in the mean energy of the reconstructed jets compared to the true value. There is only a few percent shift in the energy and no apparent dependence on jet cone size. The right plot shows the jet energy resolution.

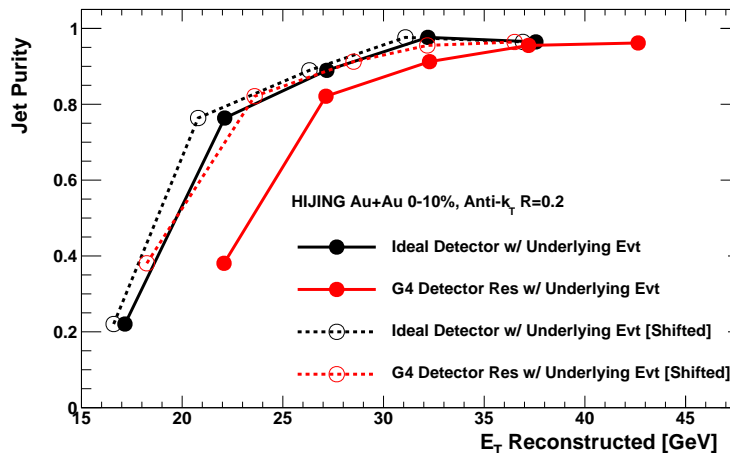


**Figure 4.14:** Results for the jet purity ( $S/(S+B)$ ) in terms of matched true and fake jets in 0–10% Au+Au collisions from HIJING. The purity values are for an ideal detector (i.e. sPHENIX segmentation with perfect resolution) and then including the GEANT4 parametrized EMCal and HCal resolutions. Both results are then shifted down in  $E_T$  by the reconstructed energy bias.

The fast simulation results described above have been re-run with the inclusion of the detector resolutions as parametrized from the single particle GEANT4 results — detailed in Section 3.4. The results shown in Figures 4.10 and 4.11 remain quite similar with the detector resolution included, though with an overall shift of all the distributions to higher  $E_T$  due to the additional blurring on falling spectra. For  $R = 0.2$  jets, the smearing due to detector resolution is comparable to the effect

of the underlying event and for larger jet cones the effect of the underlying event is found to be much larger than detector resolution effects. Figure 4.14 shows the jet purity for  $R = 0.2$  jets as a function of reconstructed  $E_T$ . The solid black (red) points correspond to the cases without (with) detector resolution effects. Also shown as open points are both results shifted down in energy by the average reconstructed energy bias as determined from the reconstructed matched jet sample. One observes that the relative true and fake jet contributions are the same for the equivalent true jet energy ranges.



#### 4.4.2 Underlying Event and Detector Effects

To further evaluate possible differences between the fast parameterized and full GEANT4 simulations of the jet performance, a study of the underlying event  $E_T$  distributions was conducted. In this study, the total transverse energy ( $\Sigma E_T$ ) in fixed position windows with a large acceptance in  $\Delta\phi \times \Delta\eta$  was compared in HIJING Au+Au  $b = 4$  fm and  $b = 8$  fm events under three different models of the detector response: first, the truth transverse energy was summed for all final-state, visible particles in the HIJING event record; second, the  $\Sigma E_T$  was measured after a fast parameterization of the detector response; third, the  $\Sigma E_T$  was measured in calorimeter towers in the window after a full GEANT4 simulation. The  $\Sigma E_T$  thus constructed was measured for the same events and in the same regions for each model of the response.

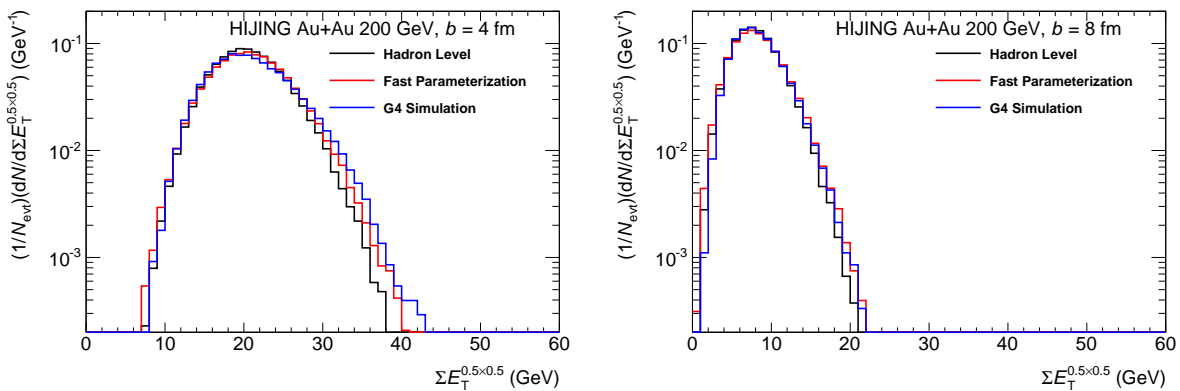


**Figure 4.15:** Distributions of the total transverse energy in  $\Delta\eta \times \Delta\phi = 0.5 \times 0.5$  regions ( $\Sigma E_T^{0.5 \times 0.5}$ ) in HIJING Au+Au  $\sqrt{s_{NN}} = 200$  GeV events with  $b = 4$  fm (left panel) and  $b = 8$  fm (right panel). The total energy is shown at the final state hadron level (black lines), with a fast parameterization of the detector response (red lines) and with a full GEANT4-based simulation (blue lines).

Figure 4.15 shows an example of the  $\Sigma E_T$  distributions for windows of size  $\Delta\eta \times \Delta\phi = 0.5 \times 0.5$  (corresponding approximately to the area under an  $R = 0.3$  jet), for the  $b = 4$  fm and  $b = 8$  fm HIJING. The distributions are broadly similar, albeit with slight differences in the shapes arising from the  $E_T$ -dependent resolution introduced by the fast parameterized and GEANT4 simulations. Figure 4.16 quantifies the mean and root mean square values of the  $\Sigma E_T$  distributions for each model of the detector response. The panels show these quantities for different choices of window size and separately for  $b = 4$  fm and  $b = 8$  fm HIJING events. Generally, the fast parameterized and GEANT4 results reproduce the mean of the original truth distributions well, but with slightly larger widths. These initial studies demonstrate that while there are modest differences between the different models of the detector response, the main features of the  $\Sigma E_T$  distributions in these high-multiplicity events are driven by the event to event fluctuations of the soft particle production and not by the model of the detector resolution.

Beyond effects due to various degrees of detector modeling realism, one could be concerned that any particular method for dealing with the underlying event could bias the obtained results. In fact, there are a number of alternate approaches in current to account for the effects of the underlying event on jet observables. The sPHENIX detector has the capabilities to investigate multiple methods, not only to gauge systematic uncertainties on a single result, but also to study the physics issues

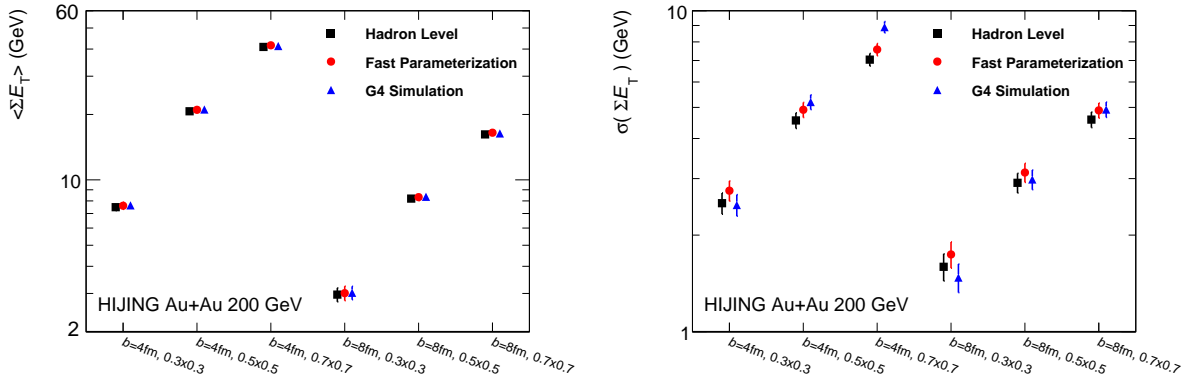


**Figure 4.16:** Means (left panel) and RMS values (right panel) of the total transverse energy in finite-sized regions ( $\Sigma E_T$ ), in HIJING Au+Au  $\sqrt{s_{NN}} = 200$  GeV events. The horizontal axis shows the results for HIJING events at different impact parameter ( $b = 4$  fm and  $b = 8$  fm) and for regions of different  $\Delta\eta \times \Delta\phi$  size ( $0.3 \times 0.3$ ,  $0.5 \times 0.5$  and  $0.7 \times 0.7$ ). Results are shown for the total energy at the final state hadron level (black lines), with a fast parameterization of the detector response (red lines) and with a full GEANT4-based simulation (blue lines).

highlighted by the different methods.

In Section 4.4.1, we described an approach for subtracting contributions to the jet signal based on a method used by the ATLAS experiment. Here we show briefly the potential for a different technique, used by both the STAR and ALICE experiments, in which the background in A++A and  $p+A$  events is calculated event-by-event and then subtracted jet-by-jet using the formula  $p_{T,jet} = p_{T,jet}^{rec} \rho_{ch} \times A_{jet}$ , where the charged background energy density  $\rho_{ch}$  is calculated as the median of  $p_T / A_{jet}$  and  $A_{jet}$  is the jet area as determined by the jet finder.

The philosophy behind this method is different from the ATLAS method of subtracting the background event prior to reconstructing the measured jets. This is a correction to the jet energy scale (JES), but only for the effect of the average background density, and does not correct for the additional smearing to the jet energy resolution (JER) the fluctuations within the event cause. The fluctuations depend both on the jet resolution parameter, the minimum  $p_T$  of the jet constituents and the centrality of the event. Additionally, the fluctuations are smaller for the charged only background as any fluctuations within the neutral sector are neglected. ALICE employs two methods to calculate the background, but the default method is the random cone method. In each event, a random cone is thrown with the same  $R$  as the jet resolution parameter and the observable  $\delta p_T$  is constructed by the following formula:  $\delta p_T = p_{T,jet}^{rec} \rho_{ch} \pi R^2$ . This distribution is shown for  $R = 0.2$  full jets with the minimum constituent cut in the 10% most central events in Figure 4.17. This method additionally quantifies the effect of jet overlap, as can be seen by the right hand tail in this figure.

The STAR experiment has used as approach very similar to that used by the ALICE experiment. Figure 4.18 shows the result of running the anti- $k_T$  jet finder on a raw, unmodified heavy ion event. The jets found by this procedure include some measure of energy from the underlying event. A distribution of jet energies relative to the median for a sample of similar events is then formed (left panel of Figure 4.18). The ensemble median energy is subtracted from the initial energy

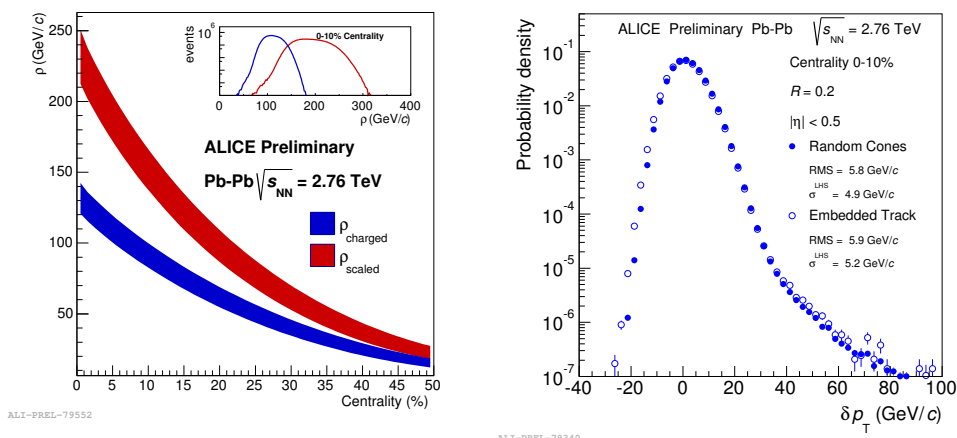


**Figure 4.17:** (left) The charged background energy density,  $\rho_{\text{ch}}$ , is shown in blue and the total energy density is shown in red. (right) The distribution of  $\delta p_T$  for  $R = 0.2$  full jets with a  $p_T$  constituent cut of 150 MeV/c for tracks and 350 MeV for clusters is shown as calculated by the random cones method in solid circles and the embedded track method in open circles.

reconstructed for each jet found.

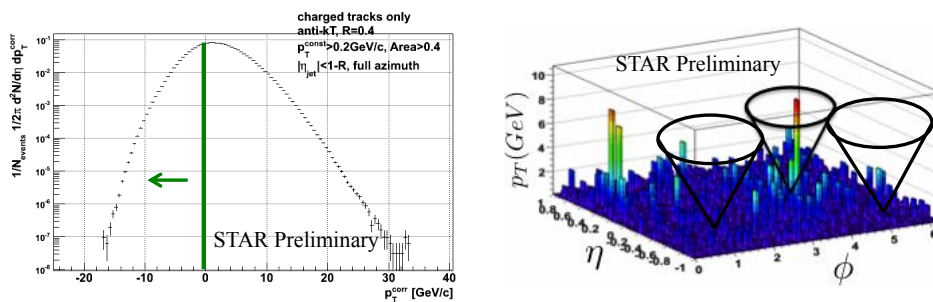


**Figure 4.18:** Preliminary result from STAR showing how jet candidates are found using the unmodified information in the event. A distribution of jet energies relative to the ensemble median is then formed and is taken as the jet signal.

sPHENIX will be able to reproduce these methods and study their efficacy for producing physics observables and for constraining and understanding systematic uncertainties.

### 4.4.3 Inclusive Jet Yield in Au+Au Collisions

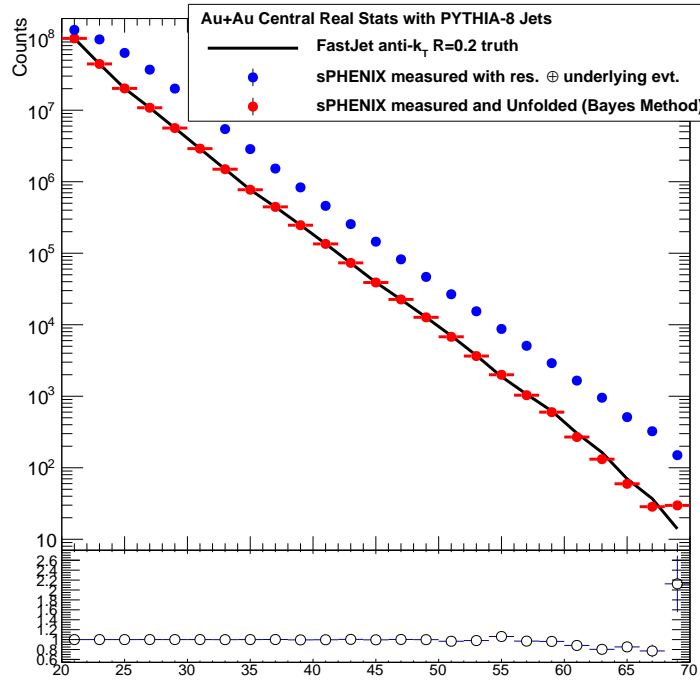


**Figure 4.19:** Effect of smearing the inclusive jet spectrum in Au+Au collisions. The jets found by FASTJET are smeared by the jet resolution contributions from the detector and the underlying event fluctuations. The unfolded spectrum from the Iterative Bayes method is shown and the ratio of the unfolded to the true  $p_T$  spectrum (lower panel).

The inclusive jet spectrum is the most important first measurement to assess the overall level of jet quenching in RHIC collisions. The results shown in Figure 4.19 were obtained by the very fast simulation approach described above. PYTHIA was used to generate events and the final state particles were sent to FASTJET in order to reconstruct jets. The resulting jet energy spectrum was smeared by the jet resolution determined for  $p+p$  collisions from GEANT4, and an additional smearing by the underlying event fluctuations (determined from the full 0–10% central HIJING fast simulation). Finally, an unfolding procedure was used to recover the truth spectrum. The ratio shown at the bottom of the plot shows that the unfolding is very effective.

As an estimate of the uncertainties on a jet  $R_{AA}$  measurement from one year of RHIC running, the uncertainties from Figures 4.6 and 4.19 are propagated and shown in Figure 4.20. For  $E_T < 50$  GeV the point to point uncertainties are very small. Also shown is an estimated systematic uncertainty including the effects from unfolding. All points are shown projected at  $R_{AA} = 1$ , and we show for comparison the predicted jet  $R_{AA}$  including radiative and collisional energy loss and broadening from Ref. [102].

### 4.4.4 Dijets in Au+Au collisions

Fake jets contaminate dijet observables much less than they do the inclusive jet measurement. In the case of inclusive jets, one is working with a sample of  $10^{10}$  central Au+Au events in a typical

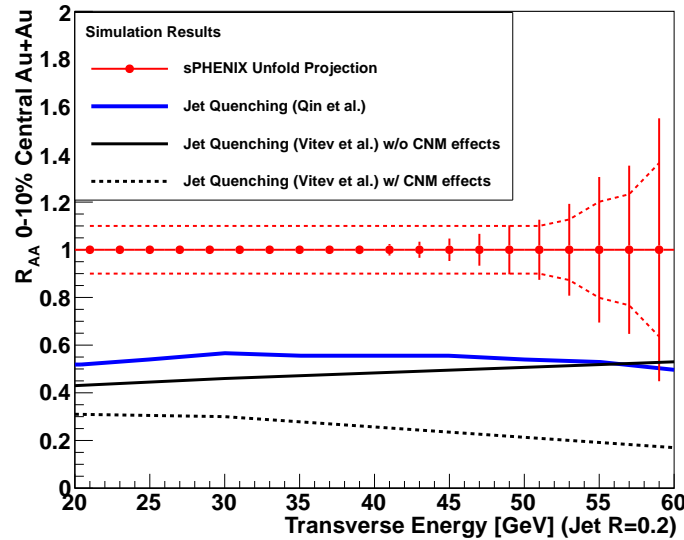


**Figure 4.20:** Single inclusive jet  $R_{AA}$  with  $R = 0.2$  for Au+Au central events from the unfolding of the  $p+p$  and Au+Au spectra with an estimated systematic uncertainty as a multiplicative factor of approximately  $\pm 10\%$ . Also shown are the predictions from a calculation including radiation and collisional energy loss and broadening [102] and another with and without cold nuclear matter effects [60, 61, 62] (as discussed in Section 1.6).

RHIC year, so even if it is only a rare fluctuation in the background that will be reconstructed as a real jet, there is a huge sample of events in which to look for such fluctuations.

The case of dijet correlations is very different. There are  $10^6$  clean trigger jets above  $E_T = 30$  GeV in central Au+Au collisions in a RHIC year — detailed in Figure 1.49. This means there is a factor of  $10^4$  fewer chances to find the rare background fluctuation that appears to be a true jet in the opposite hemisphere. Also, the presence of a high energy jet, for which the fake rate is known to be low, tags the presence of a hard process occurring in the event, and thus dramatically reduces the probability of a jet in the opposite hemisphere being a fake. Because of these considerations, one can go to much lower  $p_T$  for the away side partner of a dijet pair. Studies presented here include away side jets down to 5 GeV, and we have found that the fake jet rate remains small for the associated jets, even at these low jet energies.

In order to address the sensitivity to modifications of the  $A_j$  distributions that might be expected at RHIC here we compare PYTHIA simulations with those from PYQUEN [160] (a jet quenching parton shower model with parameters tuned to RHIC data). All the PYQUEN events generated are for central Au+Au events with  $b = 2$  fm. Figure 4.21 shows the particle level (i.e truth)  $A_j$  distributions and how they are reconstructed after being embedded in a central Au+Au event with a parametrized detector smearing and segmentation applied. As described above, the full iterative underlying event subtraction method is applied. The simulated measured distributions (middle panel of Figure 4.21) show the effects of the smearing; and the distinction between the PYTHIA and PYQUEN distributions remain large. An unfolding procedure can be applied to these embedded distributions to regain the true distributions. However, as in the  $p+p$  case discussed in Section 4.3.2 this should involve a full two-dimensional unfolding. Applying the same “unfolding” applied to

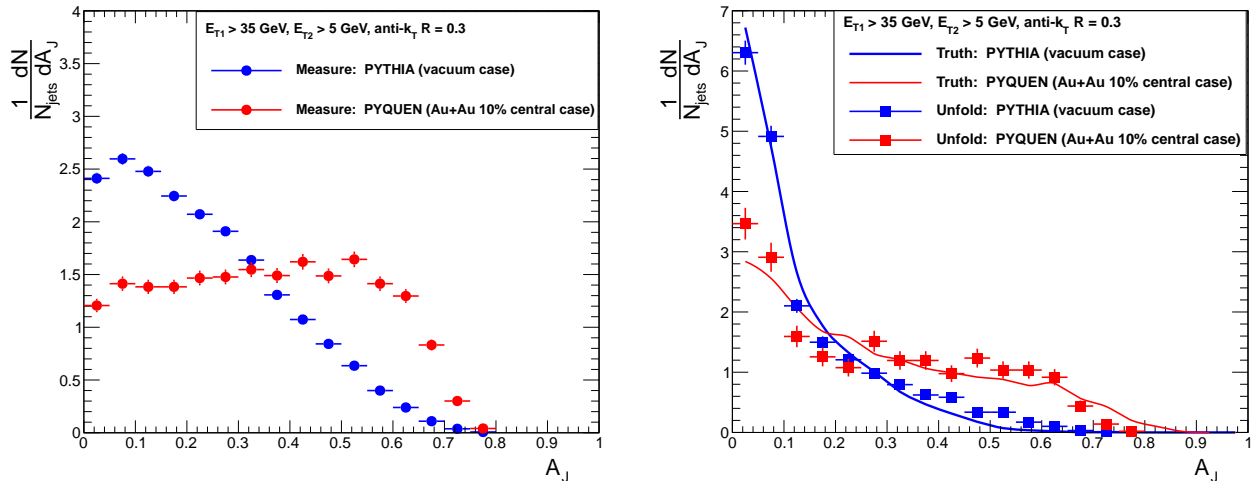


**Figure 4.21:** The effect of smearing on  $A_J$  for  $R = 0.3$  jets. The left panel shows the effect of smearing on the ratio determined from jets reconstructed after embedding in Au+Au events. Although smeared, the reconstructed data still show a distinct difference between the quenched and unquenched results. The right panel shows the results of the “unfolding” procedure discussed in Section 4.3.2.

the  $p+p$  case where the smearing of the trigger jet is taken as the dominant effect recovers most of the original distribution, as shown in the lower panel of Figure 4.21. Again, this does not replace a full unfolding procedure, but it does show that the reconstruction is well under control and unfolding will be possible despite the presence of a large fluctuations in the underlying event, after baseline and flow subtraction.

## 4.5 Extended kinematics and surface bias engineering

Thus far we have documented a range of jet energy, radius, and collision centralities over which inclusive jets dominate above backgrounds and provide clean measurements of  $R_{AA}$  and  $A_J$  for example. One can significantly extend the jet radius to larger values and energies to lower values through various fake jet rejection methods including matching to track jets, identification of individual particle energies in the jet (e.g. tracks or clusters) and setting minimum energy thresholds, jet shape cuts, and more. As we demonstrate here, sPHENIX will have the full complement of these methods available (thus having complementary overlap with existing STAR jet observables). All of these rejection methods present a bias on the jet sample that often anti-correlates with the expected modification in the quark-gluon plasma medium.

Experiments have employed fake jet rejection cuts to substantially extend the high purity jet energy range accessible in central heavy ion collisions — for example see Refs. [11, 89]. With the sPHENIX detector we can utilize track + electromagnetic jets matched to fully calorimetric jets in a similar fashion. In addition to extending the measurable jet energy range to lower energies, for energies with high purity without any selection one can turn this method into a powerful tool to engineer the degree of jet surface emission. For example, in the sample of  $10^5$  jets with  $R = 0.4$  and  $E_T > 40 \text{ GeV}$ , we can measure a high purity sample of reconstructed jets in central Au+Au collisions. We can then dial in the required track + electromagnetic cluster jet characteristics to achieve a particular

surface bias — as proposed by Renk [99] and shown earlier in Figure 1.24.

One can also incorporate electromagnetic clusters, which provide additional input to the alternate jet reconstruction. The electromagnetic clusters and tracks have the same minimum energy cut and are then input to the FASTJET algorithm. Figure 4.22 shows the jet purity for different jet radii  $R = 0.2, 0.3, 0.4, 0.5$  with a nominal track + electromagnetic jet match requirement ( $E_T > 7$  GeV for the match jet,  $E_T > 3$  GeV for the electromagnetic cluster and charged track) in central Au+Au events. The results are very good and indicate that even  $R = 0.5$  jets can be reconstructed in the most central Au+Au events. The effects of the underlying event on jet observables are most severe in central Au+Au events, and these results demonstrate the dramatically increased range for jet reconstruction in mid-central Au+Au collisions, where significant jet quenching effects have already been measured including the theoretically challenging high  $p_T$  hadron azimuthal anisotropy.

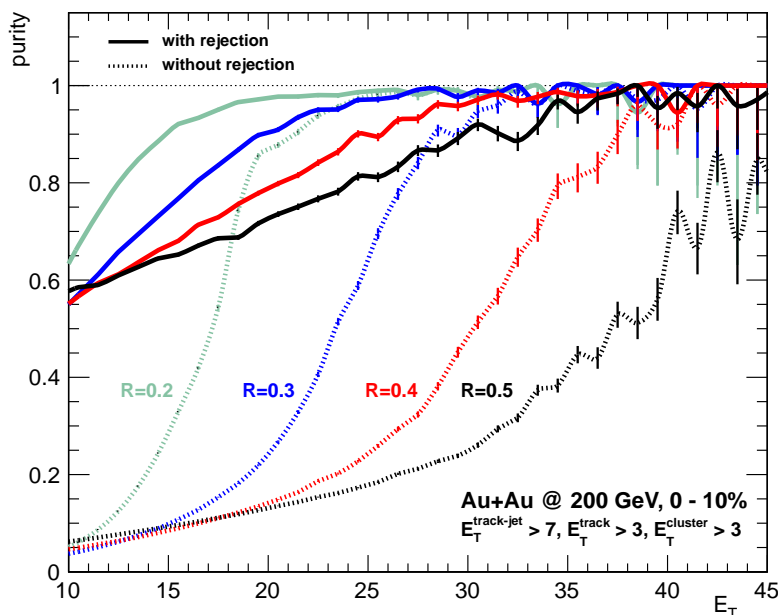


**Figure 4.22:** Purity results for  $R = 0.2, 0.3, 0.4, 0.5$  anti- $k_T$  calorimetric reconstructed jets in 0–10% central Au+Au HIJING events. The dashed lines are without any track and electromagnetic cluster jet match requirement and the solid lines are with the match requirement. The purities are significant higher for mid-central collision geometries.

sPHENIX will be also able to reproduce existing jet measurements at RHIC, complete with the biases inherent in the various techniques used to date. However, the wider capabilities of sPHENIX will enable us able to do more than merely confirm earlier results. We will be able to place those results along a spectrum of bias and to study the effect on the jet observables of the alteration or removal of that bias.

Figure 4.23 shows a preliminary result from the STAR collaboration of  $A_J$  for jets in events triggered on the presence of a single EMCAL tower above 5.4 GeV. The left panel shows  $A_J$  for  $R = 0.2$  jets; the right for  $R = 0.4$  jets. When a cut of  $p_T > 2$  GeV/ $c$  is placed on the constituents, there is a distinct

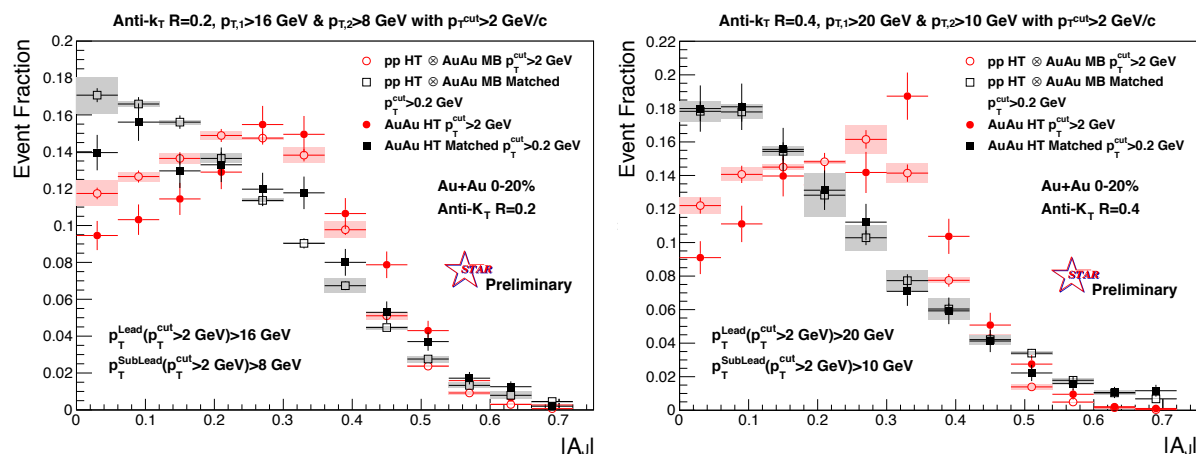


**Figure 4.23:** STAR result for  $A_J$  for  $R = 0.2$  and  $R = 0.4$  jets, triggered on a high  $E_T$  electromagnetic calorimeter tower. When lower  $p_T$  constituents are included in the  $R = 0.4$  jets, the shape of the  $A_J$  distribution is essentially identical for  $p+p$  and Au+Au.

difference in the  $A_J$  distributions for  $R = 0.2$  that disappears for the larger  $R = 0.4$  jets, presumably because the larger radius recover the full energy of the medium-modified jets. sPHENIX will be able to used jets triggered in a wide variety of ways as inputs to physics analyses.



## 4.6 Fragmentation Function and Photon-Jet Observables

Measurements that probe the redistribution of energy within the parton shower directly are an important class of observables for understanding the underlying dynamics of jet quenching. This redistribution may take place both along the parton direction, such as may be measured through the modification of longitudinal fragmentation functions in Au+Au collisions, and transverse to the parton direction. The capability of the sPHENIX detector and the high statistics provided by RHIC will allow for measurements of the two-dimensional distribution of energy to be measured and compared between  $p+p$ ,  $p(d)+Au$ , and Au+Au collisions. Such measurements take advantage of the fully calorimetric jet and photon observables in tandem with the measurement of charged hadrons by the precision tracking capabilities.

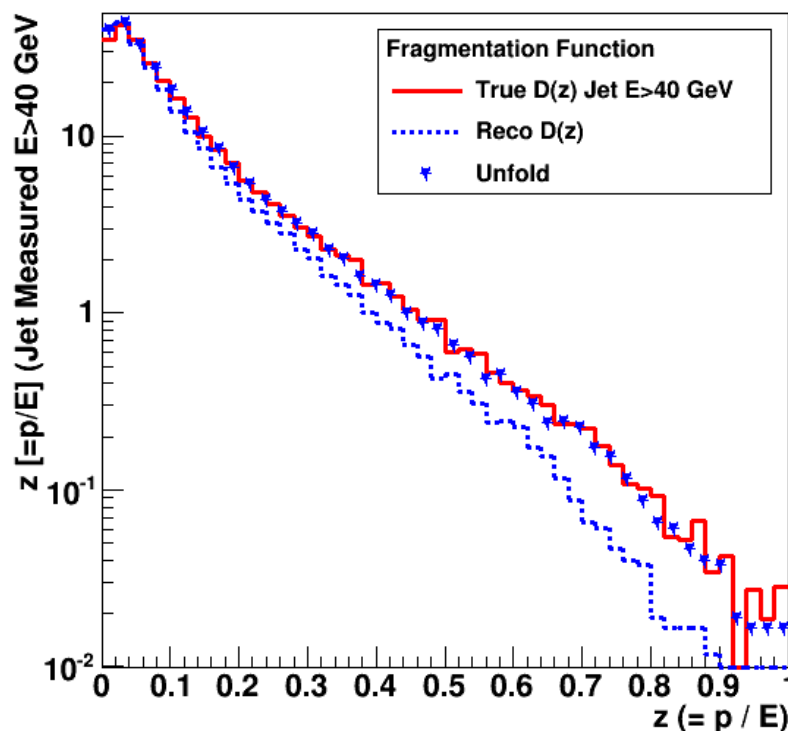


**Figure 4.24:** Demonstration of the sPHENIX capabilities for measuring the inclusive jet fragmentation function,  $D(z)$ , for  $p_T > 40$  GeV/ $c$  jets. The original “truth” distribution is shown in red, while the reconstructed level distribution is shown in the blue dashed line. The reconstructed level distribution is corrected for detector effects to give the unfolded quantity shown in blue stars.

Figure 4.24 shows the results of a fast simulation of the sPHENIX measurement capabilities for the inclusive jet fragmentation function for high- $p_T$  jets. This figure compares the truth-level  $D(z)$  quantity with the measured, detector-level  $D(z)$  which incorporates the effects of a fast parameterized detector response on the jet and hadron  $p_T$ . Due to the finite momentum resolution in both cases (and, in the case of the jet, the upfeeding from the underlying event fluctuations), the reconstructed-level  $D(z)$  is generally shifted towards lower values at fixed  $z$ . The reconstructed

level distribution is unfolded to correct for these detector effects, resulting in an unfolded  $D(z)$  distribution that is able to successfully recover the original truth-level  $D(z)$ . Furthermore, the statistical uncertainties used in the plot are chosen to correspond to that available in a 22 week Au+Au run. This figure demonstrates the plausibility of measuring the fragmentation function within sPHENIX.

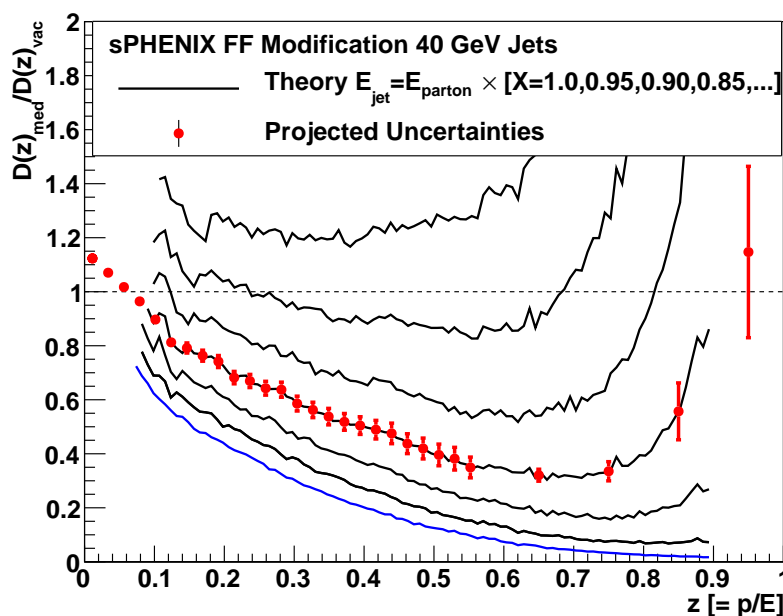


**Figure 4.25:** Modified fragmentation function  $D(z)$  in the medium [169] expressed as the ratio of the modified  $D(z)$  to that assuming vacuum fragmentation. The different black curves show the results of different assumptions for how much of the parton energy is retained in the jet cone,  $x$ , with the original prediction corresponding to  $x = 1.0$  shown as the lower blue curve. The projected statistical uncertainties achievable for 22 weeks and 10 weeks of Au+Au and  $p+p$  data-taking are shown on top of the curve at  $x = 0.85$ .

When combined with a reference measurement of the unquenched fragmentation function in  $p+p$  collisions, sPHENIX will be able to make detailed measurements of the medium modifications to the longitudinal structure of the jet. Figure 4.25 shows a calculation for the ratio of  $D(z)$  in 200 GeV Au+Au to  $p+p$  collisions [169], under different assumptions of how much of the total parton energy is recovered in the jet cone. The red points in the figure show the projected statistical uncertainty for a particular value of the ratio, corresponding to the first two years of sPHENIX data-taking.

In addition to the per-jet fragmentation function, the photon capability in sPHENIX will allow for the measurement of photon-tagged jets. Although lower in statistics than measurements of inclusive jets, photon-jet events offer several crucial advantages. First, photon performance is much less sensitive to the effects of the underlying event in Au+Au collisions (i.e. there are no “fake” photons). Second, the resolution for high- $p_T$  photons, measured using only the EMCal, is better than that for full jets, which include the resolution introduced by the HCal, resulting in more modest corrections for detector effects. Third, photons provide an independent, well-calibrated

probe against which to measure jet modification. Finally, unlike the case for inclusive jets, the presence of a high- $p_T$  photon in the event substantially raises the probability that the balancing jet is a real jet, resulting a much smaller fake rate and the ability to measure to lower  $E_T$  and larger  $R$  value. This feature is particularly important because it allows for the possibility of exploring the cone size dependence of jet modification down to much lower  $E_T$  than may be possible with inclusive jet measurements only.

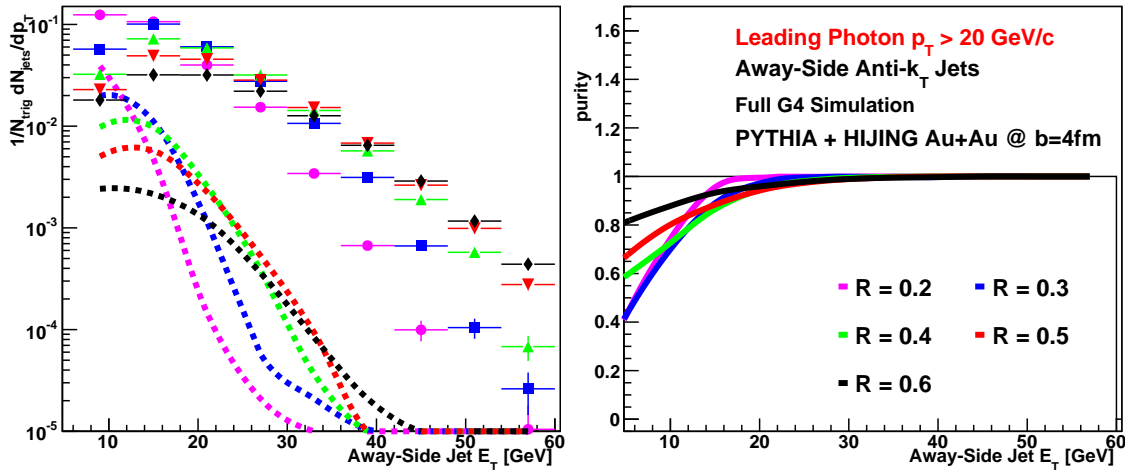


**Figure 4.26:** Demonstration of the photon-jet capability in sPHENIX, derived from a full GEANT4 simulation of PYTHIA events with a  $> 20$  GeV photon embedded into central Au+Au HIJING events. (left) Distribution of jet  $E_T$  in these events for real jets (solid markers) and fakes (dashed lines). In both cases, different colors correspond to different  $R$  values. (right) Purity of hard scattered jets as a function of jet  $E_T$ , shown for different size jets.

Two key benchmarks of the simulated performance for photon-jet measurements in sPHENIX are described below. Figure 4.26 quantitatively demonstrates, using a full GEANT4 description, the high jet purity for photon-balancing jets. In events with a  $p_T > 20$  GeV photon, the purity of away-side jets with  $E_T > 20$  GeV is  $> 90\%$  even for  $R = 0.6$  jets.

In contrast to the dijet case studied above, the  $\gamma$ -jet measurements do not compare two similar objects affected in a similar way by the presence of the underlying event. In this case, the quantity of interest is taken to be  $x \equiv E_{\text{jet}}/E_\gamma$  (rather than an asymmetry  $A_J$ ). While in a leading order QCD picture the  $\gamma$  and recoiling parton should exactly balance in energy, in reality this is not necessarily the case, resulting in a vacuum distribution of  $x$  that is peaked below 1. In particular, for small jet sizes there is a significant probability that the away side parton shower is split into more than one jet by the reconstruction procedure, with each carrying a fraction of the energy needed to balance that of the  $\gamma$ .

Figure 4.27 shows the distribution of  $x$  values for  $E_T^\gamma > 20$  GeV events with an  $R = 0.3$  jet with  $E_T^{\text{jet}} > 10$  GeV, at the truth, reconstructed and unfolded levels, for the vacuum fragmentation case as implemented in PYTHIA and for the case of the PYQUEN generator. Due to the finite jet energy resolution and the effect of split jets, both exacerbated by the underlying event in the embedded event, the reconstructed level  $x$  distribution is qualitatively different than the truth distribution. However, the PYTHIA and PYQUEN distributions are still noticeably different. The figure also shows how well an unfolding procedure can recover the original distributions. Although nominally

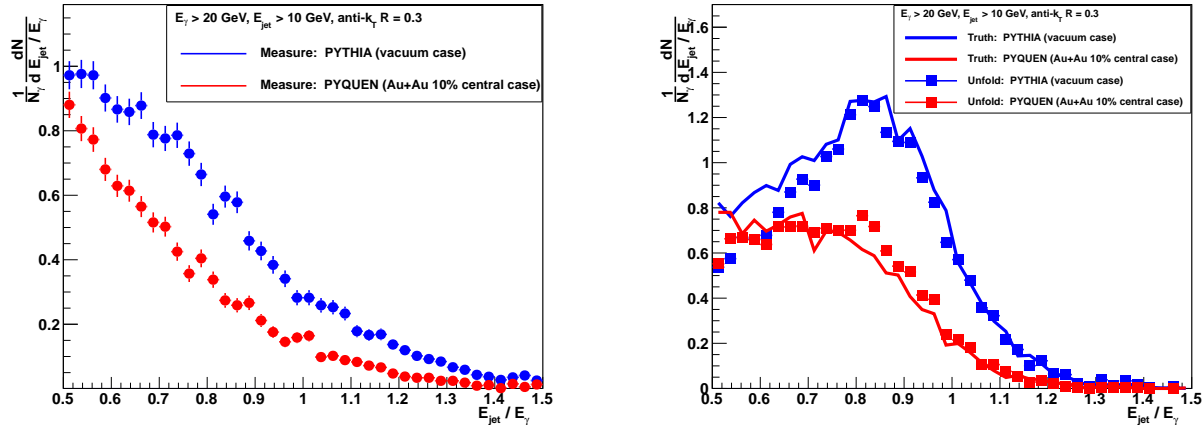


**Figure 4.27:** The effect of smearing on energy ratio  $E_{\text{jet}}/E_{\gamma}$  for  $R = 0.3$  jets. The left panel shows the effect of smearing on the ratio determined from jets reconstructed after embedding in Au+Au events. Although smeared, the reconstructed data still show a distinct difference between the quenched and unquenched results. Results of a one dimensional unfolding are compared with the truth particle level distributions in the right panel.

both the photon and the jet  $E_T$  must be unfolded, In the  $\gamma$ -jet case the unfolding may be treated to good approximation as being one-dimensional. This is because, as described above, the dominant smearing effect is on the jet energy. In the figure above, an Iterative Bayesian unfolding is performed on the detector-level  $\gamma$ -jet  $x$  distributions for the  $R = 0.3$  jets. The unfolded results compare well with the particle level distributions for both PYTHIA and PYQUEN.

While the inclusive fragmentation function and photon-jet energy balance measurements have been discussed here in detail, many additional, potentially revealing measurements will be possible. For example, measurements of the transverse momentum distribution of hadrons with respect to the jet axis or opposite side photon axis may provide additional information. Furthermore, one can use  $\gamma$ +hadron correlations to study the redistribution of energy lost by the opposite going parton. Previous results from CMS [78] and STAR [89] on  $\gamma$ +hadron correlations indicate that this energy is spread over a wide angular range. However, measurements at RHIC of  $\gamma$ +hadron correlations have not had the statistical precision or the acceptance necessary to make comparable statements about the modification to jet fragmentation. The combined jet and hadron capabilities of sPHENIX will provide useful data.

Photon-tagged jets offer another well-known experimental handle: the away-side jet is dominantly a quark-initiated one. Thus, the measurements above chiefly measure the medium modification of quark-initiated parton showers. However, at RHIC energies, an experimental handle on gluon jets is also available. Figure 4.28 shows, in a leading order picture, the breakdown of the inclusive jet cross-section by outgoing parton flavor. It can be seen that, in events with a 20–30 GeV quark jet, the away-side jet is a gluon-initiated jet approximately  $2/3^{\text{rds}}$  of the time. Thus, the presence of a quark jet, which may be indicated by a particularly harder fragmentation pattern or tighter energy profile, or by a more modest medium modification, is a good way to select gluon jets on the away side.

Similar to the photon-jet case, the presence of a narrow cone jet or a high- $p_T$  track (both of which

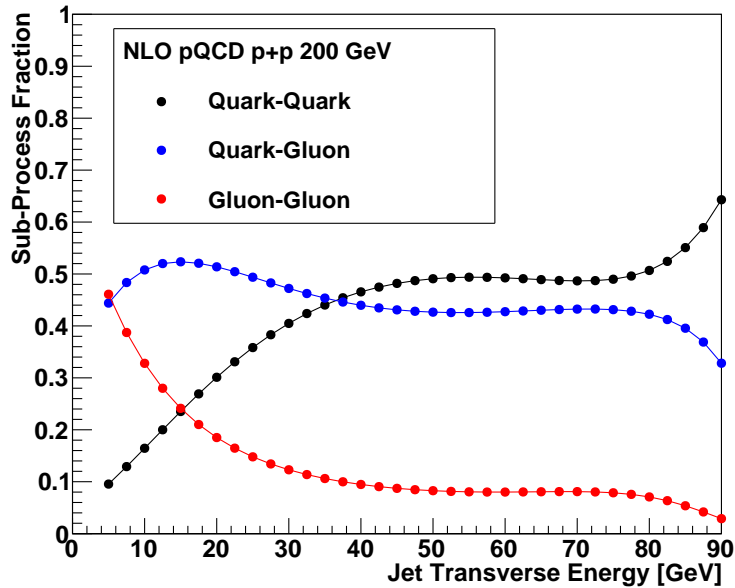


**Figure 4.28:** NLO pQCD calculation for the subprocess contributions as a function of jet transverse energy at midrapidity in  $p+p$  collisions at 200 GeV. At the lowest jet  $E_T$  gluon-gluon processes dominate, transitioning to a mixture of quark-gluon and quark-quark processes, and finally dominated by quark-quark processes near the kinematic limit of  $E_T$ .

are indicative of a quark jet) results in a purity for the away-side jet which is substantially enhanced relative to that for inclusive jets at a comparable  $E_T$ . Figure 4.29 shows the purity of away-side jets as a function of away-side jet  $E_T$  for different values of the jet radius  $R$  in the presence of an  $R = 0.3$   $E_T > 30$  GeV jet or a  $p_T > 20$  GeV/ $c$  track on the near side. It can be seen that the purity remains above 90% for  $> 20$  GeV jets, even for  $R = 0.6$  jets.

Additionally, there are other techniques which can be used to extend the kinematic reach of the away-side jet to low  $E_T$  and control the extent of the fake rate. An example of such a technique is the statistical ensemble mixing method developed by the STAR Collaboration (Figure 4.30), which has been successfully used in Au+Au collisions.

Thus, using small- $R$  jets or high- $p_T$  single tracks as a trigger object, a sample with an enhanced gluon content can be reliably selected down to low  $E_T$ . In tandem with the quark-enhanced sample selected in photon-jet events, this will allow for an experimental handle on the flavor-dependence of quenching in sPHENIX. Of course, these selections on the trigger jet will surely introduce a bias, such as in the distribution of path lengths for the away-side jet. These issues were discussed previously in Section 4.5.

As an illustration of the benefit of reconstructing trigger-balancing jets to low  $E_T$  and large  $R$  values, Figure 4.31 shows an example of a measurement enabled by this capability. The figure shows calculations from the JEWEL MC generator of the modification of the away-side jet yield as a function of jet  $E_T$  for events with a high- $E_T$  narrow jet or high- $p_T$  charged hadron. In particular, the MC code predicts a rich away-side jet cone size and  $E_T$  dependence to the modifications, in a region which would be experimentally accessible to sPHENIX given the purity studies above.

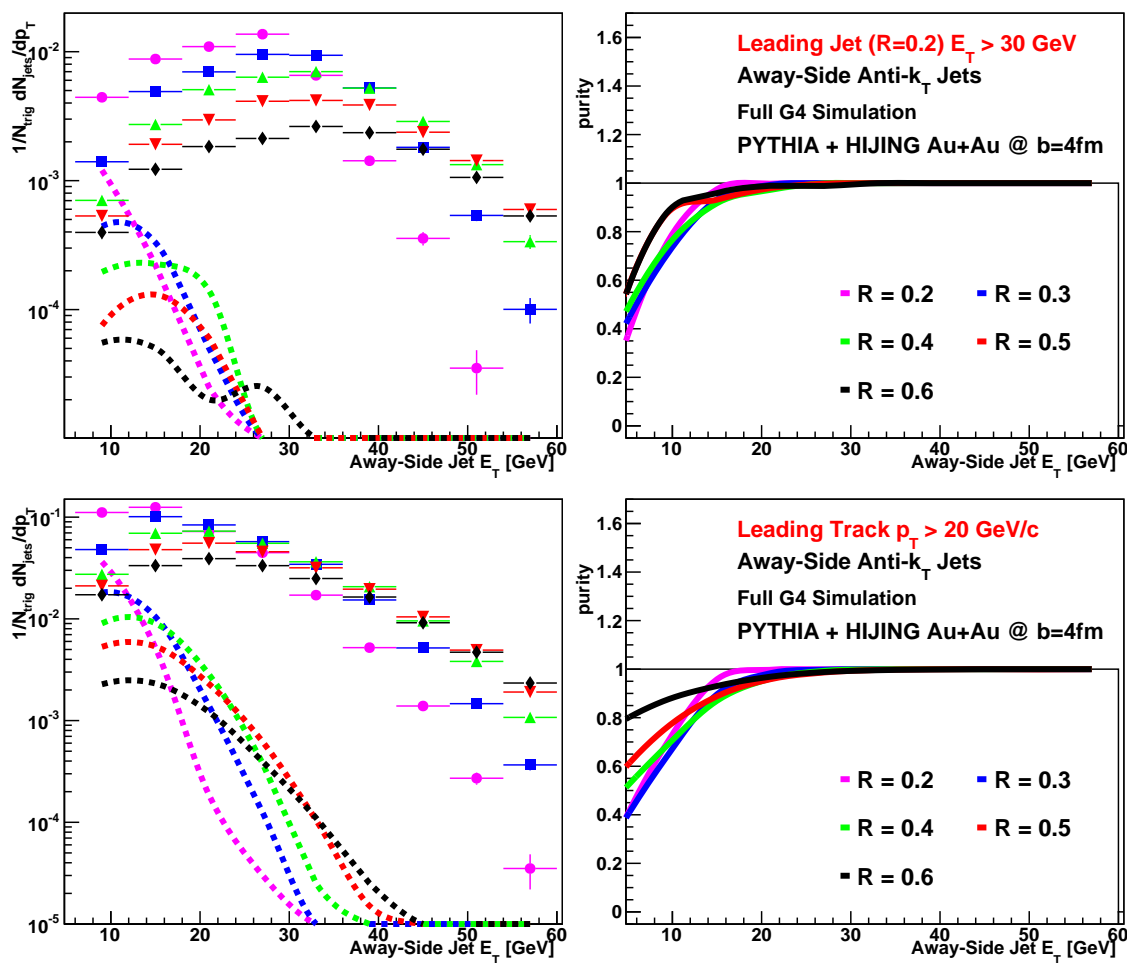


**Figure 4.29:** (upper) Full GEANT4 simulations with PYTHIA dijets embedded on central Au+Au HIJING events with reconstruction of trigger and away-side jets. The left panel shows all reconstructed away-side jets for different  $R$  values opposite to a trigger jet with  $R = 0.2$  and  $E_T > 30$  GeV. The dashed lines indicate the fake jet contributions. The right panel shows the purity of away-side jets, which is quite high even for large radius away side jets. (lower) Same quantity except now triggering on a charged hadron with  $p_T > 20$  GeV/c.

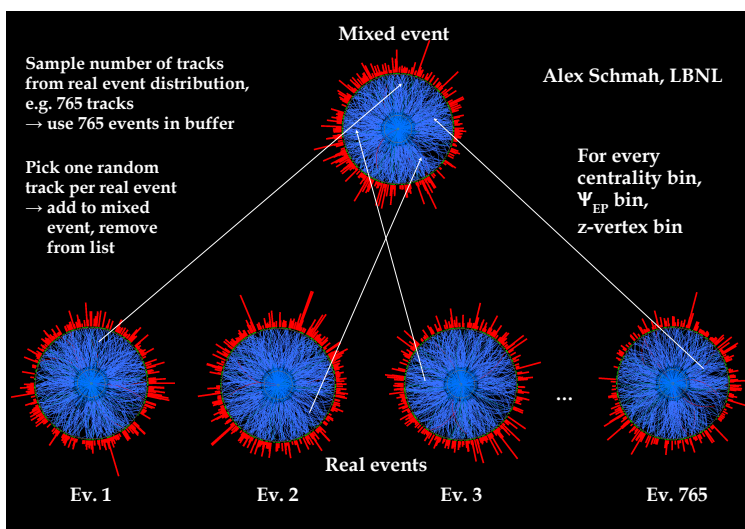


Figure 4.30: Illustration of a technique for ensemble mixing as developed by the STAR Collaboration.

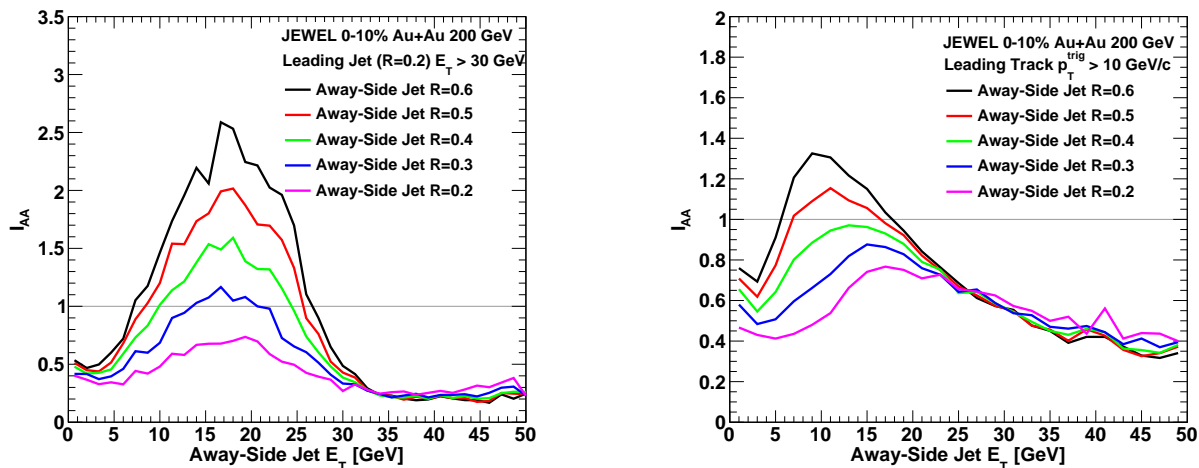


Figure 4.31: (left) Shown are JEWEL jet quenching Monte Carlo calculations in Au+Au 0-10% central collisions triggering on an anti- $k_T$  jet with  $R = 0.2$  with  $E_T > 30$  GeV and measuring the modification of away-side correlated jet yields ( $I_{AA}$ ). The away-side jet yields are calculated for different jet sizes  $R = 0.2 - 0.6$ . (right) Same quantity except now triggering on a charged hadron with  $p_T > 10$  GeV/c.

## 4.7 Heavy Quark Jets

Heavy quarks traversing the quark-gluon plasma are an excellent test of our understanding of the mechanisms of parton energy loss. Due to the finite velocity in medium there is an expected suppression of radiative energy loss at small angles relative to the heavy quark. sPHENIX has good tracking, including displaced vertex capabilities as detailed in Section 3.6.

The rates for heavy quark jets shown in Figure 1.40 indicate a substantial number of accepted jets for sPHENIX in the large data samples achievable. With a jet tagged efficiency for beauty jets of order 50%, one would have thousands of beauty jets for energy above 20 GeV and hundreds of thousands above 10 GeV. The tagging of heavy flavor dramatically reduces the “fake” jet background and may allow one to push below the 20 GeV energy range even in central Au+Au events. Detailed GEANT4 studies are at an early stage and require detailed studies to document the full capabilities.

In this section, we investigate the feasibility of  $b$ -jet tagging approaches through the requirement of charged tracks within the jet with a large distance of closest (DCA) approach to the primary vertex. This method, which exploits the long lifetime, displaced decay and high multiplicity of the  $B$  hadron, is sometimes called the “Track Counting” algorithm and has a wide use within the literature.

A description of the algorithm as it has been used in modern experiments follows below [170, 171, 172, 173]. All reconstructed charged tracks within the jet cone are considered, and their distance of closest approach to the primary vertex is determined, either for the full three dimensional distance or the two dimensional distance in the transverse plane. The DCA value is signed by comparing the vector from the primary vertex to the location of closest approach along the track trajectory to the jet vector — if the location of closest approach is within the same hemisphere as the jet vector (meaning the vectors have a positive dot product), the DCA is taken to be positive. Otherwise, it is taken to be negative. Finally, a signed DCA *significance*  $S$  is defined by dividing the reconstructed DCA value by its uncertainty,  $S = \text{DCA}/\sigma_{\text{DCA}}$ . The  $b$ -tagging algorithm operates by requiring some number of tracks to each have a significance  $S$  above some minimum value  $S_{\text{cut}}$ . As the quantity  $S_{\text{cut}}$  and the number of tracks required change, so does the performance of the algorithm as typically characterized by the efficiency for tagging  $b$ -jets and the purity after applying this cut. For a given sample of light, charm and bottom jets  $N_l, N_c$  and  $N_b$  with cut efficiencies  $\epsilon_l, \epsilon_c$  and  $\epsilon_b$  respectively, the purity  $P$  is defined as

$$P = \epsilon_b N_b / (\epsilon_l N_l + \epsilon_c N_c + \epsilon_b N_b) \quad (4.1)$$

Alternately, one can also characterize the performance of the algorithm in terms of the mis-identification probability or the rejection factor for light and charm jets. Typically, one hopes to cut in a way such that the purity of  $b$ -jets in the set of jets passing the cut is high, while still maintaining a high enough efficiency to give good statistics for the measurement.

In light quark and gluon jets, most charged hadrons originate very near the primary vertex, resulting in a distribution of  $S$  values that is a Gaussian centered at zero with a width of 1. However, some small fraction of charged tracks within the jet, such as those from the decay of strange hadrons, may have large positive significances depending on the decay kinematics. In  $b$ -jets, many charged hadrons originating from the  $B$  hadron decay will generally have large DCA significances. Thus,



requiring a jet to have one or more tracks with a large significance will preferentially select  $b$ -jets over light jets. Since  $B$  hadrons decays are accompanied by a large charged particle multiplicity on average [174], the requirement of a large number of tracks does not in and of itself adversely affect the efficiency. The goal of the following study is to quantify what tagging efficiency for  $b$ -jets can be achieved as a function of the purity of  $b$ -jets in the tagged sample.

In this study, truth-level information with a parameterization of the experimental DCA resolution was used to study the tagging performance for  $R = 0.4$  light, charm and bottom jets with  $p_T > 20$  GeV at the truth level. Separate samples of  $10^6$  PYTHIA events with  $p_T > 20$  GeV light, charm and bottom jets were generated. To quantify the performance for each type of jet, an unambiguous definition of jet flavor at the truth level is needed. Following analogous studies in heavy flavor jet tagging at the LHC [175], jet flavor is defined at the hadron (e.g.  $B$  and  $D$ ), and not parton (e.g.  $b$  and  $c$  quark), level since this better corresponds to the observed experimental signature. Bottom jets are defined as those with a  $p_T > 5$  GeV  $B$  hadron at any point in the PYTHIA ancestry within  $\Delta R < 0.4$  of the jet. Of the remaining jets, those with a  $p_T > 5$  GeV  $D$  hadron at any point in the PYTHIA ancestry within  $\Delta R < 0.4$  of the jet are defined as charm jets. Jets which are not defined as either charm or bottom jets are defined as light jets.

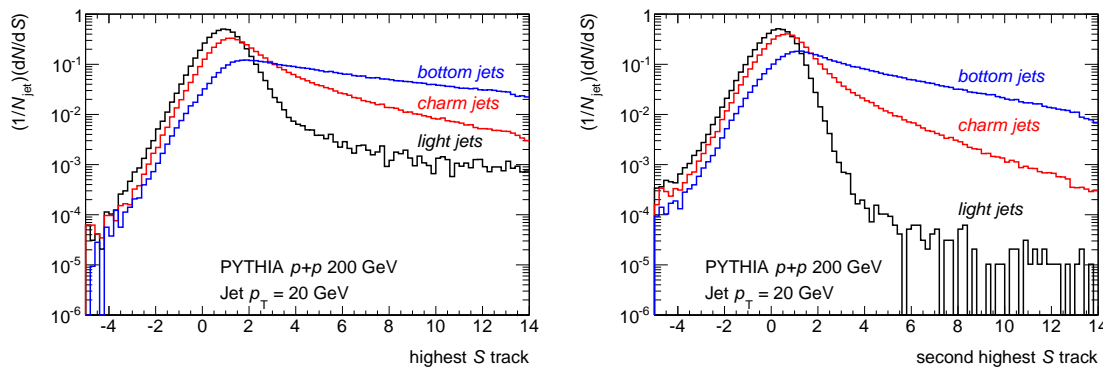


**Figure 4.32:** Distribution of the DCA significance  $S$  for the highest- $S$  track (left panel) and second highest- $S$  track (right panel) in  $p_T = 20$  GeV jets. Each panel shows the per-jet distribution for light (black), charm (red) and bottom (blue) jets.

For each jet, the set of final state charged hadrons with  $p_T > 0.5$  GeV that are within  $\Delta R < 0.4$  of the jet axis are examined. Within this study, the 2-D DCA (e.g. the DCA in the transverse plane) is used. To generate a reconstructed DCA for each charged hadron, its trajectory is projected in a straight line in the transverse plane to determine the truth DCA. Then, the DCA is smeared according to the  $p_T$ -dependent DCA resolution obtained through full GEANT4 studies of the tracking performance, as described in Section 3.6 and displayed in Figure 3.25. The significance  $S$  is calculated by dividing the smeared DCA by the nominal  $p_T$ -dependent resolution  $\sigma_{\text{DCA}}$ , taken from Gaussian fits to the core of the DCA resolutions, shown in Figure 3.26. In this way, the study incorporates a realistic description of the DCA performance in sPHENIX. Figure 4.32 shows the distribution of  $S$  values for the first and second highest  $S$  tracks in jets of the three flavors.

In modern  $b$ -jet tagging approaches, efforts are made to exclude hadrons which originate from strange decays by, for example, removing pairs of tracks which reconstruct to a  $\Lambda^0$  or  $K_s^0$  mass (called  $V^0$ 's), or by rejecting all tracks with a DCA so large that they are dominated by strange decays instead of tracks from  $b$ -jets. In this study, hadrons which originate from a  $V^0$  or with a DCA

larger than 1 mm are rejected. Such an approach will limit but not remove the high- $S$  background in light jets which still enters from, for example, decays of  $\Sigma^\pm$  baryons which produce only a single charged track associated with a neutral hadron and thus cannot be identified through an invariant mass analysis.

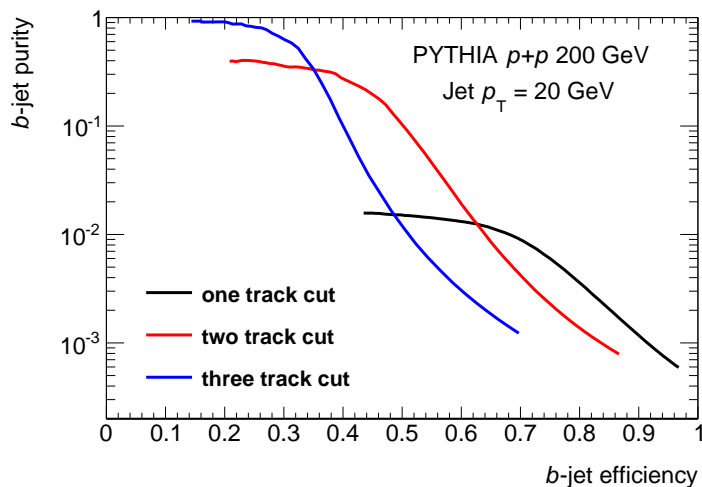


**Figure 4.33:** Performance of  $b$ -jet tagging algorithms for  $p_T = 20$  GeV jets based on requiring at least one (black), two (red) or three (blue) tracks in the jet to have a 2-D DCA significance above some minimum value. Purity vs. efficiency curves are generated by varying the minimum significance DCA

For a given cut (specified by the  $S_{\text{cut}}$  and the number of tracks required to have  $S > S_{\text{cut}}$ ), the efficiency for light, charm and bottom jets is determined. Then, the purity  $P$  of  $b$ -jets is determined following Equation 4.1, with the initial mixture of light, charm and bottom jets  $N_l$ ,  $N_c$  and  $N_b$  at  $p_T = 20$  GeV/ $c$  given by pQCD and FONLL calculations as is shown in Figures 1.49 and 1.40. The performance is quantified by plotting the  $b$ -jet efficiency  $\epsilon_b$  against the  $b$ -jet purity  $P$ , which vary inversely with one another as the details of the cut are changed.

The performance of the Track Counting algorithm in  $p+p$  collisions is summarized in Figure 4.33, showing the behavior of the algorithm requiring one, two or three tracks in the jet to all have  $S > S_{\text{cut}}$  as black, red and blue curves respectively. The figure shows, as a function of the efficiency for  $b$ -jets passing the cut, the purity of  $b$ -jets within the set of all jets that pass the cut. The efficiency vs. purity curves are generated by varying the value of  $S_{\text{cut}}$  between 0 and 5. It is evident that less stringent requirements (fewer tracks, smaller  $S_{\text{cut}}$  requirement) result in a high efficiency but a low purity. On the other hand, stricter requirements (more tracks, each of which has a large  $S > S_{\text{cut}}$ ) result in a low efficiency but a high-purity.

The presence of high-DCA tails in light jets, either from hadrons originating from strange decays or from hadrons originating from the primary vertex but with a badly reconstructed DCA, are the limiting factors in this approach. As can be seen in Figure 4.32, examining only the highest- $S$  track will reach a point of diminishing returns, as even large values of  $S_{\text{cut}}$  will still leave a background of light jets. Thus, the black curve in Figure 4.33 saturates at a given maximum purity. Requiring more tracks results in a higher maximum purity, since it is much rarer for a light jet to have two tracks with a large  $S$ , but adversely affects the tagging efficiency. Two- or three-track algorithms

are able to reach a high purity  $P > 50\%$  while still retaining a reasonable efficiency  $\epsilon_b \approx 40\text{--}50\%$ , which is a promising indication of the possible performance. When the cuts are chosen to give such a high purity, the remaining non- $b$  jet background is composed predominantly of  $c$ -jets.

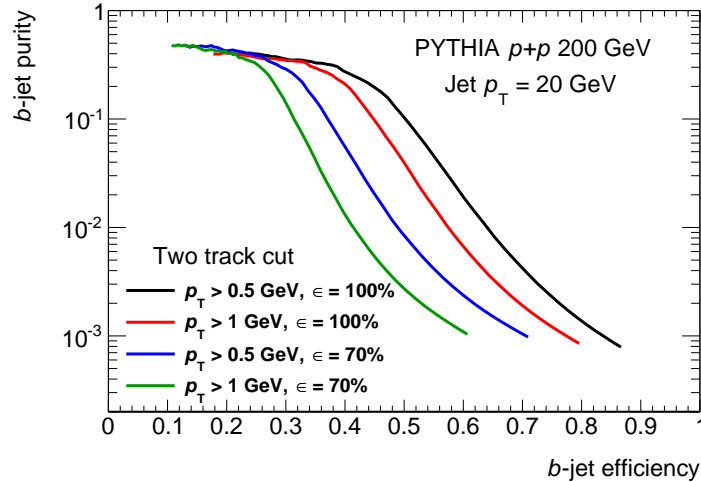


**Figure 4.34:** Performance of  $b$ -jet tagging algorithms for  $p_T = 20$  GeV jets based on requiring at least two tracks in the jet to have a 2-D DCA significance above some minimum value. Curves of different colors show the performance under different assumptions of the tracking performance and minimum track  $p_T$ . Purity vs. efficiency curves are generated by varying the minimum significance DCA

While the first results shown above have been made assuming a perfect tracking efficiency for charged hadrons with  $p_T > 0.5$  GeV, the  $b$ -jet tagging algorithm has also been studied under different assumptions of the tracking performance. Figure 4.34 demonstrates how the two track-based cuts change under two variations. In the first variation the overall tracking efficiency is taken to be 70%, while in the second variation only tracks with  $p_T > 1$  GeV are considered. Both variations are also considered together. Since the tracking design and offline tracking reconstruction parameters are still being optimized for a high-multiplicity environment, these variations are meant to bracket a reasonable range of the possible tracking performance. As expected, the performance systematically degrades with decreasing efficiency. Additionally, restrictions to the track  $p_T$  decrease the multiplicity of tracks which are available to pass the cuts and thus reduce the efficiency as well. This study highlights the necessity of robust tracking capability in sPHENIX to carry out a  $b$ -jet program. In particular, high efficiency in the inner pixel layers, which determine the DCA, is required.

Additional studies have been performed to determine how the performance of the algorithms may be affected by the presence of the underlying event in Au+Au events. The large amount of UE charged particles within the jet cone cannot be experimentally distinguished from those arising from the jet fragmentation and  $B$  hadron decay, and will each have their own reconstructed DCA significance. Therefore, for a given  $b$ -jet tagging cut, the efficiency for all jet flavors will increase, as the addition of extra tracks will give additional opportunities for a jet to have the requisite number of tracks with  $S > S_{\text{cut}}$ .

To quantify the effect on the performance, jets were randomly embedded into HIJING events with

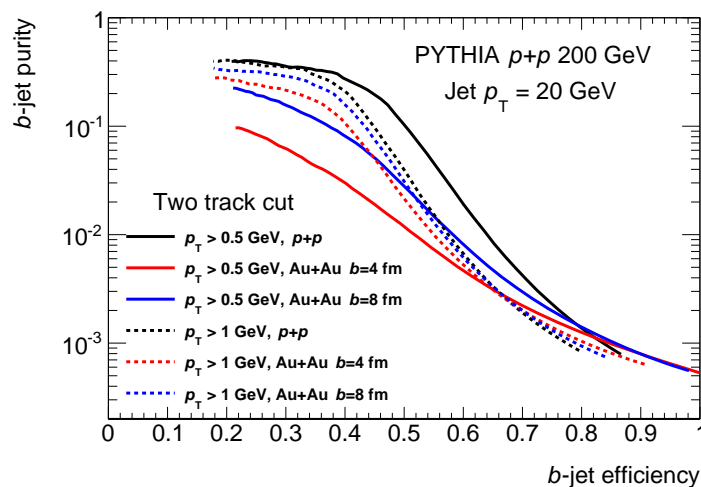


**Figure 4.35:** Performance of  $b$ -jet tagging algorithms for  $p_T = 20$  GeV jets based on requiring at least two tracks in the jet to have a 2-D DCA significance above some minimum value. Curves of different colors show the performance in the presence of different heavy ion backgrounds, while different line styles correspond to different choices of the minimum track  $p_T$ . Purity vs. efficiency curves are generated by varying the minimum significance DCA

$b = 4$  fm and  $b = 8$  fm, and the additional charged particles from the underlying event particles were assumed to originate from the primary vertex but otherwise have the same DCA resolution as determined in GEANT4 simulations in Figure 3.25. At fixed  $b$ -jet tagging efficiency, the  $b$ -jet purity was found to be systematically worse in central HIJING events than in peripheral HIJING events, and worse there than in the PYTHIA only events. In particular, the two-track cut with  $p_T > 0.5$  GeV track was no longer found to give sufficiently good performance, necessitating the need to only examine tracks with  $p_T > 1$  GeV (since the additional number of UE tracks is smaller) or to require three tracks.

Figure 4.35 summarizes the performance for the two-track cuts, showing how the same cuts perform in the  $p+p$  only case and after embedding into  $b = 4$  fm and  $b = 8$  fm HIJING events. Although the performance of the algorithm with  $p_T > 0.5$  GeV tracks is very sensitive to the UE background, we observe that even a mild track  $p_T$  requirement of 1 GeV makes the algorithm much more resilient against the effects of the UE. At the moment, this study focuses on the effects of the UE on the tagging performance, and does not consider the additional effects of the larger jet energy resolution introduced by the presence of UE fluctuations.

The studies detailed here have demonstrated that  $b$ -jet tagging through the identification of associated tracks with a large distance of closest approach with respect to the primary vertex can reach a high  $b$ -jet purity while still maintaining good  $b$ -jet efficiency, and is a plausible approach for  $b$ -jet tagging in sPHENIX. However, they have also demonstrated the need for high-efficiency, precision tracking within sPHENIX to achieve reasonable  $b$ -jet tagging performance. These studies have been performed at the “truth” hadron level using PYTHIA and HIJING events. However, they incorporate a description of the DCA resolution (the main driver of the  $b$ -jet identification and light jet rejection capability) as determined with full GEANT4 simulations of the tracking performance. Future studies will be needed to determine the role of other detector effects, such as the degree

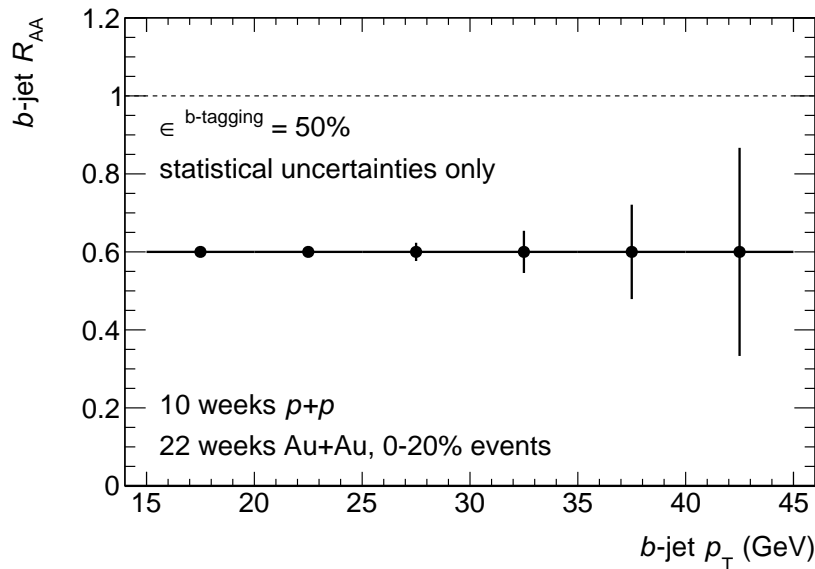


**Figure 4.36:** Projected statistical uncertainties on the  $R_{AA}$  for  $b$ -jets in 0–20% Au+Au events, assuming an overall suppression of  $R_{AA} = 0.6$ , a  $b$ -jet tagging efficiency of 50%,  $\mathcal{L} = 630 \text{ pb}^{-1}$  of  $p+p$  events and  $0.6 \times 10^{12}$  sampled minimum bias Au+Au events.

to which a realistic jet energy scale non-closure and finite jet energy resolution affect the tagging performance for jets at a given reconstructed (rather than truth)  $p_T$ .

Additional studies of  $b$ -jet tagging through the identification of an electron with large momentum transverse to the jet axis ( $p_T^{\text{rel}}$ ), often called the “Soft Lepton Tagging” (SLT) method [176], have resulted in the similar conclusion that a high  $b$ -jet purity is achievable while maintaining good efficiency. (In the case of the SLT method, the overall efficiency is with respect to the fraction of  $b$ -jets which have a semileptonic decay and thus produce an electron.) In this case, the misidentification of light jets as  $b$ -jets is due to the possibility of pions being erroneously identified as electrons. Thus, unlike the Track Counting method, the SLT performance is defined much more by the electron identification than the DCA reconstruction performance in sPHENIX. Having several distinct  $b$ -jet tagging approaches is attractive, because it allows for independent cross-calibration of the algorithms with respect to one another. However studies of the SLT method, while promising, are still at an early stage and are not detailed here. Early studies of  $b$ -jet tagging through the direct reconstruction of the displaced secondary vertex, a popular method within the LHC experiments [177, 178], are also underway. Finally, the performance of the Track Counting algorithm has been benchmarked above using simulations. However, there are important  $b$ -tagging methods which use data-driven approaches to boot-strap the efficiency and purity of the method without the need for detailed MC input. An example of these is the jet probability algorithm [179], which uses the negative DCA-tails of tracks in data as a reference against which to understand the light jet contribution to the set of jets with tracks that have a large positive DCA.

A statistical projection for the  $b$ -jet  $R_{AA}$  in central Au+Au events is shown in Figure 4.36. This projection is constructed through the FONLL-based predictions of the  $b$ -jet rates as a function of  $p_T$  as shown in Figure 1.40, an assumption of the total luminosity received in Au+Au and  $p+p$  data-taking as detailed in Section 3.8, and a nominal combined  $b$ -jet reconstruction and tagging

efficiency of 50%. This projection indicates that with the given  $p_T$  binning, the  $R_{AA}$  will have good statistical power out to 40 GeV, enabling a measurement of inclusive  $b$ -jet suppression over a large kinematic range. Furthermore,  $b$ -tagged jet-hadron correlation analyses (such as those described in Sections 4.5 and 4.6) may offer the opportunity to probe how the internal structure of heavy quark-initiated jets is modified by the medium.

Reconstruction of charm jets with similar methods described above is very challenging. However, with the ability to reconstruct secondary vertices, we can reconstruct  $D$  mesons via their  $\pi + K$  decay channel for example and then associate them with reconstructed jets via the calorimeter. Shown in Figure 4.37 are the simulated reconstructed invariant mass for all charged particle pairs assuming one is a pion and one is a kaon in 0-10% central Au+Au collisions. The histograms are the real  $D$  meson contribution where the daughter product masses are assigned correctly and where they are swapped. The simulation includes HIJING generated uncorrelated and correlated backgrounds. The signal to background is small at low  $p_T$  as expected and increases significantly at higher  $p_T$ . The precision secondary vertex reconstruction provides the important background suppression. Associating these  $D$  mesons with reconstructed jets then allows a measure of the fragmentation functions which is predicting to have large energy loss sensitivity.

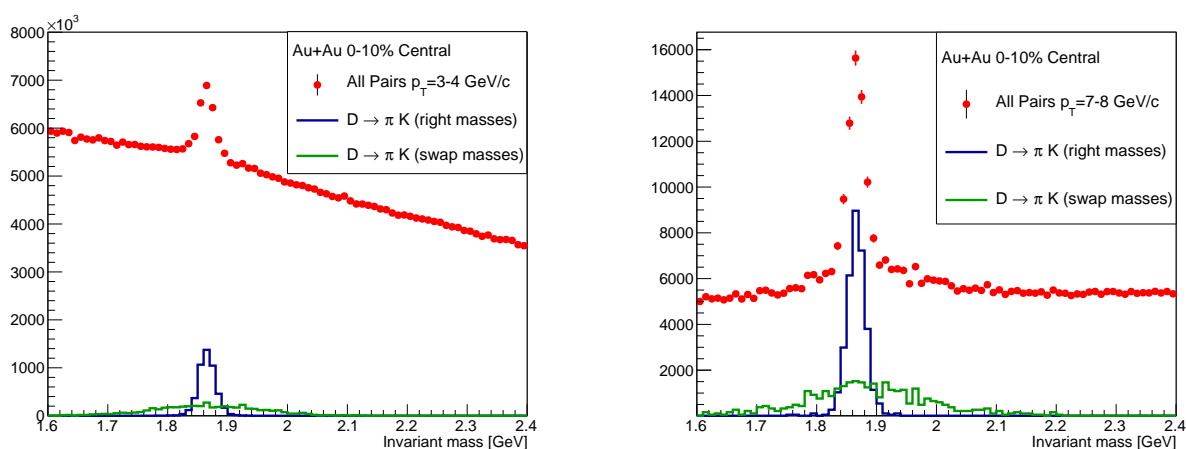


**Figure 4.37:** Shown are the invariant mass distributions of reconstructed charged particle track pairs in  $p_T$  bins of 3-4 GeV/c (left) and 7-8 GeV/c (right). The histograms indicate the contribution from correctly matched  $D$  mesons and cases where the daughter mass assumption is swapped.

## 4.8 Proton-Nucleus Collision Jet Physics

In addition to a rich program of jet studies of hot nuclear matter, sPHENIX will be able to capitalize on its capabilities to study high- $p_T$  processes in “cold” nuclear systems, provided by a high statistics  $p$ +Au 200 GeV run. Measurements of hadron, jet and photon cross-sections in  $p$ +Au collisions are important for a number of reasons. At their most basic level, they provide an overall test of pQCD calculations of hard processes based on the standard collinear factorization and parton distribution function formalism. They are also sensitive to the so-called “cold nuclear matter” effects, which may arise from a number of sources including the modification of the parton densities in the nuclear environment, the initial state energy loss of the hard scattering partons, and so forth. More

generally,  $p$ +Au collisions are a useful laboratory within which to understand the interplay between hard processes and experimental handles on the collision geometry.

While the above motivations address interesting physics questions in and of themselves,  $p$ +Au collisions are also crucial experimental context for the sPHENIX physics program, since they will provide the reference against which to interpret the modifications of hard process rates and jet shapes observed in Au+Au collisions.

Figure 4.38 shows the projected statistical uncertainties for the nuclear modification factor  $R_{pAu}$  in 200 GeV  $p$ +Au collisions corresponding to the first two years of sPHENIX data-taking. The  $R_{pAu}$  projections for unidentified charged hadrons, inclusive fully reconstructed jets, and even  $b$ -tagged jets are shown. (Measurements of direct photons, while not shown in this compilation, would have modestly more statistics than the  $b$ -jets, extending  $\approx 5$ -10 GeV/ $c$  farther in  $p_T$ .)

Recent LHC data on jet and hadron production in  $p$ +Pb collisions at 5.02 TeV has revealed several striking and unexpected results. Figure 4.39 compares the  $R_{pPb}$  for charged particles and jets at mid-rapidity in minimum bias  $p$ +Pb collisions. While the overall jet rate is in line with the geometric expectation [181] (modulo some small effects from the modification of the parton distribution functions), the charged particle  $R_{pPb}$  shows an unexpected rise above the geometric expectation [180, 182]. This anomalous  $R_{pPb}$  presents a strong challenge to nPDF-based pictures of  $p$ +A collisions, and its implications on the  $p_T$ -dependence of the charged hadron  $R_{AA}$  observed in Pb+Pb collisions is still an open question.

sPHENIX is situated in a prime kinematic region to investigate this effect. As shown in Figure 4.38, sPHENIX will have excellent statistics for charged hadrons and jets in a large overlapping  $p_T$  range, allowing for simultaneous measurements of the jet and hadron  $R_{pAu}$ . In particular, sPHENIX will be able to measure the charged particle spectrum in  $p$ +Au in the 20–40 GeV/ $c$  range, where the anomalous  $R_{pPb}$  at the LHC has the strongest  $p_T$  dependence. Furthermore, unlike the LHC experiments, sPHENIX will be able to benefit from  $p$ + $p$  reference data at the same collision energy and center of mass frame as the  $p$ +Au data, resulting in potentially smaller systematic uncertainties.

The LHC data have also revealed a striking pattern of jet modification with respect to the  $p$ +Pb event centrality. Measurements of inclusive jet production at ATLAS [181] and dijet production at CMS [184] have shown an unexpected excess of jets and dijets in apparently peripheral collisions and a suppression in apparently central ones. Furthermore, these effects were found to be systematically larger in the forward (downstream proton) direction, where any biases on the centrality determination (typically characterized with detectors in the downstream Pb direction) from the presence of the hard process are expected to be systematically smaller. The left panels of Figure 4.40 shows a kinematic pattern discovered by ATLAS in the suppression of the central to peripheral ratio  $R_{CP}$  of these jet spectra. In the figure, the  $R_{CP}$  over a wide rapidity range is seen to only depend on the total jet energy  $p$ . An analogous effect had been previously observed at mid-rapidity in a preliminary measurement of jets in  $d$ +Au by PHENIX [183], shown in the right panel of Figure 4.40.

sPHENIX is poised to investigate these effects using full jets over a large kinematic range. Although the projected  $R_{pAu}$  in Figure 4.38 is for minimum bias  $p$ +Au events, the centrality-selected  $R_{pAu}$  will have only modestly larger statistical uncertainties. This will be important for investigating the  $p_T$  dependence of any jet modification, which the LHC results imply systematically grows with the total jet energy. Furthermore, due to the large dijet containment fraction within the

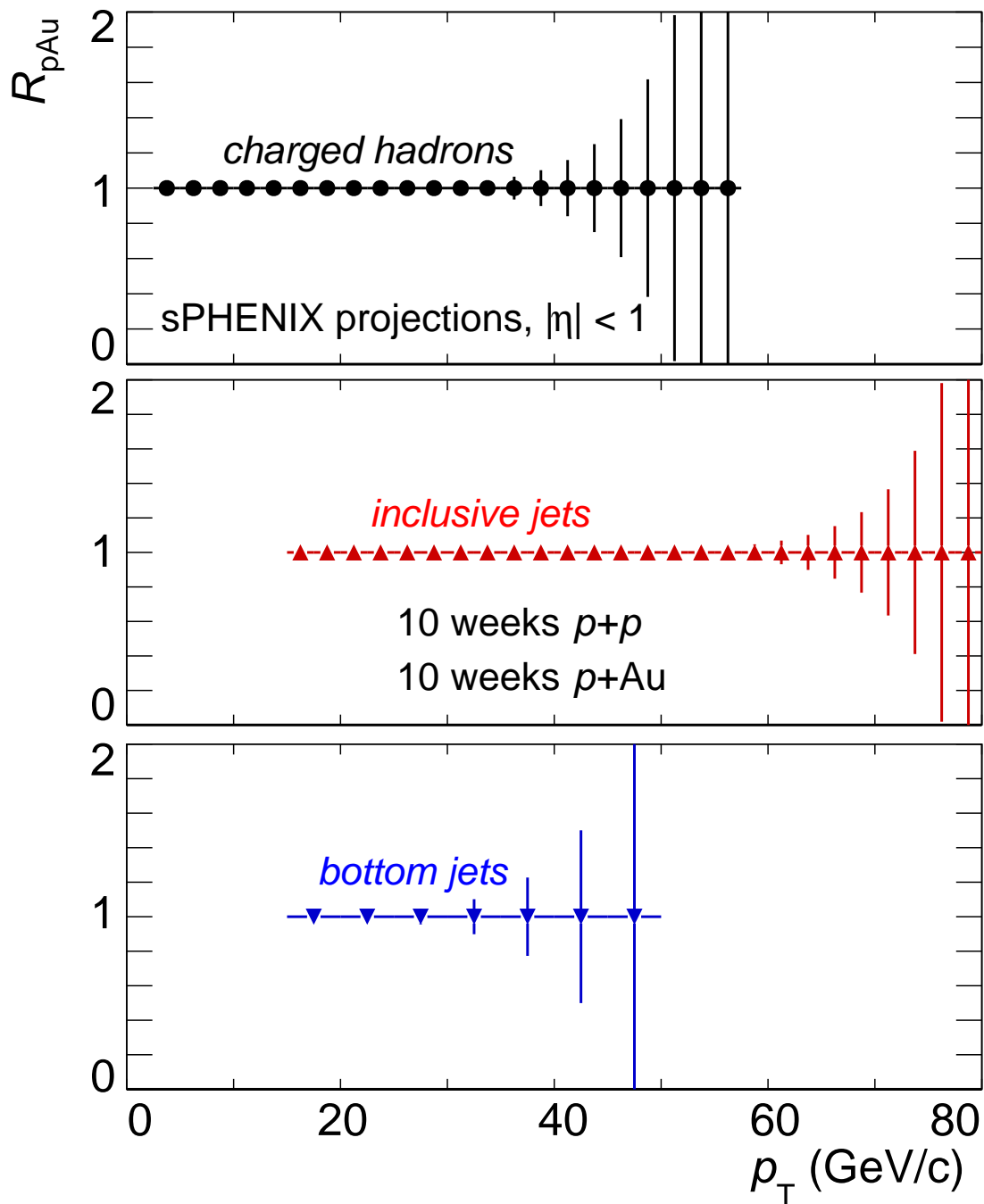


**Figure 4.38:** Projected statistical uncertainties on the  $R_{pAu}$  for charged pions (top plot), inclusive jets (middle plot) and  $b$ -jets (bottom plot) for minimum bias  $p+Au$  events, assuming no overall modification ( $R_{pAu} = 1$ ), a  $b$ -jet tagging efficiency of 50%, corresponding to 10 weeks of minimum bias  $p+Au$  and  $p+p$  running.



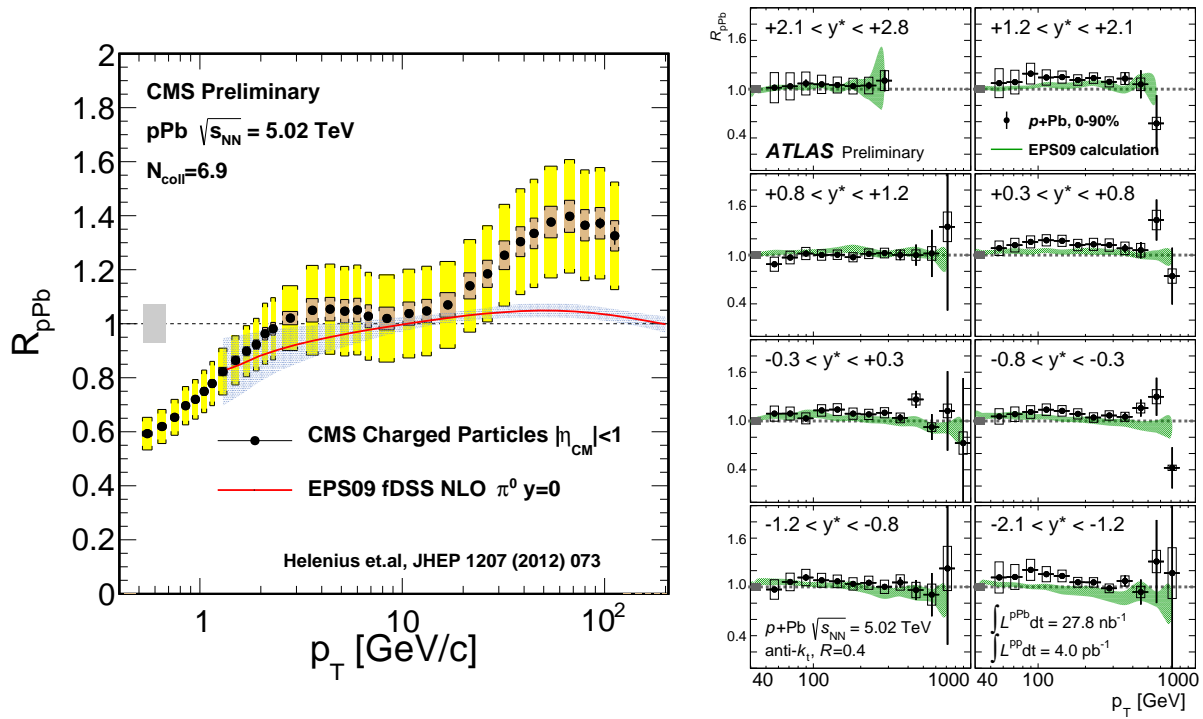


**Figure 4.39:** left:  $R_{pPb}$  for mid-rapidity charged particles as a function of  $p_T$  as measured by CMS [180]. Right:  $R_{pPb}$  for inclusive full jets as a function of jet  $p_T$ , with each panel at a fixed center of mass rapidity  $y^*$ , as measured by ATLAS [181].

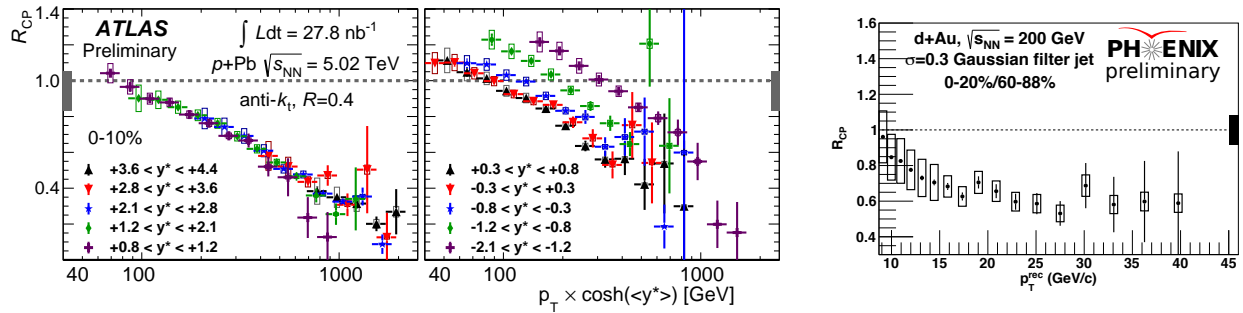


**Figure 4.40:** left and center: Central to peripheral ratio ( $R_{CP}$ ) for inclusive jets shown as a function of the approximate total jet energy  $p = p_T \times \cosh(y^*)$ , showing multiple  $y^*$  selections in the forward (left plot) and mid-rapidity (center plot) regions, as measured by ATLAS [181]. Right:  $R_{CP}$  for inclusive jets at mid-rapidity as a function of the detector-level jet  $p_T$  as measured by PHENIX [183].

sPHENIX acceptance, measurements of dijet production, which have a better connection to the hard scattering kinematics ( $x_p, x_{Au}, Q^2$ ), will also be possible. More generally, the nature of the correlations between hard processes and the soft particle production which gives the centrality signal at forward rapidities in  $p+p$  and  $p+Au$  collisions can be systematically studied with high statistics.

Finally, the  $b$ -jet tagging capabilities being developed at sPHENIX will allow for a measurement of the  $b$ -jet  $R_{pAu}$  (shown in Figure 4.38) as a benchmark against which to interpret the  $b$ -jet  $R_{AA}$ ,

analogous to the recent measurement by CMS [185].

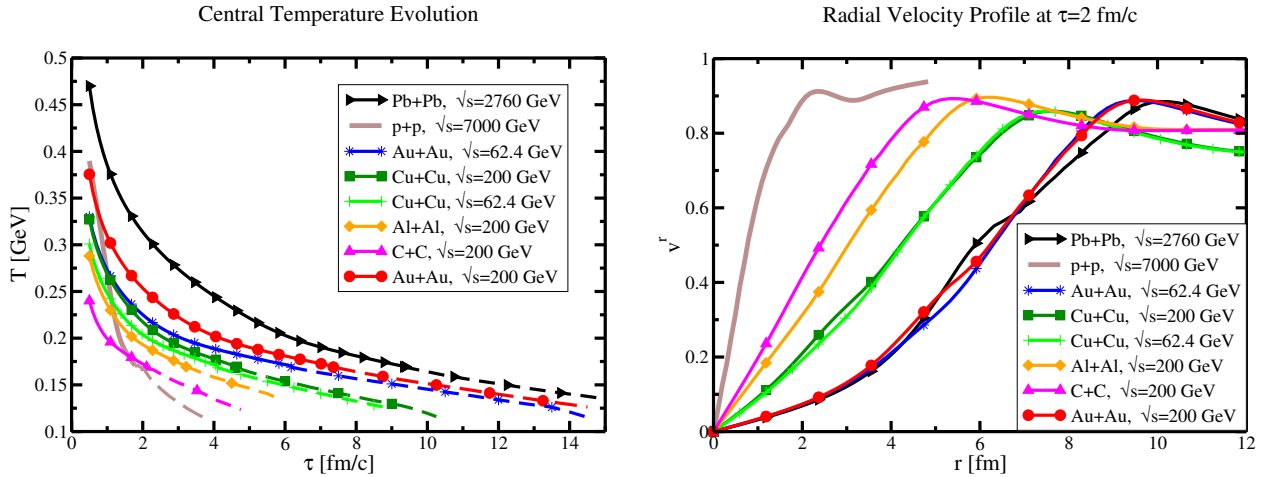


**Figure 4.41:** (left) Temperature profile for the central  $r = 0$  cell as a function of time from full dynamical calculations [69] for various collision species and energies. (right) The same calculation with results for the transverse flow velocity profile at time  $\tau = 2$  fm/c.

## 4.9 Jet physics at lower RHIC energies

If additional running time becomes available and if physics investigations indicate interest in this direction, there is the potential for extending sPHENIX jet measurements to lower energies and with lighter ions at RHIC. Shown in Figure 4.41 are the temperature profile for the central cell (left) and the flow velocity profile at  $\tau = 2$  fm/c for various collision species and energies [69]. The calculations including pre-equilibrium dynamics, viscous hydrodynamics, and hadronic cascade are for the central cell. These results indicate that the lever arm in temperature and medium dynamics that can be extended with lower energy collisions and careful selection of light ion collisions. Measurements of jet observables in light ions at  $\sqrt{s_{NN}} = 200$  GeV with statistics comparable to the Au+Au results previously discussed can be obtained in 10 weeks of physics running, and have significantly lower underlying event backgrounds.

As an example, for lower energy running, in a 20 week running period, one can sample 10 billions Au+Au events at  $\sqrt{s_{NN}} = 100$  GeV. Although the background multiplicity in these events is lower than in corresponding collisions at  $\sqrt{s_{NN}} = 200$  GeV, the true jet spectrum at the lower collision energy is steeper. NLO calculations have been performed and projected for the most central 20% Au+Au collisions at  $\sqrt{s_{NN}} = 100$  GeV. The projected luminosity delivered by the collider is lower than in the 200 GeV case, and one still can obtain a substantial sample of jets reaching out to 35 GeV. We have performed simulations to demonstrate that we can reconstruct jets in this environment.

A procedure identical to that used for evaluating the jet finding performance at the top RHIC energy was followed to evaluate the jet finding performance for Au+Au collisions at  $\sqrt{s_{NN}} = 100$  GeV. A sample of 400 million HIJING events at the lower collision energy was generated and the procedure of Section 4.4.1 was employed. The results are shown in Figure 4.42. The effects of the steeper jet spectrum and of the reduced multiplicity at the lower collision energy largely negate one another, and the true jet signal dominates over the background at transverse energies quite similar to that seen for  $\sqrt{s_{NN}} = 200$  GeV.

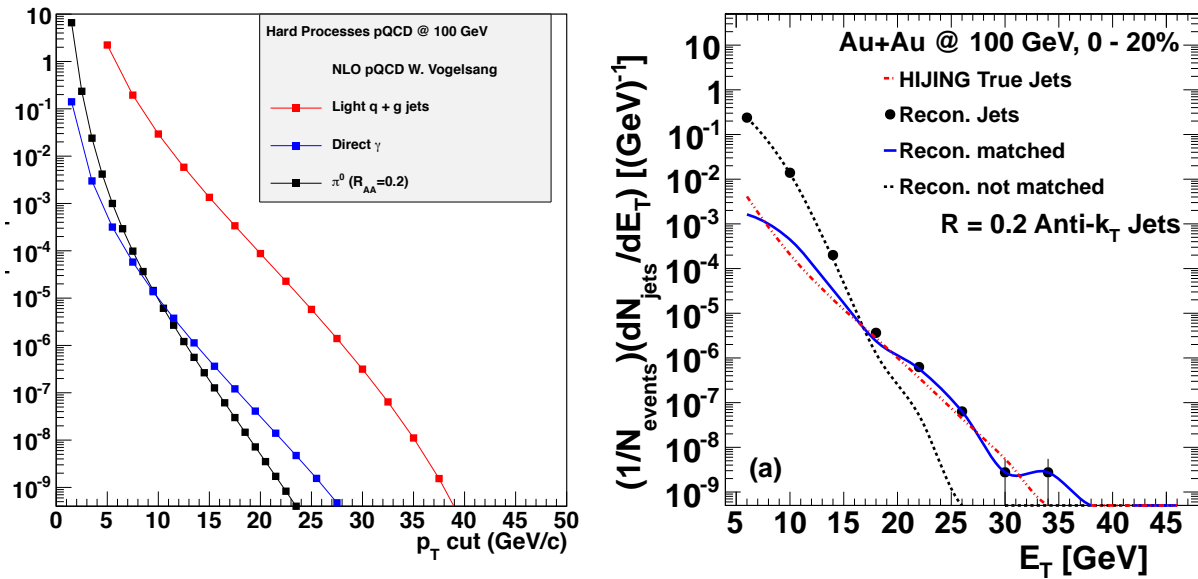


**Figure 4.42:** (left) Jet, photon and  $\pi^0$  rates with  $|\eta| < 1.0$  from NLO pQCD [143]. A nominal 20 week RHIC run corresponds to 1.7 billion central Au+Au events at  $\sqrt{s_{NN}} = 100$  GeV. (right) Results of a fake jet study at  $\sqrt{s_{NN}} = 100$  GeV for the most central 20% of the cross section. The anti- $k_T$  algorithm with  $R = 0.2$  was used to reconstruct jets. True jets dominate over fake jets for  $E_T > 20$  GeV.

## 4.10 Jet Physics Summary

Overall we conclude that a robust jet, dijet,  $\gamma$ -jet, fragmentation function program with high statistics is achievable with the sPHENIX detector upgrade. These observables indicate excellent discriminating ability between scenarios with different medium coupling strengths and jet quenching mechanisms.

Figure 4.43 shows the projected statistical uncertainties for the  $R_{AA}$  of single inclusive hard probes that will be possible within the first two years of sPHENIX operations. This figure demonstrates that the large acceptance and physics capabilities of the sPHENIX detector, along with the projected performance of RHIC, would allow measurements of jet quenching over a very large kinematic kinematic. sPHENIX would have enough statistics to measure the overall suppression of inclusive jets out to  $\approx 70$ – $80$  GeV/c, single hadrons and photons out to  $\approx 50$  GeV/c, and  $b$ -tagged jets to 40 GeV/c in 0–20% Au+Au events.

The statistical uncertainties in mid-central and mid-peripheral centrality selections (such as 30–50% collisions) would only be modestly larger, allowing for precise differential measurements such as the  $R_{AA}$  as a function of the angle with respect to the reaction plane. Finally, it should be noted that the statistical uncertainty in the  $R_{AA}$  is limited by the  $p+p$ , not the Au+Au, luminosity. Thus, any increase in the nominal  $p+p$  dataset of 10 weeks would only serve to improve the  $p_T$  reach of all  $R_{AA}$  measurements, and measurements which rely only on the Au+Au data would potentially have an even larger kinematic reach.

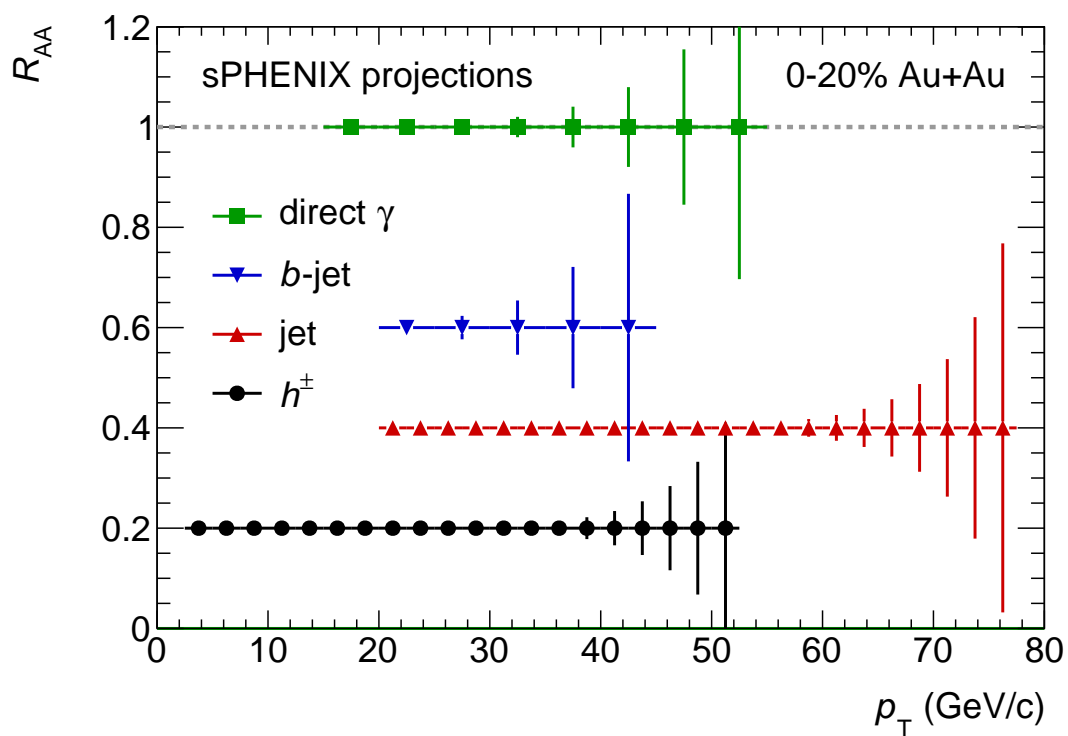


**Figure 4.43:** Projected statistical uncertainties on the  $R_{AA}$  for inclusive photons (green points, assuming  $R_{AA} = 1$ ),  $b$ -jets (blue points, assuming  $R_{AA} = 0.6$ ), inclusive jets (red points, assuming  $R_{AA} = 0.4$ ) and charged hadrons (black points, assuming  $R_{AA} = 0.2$ ). These projections are made with a  $b$ -jet tagging efficiency of 50%, 10 weeks of  $p+p$  and 22 weeks of Au+Au data taking.

## 4.11 Beauty Quarkonia Performance

Measurements of beauty quarkonia, the Upsilon states, provide critical information by probing the quark-gluon plasma at different length scales determined by the size of the state. Here we detail the sPHENIX measurement capabilities to access this physics with precision.

We first report on the expected yield and line shape of the  $Y(1S)$ ,  $Y(2S)$  and  $Y(3S)$  signal from decays to dielectrons. The results were obtained with single simulated  $Y$  events in a GEANT4 simulation with the reference sPHENIX silicon tracking configuration inside the BaBar solenoid.

The baseline  $p+p$  cross section for  $Y(1S + 2S + 3S)$  of  $B_{ee}d\sigma/dy|_{y=0} = 108 \pm 38(stat) \pm 15(sys) \pm 11(global)$  pb is taken from a PHENIX central arm measurement [127]. The rapidity dependence was taken from PYTHIA. The relative yields of the three  $Y$  states were taken from CDF measurements at 1.8 TeV [186]. Estimates of the  $Y$  yields for the three states in sPHENIX are shown in Table 4.1 for a 10 week  $p+p$  run, a 22 week Au+Au run and a 10 week  $p+Au$  run. These projections assume binary scaling and no suppression of any of the  $Y$  states in Au+Au or  $p+Au$  collisions. The yields are calculated using the electron identification efficiencies shown in the table, which are dependent on the event multiplicity. The electron pair identification efficiency of 49% in central Au+Au collisions corresponds to a hadron rejection of 90 in the EMCal and HCal, based on a full GEANT4 study of central Hijing events.

The Au+Au data sample consists of 100 B minimum bias events. The  $p+p$  and  $p+Au$  data for Upsilon states will be obtained using a trigger. The trigger efficiency at the needed rejection is estimated to be  $>90\%$  for  $p+p$  events. A trigger efficiency of 90% is assumed for central  $p+Au$  events.

**Table 4.1:** The yields of the three  $Y$  states obtained in 10 weeks of  $p+p$ , 22 weeks of Au+Au and 10 weeks of  $p+Au$  RHIC running. All yields include the effect of electron identification efficiency. The numbers for Au+Au and  $p+Au$  are calculated assuming no suppression of any of the  $Y$  state yields.

Species	$\int L dt ( Z  < 10\text{cm})$	Events	$\langle N_{coll} \rangle$	eID eff.	Y(1S)	Y(2S)	Y(3S)
$p+p$	$175 \text{ pb}^{-1}$	7350 B	1	0.9	8770	2205	1155
Au+Au (MB)		100 B	240.4	0.57	16240	4080	2140
Au+Au (0–10%)		10 B	962	0.49	5625	1415	740
$p+Au$ (MB)	$960 \text{ nb}^{-1}$	1680 B	4.3	0.84	6560	1650	860
$p+Au$ (0–20%)		336 B	8.2	0.8	2360	592	311

A critical question is whether the proposed tracking system is capable of adequately resolving the  $Y(1S)$ ,  $Y(2S)$  and  $Y(3S)$  states from each other. To answer this we have performed GEANT4 simulations with the reference tracking configuration, containing seven silicon tracking layers covering  $2\pi$  in azimuth and two units in pseudorapidity, with specifications given in Table 3.2.

The reconstructed mass spectrum for dielectron decays (signal only) is shown in Figure 4.44,

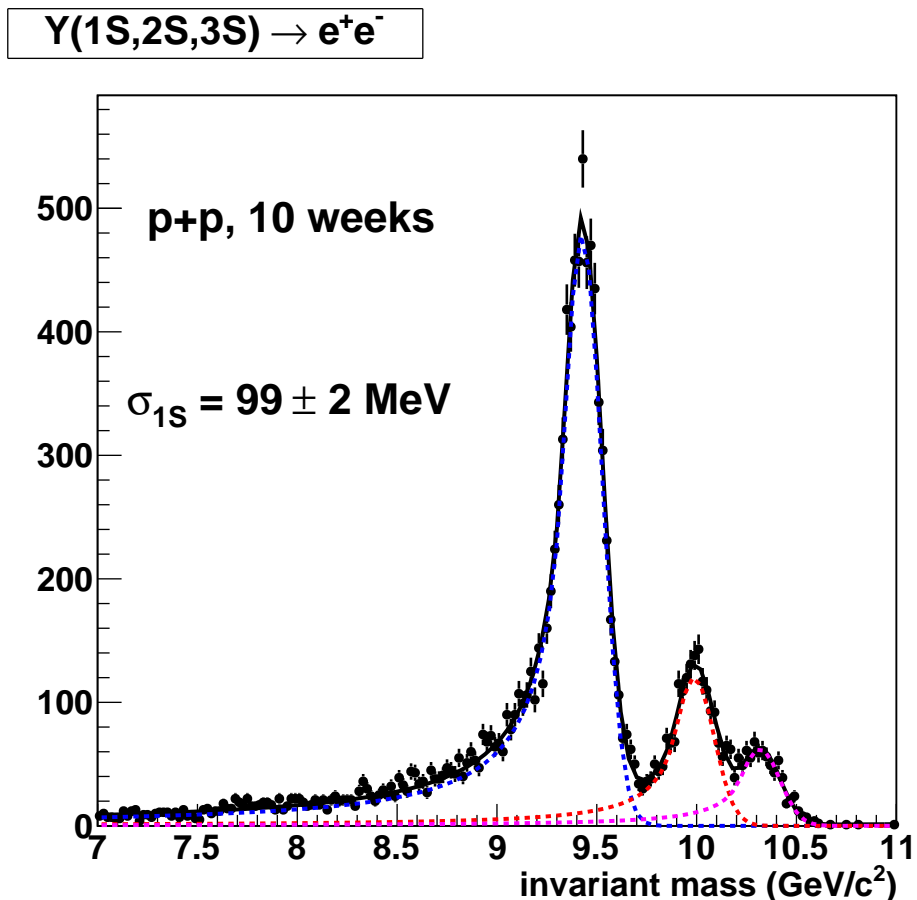


**Figure 4.44:** The mass spectrum (signal only) from reconstructed electron decay tracks for the three Upsilon states combined. The yield corresponds to that for 10 weeks of  $p+p$  running, including the effects of electron identification efficiency and trigger efficiency.

including a fit using a Crystal Ball function that accounts for the radiative tail contribution at low invariant mass [187]. This example spectrum contains the number of Upsilon states expected in 10 weeks of  $p+p$  running. There are significant low mass tails on the Upsilon mass peaks due to radiative energy loss in the material of the silicon tracker. However at the mass resolution of 99 MeV obtained with the reference design, and the relatively low thickness of the tracker (about 10% of a radiation length), the peaks are well defined and easily obtained from the Crystal Ball fit.

In  $p+p$ ,  $p+Au$  and  $Au+Au$ , the background under the Upsilon peaks contains an irreducible physics background due to dileptons from correlated charm, correlated bottom and Drell-Yan. There is also combinatorial background from misidentified charged pions. The latter can be estimated and removed by like sign or mixed event subtraction. To study the physics background, correlated charm and bottom di-electron invariant mass distributions predicted by PYTHIA were normalized to the PHENIX measured charm and bottom cross-sections in  $Au+Au$  collisions. The PYTHIA Drell-Yan di-electron invariant mass distribution was normalized to a theoretical prediction by W. Vogelsang (private communication).

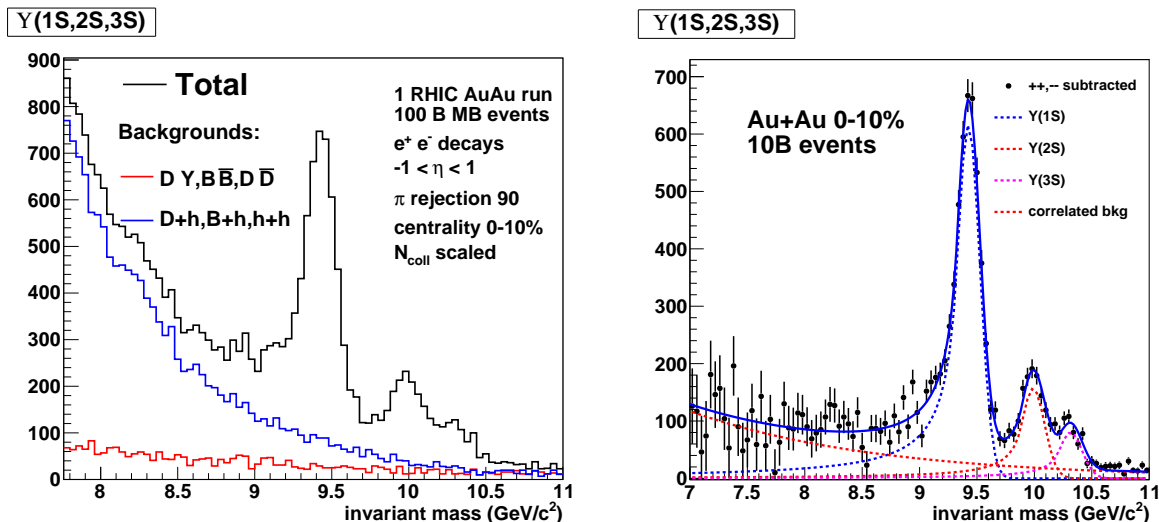


**Figure 4.45:** (Left) The signal plus background in the Upsilon mass region for ten billion 0–10% central Au+Au events, assuming a pion rejection factor of 90, with the signal reduced by a pair identification efficiency of 49%. The combined backgrounds due to correlated bottom, correlated charm, and Drell-Yan are shown as the red curve. The combined backgrounds due to fake electrons combining with themselves, bottom, and charm are shown as the blue line. (Right) The expected invariant mass distribution for ten billion 0–10% central Au+Au events, after subtraction of combinatorial background using the like-sign method. The remaining background from correlated bottom, charm and Drell-Yan is not removed by like sign subtraction. It must be estimated and subtracted.

The combinatorial background was studied by generating events with fake electrons due to misidentified pions, using input pion distributions taken from PHENIX measured  $\pi^0$  spectra in Au+Au collisions. A  $p_T$ -independent rejection factor was applied to the  $\pi^{+/-}$  spectra to imitate fake electron spectra. For the 0–10% most central Au+Au collisions a rejection factor of 90 is assumed at a single electron track efficiency of 70% (giving a pair efficiency of 49%). The pair efficiency is increased to 90% as Au+Au collisions become more peripheral. The combinatorial background due to misidentified pions is assumed here to be zero in  $p+p$  collisions, with an electron matching efficiency of greater than 90%. The rejections in central Au+Au collisions are derived from GEANT4 studies of the electromagnetic calorimeter response to electrons and charged pions. The efficiencies are obtained by embedding electrons in HIJING events. The rejection and efficiency are still being optimized for the detector configuration relevant for electron identification.

All combinations of fake electrons from misidentified pions were made with each other, and with high  $p_T$  electrons from physics sources. The combinatorial background is found to be dominated by pairs of misidentified pions, with only 30% or so coming from combinations of misidentified pions with electrons. The results are summarized in Figure 4.45 (left), which shows the signal + background in the Y mass region for the ten billion 0–10% most central events, along with our estimates of the total correlated physics background and the total uncorrelated combinatoric backgrounds. In Figure 4.45 (right) we show the di-electron invariant mass distribution for ten billion 0–10% central Au+Au events after the combinatorial background has been removed by subtracting all like-sign pairs.



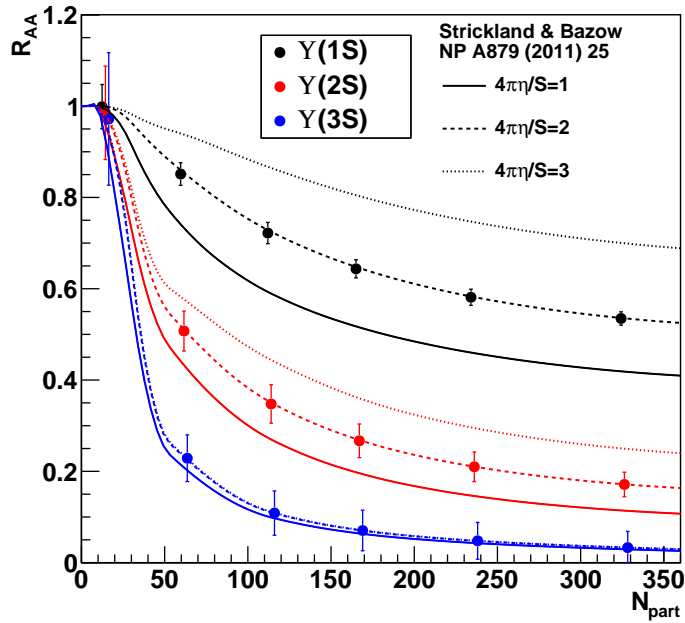


**Figure 4.46:** Estimate of the statistical precision of a measurement of the Y states in Au+Au collisions using sPHENIX, assuming that the measured  $R_{AA}$  is equal to the results of a recent theory calculation [188]. The yields assume 100 billion recorded Au+Au events.

From Figure 4.45 (left) we estimate that without Y suppression the S/B ratios are Y(1S): 1.6, Y(2S): 0.9, and Y(3S): 0.8 for central Au+Au collisions. Using our estimates of the signal and S/B ratio at each centrality as the unsuppressed baseline, we show in Figure 4.46 the expected statistical precision of the measured  $R_{AA}$  for 100 billion recorded Au+Au events assuming that the suppression for each state is equal to that from a theory calculation [188]. For each state, at each value of  $N_{part}$ , both the Y yield and the S/B ratio were reduced together by the predicted suppression level.

The  $p_T$  dependence of the Y modification in nuclear collisions places strong constraints on models, so we present here some estimates of the statistical precision we expect from measurements with sPHENIX. Figure 4.47 shows the expected yields as a function of  $p_T$  for 10 weeks of  $p+p$  running — the baseline for the  $R_{AA}$  measurement. The expected statistical precision of the measured Au+Au  $R_{AA}$  versus  $p_T$  is illustrated in Figure 4.48. These estimates are made assuming that the signal to background ratio is independent of  $p_T$ . Estimates are shown assuming no suppression of the Y states (left panel) and assuming the suppression predicted in [188] (right panel).

The expected statistical precision for Y measurements with sPHENIX in a 10 week  $p+Au$  run is illustrated in Figure 4.49. The suppression values used in the plot are set to match the double ratios of  $Y(2S)/Y(1S)$  and  $Y(3S)/Y(1S)$  measured by CMS at 5.02 TeV collision energy in  $p+Pb$  and  $p+p$  collisions. The Y(1S) is taken to be unsuppressed except for the modified feed down from the excited states, and the suppression of the Y(2S) and Y(3S) states is arbitrarily taken to be linear with centrality. The signal to background ratios in  $p+Au$  collisions are taken to be the same as

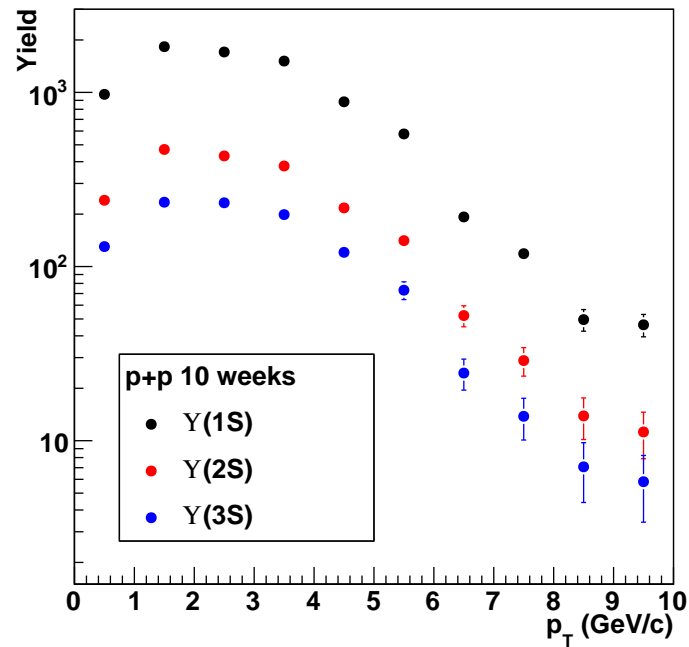


**Figure 4.47:** Estimate of the yields expected for the three  $Y$  states as a function of  $p_T$  from a 10 week  $p+p$  run.

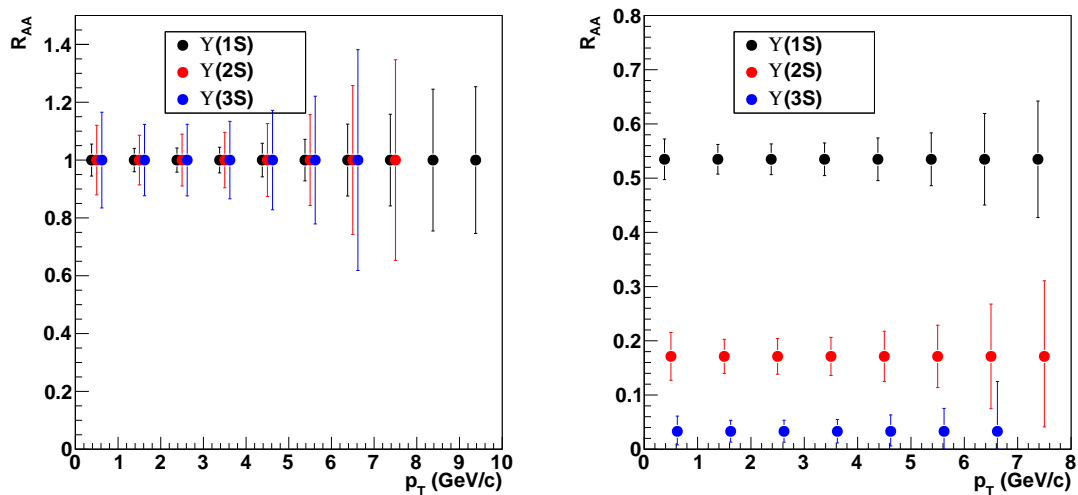


**Figure 4.48:** Estimate of the statistical precision of a measurement of  $R_{AA}$  versus  $p_T$  for the  $Y$  states using sPHENIX, for the most central 0–10% of events. The left panel shows the result if there is no suppression, the right panel shows the result assuming that the measured  $R_{AA}$  is equal to the theory results in [188]. The yields assume 100 billion recorded Au+Au events.

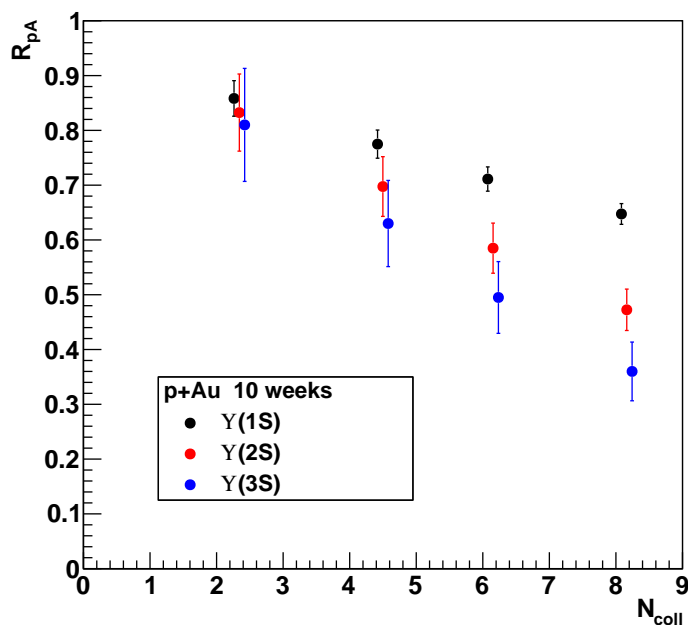


**Figure 4.49:** Estimate of the statistical precision of a measurement of  $R_{p\text{Au}}$  for the Y states using sPHENIX, in four centrality bins. The suppression is taken to be linear with centrality and the centrality integrated suppression for each state is set to match the double ratios of  $Y(2S)/Y(1S)$  and  $Y(3S)/Y(1S)$  measured by CMS at 5.02 TeV collision energy in  $p+\text{Pb}$  and  $p+p$  collisions. The yields are for 10 weeks of  $p+\text{Au}$  running.

those in peripheral Au+Au collisions.

We conclude from these results that the proposed upgrade to the sPHENIX detector would provide an excellent Y measurement, and would have the required mass resolution and S/B to separate the Y(1S) state from the Y(2S) and Y(3S) states. Further, we expect that by fitting a line shape — which could be determined very well from the Y(1S) peak — we could extract the Y(2S) and Y(3S) yields separately with precision.

The expected higher statistics from the LHC experimental measurements of Upsilon over the next decade underscore the need for measurements at RHIC with sufficient statistics to differentiate cold and hot nuclear matters effects. In particular the almost order of magnitude larger acceptance for sPHENIX compared with the STAR MTD enables the precision required in  $p+p$ ,  $p+\text{Au}$  and Au+Au to test models for the onset of suppression, where CMS already observes differential suppression of the three states.



## Appendix A

# Forward Hadronic Calorimeter and Barrel Preshower Options

The sPHENIX detector reference design presented in this proposal consists primarily of a superconducting solenoid surrounded by calorimetry and tracking covering  $|\eta| < 1.1$ . This foundation presents intriguing possibilities for physics opportunities which would be enabled by instrumentation beyond the base detector. In particular, exciting physics in polarized  $p+p$  and  $p+Au$  collisions enabled by a forward detector has been documented in Ref. [2], and is referred to as fsPHENIX. We believe these opportunities are very interesting, and at the same time, we have segregated their description from the main part of the proposal to convey clearly their relationship to the base sPHENIX detector. We present two such additional detector systems and the physics they would provide here in this Appendix.

The first is a Forward Hadronic Calorimeter that would extend the jet coverage significantly with particular physics emphasis in  $p+p$  and  $p+Au$  collisions. The initial design explored here is with this Forward Calorimeter acting as the endcap of the BaBar solenoid. This could be an initial configuration with later moving it back as part of the integrated fsPHENIX design, again detailed in Ref. [2]. This simple configuration captures the essential physics enabled by increased acceptance in  $A+A$  collisions, and could be considered a first step towards the fsPHENIX design if the calorimeter were moved back and extended to accommodate the fsPHENIX forward arm. Such a calorimeter system would deliver physics in itself and also represents a step towards the broader fsPHENIX program.

The second is a barrel preshower detector in front of the Electromagnetic Calorimeter, that would improve the signal to background for direct photon measurements particularly in the range  $p_T \approx 10\text{--}20$  GeV/c.

### A.1 Forward Hadronic Calorimeter

There is a great deal of enthusiasm in the Collaboration for the physics enabled by instrumentation at forward rapidities. For the cases of  $p+p$  and  $p+A$ , the Collaboration has produced a white paper detailing the many physics opportunities of forward measurements [2].

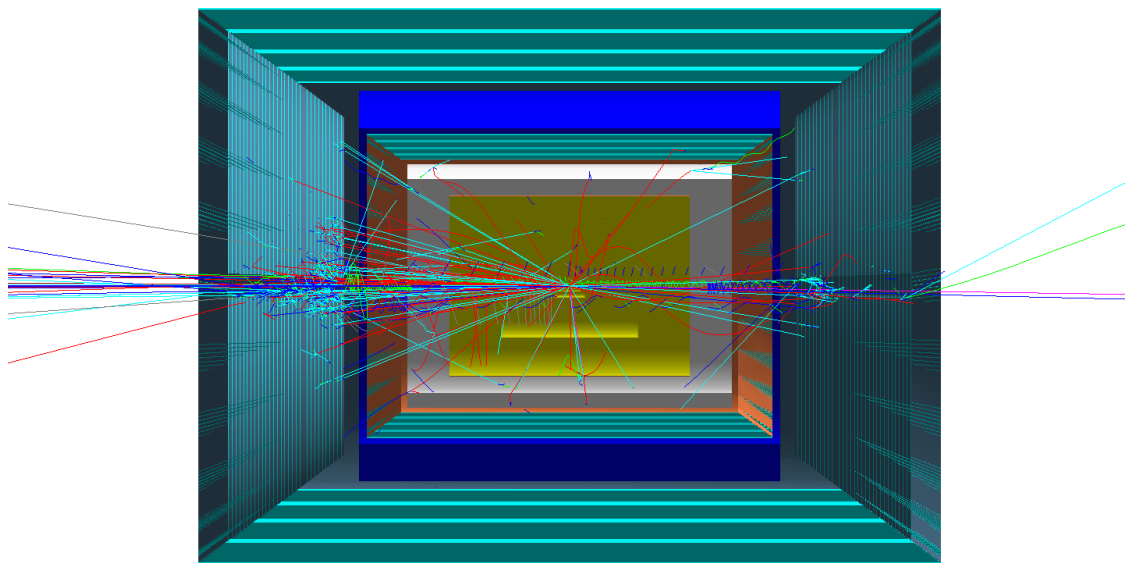


**Figure A.1:** Event display for a central HIJING  $p+A$  collision at  $\sqrt{s} = 200$  GeV. This detector concept adds calorimetrically instrumented endcaps to the sPHENIX barrel tracking and calorimetry.

For  $A+A$  collisions, forward calorimeter (fHCAL) coverage would augment the base sPHENIX program in at least two key ways: one, it provides event characterization (centrality, event plane) away from observables measured at mid-rapidity; and, two, an fHCAL effectively extends the acceptance of the sPHENIX barrel, enabling jet and dijet measurements over wider rapidity range and potentially up to  $\eta = 4$ .

Extending the acceptance of hadronic calorimetry to forward rapidity amplifies the already substantial complementarity of the RHIC and LHC heavy-ion programs, with forward RHIC and mid-rapidity LHC measurements enabling access to similar Bjorken  $x$  values. A global analysis of experimental data at the LHC and RHIC including the forward suppression region is crucial for a precision study and understanding of the  $p+A$  physics.

There are various possibilities for instrumenting the forward acceptance, with one option being to transform the steel flux-returning endcaps of the base sPHENIX design into active steel and scintillator calorimeters. The fHCAL then works as an active flux return yoke of the solenoidal magnet of the sPHENIX barrel.

Figure A.1 shows an event for a central HIJING  $p+A$  collision at  $\sqrt{s} = 200$  GeV and  $b = 4$  fm. There is no gap between the barrel hadron calorimeter and the forward hadron calorimeter (fHCAL) at  $\eta = 1.1$ . The fHCALs are shown located on both ends of sPHENIX in order to study what a very large  $\eta$  acceptance can provide for sPHENIX, and to enable simulations of the back-scattered secondary particles from flux return yoke.

For the current study of the detector performance, the fHCAL is assumed to have the geometry of a truncated cone, and to be located at  $z = 2$  m. The projective tower segmentation in polar and azimuthal angles is defined to be roughly  $10 \text{ cm} \times 10 \text{ cm}$  per tower. The shower size defines the tower size, which naturally leads to large  $\Delta\eta \times \Delta\phi$  tower size. The outermost ring of towers has a

segmentation that matches the azimuthal segmentation of the central barrel. Each tower consists of 30 layers of iron and scintillator (= 4:1) and is one meter deep. The sampling fraction is estimated to be 4.3%.

The jet reconstruction resolution of the fHCAL has been studied using full GEANT4 simulations for both  $p+p$  collisions and central  $p+Au$  collisions. in Figure A.2. The acceptance was divided in three regions:  $0.7 < \eta < 1.3$  where the central and forward calorimeter come together,  $1.3 < \eta < 2.3$  where each forward calorimeter blocks cover  $d\phi$  of 0.1–0.2 rad, and  $2.3 < \eta < 2.9$  where each forward calorimeter blocks cover  $d\phi$  of 0.2–0.4 rad.

In the first stage, full PYTHIA events were generated which contain at least one forward-going single jet. The energy and direction for the truth jet was calculated with FASTJET anti- $k_T$  algorithm [159] with  $R = 0.4$  and  $0.6$  using the PYTHIA generated particles. Then the full event was simulated in the GEANT4 setup. The tower energy was reconstructed from the energy deposition in the active components in all four calorimeter systems (forward hadron calorimeter, central EM calorimeter and two layers of hadron calorimeters). All calorimeter towers were analyzed using FASTJET anti- $k_T$  algorithm to again form the GEANT4 simulated jets. By comparing the truth and GEANT4 jets, the resolution for energy and angle for the jets were shown as the open markers in Figure A.2. The energy resolution in the forward direction roughly matches that in the central direction (Figure 4.3). For jets of  $E_{jet} > 20$  GeV, the direction determination is better than 60 mrad for  $\eta < 2.3$ , and better than 0.12 rad for  $2.3 < \eta < 2.9$ . This resolution presents a minor effect in kinematic and azimuthal asymmetry smearing for jets measurements in  $p+p$ . In addition, no obvious energy leakage was observed up to jet energy of 50 GeV.

In the second stage, the PYTHIA particles were embedded in central HIJING  $p+A$  collisions with impact parameter  $b$  varying between 0 and 4 fm. The embedded event was simulated through the full GEANT4 setup again and formed jets in the  $p+A$  collisions. These jets were also comparing to the truth jet based on the original PYTHIA particles, and the resolutions are shown in closed circle markers as in Figure A.2. As expected, the anti- $k_T$   $R = 0.4$  jets show less deterioration in performance when compared with the anti- $k_T$   $R = 0.6$  jets, and the effect from  $p+A$  background is stronger for the more forward directions (e.g.,  $2.3 < \eta < 2.9$ ). However, the change of jet performance with  $p+A$  background is less than 20%.

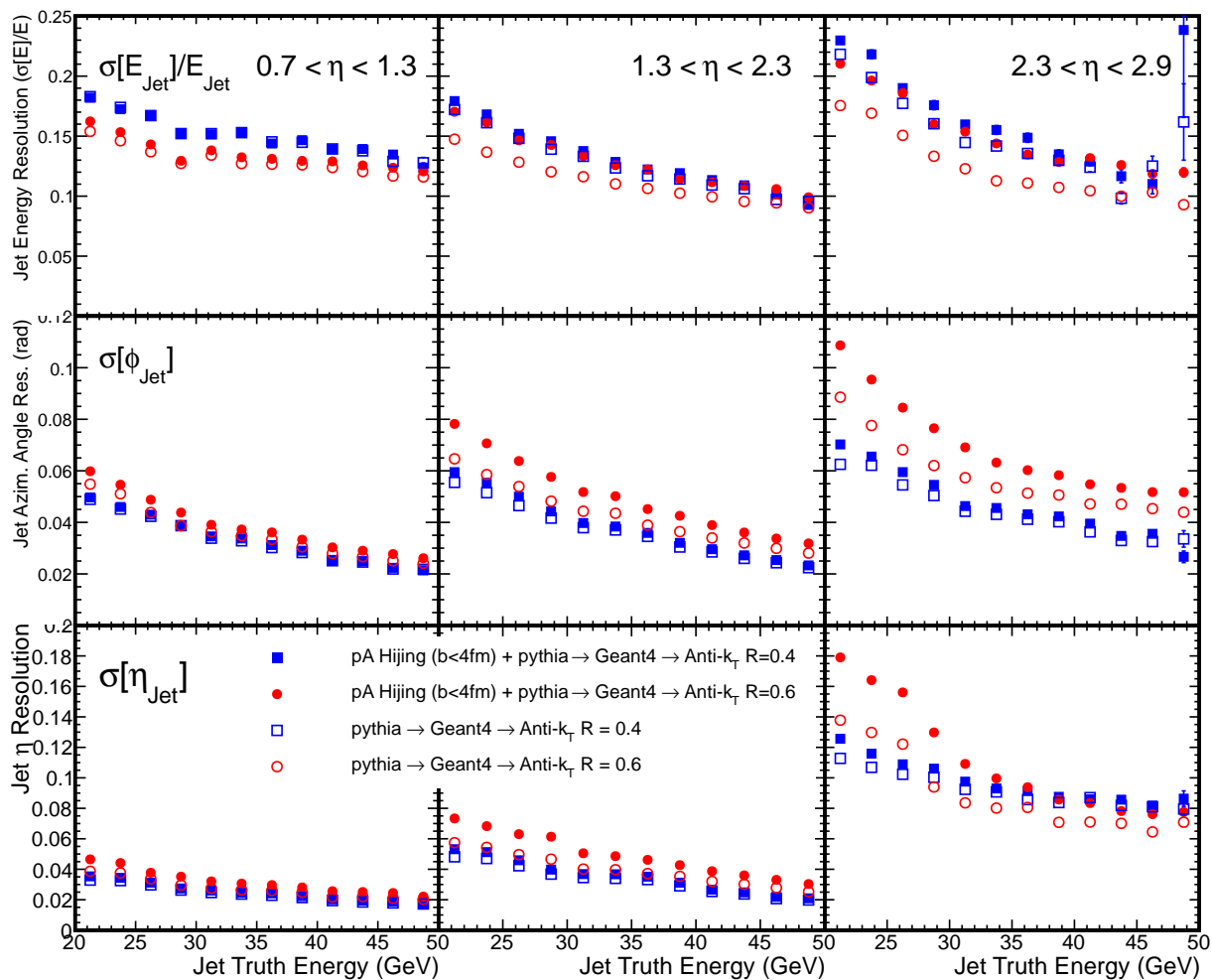


**Figure A.2:** The GEANT4 simulated jet resolution of single jets for energy (top row),  $\phi$  (middle row) and  $\eta$  (bottom row) in  $p+p$  (open markers) and  $p+A$  (closed markers) collisions reconstructed with the FASTJET anti- $k_T$  algorithm with  $R = 0.4$  (blue) and  $R = 0.6$  (red).



## A.2 Preshower

The measurement of direct photons in  $p+p$ ,  $p+Au$ , and  $Au+Au$  collisions represents a golden channel for measuring the energy loss of the opposing quark and the medium response – see Section 1.7 for details. For  $p_T$  greater than 20 GeV/ $c$ , the direct photon signal to background is significantly greater than one in central  $Au+Au$  events and isolation cuts can be utilized effectively in  $p+p$  and  $p+Au$  collisions as well. There is a proposal to include a preshower detector in front of the barrel electromagnetic calorimeter (EMCal) to enhance the direct photon signal to background in order to increase the kinematic range and give a larger statistical sample, particularly for  $p_T \approx 10\text{-}20$  GeV/ $c$ . In addition, this would extend the neutral pion measurements to significantly higher  $p_T$  than the EMCal alone.

The preshower concept is to provide discrimination between single photons and close-by pairs of photons, primarily from  $\pi^0$  decays. The proposed preshower detector is to be placed right in front of the electromagnetic calorimeter, at  $\sim 88$  cm in radius from the beam line. The total area is  $\sim 12$  m<sup>2</sup> if covering the entire sPHENIX acceptance of  $|\eta| < 1.1$ . The current plan is to cover  $\sim 25\%$  of the acceptance to lower the construction cost while maintaining the physics capabilities. The design consists of a tungsten converter,  $\sim 2$  radiation lengths thick, followed by a single-layer silicon pad detector. We have implemented this geometry in the sPHENIX GEANT4 simulations with two pad sizes of 5 mm  $\times$  5 mm and 10 mm  $\times$  10 mm. We are currently working to optimize the pad size in terms of achieving a good  $\pi^0$  identification over a wide transverse momentum range, and keeping the number of readout channels at a reasonable level, 30–120 k. These pad sizes result in occupancies of  $\sim 3\%$  or less in central  $Au+Au$  collisions at 200 GeV as determined from full HIJING events run through GEANT4. A common readout scheme to the sPHENIX silicon tracking layers using the SVX4 chip is one option being explored.

A cluster algorithm applied to the EMCal, combined with a cluster shape metric, indicates good separation of single photon from two photon showers up to 8-10 GeV, after which the discrimination degrades quickly. Shown in the left panel of Figure A.3 is the efficiency for selecting direct photons and two-photons from  $\pi^0$  with EMCal selection only, EMCal selection with a Preshower with 10 $\times$ 10 pads, and then for 5 $\times$ 5 pads. Note that Preshower and EMCal cuts are set to reject two-photon showers, thus enhancing the signal to background for direct photons. One can see that the EMCal alone works quite well at 5 GeV, and already by 10 GeV provides limited discrimination. The right panel of Figure A.3 shows the enhancement in the signal to background (S/B) with the different selections. Currently a factor of five improvement in S/B is achieved and we believe with an optimized pad configuration can be increased. We note that the EMCal resolution has a negligible change in resolution with the preshower included in the GEANT4 simulation.

The potential for extending the sPHENIX capabilities in this way has attracted significant international interest, including from Japanese and Korean institutions. Our goal is to have this upgrade installed and available for physics on day-one. Funding through proposals to US-Japan and JSPS are being pursued toward the goal.

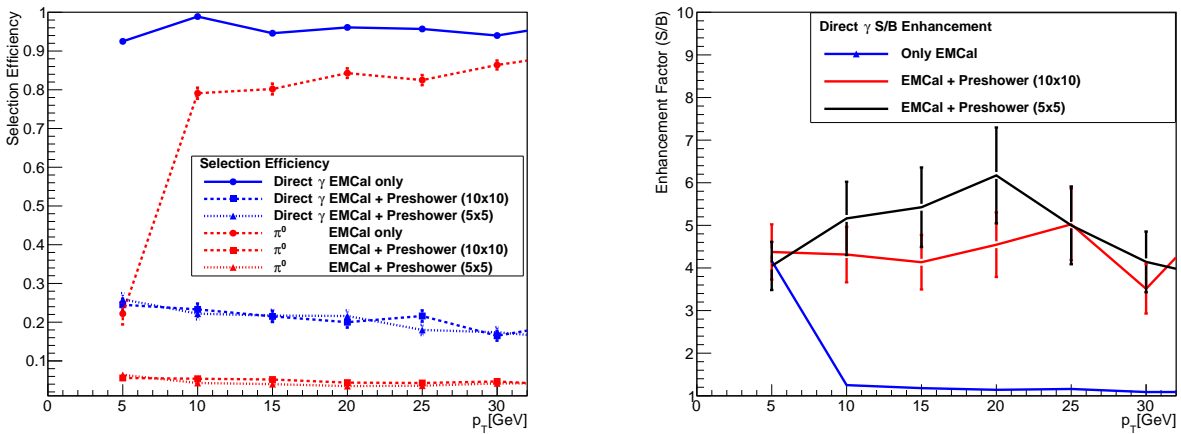


**Figure A.3:** (Left) Efficiency for direct photons and two-pairs from neutral pion decay as a function of  $p_T$  for different EMCal and Preshower cuts. (Right) The corresponding enhancement in the direct photon S/B as a function of  $p_T$ . Note that no isolation cuts are applied.

## Appendix B

# Evolution to an EIC Detector

The Nuclear Physics QCD community long term plan centers on the realization of an Electron Ion Collider (EIC). Brookhaven National Laboratory is working towards a specific realization of an EIC with a potential turn-on date of 2025 with an electron beam energy up to 21.2 GeV, hadron beam energies up to 255 GeV for protons and 100 GeV/nucleon for gold ions, and design luminosities of  $10^{33} \text{ cm}^{-2}\text{s}^{-1}$  for 15.0 GeV on 255 GeV  $e+p$  collisions. The EIC detector proposed here, built on the foundation of sPHENIX, will have excellent performance for a broad range of exciting EIC physics measurements, providing powerful investigations not currently available that will dramatically advance our understanding of how quantum chromodynamics binds the proton and forms nuclear matter.

From the beginning, it was realized that the sPHENIX detector design, with its large bore superconducting solenoid, midrapidity calorimetry, open geometry, coupled with the existing investment in infrastructure in the PHENIX interaction region, provides an excellent foundation for an EIC detector. With this in mind, EIC design considerations for the sPHENIX proposal have been incorporated from the start [189].

A full engineering rendering of the proposed detector — showing how it builds upon sPHENIX — is shown in Figure B.1. In addition to fully utilizing the sPHENIX superconducting solenoid and barrel calorimetry, new detectors are added in the barrel and electron-going and hadron-going directions. In the electron-going direction a crystal calorimeter is added for electron identification and precision resolution. A compact time projection chamber, augmented by additional forward and backward angle GEM detectors, provides full tracking coverage. In the hadron-going direction, behind the tracking is electromagnetic and hadronic calorimetry. Critical particle identification capabilities are incorporated via a barrel DIRC, and in the hadron-going direction, a gas RICH and an aerogel RICH.

The physics case for an EIC is documented in depth in the EIC White Paper [190]. An EIC will enable major scientific advances in at least three main areas: 1) Detailed imaging of the spin and momentum structure of the nucleon; 2) Investigation of the onset of gluon saturation in heavy nuclei; and 3) Study of hadronization in cold nuclear matter. In this document we review each area with a focus on the connection to detector acceptance and performance requirements. We consider each subsystem in sufficient detail to be able to map out the performance using both parametrized and full GEANT4 simulations. We find a broad suite of observables where this EIC

detector realization has excellent capabilities.

The EIC detector built around the BaBar magnet and sPHENIX calorimetry capably addresses most all of the physics enabled at this EIC machine. We believe we have struck a strong balance between capabilities and costs for this proposed detector, but there remain clear targets for augmenting those capabilities—for instance, by adding a silicon vertex detector to enable measurements of open charm observables (e.g.,  $F_2^c$ ). In addition, there is a possibility to upgrade eRHIC to even higher energy electron beams at a future date, and we believe EIC detector built around the BaBar magnet and sPHENIX calorimetry provides an excellent base upon which an upgraded detector capable of exploiting the physics potential of those collisions could be built. There is also the potential, if one can realize appropriate instrumentation in the hadron-going direction while  $p+p$  and  $p+A$  collisions are still available in RHIC, to pursue a rich program of forward physics measurements.

The PHENIX collaboration itself has outstanding detector expertise and technical support as a base for the construction of an EIC detector. Nonetheless, we view EIC detector built around the BaBar magnet and sPHENIX calorimetry being by constructed and operated by a fundamentally new collaboration that would require and welcome the addition of new institutions bringing with them additional detector expertise, physics insights, and scientific leadership.

The PHENIX collaboration was asked to produce a document detailing the capabilities of an EIC detector utilizing electron beams of 5-10 GeV. That document, as submitted in October 2013, is included as the remainder of this Appendix. We note that now higher initial electron beam energies are envisioned and the detector concept is readily being adapted to take full advantage of this additional physics potential.

This Appendix is organized as follows. Section B.1 illustrates the wide spectrum of EIC physics that can be addressed. Section B.4 describes the detector requirements that follow from that physics and which drive this EIC detector design. Section B.5 details the EIC detector concept and shows its performance for key measurements.

## B.1 Physics at an Electron-Ion Collider

The 2007 Nuclear Physics Long Range Plan [191] states that the Electron-Ion Collider (EIC) embodies “the vision for reaching the next QCD frontier.” In this Chapter we review the primary physics goals as detailed in the EIC White Paper [190] and the broad physics program that can be carried out with the ePHENIX detector.

### B.1.1 Fundamental questions addressed by the EIC

The EIC is designed to address several important question that are described in detail in the recent EIC White Paper [190]. Quoting from the White Paper, these questions are reproduced here:

- **How are the sea quarks and gluons, and their spins, distributed in space and momentum inside the nucleon?** How are these quark and gluon distributions correlated with overall nucleon properties, such as spin direction? What is the role of the orbital motion of sea quarks and gluons in building the nucleon spin?

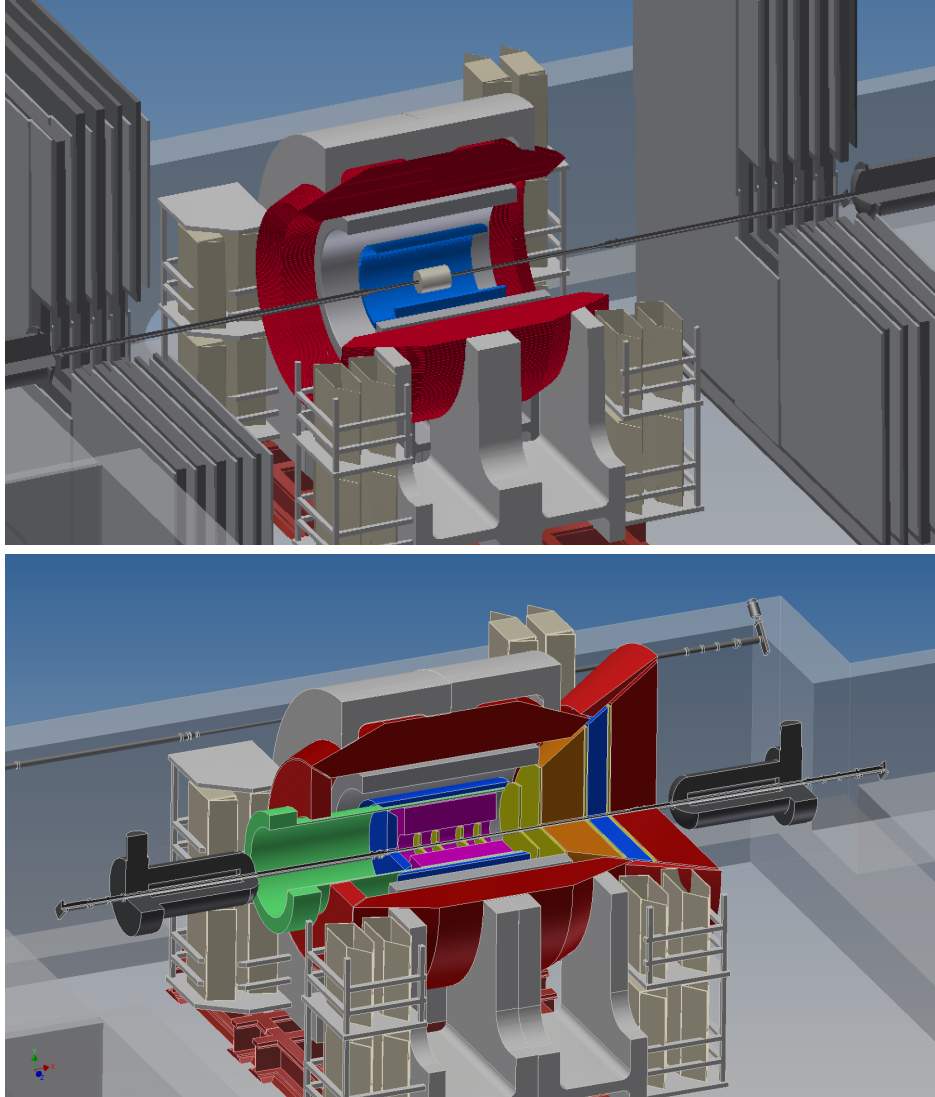


**Figure B.1:** The evolution of the sPHENIX detector, with its focus on jets and hard probes in heavy-ion collisions, into ePHENIX, with additional capabilities supporting its focus on  $e+p$  and  $e+A$  collisions. (top) The sPHENIX detector in the existing PHENIX experimental hall. (bottom) The EIC detector, in the same hall, showing the reuse of the superconducting solenoid and the electromagnetic and hadronic calorimeter system. The eRHIC focusing quadrupoles, each located 4.5 m from the interaction point, and the height of the beam pipe above the concrete floor, set the dominant physical constraints on the allowable dimensions of the EIC detector.

- **Where does the saturation of gluon densities set in?** Is there a simple boundary that separates this region from that of more dilute quark-gluon matter? If so, how do the distributions of quarks and gluons change as one crosses the boundary? Does this saturation produce matter of universal properties in the nucleon and all nuclei viewed at nearly the speed of light?
- **How does the nuclear environment affect the distribution of quarks and gluons and their interactions in nuclei?** How does the transverse spatial distribution of gluons compare to that in the nucleon? How does nuclear matter respond to a fast moving color charge passing through it? What drives the time scale for color neutralization and eventual hadronization?

The White Paper describes in detail the “golden” measurements in inclusive Deep Inelastic Scattering (DIS), Semi-Inclusive DIS (SIDIS), and exclusive scattering at a future  $e+p$  and  $e+A$  collider which will address the above questions employing a perfect detector.

## B.2 eRHIC: realizing the Electron-Ion Collider

The accelerator requirements for an EIC that can answer the questions listed above are spelled out in the EIC White Paper [190]. Two possible designs are presented based on current facilities: (1) the eRHIC design, which adds a Energy Recovery LINAC to the existing RHIC complex at Brookhaven National Laboratory (BNL) which can accelerate polarized protons up to 250 GeV and ions such as gold up to 100 GeV/nucleon, and (2) the EElectron-Ion Collider (ELIC) design, which uses the 12 GeV Upgrade of CEBAF at Jefferson Laboratory with a new electron and ion collider complex.

As per the charge from the Brookhaven National Laboratory Associate Lab Director, we consider the following eRHIC design parameters:

- A polarized electron beam with energy up to 10 GeV and polarization of 70%,
- A polarized proton beam with energy up to 250 GeV and polarization of 70%,
- An ion beam which can run a range of nuclei from deuteron to gold and uranium with energy up to 100 GeV/nucleon for gold,
- Luminosity with a 10 GeV electron beam of  $10^{33} \text{ cm}^{-2}\text{s}^{-1}$  for  $e+p$  with 250 GeV proton beam energy, and  $6 \times 10^{32} \text{ cm}^{-2}\text{s}^{-1}$  for  $e+A$  with 100 GeV ion beams.

## B.3 Physics Deliverables

The three fundamental and compelling questions in QCD to be addressed by the EIC discussed in Section B.1.1 can be broken down in to five golden measurements suggested in the EIC White Paper [190].

The first three relate to using the proton as a laboratory for fundamental QCD studies.

- **The longitudinal spin of the proton:** With the good resolution calorimetry and tracking in ePHENIX, Inclusive DIS measurements in polarized  $e+p$  collisions will decisively determine the gluon and quark spin contributions to the proton spin. Further, planned particle identification capabilities will allow ePHENIX to pin down the spin contributions from the different quark flavors.
- **Transverse motion of quarks and gluons in the proton:** With the excellent particle identification capabilities of ePHENIX and the high luminosity of eRHIC, unparalleled SIDIS measurements will be possible, and enable us to explore and understand how the intrinsic motion of partons in the nucleon is correlated with the nucleon or parton spin.
- **Tomographic imaging of the proton:** The large acceptance of ePHENIX for tracking and calorimetry, far forward proton and neutron detector capabilities, the high luminosity of eRHIC and the phase space accessible in a collider geometry enables ePHENIX to significantly extend the kinematic coverage of exclusive measurements such as Deeply Virtual Compton Scattering (DVCS). With these, detailed images of how (sea) quarks and gluons are distributed in the proton will become possible for the first time.

The following two relate to extending these techniques to the heaviest stable nuclei.

- **Hadronization and its modification in nuclear matter:** With ePHENIX PID and the versatility of eRHIC to collide many different ions, measurements of identified hadrons in  $e+p$  and  $e+A$  will allow precise study of how quarks hadronize in vacuum and in nuclear matter.
- **QCD matter at extreme gluon density:** ePHENIX will enable measurements of diffractive and total DIS cross-sections in  $e+A$  and  $e+p$ . Since the diffractive cross section is viewed as a double gluon exchange process, the comparison of diffraction to total cross section in  $e+A$  and  $e+p$  is a very sensitive indicator of the gluon saturation region. ePHENIX would be an ideal detector to explore and study this with high precision.

Below we discuss each of these points in more detail and with specific details on the ePHENIX capabilities.

### The proton as a laboratory for QCD

Deep Inelastic Scattering experiments over the last several decades have greatly enhanced our understanding of the proton substructure. Measurements with colliding beams at H1 and ZEUS at HERA have mapped out the momentum distributions of quarks and gluons, and shown that the gluons carry roughly half of the proton momentum. Fixed target experiments, with polarized nucleons and leptons at SLAC, CERN, DESY and JLab have revealed new surprises about proton structure, finding that only a small fraction of the proton spin comes from the quark spin and that there is significant correlation between the intrinsic motion of quarks and the nucleon spin. Measurements at both fixed target and colliders have started to image the proton through exclusive measurements.

eRHIC will greatly enhance the kinematic coverage for DIS with polarized beams, as shown in Figure B.2. With the capabilities of ePHENIX, we will significantly extend our understanding of

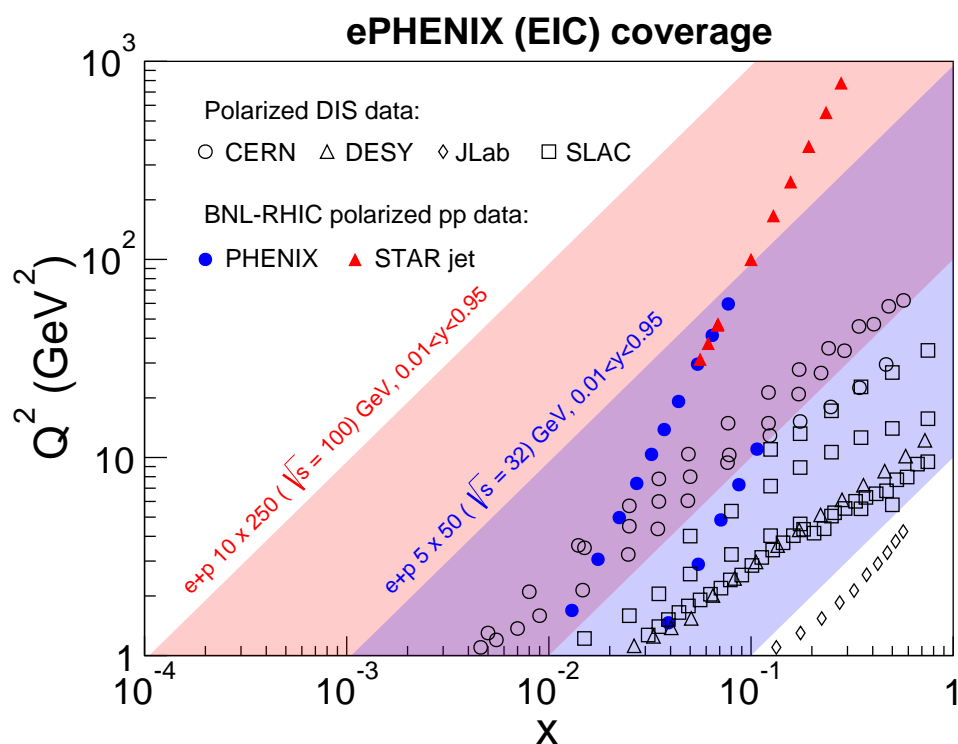


**Figure B.2:** Kinematic coverage of ePHENIX for two beam energy configurations,  $10 \times 250$  GeV and  $5 \times 50$  GeV, which show the range of eRHIC capabilities. Also shown are data from current polarized fixed target DIS experiments and RHIC  $p+p$  collisions.

the proton. The gluon and flavor dependent sea quark spin contributions to the proton spin will be determined, as will the possible orbital angular momentum contributions. The spatial and momentum distributions of (sea) quarks and gluons can be mapped, giving a multidimensional description of the proton.

**Longitudinal spin of the proton** The puzzle of the proton spin, to which the quark spin only contributes roughly a third, has spurred two decades of study. Measurements from fixed target polarized DIS have determined the quark contribution, but are less sensitive to the gluon due to the small kinematic coverage. Current RHIC measurements indicate that the gluon spin contribution may be comparable or even larger than the quark spin contribution, but due to the limited coverage at low longitudinal momentum fraction,  $x$ , large uncertainty remains, as is shown in Figure B.3 (yellow band).

Determining the gluon longitudinal spin contribution is a primary goal of the EIC and of ePHENIX, and will be possible due to the large reach in  $x$  and four-momentum transfer squared,  $Q^2$ . Figure B.3 shows the expected impact from ePHENIX measurements of inclusive DIS on the uncertainty of the gluon helicity distribution as a function of  $x$ .

With the ePHENIX particle identification (PID) detectors, measurements of pions and kaons will greatly improve on the determination of the sea quark longitudinal spin distribution as well,



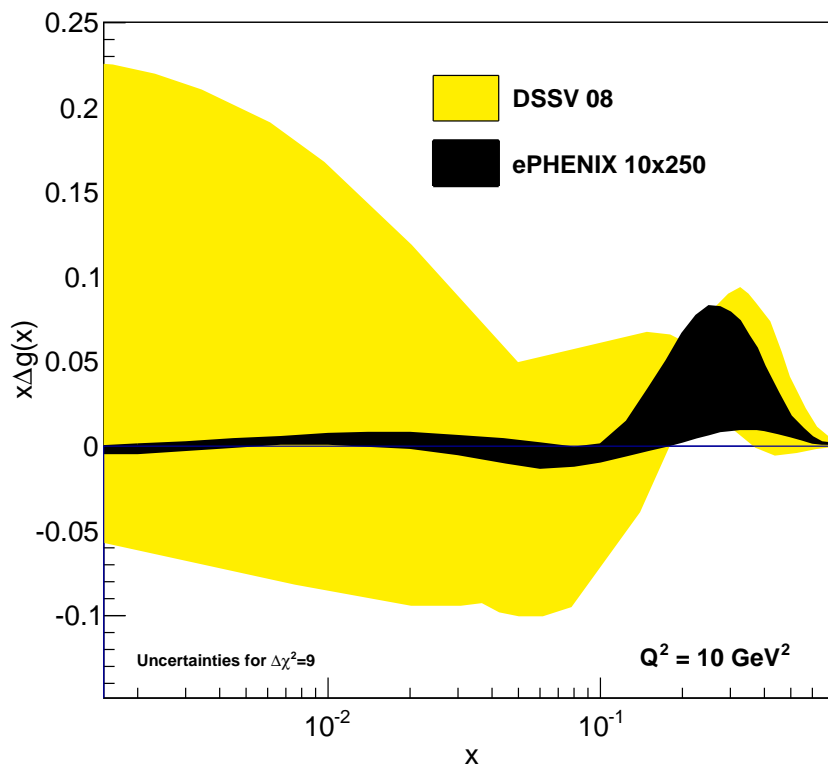


**Figure B.3:** The projected reduction in the uncertainty (black) on the gluon longitudinal spin distribution based on simulated PYTHIA events corresponding to an integrated luminosity of  $10 \text{ fb}^{-1}$  at the  $10 \text{ GeV} \times 250 \text{ GeV}$  beam energy configuration. A 1% systematic uncertainty in beam and target polarization is applied. The yellow area shows the uncertainty from current data based on the analysis in Ref. [192].

including that of the strange quark,  $\Delta s$ , which has been of particular interest in the last few decades, because of the contradictory results obtained from different data. Current global analyses use hyperon beta decay to constrain  $\Delta s$ , which indicates a negative value for the full integral over  $x$ . Fixed target SIDIS measurements of kaon asymmetries, which directly probe  $\Delta s$ , though at low values of  $Q^2$  and in a limited  $x$  range, find a positive contribution for  $x > 0.01$ . eRHIC provides data over a wide  $x$  and  $Q^2$  range. Further, ePHENIX will provide excellent particle ID capability to identify kaons and allow direct measurements of strangeness spin contribution to the nucleon down to  $\sim 2 \times 10^{-4}$ .

**Transverse motion of quarks and gluons in the proton** Large transverse spin asymmetries measured in fixed target SIDIS in the past decade have spurred significant theoretical work. These asymmetries relate to the transversity distribution, the correlation between the transverse spin of the proton and a transversely polarized quark in it, and Transverse Momentum Distributions (TMDs), such as the Sivers or Boer-Mulders distributions, which describe correlations between either the proton or quark spin and the quark intrinsic motion, specifically the transverse momentum of the quark.

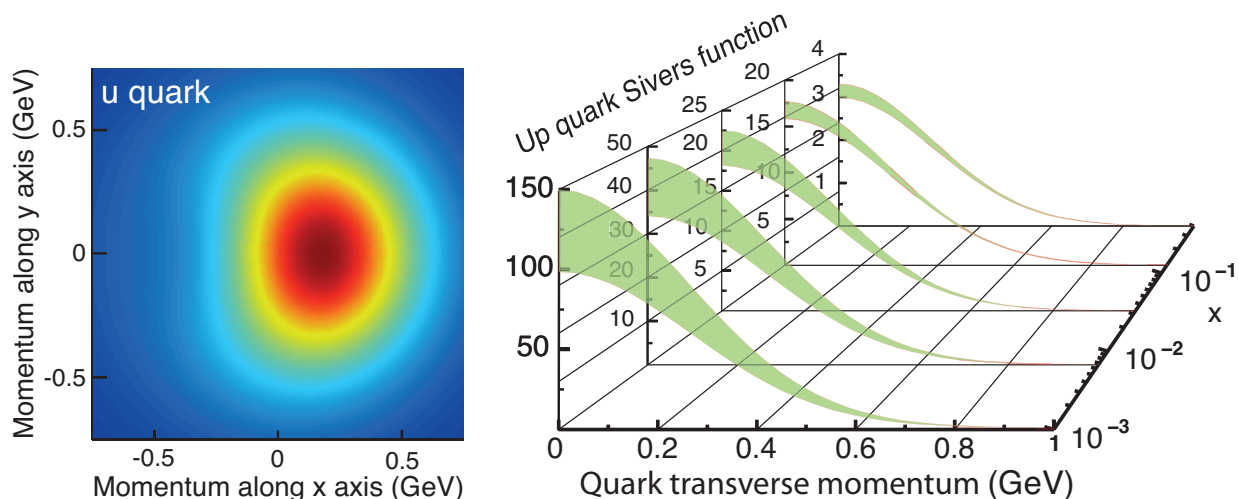


**Figure B.4:** [Reproduced from Ref. [190].] (left) The transverse-momentum distribution of an up quark with longitudinal momentum fraction  $x = 0.1$  in a transversely polarized proton moving in the  $z$ -direction, while polarized in the  $y$ -direction. The color code indicates the probability of finding the up quarks. (right) The transverse-momentum profile of the up quark Sivers function at five  $x$  values accessible with the kinematics available at eRHIC, and corresponding statistical uncertainties.

With measurements of identified pions and kaons, these asymmetries give a 2+1 dimensional description of the spin and momentum distributions of different quark flavors in the proton, such as is shown in Figure B.4.

Current measurements, however, are only able to probe a small region in  $x$  and  $Q^2$ , limiting the description to the valence quark region. Understanding of how the sea quarks and gluons contribute requires a larger kinematic range, such as provided at eRHIC. With the PID capabilities of ePHENIX, asymmetry measurements with transversely polarized nucleons and electrons in SIDIS will enable the study of these TMDs over most of this range, significantly expanding our knowledge of the proton structure. The constraint on the Sivers distributions was discussed in the EIC White Paper [190], with the expectations shown in Figure B.4. For the first time, determination of the Sivers distribution over a wide range in  $x$  will be possible, including the low  $x$  region where gluons dominate.

The transversity distribution, when coupled with the Collins fragmentation asymmetry, would result in an azimuthal asymmetry in the hadron production. This has been called the Collins effect, and is a measurement that goes to the heart of establishing the transversity distribution in a proton [193]. Measurement over the wide kinematic region would not only allow us to measure transversity, but the wide  $x$ -coverage possible at eRHIC would afford the first reliable measurement of the tensor charge of the proton (the integral over  $x$  of the transversity distribution). No other currently operational or planned facility can do this.

**Tomographic imaging of the proton** Hard exclusive processes such as the Deeply Virtual Compton Scattering (DVCS) and Deeply Virtual Vector Meson production (DVVM) involve interactions between the virtual photon and the partons in the proton without breaking the proton, resulting

in the production of a real photon in DVCS or a vector meson in DVVM processes. Just as elastic lepton-nucleon scattering gives information on the spatial distribution of the electric charge and magnetization in the nucleon, DVCS and DVVM processes probe the transverse distribution of quarks, anti-quarks and gluons. This information is encoded in generalized parton distributions (GPDs), which quantify the distributions of quarks and gluons in terms of their positions in the transverse plane and longitudinal momentum fraction, providing 2+1 dimensional imaging of the nucleon. Measurements with polarized beams enable studies of spin-orbit correlations of quarks and gluons in the nucleon, by correlating the shift in the parton transverse distribution and proton transverse polarization. It is intuitively connected with orbital angular momentum carried by partons in the nucleon and hence of great interest in addressing the nucleon spin puzzle (nucleon spin decomposition) [194].

The existing data on GPDs from fixed target experiments cover only a limited kinematical range of  $t$  (the squared momentum transfer to the proton), medium to high  $x$  and low  $Q^2$ . The  $t$  is connected through the Fourier transform with the impact parameter range probed. While data from HERA collider experiments (ZEUS and H1) covered lower  $x$  and a wide range in  $Q^2$ , they are statistically limited. Furthermore, the HERA proton beams were unpolarized, so ZEUS and H1 were not able to study the proton-spin dependence in these measurements. With its large acceptance, excellent detection capabilities, high luminosity and broad range of energies of the polarized proton/helium beams available at eRHIC, ePHENIX will provide high precision data over a wide range of  $x$ ,  $Q^2$  and  $t$ . The wide range in  $t$  possible at eRHIC is of crucial importance, and will be achieved by integrating Roman Pot detectors in the accelerator lattice from the outset. Similar measurements performed with ion beams will allow analogous imaging of nuclei, allowing the first look at the parton distributions inside the nuclei.

The EIC White Paper demonstrates the precision that can be achieved in such a program with Deeply Virtual Compton Scattering (DVCS) and exclusive  $J/\psi$  production. The detector requirements for such measurements discussed in the White Paper and what we propose as ePHENIX are similar. For such, we expect ePHENIX will be able to make high impact measurements of GPDs.

### Nucleus as a laboratory for QCD

Electron scattering interactions from nuclei allow key tests of the modification of parton distribution functions in nuclei of various sizes. The EIC has the unprecedented energy reach to probe deep into the low- $x$  quark and gluon region where there are predictions of significant non-linear evolution effects and possibly the realization of a universal state of the QCD vacuum at high gluon density. In addition, rather than looking at the modified number of deep inelastic scatterings, one can study via SIDIS the changes in the process of a highly virtual struck quark to color neutralize and eventually hadronize when in the presence of a nuclear medium.

**Hadronization and its modification in nuclear matter** Deep inelastic scattering with heavy nuclear targets provides an effective stop watch and meter stick with which one can measure the color neutralization and hadronization times, and understand important details of partonic interactions with the nucleus. By varying the size of the nuclear target (at eRHIC all the way up to uranium) and changing key DIS parameters ( $Q^2, \nu, z, p_T^2, \phi$ ) one can calibrate this watch and meter stick. Figure B.5 shows the kinematic reach for 5 GeV electrons scattering from 100 GeV/nucleon heavy

nuclei in terms of the initial virtuality  $Q^2$  and the energy of the struck quark in the nuclear rest frame  $\nu$ . Earlier experiments with fixed targets have measured very interesting modifications in apparent fragmentation functions, and yet those results are limited to small values of  $Q^2$  and  $\nu$ . In the case of the published HERMES results [195] in Fig. B.5, one observes a dramatic decrease in the number of high- $z$  hadrons (those with a large fraction of the struck quark momentum) in scattering from nuclear targets. There are many possible explanations of the experimental results, including parton energy loss due to multiple scattering in the nucleus and induced gluon radiation — a similar mechanism has been used to explain the “jet quenching” phenomena discovered in heavy ion collisions at RHIC. Other theoretical frameworks predict a strong correlation between a short color neutralization timescale and high- $z$  resulting processes. An excellent review of the various theoretical approaches is given in Ref. [196]. Figure B.5 also shows the expected statistical precision with the ePHENIX PID capabilities over the full  $\nu$  range in one  $Q^2$  bin.

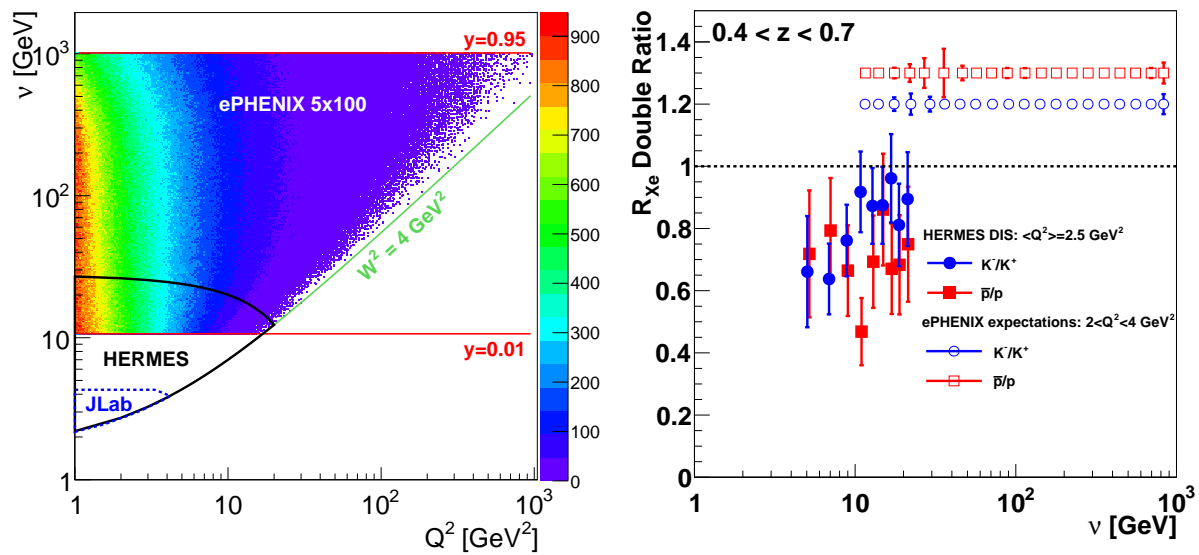


**Figure B.5:** (left) Shown is the very large virtuality  $Q^2$  and  $\nu$  coverage for ePHENIX (EIC) measurements with collisions of 5 GeV electrons on 100 GeV/nucleon heavy nuclei. The  $z$ -axis color scale shows the relative distribution of events from the PYTHIA event generator. Also shown are the kinematic reach for the CLAS experiment at JLab [197] and for the HERMES results [195]. (right) Experimental data from HERMES [195] on the modified fragmentation from xenon targets ( $R_{Xe}$ ) in the range  $0.4 < z < 0.7$  and with average  $\langle Q^2 \rangle = 2.5 \text{ GeV}^2$ . The filled points are the double ratio for antiprotons relative to protons (red) and for  $K^-$  relative to  $K^+$  (blue). ePHENIX will measure with precision the modified fragmentation distribution with excellent  $\pi, K, p$  particle identification over a very broad range of  $Q^2$  and  $\nu$ . The open symbols show the expected statistical precision for ePHENIX with its particle identification capabilities for one bin in  $Q^2$ ,  $2 < Q^2 < 4 \text{ GeV}^2$  based on  $2 \text{ fb}^{-1}$  at the  $5 \text{ GeV} \times 100 \text{ GeV}$  beam energy configuration.

If the struck quark remains an undressed color charge while it traverses the nucleus, one might expect that the ratio of final state hadrons ( $\pi^+, K^+, p$  and their anti-particles) would show the same degree of nuclear modification. Shown in the right panel of Figure B.5 are the double ratios of modifications  $R_{Xe}$  with a xenon target for antiprotons to protons and  $K^-$  to  $K^+$ . It is notable that there is a larger suppression for the hadrons with a larger cross section with nucleons (e.g.  $\sigma_{\bar{p}+N} > \sigma_{p+N}$  and  $\sigma_{K^-+N} > \sigma_{K^++N}$ ). If this is due to hadronization occurring within the nucleus, then inelastic collisions can result in the differential attenuation. How does this attenuation vary

with the energy of the struck quark? The EIC realization has the enormous reach in the energy of the struck quark  $\nu$  at fixed  $Q^2$  to measure the full evolution with high statistics. As demonstrated in this document, ePHENIX will have excellent  $\pi, K, p$  particle identification to make exactly this measurement with high statistics. In addition, one can vary the virtuality which is also expected to play a significant role in the length scale probed in the nucleus and thus rate of initial radiation.

Tests with charm mesons via displaced vertex measurements are not in the initial suite of ePHENIX capabilities, and could be added with a later inner thin silicon detector. Measurements of the interactions of charm quarks with the nucleus would be quite interesting in the context of suppressed radiation due to the “dead-cone” effect. However, the relation to kinematic variables  $z$  and  $\nu$  may depend on the balance of DIS events from intrinsic charm as opposed to photon-gluon fusion reactions resulting in  $c\bar{c}$  pair production.

**QCD matter at extreme gluon density** A key goal of any future EIC is to explore the gluonic matter at low  $x$ , where it is anticipated that the density of gluons will saturate as the rate of gluon recombination balances that of gluon splitting. In fact, there are well known modifications to the quark distribution functions in nuclei that have significant  $x$  dependence: high  $x$  Fermi motion effects, then the EMC suppression, anti-shadowing enhancement, and finally nuclear shadowing at the lowest  $x$ . The ePHENIX detector, combined with the large kinematic reach of an  $e+A$  collider, is in an excellent position to map this physics out in the gluon sector.

The lowest  $x$  regime with saturated gluon densities is unique to QCD, as gluons carry the QCD charge, “color”, and so interact with themselves. In order to explore this saturation region, one must probe nuclear matter at high center-of-mass energy, so as to reach as low in  $x$  as possible while still in the perturbative QCD regime (i.e.,  $Q^2 > 1 \text{ GeV}^2$ ). Generally, a saturation scale,  $Q_s$ , is defined to indicate the onset of saturation (where the gluon splitting and recombination balance each other), with  $Q_s$  falling as  $x$  increases. In reality the point at which recombination starts to balance the gluon splitting is a range in  $x$  and  $Q^2$  and so making measurements over a wide range in  $x$  and  $Q^2$  is necessary to fully understand these effects.

eRHIC will have a significantly lower center-of-mass energy than HERA, and so cannot improve upon the minimum  $x$  probed with measurements in  $e+p$ . However, eRHIC will also be capable of accelerating heavy ions in  $e+A$  collisions. As the  $x$  probed is related to the resolution of the probe, collisions at the same  $Q^2$  can resolve significantly lower  $x$  due to the larger extent of the nucleus: the partons in the highly accelerated nucleus are probed coherently. This effectively reduces the  $x$  probed in  $e+A$  collisions by a factor of  $A^{1/3}$ , with  $A$  the atomic weight, as this is proportional to the size of the nucleus. At the energies planned for eRHIC, based on measurements in  $p(d)+A$ , one expects saturation effects in inclusive DIS in  $e+A$ .

Figure B.6 shows the  $x$  and  $Q^2$  coverage of ePHENIX for the  $10 \text{ GeV} \times 100 \text{ GeV/nucleon}$  configuration compared with the current fixed target data. Two red lines are drawn, one (solid) showing expectations of  $Q_s^2$  in  $e+Au$  and the other (dashed) showing the expected turn on of geometric scaling, which relates to the saturation scale by  $Q_{max}^2 = Q_s^4 / \Lambda_{QCD}^2$ . The shaded red region is where ePHENIX can search for saturation effects.

As described in the EIC White Paper [190], it can be even more effective to explore this region of dense gluonic matter with diffractive physics, where at least two gluons are exchanged in the interaction. Therefore, a primary measurement to probe saturation effects at eRHIC will

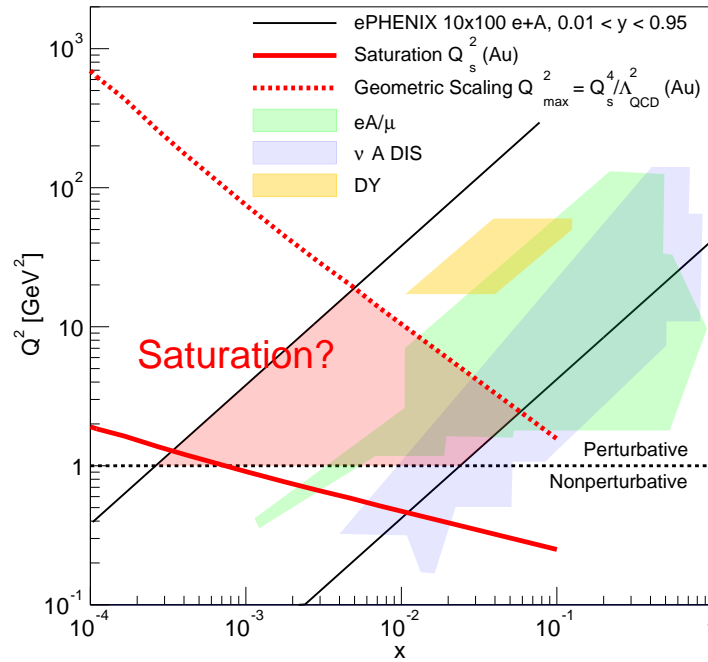


**Figure B.6:** Shown is the coverage in  $x$  and  $Q^2$  for the EIC and the ePHENIX detector for 10 GeV electrons on 100 GeV/nucleon heavy nuclei. The two black lines indicate the kinematic coverage with selections on the inelasticity  $0.01 < y < 0.95$  (which might be slightly reduced depending on the final electron purity at low momentum). Also shown are the kinematic coverage by previous experiments in  $e+A$  and  $\nu+A$  DIS and also Drell-Yan measurements. The red solid line is an estimate of the  $x$  dependence for the saturation scale  $Q_s^2$ . The region where this universal saturated matter dictates the physics is estimated to extend over the geometric scaling region up to  $Q_{max}^2 = Q_s^4 / \Lambda_{QCD}^2$  shown by the red dashed line [198].

be comparing the diffractive-to-total cross-section from  $e+p$  and  $e+A$ . The ratio of these cross-sections will directly relate to the size of any saturation effects. Figure B.7, taken from the EIC white paper [190], shows the prediction of one saturation model for this cross-section ratio with and without saturation, indicating large possible effects. Note that the statistical and systematic uncertainties in this plot are scaled up by a factor of 10 in order to be visible. This measurement relies on measuring events with a large rapidity gap, which is the signature of diffractive events due to the fact that the hadron remains intact after the scattering (though in the case of ions, the nucleus may still break up). The ePHENIX detector will have wide calorimetric coverage, and so will be able to make a measurement of the ratio of diffractive-to-total cross-sections with comparable precision as shown in Figure B.7.

## B.4 Detector Requirements

The detector requirements for Deep Inelastic Scattering measurements are well established by previous DIS experiments (H1, ZEUS, HERMES, COMPASS, etc.) and by EIC group studies [190,

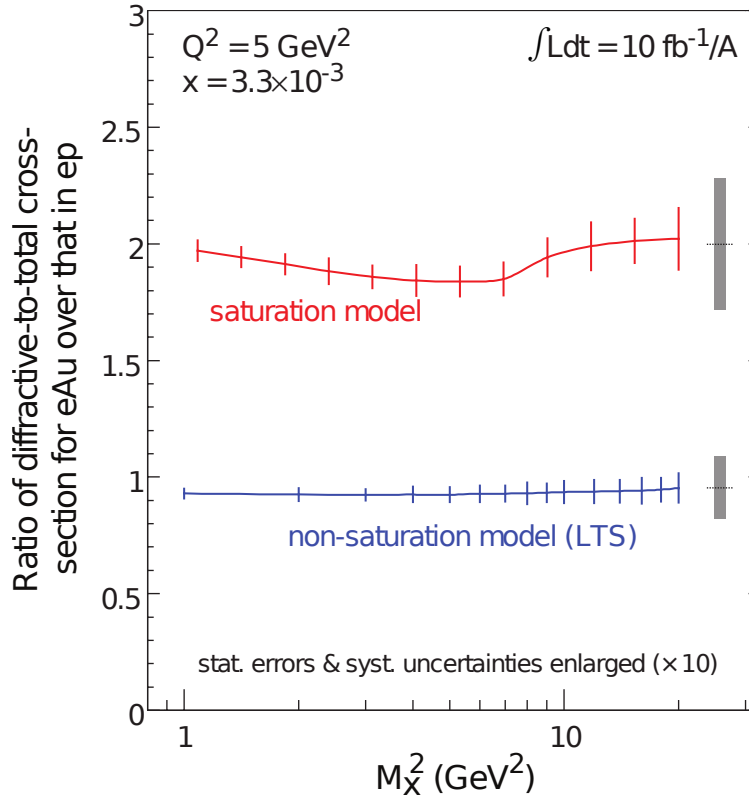


**Figure B.7:** [Reproduced from Ref. [190].] Ratio of diffractive-to-total cross-section for  $e+Au$  normalized to  $e+p$  plotted as a function of the squared mass of the hadronic final state,  $M_X^2$ . The expected uncertainties for  $10 \text{ fb}^{-1}$  are scaled by a factor of 10 to be visible. The ePHENIX detector will have similar capabilities as was assumed for this plot, and will achieve similar precision.

196]. Table B.1 summarizes these basic requirements and how ePHENIX would meet them. After a brief overview of the relevant kinematic variables, detailed studies are presented in this chapter.

The suggested ePHENIX detector configuration is shown in Figure B.1. It is built around the sPHENIX detector, which is a superconducting solenoid and electromagnetic and hadronic calorimeter in the central region ( $-1 < \eta < 1$  for pseudorapidity  $\eta$ ). This proposal would add to that detector the following detector subsystems:

**electron-going direction** ( $-4 < \eta < -1$ ): High resolution Crystal EMCAL with GEM tracking.

**Barrel** ( $-1 < \eta < 1$ ): Compact-TPC for low mass tracking and PID for momentum  $p < 4 \text{ GeV}/c$  with DIRC

**hadron-going direction** ( $1 < \eta < 4$ ): Hadronic and Electromagnetic calorimeters, GEM trackers, and Aerogel-based ( $1 < \eta < 2$ ) and gas-based RICH for PID up to momentum  $p \sim 50 \text{ GeV}$ .

**Far-Forward in hadron-going direction:** Roman Pots and Zero-Degree Calorimeter.

**Table B.1:** Detector requirements

Detector requirements	Detector solution
<p><b>Electron-ID:</b> High purity ( 99%) identification of the scattered lepton over hadron and photon background <i>Important for electron-going direction and barrel acceptance</i></p>	<p>Electromagnetic Calorimetry and charged particle tracking Minimum material budget before EMCal Good energy and tracking resolution for <math>E/p</math> matching</p>
<p><b>Resolution in <math>x</math> and <math>Q^2</math>:</b> Excellent momentum and angle resolution of the scattered lepton to provide high survival probability ( 80%) in each <math>(x, Q^2)</math> bin (important for unfolding) <i>Important for electron-going direction and barrel acceptance</i></p>	<p>High resolution EMCal and tracking in electron-going direction Good (tracking) momentum resolution for <math>E'_e &lt; 10</math> GeV in barrel Good (EMCal) energy resolution for <math>E'_e &gt; 10</math> GeV in barrel</p>
<p><b>Hadron identification:</b> &gt; 90% efficiency and &gt; 95% purity</p>	<p>In barrel acceptance: DIRC for <math>p_h &lt; 4</math> GeV/c In hadron-going direction: Aerogel for lower momentum and gas RICH for higher momentum</p>
<p><b>Wide acceptance for leptons and photons in DVCS:</b> Ability to measure DVCS lepton and photon within <math>-4 &lt; \eta &lt; 4</math></p>	<p>EMCal and tracking with good resolution over for lepton and photon measurements covering <math>-4 &lt; \eta &lt; 4</math></p>
<p><b>Electron/Photon separation:</b> Separate DVCS photon and electron in electron-going direction</p>	<p>High granularity EMCal in electron-going direction</p>
<p><b>Measurement of scattered proton in exclusive processes</b></p>	<p>Roman pots in hadron-going direction</p>
<p><b>"Rapidity gap" measurement capabilities:</b> Measure particles in <math>-2 &lt; \eta &lt; 4</math> for diffractive event identification</p>	<p>Hadronic calorimetry covering <math>-1 &lt; \eta &lt; 5</math>, and EMCal covering <math>-4 &lt; \eta &lt; 4</math></p>
<p><b>Forward Zero-Degree calorimetry:</b> Measure neutrons from nucleus breakup in diffractive <math>e+A</math> events</p>	<p>Zero-Degree calorimeter in hadron-going direction planned, in coordination with CAD</p>



### B.4.1 Kinematics

In DIS, a lepton is scattered off a target hadron via the exchange of a virtual boson, which for electron beam energy  $E_e < 10$  GeV can always be taken as a virtual photon. Defining the four-momenta of the incoming and scattered electron and the incoming proton as  $k$ ,  $k'$  and  $p$  respectively, we can define the following Lorentz invariant quantities:

$$s \equiv (k + p)^2 = 4E_e E_p \quad (\text{B.1})$$

$$Q^2 \equiv -q^2 = -(k - k')^2 = 2E_e E'_e (1 - \cos\theta) \quad (\text{B.2})$$

$$y \equiv \frac{p \cdot q}{k \cdot p} = 1 - \frac{E'_e}{E_e} + \frac{Q^2}{4E_e^2} \quad (\text{B.3})$$

$$x \equiv \frac{Q^2}{2p \cdot q} = \frac{Q^2}{ys} \quad (\text{B.4})$$

$$\nu \equiv \frac{p \cdot q}{M} = \frac{Q^2}{2Mx} \quad (\text{B.5})$$

where  $s$  is the center-of-mass energy squared,  $q$  is the 4-momentum transferred from scattered electron and  $Q^2$  is the virtuality of the photon which gives the resolution scale of the scattering,  $y$  is the inelasticity of the scattering and  $x$  is Bjorken  $x$ , the fractional momentum carried by the struck parton. Here, we have also written these in the lab frame in terms of the measured scattering angle,  $\theta$  and the energies of the proton and incoming and scattered electron,  $E_p$ ,  $E_e$  and  $E'_e$ , respectively, under the approximation that the electron and proton mass are small compared to the beam energies.

For inclusive DIS, where only the kinematics of the scattered lepton are measured, Eq. B.1–B.5 fully describe the event. For SIDIS, in which a final state hadron is also measured, additional variables are needed. The fraction of the scattered parton's momentum carried by the hadron is defined as

$$z \equiv \frac{p_h \cdot p}{q \cdot p} \quad (\text{B.6})$$

where  $p_h$  is the four-momentum of the measured hadron. Further, we can define  $p_{h\perp}$  as the transverse momentum of the hadron w.r.t. the virtual photon, in the center-of-mass frame of the proton (or ion) and virtual photon.

For exclusive processes, in addition to the scattered lepton, the final state photon in DVCS or meson in Deeply Virtual Meson Production as well as the scattered proton are measured. In this case, another kinematic variable is introduced – the squared momentum transfer to the proton,  $t$ , defined as

$$t \equiv (p' - p)^2 \quad (\text{B.7})$$

where  $p'$  is the four-momentum of the scattered proton.

### B.4.2 Inclusive DIS and scattered electron measurements

In inclusive DIS, where only the kinematics of the scattered electron are necessary, the primary requirements of any detector are electron identification and sufficient resolution in  $x$  and  $Q^2$ , which in turn mandates good energy and angle resolution for the scattered electron measurements (Eq. B.2–B.4).

## Electron Identification

In collider geometry, the DIS electrons are scattered mainly in the electron-going direction and central rapidities (barrel acceptance), see Figure B.8. Central rapidity selects scatterings with higher  $Q^2$  and higher  $x$  (due to its correlation with  $Q^2$ ). The higher the electron beam energy, the more scattering there is in the electron-going direction. The energy of the scattered electron varies in the range from zero up to the electron beam energy and even to higher values for electrons detected in the barrel acceptance, see Figure B.8.

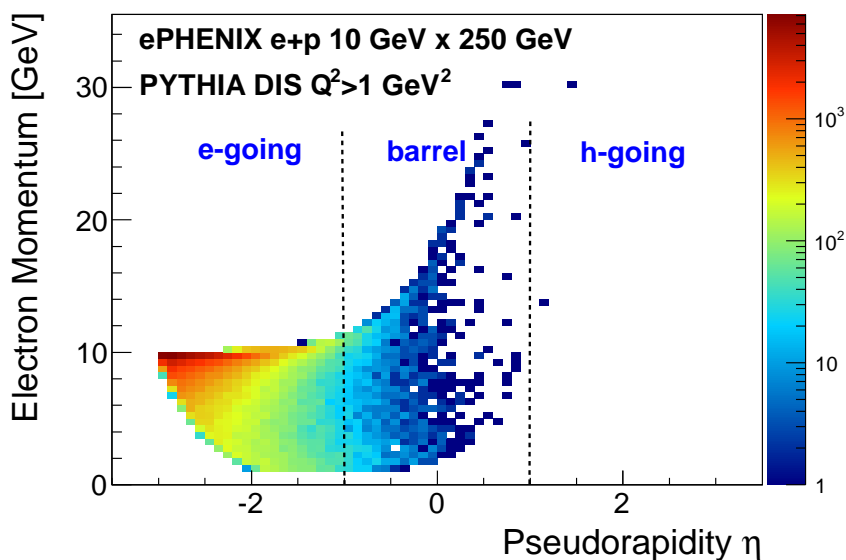


**Figure B.8:** Shown is the distribution of scattered electrons in pseudorapidity and energy. The results are from PYTHIA DIS simulations for  $e+p$  collisions with  $10 \text{ GeV} \times 250 \text{ GeV}$  beam energies. The events are selected as DIS with  $Q^2 > 1 \text{ GeV}^2$ .

Collider kinematics allow clear separation of the scattered electrons from other DIS fragments — hadrons and their decay products — which are detected preferably in the hadron-going direction, leaving much softer spectra in the central region and the electron-going direction. Figure B.9 shows scattered electron momentum spectra along with photon (mainly from hadron decays) and charged pion spectra. For the 10 GeV electron beam, hadronic and photonic backgrounds are small above  $\sim 5 \text{ GeV}/c$ , but increase rapidly at lower momenta.

The different response of the EMCal to hadrons and electrons, along with a direct comparison of energy deposited in the EMCal and momentum measured in the tracking system (i.e.,  $E/p$  matching) provides a significant suppression of hadronic background in DIS scattered electron measurements: from a factor of 20–30 at momenta near  $1 \text{ GeV}/c$  to a factor of greater than 100 for momenta above  $3 \text{ GeV}/c$ . Figure B.10 shows the effectiveness of electron identification with the EMCal and tracking, providing high purity for DIS scattered electron measurements at momenta  $>3 \text{ GeV}/c$  for the 10 GeV electron beam (and  $>1.5 \text{ GeV}/c$  for the 5 GeV electron beam). The evaluations above are done with a parametrized response of the EMCal to hadrons

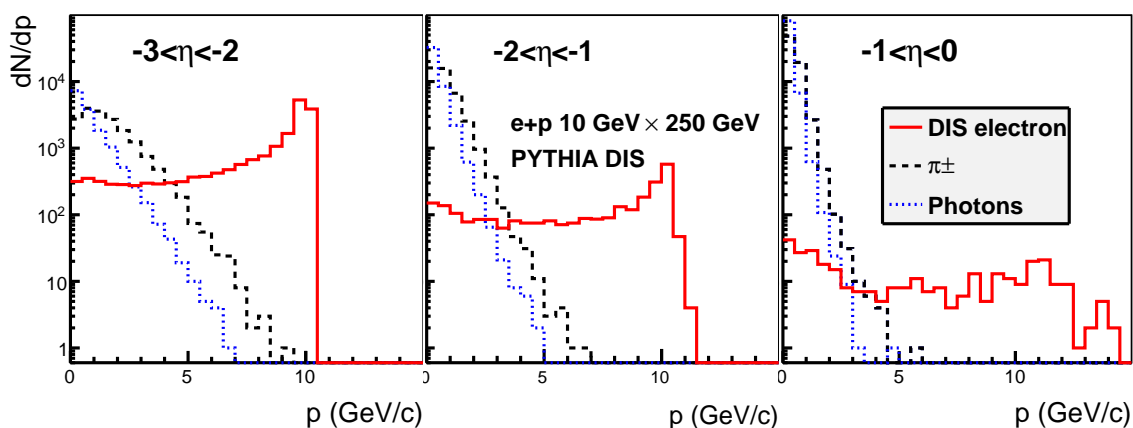


**Figure B.9:** For 10 GeV  $\times$  250 GeV beam energy configuration: Momentum spectra for scattered electron (red), charged pions (black) and photons (blue).

and electrons, and EMCal and tracking resolutions described in Sections B.5.3 and B.5.2. Further enhanced electron identification is expected from the use of the transverse shower profile. We are also studying possible electron identification improvement with longitudinal segmentation in the crystal calorimeter in the electron-going direction. These are expected to move the detector capabilities for high purity electron identification down to 2 GeV/c (1 GeV/c) for 10 GeV (5 GeV) electron beam, which only marginally limits the  $(x, Q^2)$  space probed in our measurements, see Figure B.11.

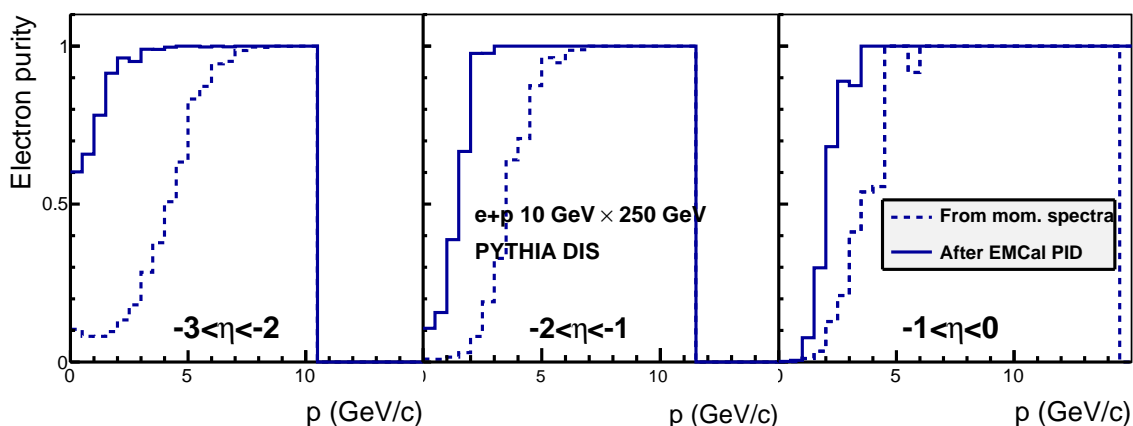


**Figure B.10:** For 10 GeV  $\times$  250 GeV beam energy configuration: The fraction of charged particles from DIS electrons before electron identification (dotted) and after identification with the EMCal response and  $E/p$  matching (solid).

Photon conversion in material between the collision point and the tracker (mainly beam pipe, with thickness as small as 0.3% of radiation length) is not expected to contribute sizable background. Moreover, conversion electron-positron pairs will be well identified by our tracking system in the

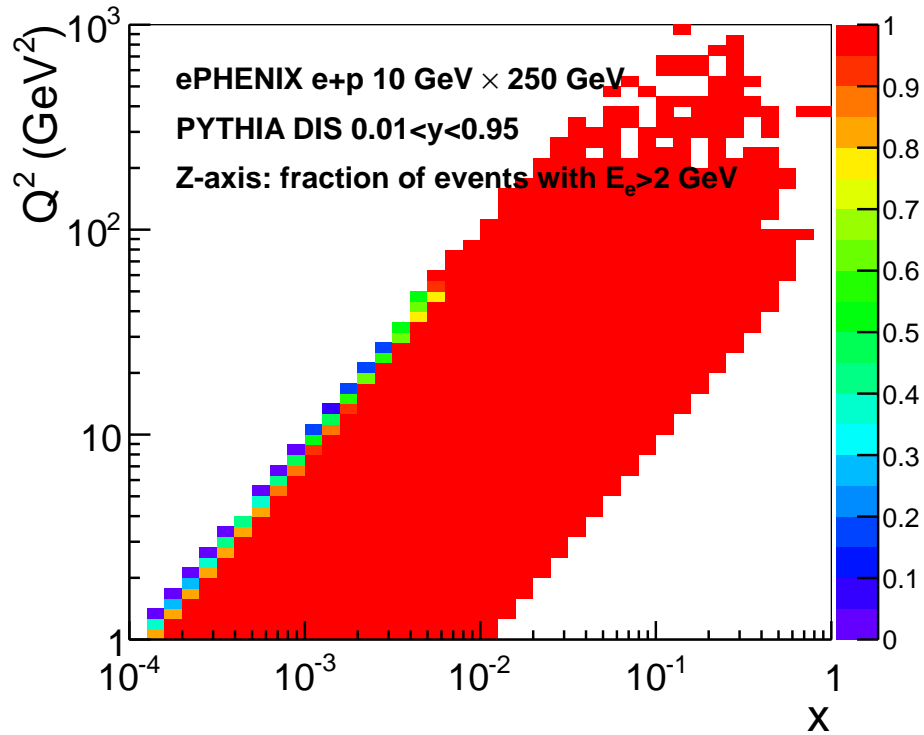


**Figure B.11:** For 10 GeV × 250 GeV beam energy configuration: The color axis indicates the fraction of events in  $(x, Q^2)$  space surviving after a  $> 2$  GeV energy cut on the DIS scattered electron.

magnetic field and additionally suppressed by E/p matching cut. A detailed GEANT simulation study is ongoing to quantify this effect.

#### Resolution in $x$ and $Q^2$ and bin survival probability

Measurements of the scattered electron energy and polar angle impact the DIS kinematic reconstruction, Eq. B.2–B.4. Unfolding techniques are generally used to correct for smearing in  $(x, Q^2)$  due to detector effects, and the effectiveness of this technique depends on the degree to which events migrate from their true  $(x, Q^2)$  bin to another. This migration can be characterized by the likelihood of an event remaining in its true  $(x, Q^2)$  bin — the bin survival probability.

The energy resolution  $\sigma_E$  is directly propagated to  $\sigma_{Q^2}$ , so that  $\sigma_{Q^2}/Q^2 = \sigma_E/E$ . The EMCal energy and tracking momentum resolutions will provide excellent precision for  $Q^2$  measurements. Conversely, the  $\sigma_x$  resolution is magnified by a factor of  $1/y$  as  $\sigma_x/x = 1/y \cdot \sigma_E/E$ , and so the energy resolution in this approach effectively defines the limit of our kinematic reach at low  $y$ .

Figure B.12 shows the relative resolution in  $Q^2$  and  $x$  measurements using the standard “electron” method, in which the scattered electron is measured. While the  $Q^2$  relative uncertainty,  $\sigma_{Q^2}/Q^2$ , is better than 10% over whole  $x$ - $Q^2$  acceptance, the relative uncertainty on  $x$ ,  $\sigma_x/x$ , clearly

demonstrates its  $y$ -dependence (the same  $y$  points are on the diagonal, as from Eq. B.4,  $Q^2 = syx$ ). The step in resolution around  $Q^2 = 50 \text{ GeV}^2$  in these plots corresponds to the transition from the electron-going direction to the barrel acceptance, which differ mainly in the resolution of the different electromagnetic calorimeters covering those two regions of the acceptance. All of this translates to the statistics survival probability in a bin shown in Figure B.13, which is calculated for five bins per decade in each of  $x$  and  $Q^2$ . The survival probability is  $> 80\%$  for  $y > 0.1$  in the electron-going direction and for  $y > 0.3$  in the barrel acceptance.

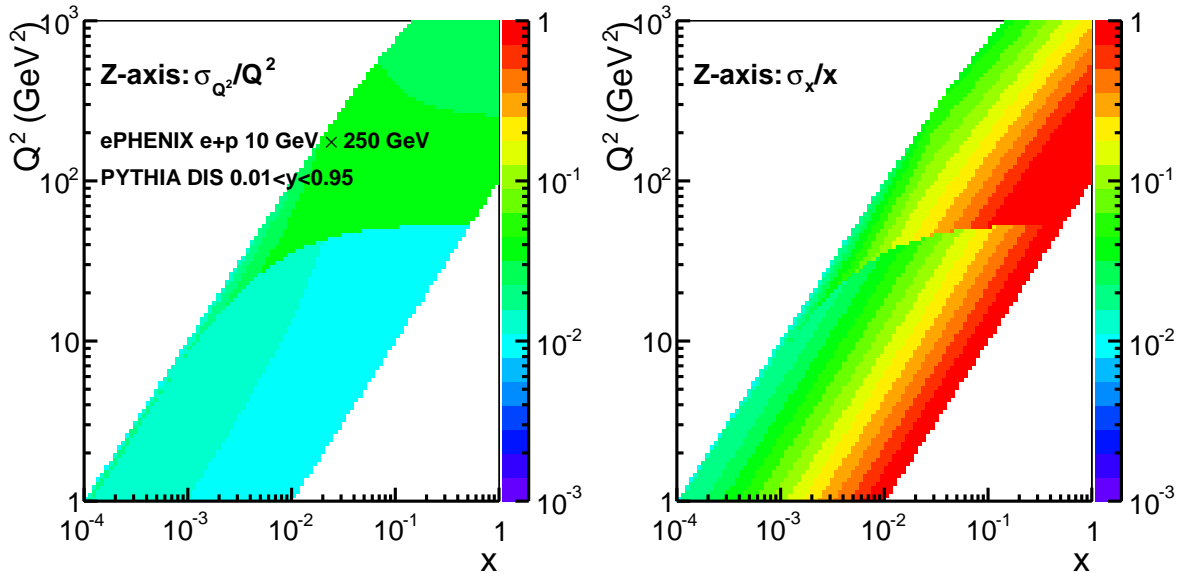


**Figure B.12:** For 10 GeV  $\times$  250 GeV beam energy configuration: the relative resolution for  $Q^2$  (left) and  $x$  (right) as a function of  $(x, Q^2)$ .

The effect of the polar angle resolution  $\theta$  in Eq. B.2–B.4, is the biggest for forward scattering (small  $\theta$ ). It was found that crystal EMCal position resolution (better than 3 mm for  $> 1 \text{ GeV}$  electrons, see Section B.5.3) provides enough precision for scattered electron angle measurements, so that it affects the statistics migration in bins on Figure B.13 only marginally.

The Jacquet-Blondel method using the hadronic final state is an alternative approach to reconstruct DIS kinematics. Its resolution for inelasticity  $y$ , and hence for  $x$ , is nearly flat, so it provides much better precision for  $x$  determination than the “electron” method, in the region with small  $y$ . It is also better in the higher  $Q^2$  region corresponding to the barrel acceptance, where the resolution of the “electron” method is limited by the EMCal resolution.

The Jacquet-Blondel method requires the measurement of all final state hadrons produced in  $e+p$  or  $e+A$  scattering. A study with the PYTHIA generator shows that the precision of this approach does not deteriorate if the hadron detection capabilities are limited to  $|\eta| < 4$ . This method provides relative precision for the measurement of  $x$  of better than 20%, which satisfies the bin statistics migration criteria discussed above. It was found that for  $y < 0.3$  the precision of this approach deteriorates only slightly when hadron measurements are limited to the barrel and forward acceptance  $-1 < \eta < 4$  (the acceptances we plan to equip with hadron identification

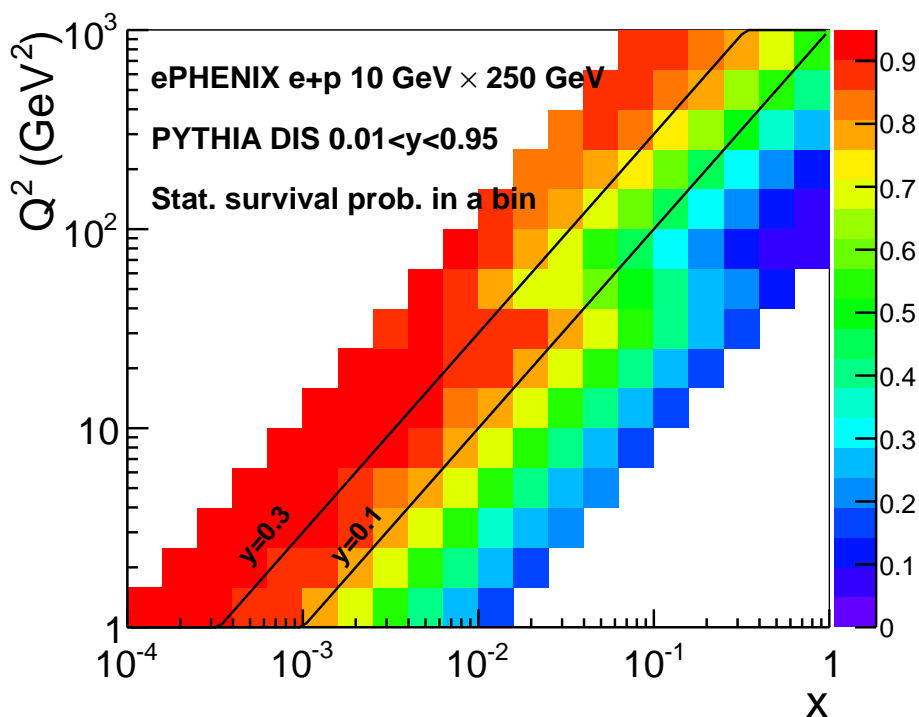


**Figure B.13:** For 10 GeV × 250 GeV beam energy configuration: Statistics survivability in  $(x, Q^2)$  bins.

capabilities, see Section B.5.5). As was shown above, measurements at higher  $y$  are well provided by the “electron” method.

Therefore, combining the electron and hadronic final state measurements provides precise determination of basic kinematic variable  $x$ ,  $y$  and  $Q^2$  in the whole kinematical space.

QED radiative effects (radiation of real or virtual photons) are another source of smearing which is usually corrected with unfolding techniques. Unlike energy-momentum resolutions which introduces Gaussian-like smearing, radiative corrections are tail-like. They can be responsible for as much as 10–20% of statistics migrating away from a bin, and dominate over energy-momentum smearing at higher  $y$  (compare to Figure B.13).

### B.4.3 Semi-inclusive DIS and hadron ID

As was discussed in Chapter B.1, measurements of hadrons in SIDIS events are necessary to determine both the (sea)quark separated helicity distributions and TMDs. It is also important for understanding the hadronization process in nuclear matter. For these measurements, one needs to identify the hadron, particularly in the case of pions and kaons. In this section, we discuss the kinematic ranges of interest for pions, kaons and protons, and in Chapter B.5, we discuss technology choices which can effectively make these measurements.

Figure B.14 shows the yields of positively charged hadrons as a function of momentum and pseudorapidity for the 10 GeV  $\times$  250 GeV beam configuration. A minimum  $z$  cut of  $z > 0.2$  to remove soft physics effects and beam remnant is applied. For  $\eta < 0$ , the hadron momenta are limited by the electron beam momentum, while in the hadron-going direction, the hadron momenta extend almost to the full proton beam energy. The results are similar for other beam energy configurations.

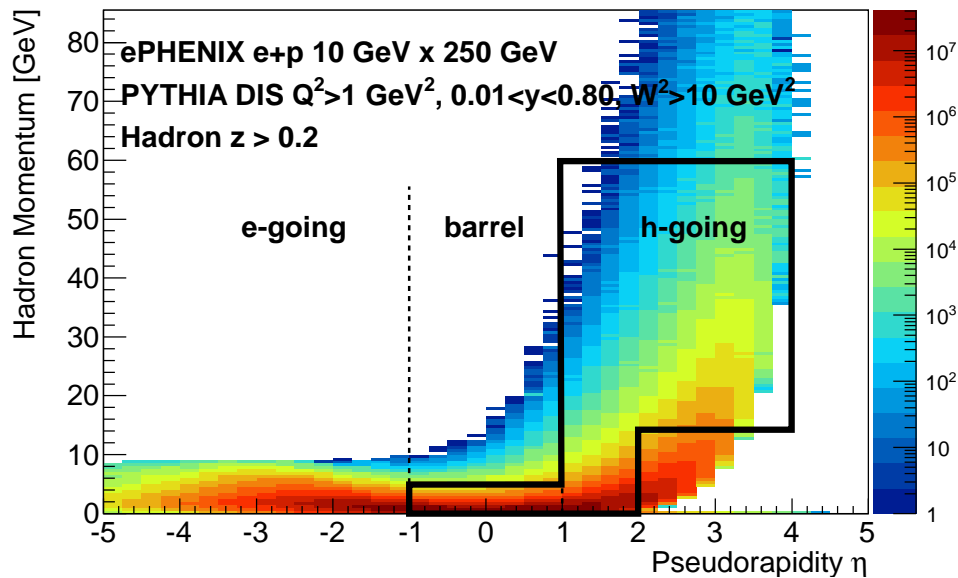


**Figure B.14:** Shown is the distribution of hadrons from DIS events in  $e+p$  as a function of momentum and pseudorapidity, based on PYTHIA simulations of the 10 GeV  $\times$  250 GeV beam energy configuration. The black outline indicates the pseudorapidity and momentum range covered for kaons by the planned PID detectors in ePHENIX.

As was stated above, ePHENIX will have three PID systems: (1) a DIRC covering  $|\eta| < 1$  providing  $\pi$ - $K$  separation below 3.5–4 GeV/ $c$  (depending on purity and efficiency requirements), (2) an aerogel based RICH covering  $1 < \eta < 2$  providing  $\pi$ - $K$  ( $K$ - $p$ ) separation below 6 (10) GeV/ $c$  and (3) a gas based RICH covering  $1 < \eta < 4$  providing  $\pi$ - $K$  separation for  $3 < p < 50$  GeV/ $c$  and  $K$  -  $p$  separation for  $15 < p < 60$  GeV/ $c$  (depending on the balance between efficiency and purity chosen). Based on these numbers, the PID for kaons would cover the  $\eta$  and  $p$  region outlined in black in Figure B.14. The resulting ePHENIX  $x$  and  $Q^2$  coverage for SIDIS events with an identified kaon is shown in Figure B.15, for low ( $0.30 < z < 0.35$ ) and high ( $0.70 < z < 0.75$ )  $z$  bins, along with lines indicating the accessible DIS  $y$  range ( $0.01 < y < 0.95$ ).

Figure B.16 shows the impact on the  $x$  and  $Q^2$  coverage of removing one of the three PID detectors planned for ePHENIX at low and high  $z$ . The plots show the ratio of kaon yields when using only two PID detectors to those with all three detectors (i.e., standard ePHENIX). If the gas-based RICH detector is removed (left), the high  $x$  reach, particularly at high  $Q^2$ , is lost. If the aerogel-based RICH is removed (middle), sensitivity to the region of moderate  $x$ ,  $Q^2$  and  $y$  is lost. Finally, if the

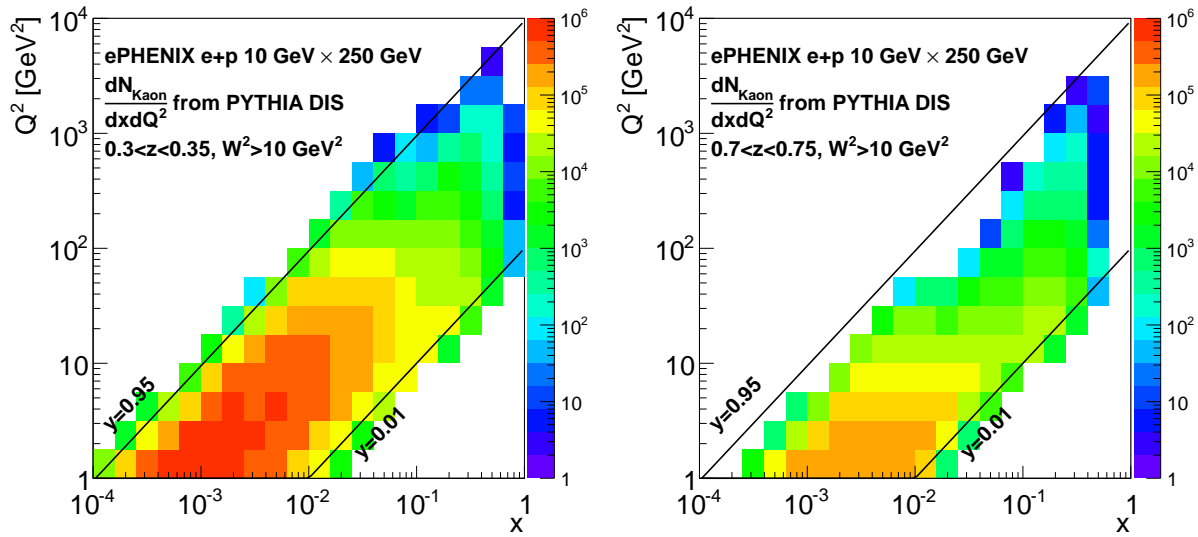


**Figure B.15:**  $x$  and  $Q^2$  distribution of events with kaons which can be identified with the ePHENIX PID detectors in expected binning at (left) low and (right) high  $z$ .

DIRC is removed, significant kinematic coverage at low  $x$ , as well as moderate  $x$  and high  $Q^2$  is lost. To achieve a wide  $x$  and  $Q^2$  coverage, all three detectors are necessary. Extending the aerogel-based RICH to  $\eta > 2$  does not extend the kinematic coverage; the momentum range covered by such a detector corresponds to very low values of  $y$ .

#### B.4.4 Exclusive DIS

Among exclusive processes, Deeply Virtual Compton Scattering (DVCS) is of special interest (see Section B.3). The produced DVCS photon energy versus pseudorapidity distribution is shown in Figure B.17. Most of the photons fall in the electron-going direction and the barrel (central rapidity) acceptance. The photon energy for  $-1 < \eta < 1$  varies in the range  $\sim 1\text{--}4$  GeV/ $c$  and is nearly independent of the beam energy in the range considered for eRHIC. Photons in the electron-going direction are more correlated with the electron beam and have energy from 1 GeV up to electron beam energy.

Figure B.18 shows the  $x$ - $Q^2$  range covered by DVCS measurements for different rapidity ranges, emphasizing the importance of measurements over a wide rapidity range. Wide kinematical coverage is also important for separating DVCS events from Bethe-Heitler (BH) events (when a photon is radiated from the initial or final state lepton), which share the same final state. This can be done by utilizing the different kinematic distributions of DVCS and BH photons (e.g., in rapidity and inelasticity  $y$ ). The planned EMCAL and tracking cover  $|\eta| < 4$  (Section B.5.3 and B.5.2) and will provide excellent capabilities for DVCS measurements.

To ensure the reliable separation of electromagnetic showers in the EMCAL from the scattered electron and the DVCS photon, sufficient EMCAL granularity is necessary. The minimal angle separation between the electron and the photon is reached for electrons with the smallest scattering



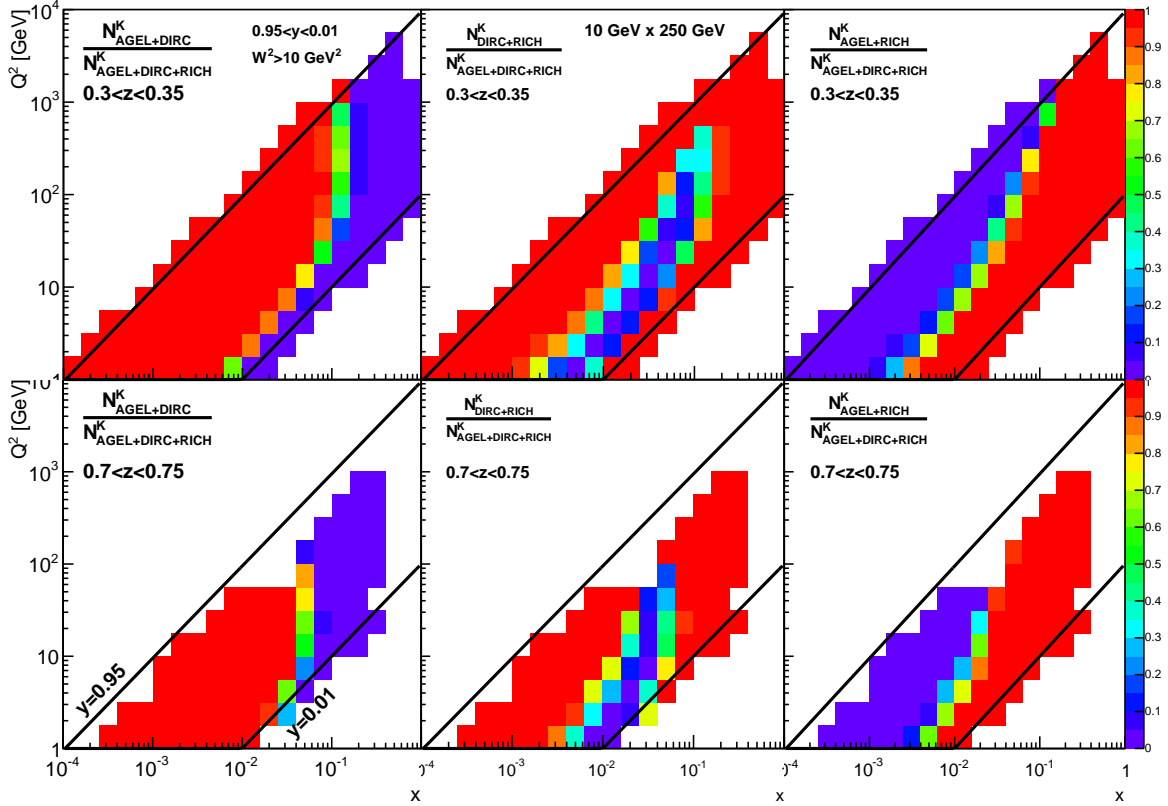


**Figure B.16:** Efficiency as a function of  $x$  and  $Q^2$  of kaon identification when comparing to baseline ePHENIX design with a DIRC, RICH and Aerogel when one of these subsystems is removed. The top three plots are for low  $z$  ( $0.3 < z < 0.35$ ) and the bottom three are for high  $z$  ( $0.7 < z < 0.75$ ). Also shown are lines indicating different values of  $y$ .

angle (i.e., the smallest  $Q^2$ ) and is inversely proportional to electron beam energy. For a 10 GeV electron beam and  $Q^2 > 1 \text{ GeV}^2$ , the minimum angle is  $\sim 0.1$  rad. The proposed crystal EMCAL in the electron-going direction, with granularity  $\sim 0.02$  rad (see Section B.5.3), will provide the necessary electron and photon shower separation.

It is also important to ensure the exclusiveness of the DVCS measurements, and so it is highly desirable to reconstruct the scattered beam proton. The proton scattering angle is inversely proportional to proton beam energy and varies from 0 to 5 mrad for 250 GeV proton beam and four-momentum transfer  $-t < 1 \text{ GeV}^2$ . It can be detected with the planned “Roman Pots” detectors located along the beam line (See Section B.5.6).

#### B.4.5 Diffractive measurements

Diffractive event measurements play an important role in nucleon and nucleus imaging. They are particularly sensitive to the gluon distribution in nuclei and hence to gluon saturation phenomena.

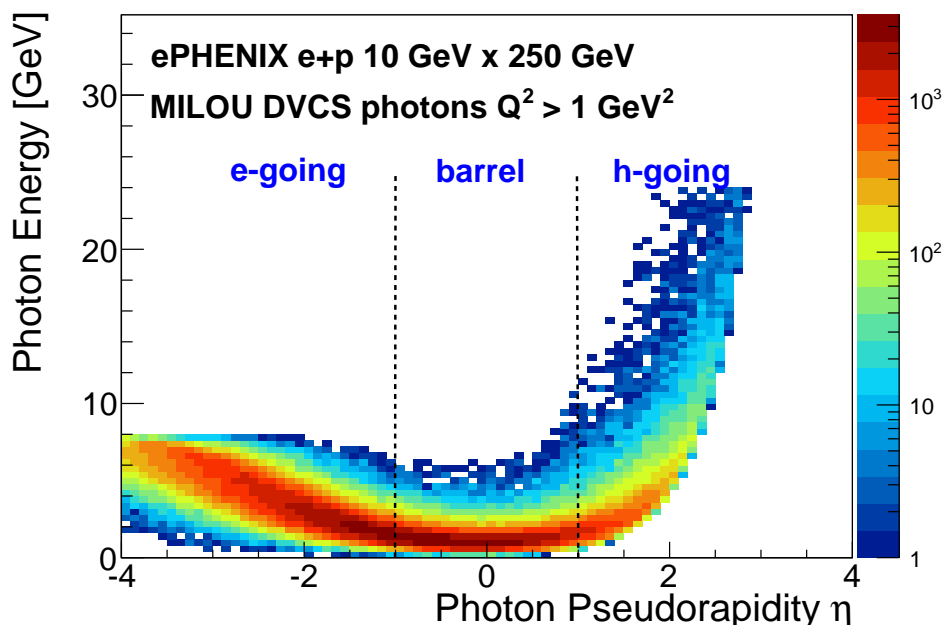


**Figure B.17:** For the  $10 \text{ GeV} \times 250 \text{ GeV}$  beam energy configuration: DVCS photon energy vs pseudorapidity distribution; the z-axis scale shows the relative distribution of events from the MILOU event generator.

Diffractive events are characterized by a rapidity gap, i.e. an angular region in the direction of the scattered proton or nucleus devoid of other particles. Figure B.19 shows the pseudorapidity distribution for the most forward going particle in DIS events and in diffractive events. Extending the forward acceptance of the detector to  $\eta = 4$  and beyond is important if one is to have good capability using the rapidity gap method for detecting diffractive events and to separate them from DIS processes.

The planned ePHENIX EMCal and tracking coverage of  $|\eta| < 4$  and hadronic calorimetry coverage of  $-1 < \eta < 5$  are expected to provide excellent identification capabilities for diffractive events. In addition, to separate coherent (the nucleus remains intact) and incoherent (the nucleus excites and breaks up) diffractive events, we plan to place a zero degree calorimeter after the first RHIC dipole magnet (see Section B.5.6), which is expected to be very efficient at detecting nuclear break-up by measuring the emitted neutrons.

## B.5 Detector Concept

A full engineering rendering of ePHENIX is shown in Figure B.20. The drawing shows the ePHENIX detector in the existing PHENIX experimental hall and illustrates the reuse of the superconducting solenoid and the electromagnetic and hadronic calorimeter system of sPHENIX. The rendering also shows the final eRHIC focusing quadrupoles, each located 4.5 m from the interaction point (IP). Those magnets and the height of the beam pipe above the concrete floor, set the dominant physical

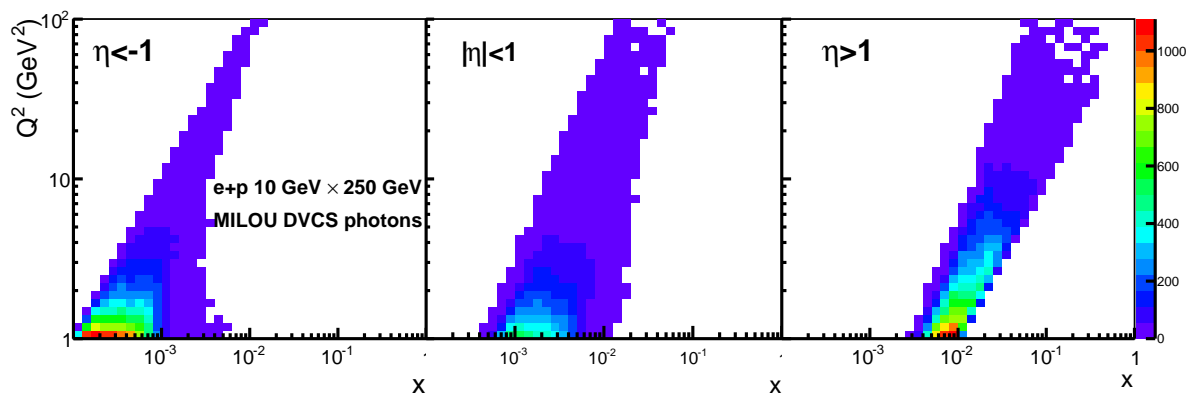


**Figure B.18:** For 10 GeV  $\times$  250 GeV beam energy configuration:  $x$ - $Q^2$  coverage for DVCS events with photon detected in the electron-going direction,  $\eta < -1$  (left), or central rapidities,  $|\eta| < 1$  (middle) and hadron-going direction,  $\eta > 1$  (right). The  $z$ -axis scale shows relative distribution of events from the MILOU event generator.

constraints on the allowable dimensions of ePHENIX. This Section will describe the ePHENIX detector concept in terms of its component subdetectors and their expected performance.

The ePHENIX detector consists of a superconducting solenoid with excellent tracking and particle identification capabilities covering a large pseudorapidity range, as shown in Figure B.21. It builds upon an excellent foundation provided by the proposed sPHENIX upgrade [199] detailed in the MIE proposal submitted to the DOE Office of Nuclear Physics by Brookhaven National Laboratory in April 2013. The strong sPHENIX focus on jets for studying the strongly-coupled quark-gluon plasma in  $p+p$ ,  $p/d+A$  and  $A+A$  is enabled by excellent electromagnetic and hadronic calorimetry in the central region ( $|\eta| < 1$ ).

The C-AD Interaction Region (IR) design at the time the Letter of Intent charge was issued had the final focusing quadrupoles of the accelerator positioned  $\pm 4.5$  m from the IP and employed a “crab crossing” to maintain high luminosity while allowing the electron and hadron beams to intersect at an angle of 10 mrad (see Figure B.33). The ePHENIX detector concept shown in Figure B.20 and Figure B.21 respects these constraints. For instance, the hadronic calorimeter in the hadron-going direction fits within the 4.5 m constraint imposed by the accelerator magnets, and the detector is aligned so that the electron beam travels along the symmetry axis of the magnetic field. Clearly, the progress of ePHENIX from concept to final design will be done in close consultation with C-AD to ensure that the design of IR and the design of the detector remain synchronized.

We have an extensive GEANT4 description of the ePHENIX detector, based on the same software framework as used in PHENIX and sPHENIX, which enables ready use of many existing PHENIX software analysis tools. An example of running a DIS event through the GEANT4 detector description is shown in Figure B.22.

The DOE funded sPHENIX subsystems which will be reused in ePHENIX are:

**Superconducting solenoid:** The sPHENIX detector concept reuses the BaBar superconducting solenoid to provide a 1.5 Tesla longitudinal tracking magnetic field. Its field is shaped in the

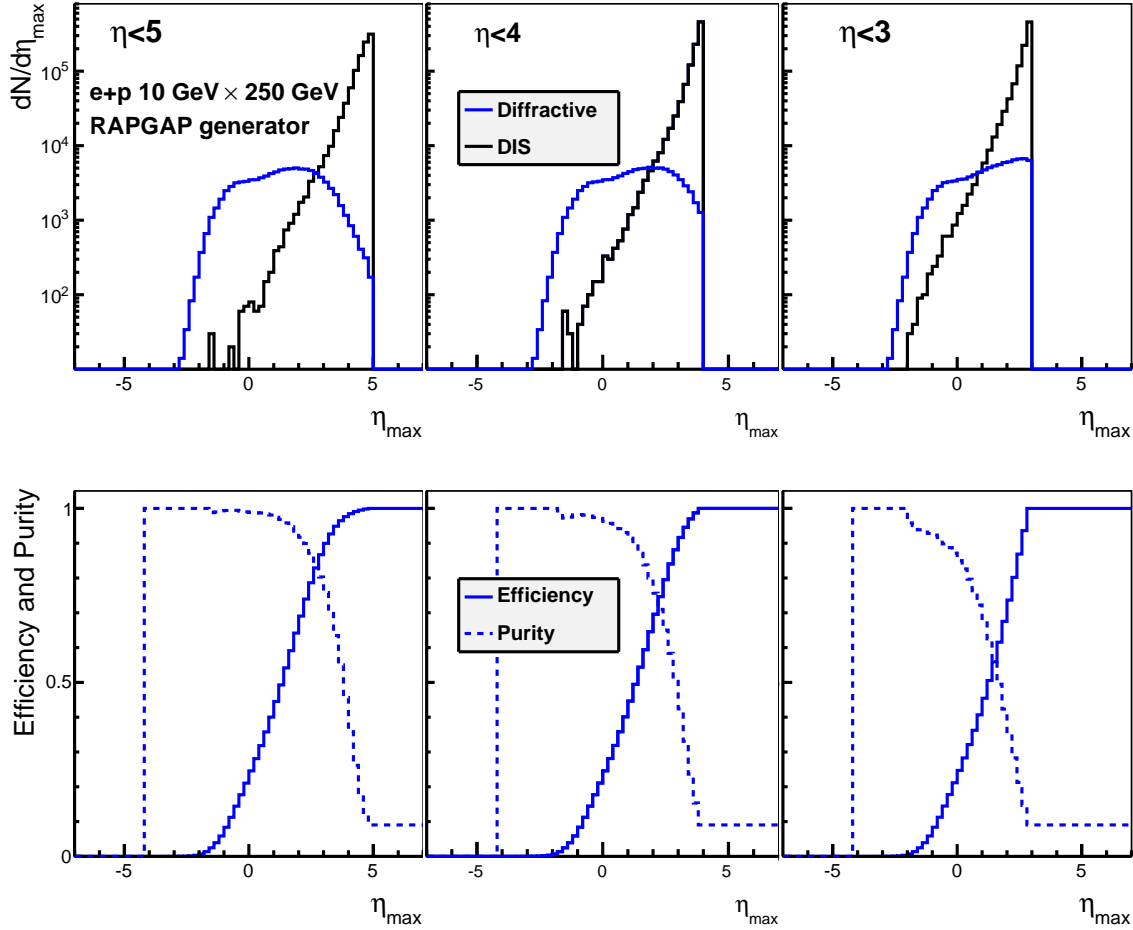


**Figure B.19:** For the  $10 \text{ GeV} \times 100 \text{ GeV}$  beam energy configuration: Top: Pseudorapidity distribution for the most forward going particle in DIS events (black) and in diffractive events (blue); Bottom: Efficiency (dashed) and purity (solid) for diffractive event identification as a function of pseudorapidity cut defining the rapidity gap, for different detector acceptance:  $|\eta| < 5$  (left),  $|\eta| < 4$  (middle),  $|\eta| < 3$  (right). Obtained using the RAPGAP generator developed at HERA and tuned to H1 and ZEUS data.

forward directions with an updated yoke design in the ePHENIX detector as discussed in Section B.5.1.

**Electromagnetic calorimeter:** A tungsten-scintillator sampling electromagnetic calorimeter with silicon photomultipliers (SiPMs) enables a compact barrel calorimeter positioned inside the bore of the superconducting solenoid. The calorimeter system provides full azimuthal coverage for  $|\eta| < 1$  with an energy resolution of  $\sim 12\%/\sqrt{E}$ . The readout is segmented into towers measuring roughly  $\Delta\eta \times \Delta\phi \sim 0.024 \times 0.024$ .

**Hadronic calorimeter:** A  $5\lambda_{\text{int}}$ -depth hadron calorimeter surrounds the solenoid. An iron-plate and scintillator sampling design provides an energy resolution of better than  $\sim 100\%/\sqrt{E}$  with full azimuthal coverage. It also serves as part of the magnetic flux return for the solenoid.

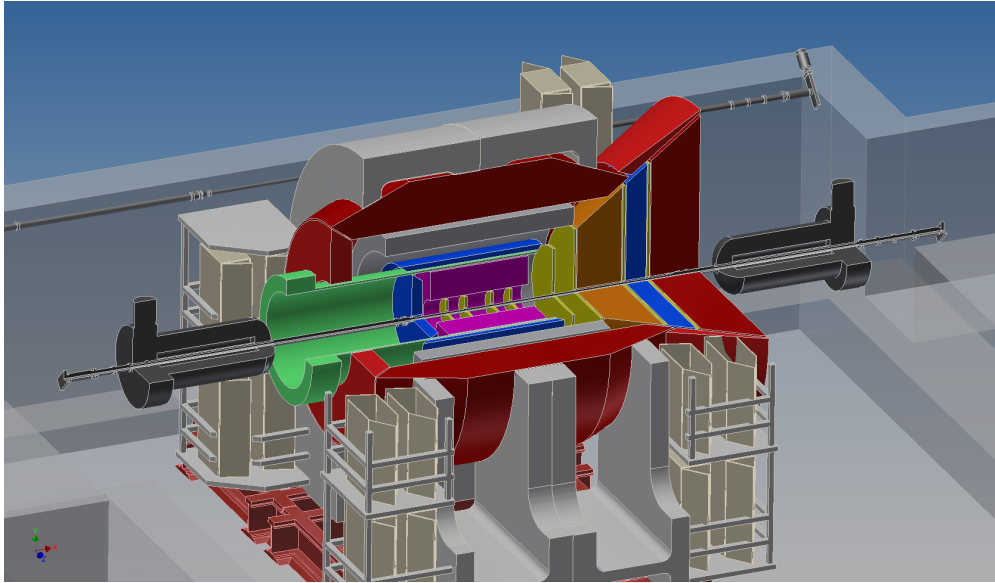


**Figure B.20:** Engineering rendering of ePHENIX in the PHENIX experimental hall. The drawing shows the location of the final eRHIC focusing quadrupoles as well as the electron bypass beamline behind the detector.

In addition, new subsystems will be added to the ePHENIX detector, which will be further discussed in this Section. These subsystems include:

**Electron going direction:** GEM detectors [200, 201] and lead-tungstate crystal electromagnetic calorimeters

**Central barrel:** Fast, compact TPC tracker and DIRC

**Hadron going direction:** GEM tracking system, gas-based RICH, aerogel-based RICH, beam-beam counter (BBC), electromagnetic and hadron calorimeter

**Beam line of hadron-going direction:** Roman pot detectors and a zero-degree calorimeter

### B.5.1 Magnet system

As with sPHENIX, ePHENIX is based around the BaBar superconducting solenoid [202] with no modifications to its inner structure. The major specifications for its coil are listed in Table B.2. A notable feature of the BaBar magnet is that the current density of the solenoid can be varied along its length, i.e., lower current density in the central region and higher current density at both ends. This is accomplished by using narrower windings (5 mm) for the last 1 m at both ends. The central winding uses 8.4 mm-width coils [202]. The main purpose of the graded current density is to maintain a high field uniformity in the bore of the solenoid, which is also a benefit for ePHENIX. This design feature enhances the momentum analyzing power in both the electron-going and hadron-going directions.

A magnetic flux return system, consisting of the forward steel/scintillator hadron calorimeter, a flaring steel lampshade, and a steel endcap not only returns the flux generated by the solenoid, but

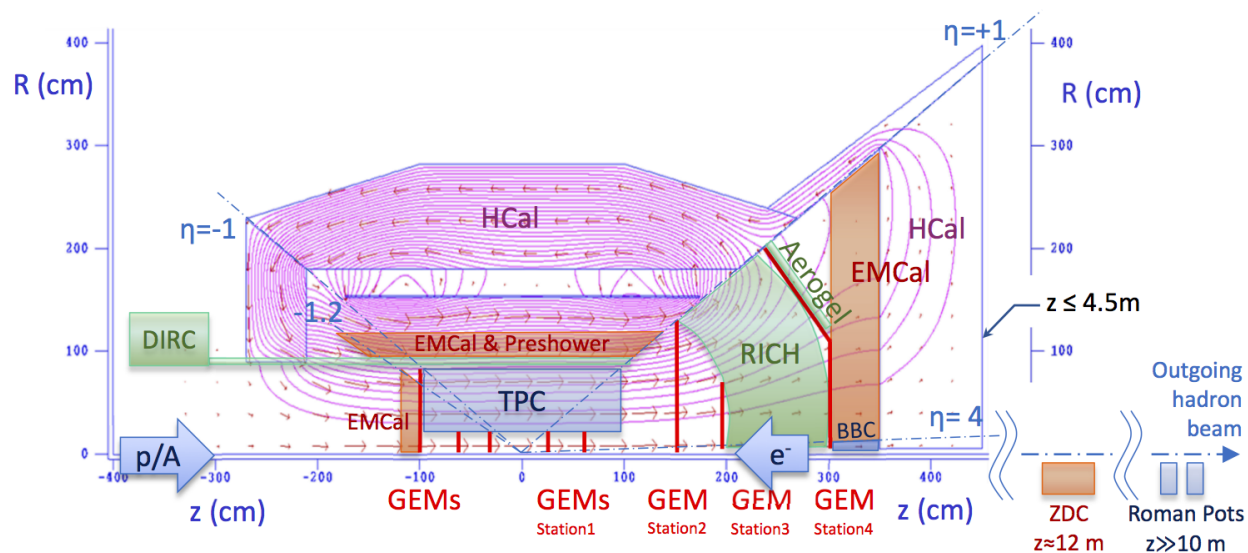


**Figure B.21:** A cross section through the top-half of the ePHENIX detector concept, showing the location of the superconducting solenoid, the barrel calorimeter system, the EMCAL in the electron-going direction and the system of tracking, particle identification detectors and calorimeters in the hadron-going direction. Forward detectors are also shown along the outgoing hadron beamline. The magenta curves are contour lines of magnetic field potential as determined using the 2D magnetic field solver, POISSON.

shapes the field in order to aid the momentum determination for particles in the hadron-going and electron-going directions. As shown in Figure B.21, the flux return system consists of the following major components:

- Forward steel/scintillator hadron calorimeter, at  $z = 3.5$  to  $4.5$  m
- Steel flux shaping lampshade, along the  $\eta \sim 1$  line
- Barrel steel/scintillator hadron calorimeter, from  $r = 1.8$  to  $2.8$  m
- Steel end cap, at  $z = -2.1$  to  $-2.7$  m and  $r > 90$  cm

The magnetic field lines were calculated and cross checked using three different 2D magnetic field solvers (POISSON, FEM, and OPERA) and are shown in Figure B.21. In the central region, a 1.5 Tesla central field along the electron beam direction is produced. The field strength variation within the central tracking volume is less than  $\pm 3\%$ .

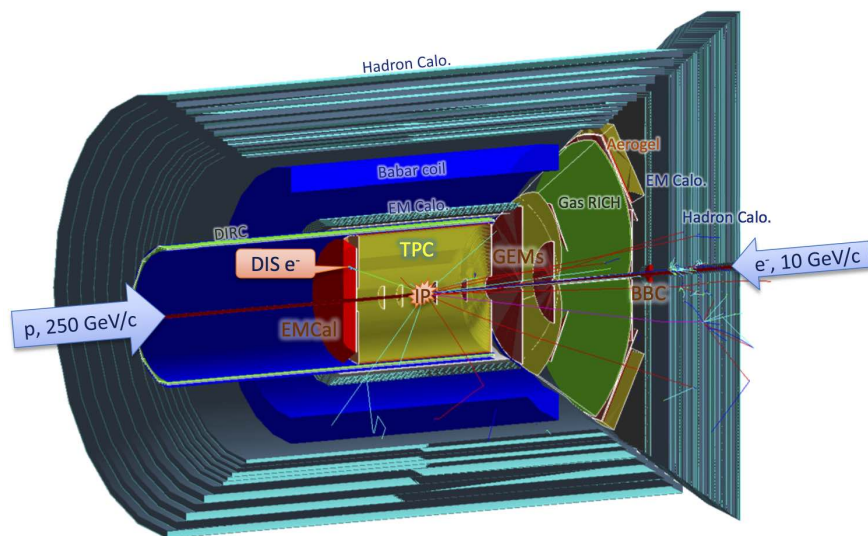


**Figure B.22:** The response of the ePHENIX detector to a single event, as determined using GEANT4. The field map in this simulation was determined using the 2D magnetic field solver OPERA. These same OPERA calculations were used to verify and validate the calculations underlying the magnetic field lines shown in Figure B.21.

**Table B.2:** Main characteristics of BaBar solenoid [202]

Central Induction	1.5 T
Winding structure	2 layers, 2/3 higher current density at both ends
Winding axial length	3512 mm
Winding mean radius	1530 mm
BaBar operation current	4596 A, 33% of critical current
Total turns	1067

### B.5.2 Vertex and Tracking

The  $z$ -location of the primary event vertex will be determined using a timing system enabling a precision of  $\Delta z \leq 5$  mm. The ePHENIX tracking system utilizes a combination of GEM and TPC trackers to cover the pseudorapidity range of  $-3 < \eta < 4$ . The momentum resolution for the full device is summarized in Figure B.23.



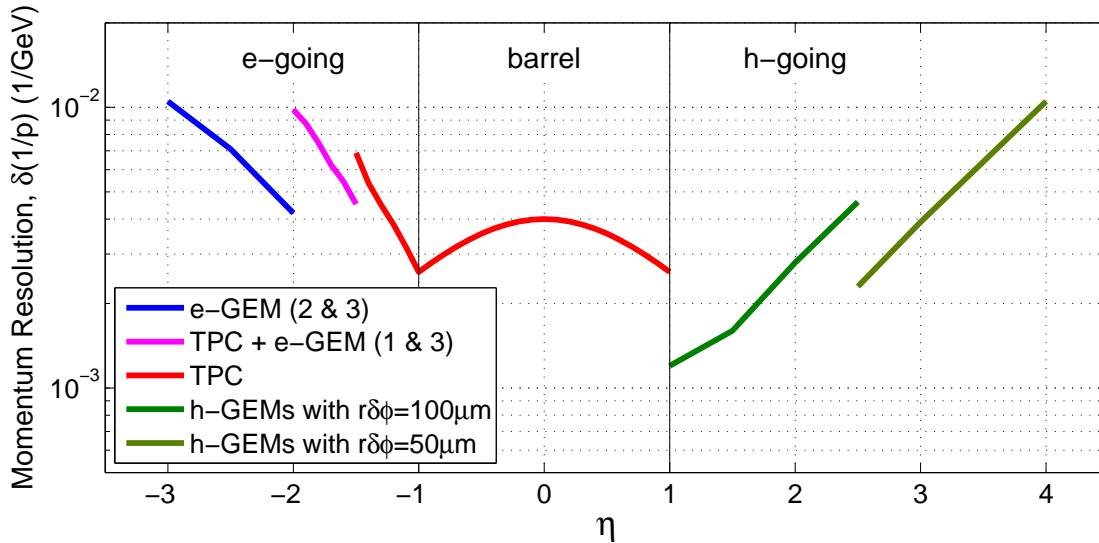


**Figure B.23:** Momentum resolution over the full pseudorapidity coverage of the planned tracking system in the high momentum limit. Multiple scattering contribution to the relative momentum resolution (not shown on the plot) was studied with GEANT4 simulation, and found to vary from below 1% at low pseudorapidity to  $\sim 3\%$  at  $|\eta|=3$ .

### Event vertex measurement

The vertex information is used for the determination of photon kinematics and for assisting the track fitting. Precise vertex information is important for momentum determination in the electron-going direction, where tight space constraints limit the possible number of tracking planes. The location of the vertex will be measured by:

- For non-exclusive processes, we propose to identify the  $z$ -location for the vertex using timing information from a BBC detector in the hadron-going direction in coincidence with the electron beam RF timing. The BBC detector covers  $\eta = 4-5$  at  $z = 3.0$  m. A timing resolution of 30 ps or better enables the measurement of the vertex with resolution of  $\Delta z = 5$  mm. It leads to a sub-dominant error for the momentum determination for the electron-going direction ( $\delta p/p = 2\%$ ). This timing resolution can be provided by the existing technology of Multigap Resistive Plate Chamber (MRPC) [203] or by microchannel plate detectors (MCP) photomultiplier [204] with a thin quartz Čerenkov radiator, a technology which is under active current development.
- We plan to measure the average transverse beam position by accumulating tracking information over the course of a one hour run. The statistical precision for the beam center determination is expected to be much smaller than the distribution of the transverse collision profile ( $\sigma_{x,y} \sim 80 \mu\text{m}$ ), and therefore a negligible contribution to the uncertainty for event-by-event vertex determination.



Tracking in the central region,  $-1 < \eta < 1$ 

A fast, compact Time Projection Chamber (TPC) will be used for tracking in the central region, occupying the central tracking volume of  $r = 15\text{--}80$  cm and  $|z| < 95$  cm and covering  $-1 < \eta < 1$ . A TPC will provide multiple high resolution space point measurements with a minimal amount of mass and multiple scattering. The design is based on a GEM readout TPC, similar to a number of TPCs that have either already been built or are currently under design. For example, the LEGS TPC [205] utilized a fine chevron-type readout pattern with a pad size of  $2\text{ mm} \times 5\text{ mm}$  and achieved a spatial resolution  $\sim 200\ \mu\text{m}$ . The use of such a readout pattern helps minimize the total channel count for the electronics and hence the total cost. The GEM TPC upgrade for ALICE [206, 207] and the large GEM readout TPC for ILC [208, 209] are other examples of large GEM TPCs that have recently been studied.

It is assumed that the TPC will have a single high voltage plane at  $z = 0$  cm and be read out on both ends, resulting in a maximum drift distance  $\sim 95$  cm. It will use a gas mixture with a fast drift time, such as 80% argon, 10%  $\text{CF}_4$  and 10%  $\text{CO}_2$ , which, at an electrical field of 650 V/m, achieves a drift speed  $\sim 10\text{ cm}/\mu\text{s}$ , and would result in a maximum drift time of 10  $\mu\text{s}$ . With a position resolution of  $\sigma(r\Delta\phi) = 300\ \mu\text{m}$  and 65 readout rows, the expected transverse momentum resolution would be  $\delta(1/p_T) = 0.4\% / (\text{GeV}/c)$  for high momentum tracks.

Tracking in hadron-going direction,  $\eta > 1$ 

The design of the magnetic flux return enables tracking in the hadron-going direction in the main and fringe fields of the BaBar magnet. Compared to a compact solenoid with no current density gradient, the BaBar magnet system improves the momentum analyzing power for forward tracks by about a factor of four due to two main factors: 1) the BaBar magnet has a length of 3.5 m, which provides a longer path length for magnetic bending; 2) the higher current density at the ends of the solenoid improves the magnetic field component transverse to forward tracks, and therefore provides higher analyzing power.

The tracking system at high  $\eta$  in the hadron-going direction utilizes four stations of GEMs.

- Station 1 consists of two planes with complementary  $\eta$  coverages. They are located at  $z = 17$  and 60 cm, respectively, covering a radius of  $r = 2\text{--}15$  cm.
- Stations 2–4 are at  $z = 150, 200, 300$  cm, respectively, covering  $\eta = 1\text{--}4$ .

The readout planes for these devices are optimized to preserve high position resolution in the azimuthal direction ( $\sim 200\ \mu\text{m}$  in  $r\delta\phi$  using a chevron-type readout with a pad size similar to the central TPC) and  $\sim 10\text{--}100$  mm in  $\delta r$ , while minimizing the readout channel cost. However, the  $r\text{-}\phi$  resolution can be improved to be better than  $100\ \mu\text{m}$ , even for tracks at larger angles (up to 45 degrees), by the use of mini-drift GEM detectors, in which a small track segment, or vector, is measured for each track at each measuring station. These detectors, which are currently under development [210], would provide improved position resolution with less material and lower cost than multiple stations of planar GEM detectors. For this letter, we assumed that a high resolution GEM readout pattern (1 mm wide chevron-type readout) with a  $r\delta\phi \sim 50\ \mu\text{m}$  for the

inner tracking region ( $\eta > 2.5$ ). For the outer tracking region ( $1 < \eta < 2.5$ ), mini-drift GEM with 2 mm chevron-type readout provide  $r\delta\phi \sim 100 \mu\text{m}$ . The momentum resolution is estimated in Figure B.23.

It should be noted that the size of the GEM trackers for Stations 2–4 are quite large ( $\sim 5\text{--}20 \text{ m}^2$ ). It is currently challenging to produce such large GEM foils and to do so at an affordable cost. However, there has been substantial progress in this area in recent years at CERN due to the need for large area GEM detectors for the CMS Forward Upgrade [211]. CERN has developed a single mask etching technology which allows fabrication of very large area GEMs (up to  $2 \text{ m} \times 0.5 \text{ m}$ ), and they plan to transfer this technology to various commercial partners (such as Tech Etch in the US, which supplied the GEM foils for the STAR Forward GEM Detector). We anticipate being able to procure such large area GEM detectors by the time they are needed for EIC.

Tracking in the electron-going direction,  $\eta < -1$

The electron direction tracking is designed to fit in the space limited by the DIRC ( $R < 80 \text{ cm}$ ) and the electromagnetic calorimeter ( $z > -100 \text{ cm}$ ). Three GEM tracking stations, located at  $z = 30, 55$  and  $98 \text{ cm}$ , are used in combination with the TPC and vertex information to determine the momentum vector.

- For  $\eta = -1.5$  to  $-1$ , TPC track segment and vertex are used
- For  $\eta = -2.0$  to  $-1.5$ , vertex, TPC track segment, GEM station 1 and 3 are used.
- For  $\eta = -3.0$  to  $-2.0$ , vertex, GEM station 2 and 3 are used.

Similar to the hadron-going direction, the position resolution for these detectors is  $r\Delta\phi \sim 50 \mu\text{m}$  for  $-3 < \eta < -2$  using 1 mm wide chevron-type readout. For  $-2 < \eta < -1$ , the mini-drift GEM technology [210] and 2 mm wide chevron-type readout provide  $r\delta\phi \sim 100 \mu\text{m}$ . The radial resolution is  $\delta r = 1 \text{ cm}$  (stations 1 and 2) and  $\delta r = 10 \text{ cm}$  (station 3). As shown in Figure B.23, a momentum resolution of  $\Delta p/p < 5\%$  can be achieved for tracks of  $p < 4 \text{ GeV}/c$  and  $-1 < \eta < -3$ , which is sufficient for the calorimeter  $E$ - $p$  matching cut for the electron identification. For DIS kinematics reconstruction the tracking radial resolution is not crucial as enough precision for scattered electron polar angle measurements will be provided by the EMCal, see Section B.4.2.

### B.5.3 Electromagnetic calorimeters

The ePHENIX detector will have full electromagnetic calorimeter coverage over  $-4 < \eta < 4$ . The sPHENIX barrel electromagnetic calorimeters will also be used in ePHENIX, covering  $-1 < \eta < 1$  with an energy resolution of  $\sim 12\%/\sqrt{E}$ . In addition, crystal and lead-scintillator electromagnetic calorimeter are planned for the electron-going and hadron-going direction, respectively. Optimization of the design of the barrel and endcap calorimeters will aim for uniform response in the overlap region between  $-1.2 < \eta < -1$ .

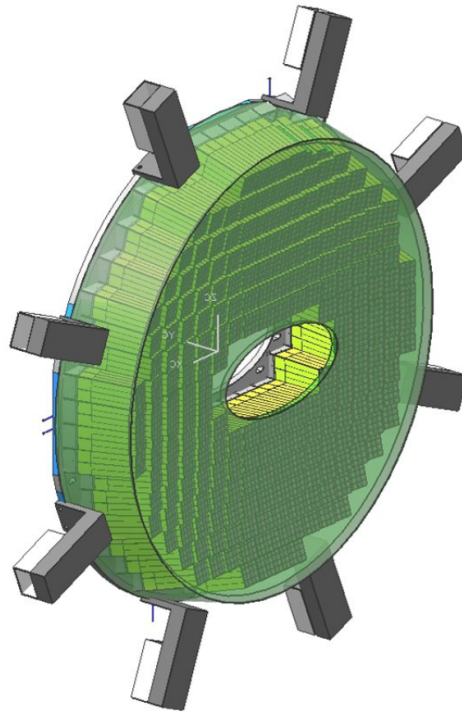


**Figure B.24:** PANDA Crystal Endcap Calorimeter [212]. The PWO crystal modules are shown in green color, which is projective towards the target.

### Crystal Electromagnetic calorimeter

The calorimeter on the electron-going side consists of an array of lead tungstate ( $\text{PbWO}_4$ ) crystals (commonly known as PWO), similar to the PANDA endcap crystal calorimeter shown in Figure B.24 [212]. An enhanced light output version of lead tungstate (PWO-II) was chosen to provide high light yield ( $\sim 20$  p.e./MeV at room temperature) at a moderate cost ( $\sim \text{€}5/\text{cm}^3$ ). It will provide an energy resolution  $\sim 1.5\%/\sqrt{E}$  and position resolution better than  $3 \text{ mm}/\sqrt{E}$  in order to measure the scattered electron energy and angle in the electron-going direction down to low momentum with high precision.

The ePHENIX PWO calorimeter will consist of  $\sim 5000$  crystals, compared with 4400 crystals for the PANDA endcap, and will have a similar size and shape to the PANDA crystals. They will be  $\sim 2 \text{ cm} \times 2 \text{ cm}$  (corresponding to one  $R_M^2$ ) and will be read out with four SiPMs. This is different than the PANDA readout, which uses large area ( $\sim 1 \text{ cm}^2$ ) APDs. The SiPMs will provide higher gain, thus simplifying the readout electronics, and will utilize the same readout electronics as the other calorimeter systems in sPHENIX. It is also expected that the cost of SiPMs will be less than that of APDs covering the same area by the time they are needed for ePHENIX.

### Lead-scintillator electromagnetic calorimeter

The electromagnetic calorimeter in the hadron-going direction consists of a lead-scintillating fiber sampling configuration, similar to the tungsten-scintillating fiber calorimeter in the central sPHENIX detector. Lead is used instead of tungsten in order to reduce the cost, but it is otherwise assumed to be of a similar geometry. It will cover the rapidity range from  $1 < \eta < 4$  and have  $0.3 X_0$  sampling (2 mm lead plates) with 1 mm scintillating fibers, which will give an energy resolution  $\sim 12\%/\sqrt{E}$ . The segmentation and readout will also be similar to the central tungsten calorimeter, with  $\sim 3 \text{ cm} \times 3 \text{ cm}$  towers (roughly  $1 R_M^2$ ) that are read out with SiPMs. This segmentation leads to  $\sim 26\text{K}$  towers. By using the same type of readout as the central calorimeter, the front end electronics and readout system will also be similar, resulting in an overall cost savings for the combined calorimeter systems.

#### B.5.4 Hadron calorimeter

The hadron calorimeter in the hadron-going direction consists of a steel-scintillating tile design with wavelength shifting fiber readout, similar to the central sPHENIX hadron calorimeter. It will be  $\sim 5 L_{abs}$  thick and cover a rapidity range from  $1 < \eta < 5$ . The steel in the absorber will also serve as part of the flux return for the solenoid magnet. The segmentation will be  $\sim 10 \text{ cm} \times 10 \text{ cm}$ , resulting in  $\sim 3000$  towers. The readout will also be with SiPMs, similar to the central sPHENIX HCAL, which will again provide an advantage in being able to use a common readout for all of the calorimeter systems.

#### B.5.5 Hadron PID detectors

Hadron PID is planned for the hadron-going and barrel regions, covering  $-1.2 < \eta < 4$ . In the hadron-going direction, two PID detectors cover complementary momentum range: a gas-based RICH detector for the higher momentum tracks and an aerogel-based RICH detector for the lower momentum region. As in the BaBar experiment [213], a DIRC detector identifies hadron species in the central barrel. In addition, the TPC detector assists with PID by providing  $dE/dx$  information for the low momentum region.

#### Gas RICH detector

High momentum hadron PID is provided by an optically focused RICH detector using a gas radiator. The main features for this RICH setup are

- One meter of  $\text{CF}_4$  gas is used as the Čerenkov radiator. The pion, kaon and proton thresholds are 4, 15 and 29 GeV, respectively.
- Čerenkov photons are focused to an approximately flat focal plane using spherical mirrors of 2 m radius, as shown in Figure B.26. The geometric center of the mirror is at  $(r, z) = (40 \text{ cm}, 100 \text{ cm})$ , as highlighted by the blue dot.

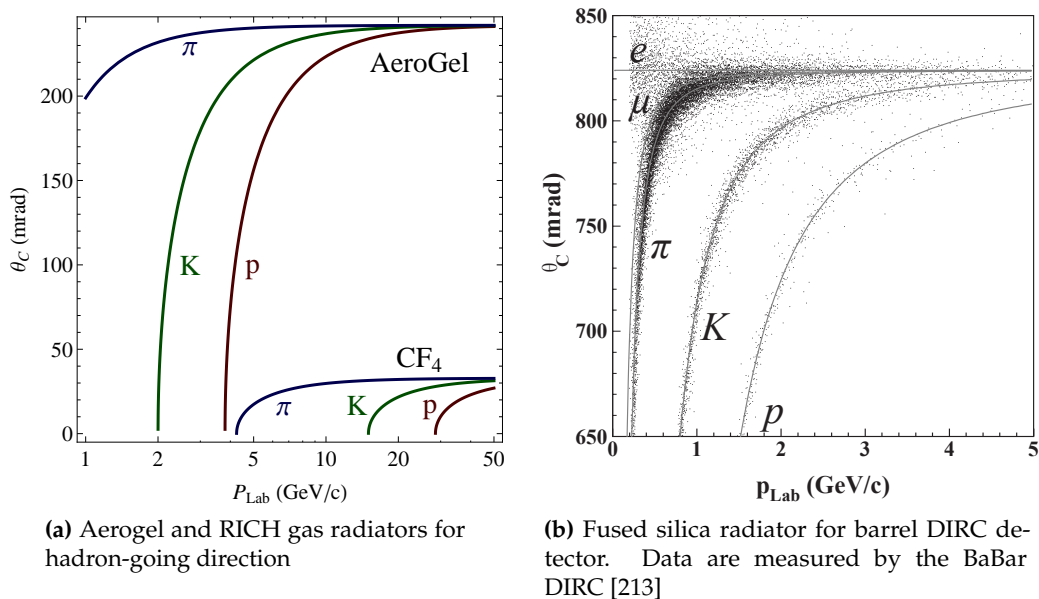


**Figure B.25:** Čerenkov angle versus momentum for various particle species.

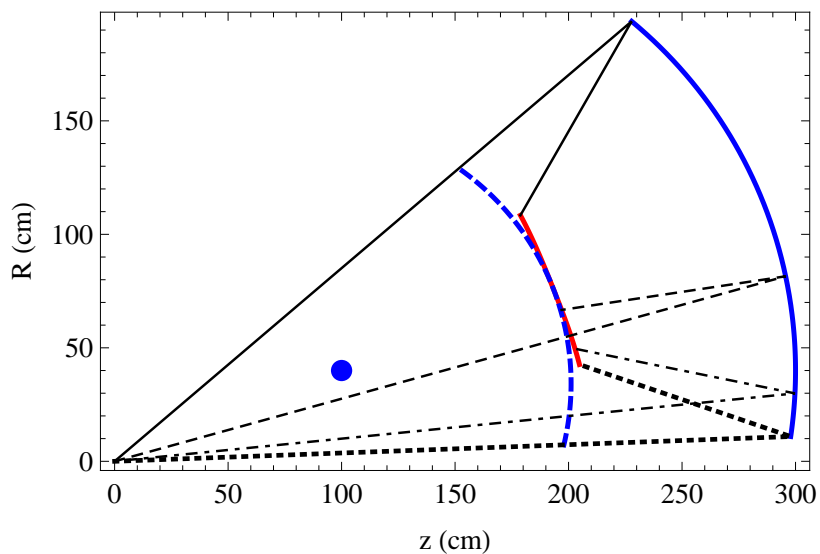


**Figure B.26:** The cross-section of the gas-based RICH detector in the  $r$ - $z$  plane that crosses the mirror center. The interaction point is centered at  $(0,0)$ . The geometric center of the mirror is shown as the blue dot at  $(r,z) = (40 \text{ cm}, 100 \text{ cm})$ . The mirror and RICH entrance window are shown by the solid and dashed blue curves, respectively. Several example tracks and the central axis of their Čerenkov light cone are illustrated by the black lines. The Čerenkov photons are reflected by the mirror to the focal plane, shown in red.

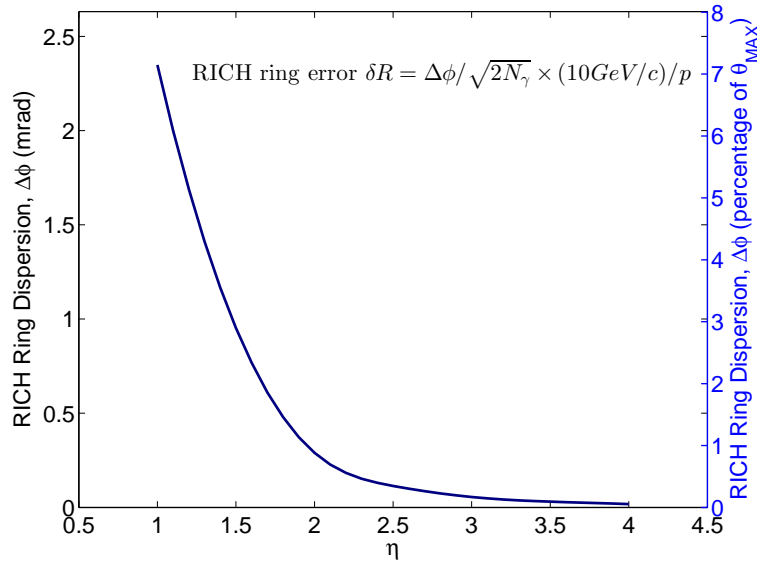


**Figure B.27:** Azimuthal angular dispersion of gas-based RICH ring due to fringe magnetic field for a  $p = 10 \text{ GeV}/c$  track. It is compared to the maximum RICH ring angle as shown on the right vertical axis.

- There are six azimuthal segmented RICH sextants.
- The photon detector consists of CsI-coated GEM detectors [214], which are installed on the focal plane. The CsI coating converts the Čerenkov photons into electrons which are then amplified by the GEM layers and readout through mini-pads. The photon detector for each RICH sextant assumes a roughly triangle shape and covers an area of  $0.3 \text{ m}^2$ .

Two distortion effects were estimated to be sub-dominant in error contributions for most cases:

- Strong residual magnetic field ( $\sim 0.5 \text{ Tesla}$ ) are present in the RICH volume. This field will bend the tracks as they radiate photons, and therefore smear the Čerenkov ring in the azimuthal direction. However, the field design ensures that the field component is mostly parallel to the track inside RICH and therefore this smearing effect is minimized. The RMS size of the smearing,  $\Delta\phi$ , is evaluated as in Figure B.27. The uncertainty contribution to the RICH ring angular radius is  $\delta R = \Delta\phi / \sqrt{2N_\gamma} (10 \text{ GeV}/c) / p$ , which is sub-dominant comparing to the photon measurement error for  $\eta > 1.5$ . The field contribution was included in the RICH performance estimation.
- For tracks that originate from an off-center vertex, their focal point may be offset from the nominal focal plane as shown in Figure B.26. The effect is  $\eta$  dependent. For the most extreme case, that a track of  $\eta = 1$  originates from the vertex of  $z = 40 \text{ cm}$  (1.5 sigma of expected vertex width), an additional relative error of  $5\% / \sqrt{N_\gamma}$  is contributed to the ring radius measurement, which averages over all vertices to below  $2\% / \sqrt{N_\gamma}$  contribution. For high  $\eta$  tracks, the difference is negligible comparing to the nominal RICH error.

We simulated the RICH performance with a radiator gas  $\text{CF}_4$  (index of refraction 1.00062). We use PYTHIA to generate the momentum distributions for pions, kaons, and protons. For each particle species, we use the momentum resolution and RICH angular resolution, to calculate the particle mass  $m(p, \theta_{Crk})$  distribution. For higher momentum tracks the combined information from tracking system and energy deposit in HCal helps to improve momentum resolution particularly at higher rapidities, where momentum resolution from tracking degrades. For example, at pseudorapidity  $\eta=4$ , the tracking momentum resolution for 50 GeV/c tracks is  $\sim 50\%$  (see Figure B.23), while HCal can provide energy measurements with precision  $100\% / \sqrt{50[\text{GeV}]} \sim 14\%$ . Our simulation showed that the HCal is very effective in improving the resolution for high momentum track measurements even when this and other tracks (usually with lower momenta) are merged in a single cluster of deposited energy in HCal. In such a case, the contribution of lower energy tracks in HCal can be evaluated and subtracted based on momentum measurements in tracking system.

Figure B.28 shows mass distributions for the most challenging high rapidity region  $\eta=4$  for different reconstructed track momenta. We make a symmetric 90% efficiency cut on the mass distributions, and calculate the purity for  $\pi, K, p$ , shown in Figure B.29. One can see high purity for all particle species up to momenta  $\sim 50$  GeV/c. Introducing asymmetric cuts on the mass distributions (and sacrificing some efficiency) extends further our capabilities for high purity hadron identification.

It is notable that the limitation on the mass resolution comes from the estimated 2.5% radius resolution per photon for the RICH from the EIC R&D RICH group. Our calculation includes the effect of the magnetic field distortion mentioned above, which is sub-dominant. This is a somewhat conservative estimate and LHCb and COMPASS have quoted values near 1% per photon. The R&D effort is working towards the best radius resolution, though there are challenges in having the light focus and readout within the gas volume in this configuration compared with LHCb or COMPASS.

### Aerogel RICH detector

The aerogel detector will provide additional particle ID for kaons in the momentum range  $\sim 3$ –15 GeV/c when used in conjunction with the gas RICH. Pions can be identified by the signal they produce in the gas RICH starting at a threshold of  $\sim 4$  GeV/c, and kaons will begin producing a signal in the aerogel at a threshold  $\sim 3$  GeV. Reconstructing a Čerenkov ring in the aerogel enables one to separate kaons from protons up to a momentum  $\sim 10$  GeV/c with reduced efficiency above that.

Measuring a ring in the aerogel detector is a challenging technical problem for a number of reasons. Due to its relatively low light output, it will require detecting single photons in the visible wavelength range with high efficiency inside the rather strong fringe field of the superconducting solenoid. Also, due to the limited space available, it is difficult to have a strong focusing element in the RICH to focus the light into a ring in a short distance. One possibility for how this might be accomplished has been proposed by the Belle II experiment [215] and is shown in Figure B.30. It uses several layers of aerogel with slightly different indices of refraction to achieve and approximate focusing of the light onto an image plane located behind the radiator. It should be possible to add additional layers of aerogel and optimize their thickness for producing the best quality ring for kaons using this technique, and therefore achieve good kaon-proton separation up to the highest momentum. One possibility for the photon detector would be large area Microchannel Plate detectors (MCPs), such as those being developed by the Large Area Picosecond Photodetector

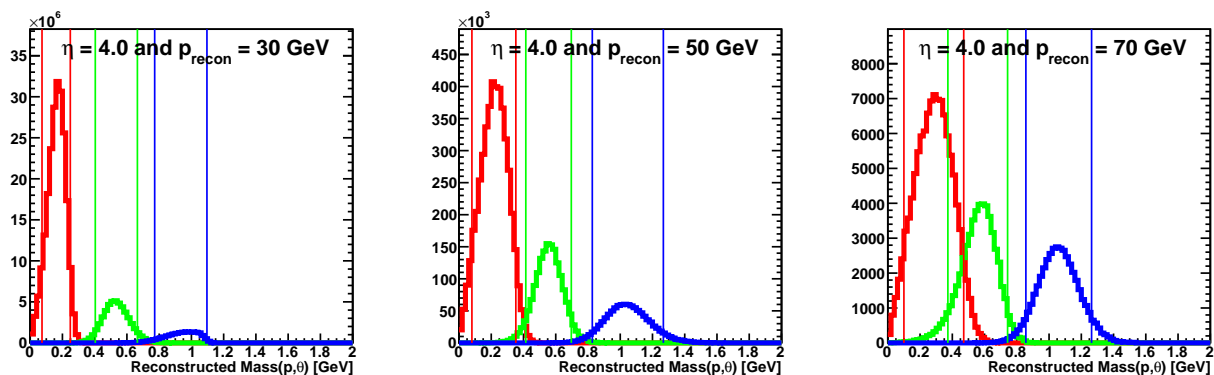


**Figure B.28:** Reconstructed mass distribution via  $m(p, \theta_{Crk})$  at  $\eta = 4$  for reconstructed momenta 30 GeV/c (left), 50 GeV/c (middle) and 70 GeV/c (right), for pions (red), kaons (green) and protons (blue), with the parent momentum and particle abundances from the PYTHIA generator. Vertical lines indicate the symmetric mass cuts corresponding to 90% efficiency. Note that particle true momentum is on the average smaller than reconstructed momentum, see Figure B.29.

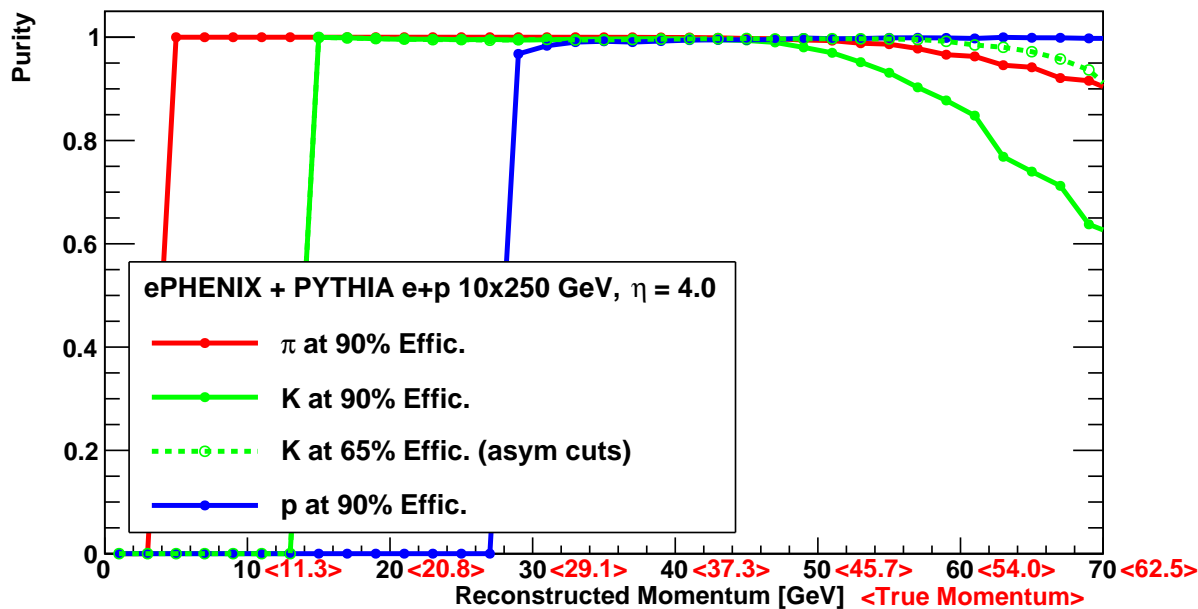


**Figure B.29:**  $\pi, K, p$  purities at pseudorapidity 4.0 as a function of reconstructed momentum, based on symmetric cut on reconstructed mass corresponding to 90% efficiency (solid lines), and asymmetric cut with stricter selection on the kaons with efficiency 65% (dashed line); Also indicated in angle brackets are the values of the average true momentum at each reconstructed momentum, which are different due to momentum smearing and sharply falling momentum spectra.



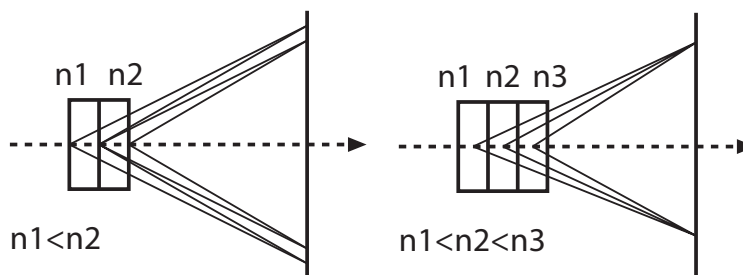


**Figure B.30:** Approximate focusing method using two (left) and three (right) layers of aerogel with slightly different indices of refraction proposed by Belle II [215]

(LAPPD) Collaboration [204]. This effort is based on utilizing flat panel screen technology to produce large area MCPs at very low cost, while also preserving their excellent timing resolution (typically  $\sim 20$ -30 ps). These devices would use multi-alkali photocathodes, which would be suitable for detecting the Cherenkov light from aerogel with high efficiency, and also provide high gain for detecting single photoelectrons. The excellent time resolution would also provide additional time of flight capability when used in conjunction with the BBC to further enhance hadron particle ID. While this is still an R&D effort, it has already produced very encouraging results and has substantial support within the high energy physics community, and we feel that this would offer an attractive low cost, high performance readout for the aerogel detector.

## DIRC

The main form of particle ID in the central region will be provided by a DIRC (Detection of Internally Reflected Čerenkov Light). The DIRC will be located at a radius of  $\sim 80$  cm and extend  $\sim 8$ -10 cm in the radial direction. As we will be using the BaBar magnet for ePHENIX, it would be a major benefit to also acquire the BaBar DIRC, which was specifically designed to fit inside this magnet, and would completely satisfy the physics requirements for ePHENIX. However, since it is not certain at this time that the BaBar DIRC will be available for ePHENIX, we consider it more as a model for the type of DIRC that would be required in terms of its construction and performance.

The BaBar DIRC, shown in Figure B.31, consists of 144 precision fabricated quartz radiator bars that collect Čerenkov light produced by charged particles traversing the bars. In the BaBar DIRC, the quartz bars were read out on one end utilizing a large water filled expansion volume to allow the light to spread out and be read out using a large number (over 10,000) 28 mm diameter photomultiplier tubes.

The BaBar design, while allowing for a conventional PMT readout without the use of any focusing elements, requires a large expansion volume and this places stringent demands on the mechanical specifications for the detector. After the shutdown of BaBar at SLAC, it was proposed to use the DIRC in the SuperB Experiment in Italy. In doing so, it was also proposed to convert the original DIRC into a Focusing DIRC (FDIRC) [216], which would utilize mirrors at the end of the radiator bars, allowing for a considerable reduction in the size of the expansion region, more highly pixellated PMTs, and an overall expected improvement in performance. We would therefore propose the same modification of the BaBar DIRC for ePHENIX, or would construct a similar FDIRC if the BaBar DIRC were not available.

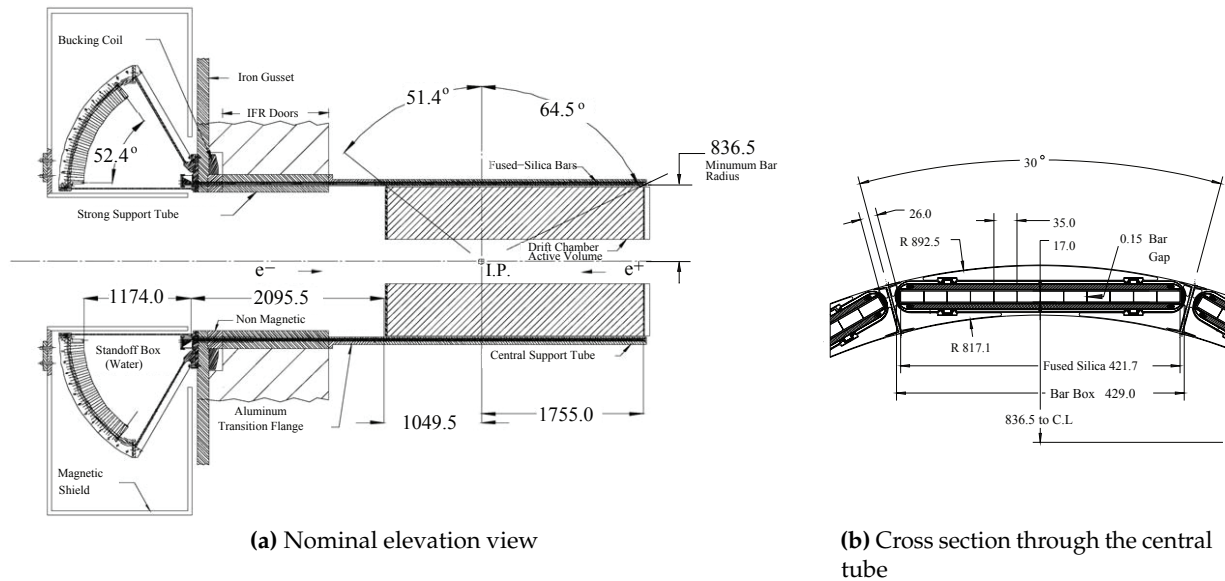


**Figure B.31:** BaBar DIRC geometry [213]. All dimensions are given in mm.

Similar to the BaBar technique [213], the hadron PID in the barrel will be analyzed using an event likelihood analysis with the DIRC and TPC  $dE/dx$  information simultaneously. A  $dE/dx$  measurement in the TPC gives very good hadron separation for very low momentum particles. But the ability of that technique to separate  $K-\pi$  and  $p-K$  drops off quickly around  $0.5 \text{ GeV}/c$  and  $0.8 \text{ GeV}/c$ , respectively. Meanwhile, the pions and kaons exceed their respective DIRC Čerenkov thresholds in this momentum region, as shown in Figure B.25. Therefore, the DIRC sensitivity for  $K-\pi$  and  $p-K$  turns on sharply. A combined analysis of both pieces of information can give high PID purity up to a few  $\text{GeV}/c$ , as shown by the BaBar experiment [213]. At higher momenta, the DIRC ring resolution limits the separation capability. As shown in Figure B.32, the  $K-\pi$  and  $p-K$  separation gradually drops below plateau above momentum of 2 and 5  $\text{GeV}/c$ , respectively. A  $\sim 20\%$  pion and kaon efficiency can still be maintained at 5  $\text{GeV}/c$ . The vast majority of hadron kinematics in SIDIS can be covered in the  $5 \times 100 \text{ GeV}/c$  collisions. In the  $10 \times 250 \text{ GeV}/c$  collisions, the low to intermediate- $z$  region in SIDIS are still well covered by this design.

### B.5.6 Beamline detectors

Two detectors will be installed near the outgoing hadron beam, downstream of the ePHENIX detector. They will be included in the eRHIC machine lattice design [190].

**Zero Degree Calorimeter:** A Zero Degree Calorimeter (ZDC) is planned for the hadron-going direction for the ePHENIX IP. Consistent with the eRHIC IR design (Figure B.33), the ZDC will be installed about 12 meters downstream of the IP centered on the hadron direction at the IP. A 5 mrad cone opening of the IP is guaranteed by the ePHENIX detector and beam line magnets. The ZDC for the current PHENIX experiment [218] and its design can be reused for this device.

**Roman Pots:** In exclusive deep inelastic  $e+p$  scattering, the final state proton will have a small

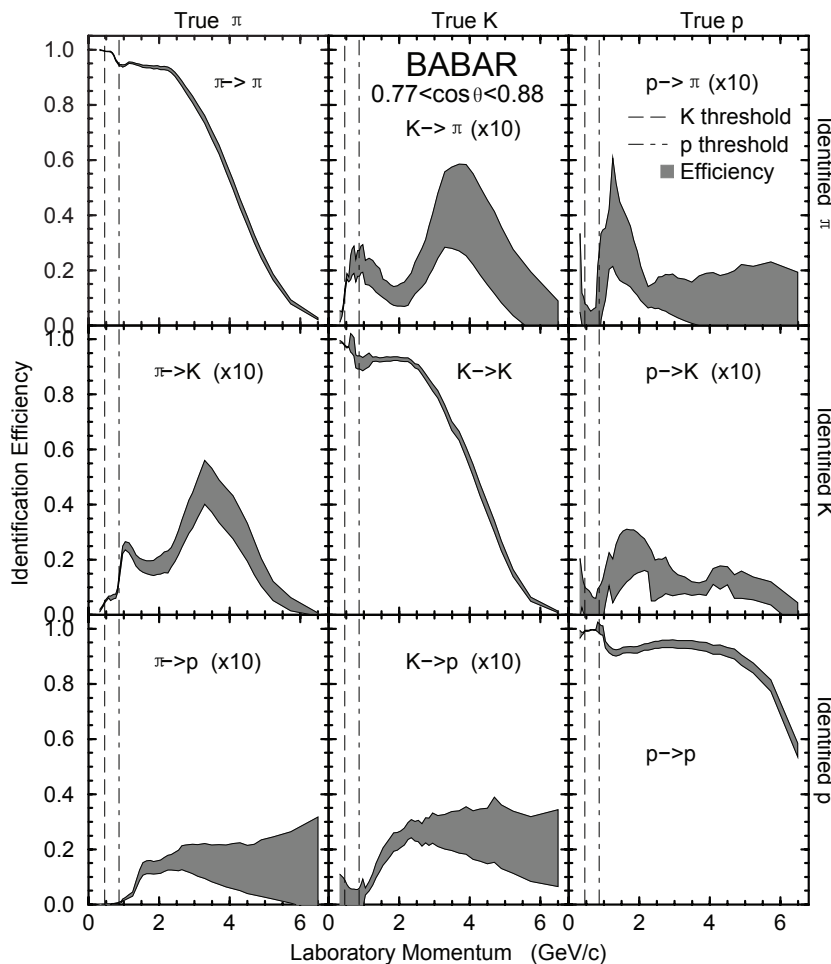


**Figure B.32:** Simulated PID Efficiency matrix and its uncertainty for  $1.0 < \eta < 1.4$  region, utilizing combined information of the BaBar DIRC and  $dE/dx$  measured in the tracking detector [213]. Note that the off-diagonal efficiency values are scaled by a factor of 10.

scattering angle and escape the main ePHENIX detector. Two silicon tracking stations (also called the Roman Pot spectrometer) will be installed close to the beam, inside the beam pipe, downstream in the hadron-going direction to capture such protons. Each of the ePHENIX Roman Pot stations utilizes four tracking modules to cover the full azimuthal angles. Each of the tracking modules can use the design of the existing STAR Roman Pots [219]. Depending on the eRHIC lattice and magnet design, their location will be around 20 meters from the IP. This Roman Pot spectrometer will provide high efficiency for the exclusive DIS events in the  $e+p$  collisions.

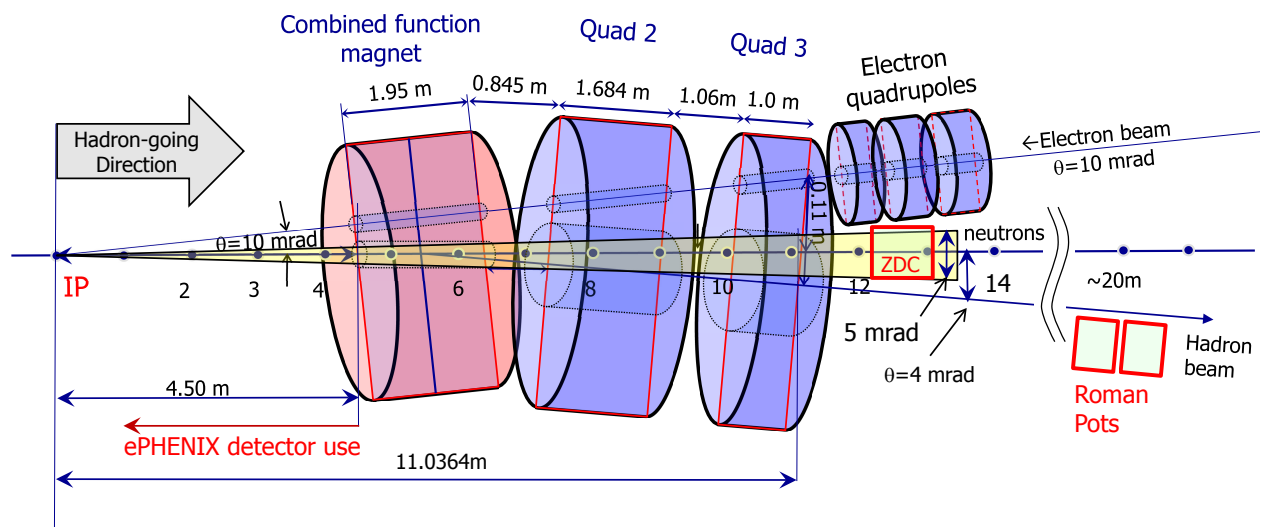


**Figure B.33:** Floor plan showing the locations of ZDC and Roman Pots relative to the ePHENIX interaction point. One layout of the interaction point magnets is also shown [217].

# List of Tables

3.1	Key characteristics of the BaBar solenoid and cryostat. . . . .	62
3.2	The parameters of the reference configuration tracking layers. . . . .	82
4.1	The yields of the three $\Upsilon$ states obtained in 10 weeks of $p+p$ , 22 weeks of Au+Au and 10 weeks of $p+Au$ RHIC running . . . . .	146
B.1	Detector requirements . . . . .	172
B.2	Main characteristics of BaBar solenoid [202] . . . . .	187



# List of Figures

1	Conceptual diagram of sPHENIX physics . . . . .	ii
2	Engineering drawing of sPHENIX, showing the superconducting solenoid containing the electromagnetic calorimeter and surrounded by the hadronic calorimeter . . .	iii
1.1	$E/3p$ and $p/T^4$ vs temperature . . . . .	1
1.2	$\eta/s$ and $T^3/\hat{q}$ vs inverse 't Hooft coupling . . . . .	4
1.3	Pushing and probing the quark-gluon plasma along three axes . . . . .	5
1.4	$\eta/s$ vs $T/T_c$ for water, nitrogen, and helium . . . . .	6
1.5	$\eta/s$ vs $T/T_c$ for various quark-gluon plasma calculations . . . . .	7
1.6	$\hat{q}$ vs $T/T_c$ in weak and strong coupling scenarios . . . . .	8
1.7	Calculations of $\hat{q}/T^3$ vs temperature, constrained by RHIC and LHC $R_{AA}$ data — including near $T_C$ enhancement scenarios of $\hat{q}/T^3$ . . . . .	9
1.8	Magnetic Monopole/CUJET 3.0 result for $\hat{q}/T^3$ vs temperature, constrained by RHIC and LHC $R_{AA}$ data . . . . .	10
1.9	Experimental $\pi^0$ $v_2$ and $R_{AA}$ along with calculations from four weakly coupled energy loss models . . . . .	11
1.10	Statistical reach of azimuthally-sensitive hard probes in sPHENIX . . . . .	12
1.11	Interaction scale for the interaction of partons with the quark-gluon plasma and possibilities for the recoil objects . . . . .	13
1.12	$T\hat{e}/\hat{q}$ as a function of the mass of the effective scattering centers in the medium . . .	14
1.13	Calculations by Coleman-Smith of the jet energy profile as a function of radius for leading and sub-leading jets . . . . .	15
1.14	$A_J$ distributions by Vitev et al. for leading jet $E_T > 50$ GeV, jet cone radius, $R = 0.6$ , and different medium coupling strengths . . . . .	16
1.15	Jet virtuality evolution in medium at RHIC and LHC . . . . .	17
1.16	The nuclear modification factor $R_{AA}$ vs transverse momentum at the SPS, RHIC, and LHC, compared to various jet quenching calculations . . . . .	18

1.17 Preliminary CMS results of jet and charged particle $R_{AA}$ in $p+A$ and Pb+Pb . . . . .	19
1.18 Scale probed in the medium via high energy partons as a function of the local temperature in the medium . . . . .	20
1.19 ATLAS $A_J$ and dijet $\Delta\phi$ distributions . . . . .	22
1.20 Fraction of dijets with $A_J < 0.15$ in Pb+Pb collisions as a function of centrality from CMS . . . . .	23
1.21 ATLAS results on the change in balance of direct photons and jets and CMS results on the $R_{AA}$ for beauty tagged jets in Pb+Pb collisions at the LHC . . . . .	23
1.22 The away-side momentum difference, $D_{AA}$ , of hadrons between Au+Au and $p+p$ events, as measured by STAR . . . . .	24
1.23 Slide from G. Roland's talk at the QCD Town Meeting (September 2014) contrasting preliminary RHIC results from STAR for jet $R_{AA}$ and dijet asymmetry $A_J$ with LHC results . . . . .	25
1.24 Dijet surface bias in YaJEM for various trigger definitions . . . . .	27
1.25 Dijet $A_J$ in VNI parton cascade compared to the CMS data and calculation for RHIC energies of $A_J$ for different values of $\alpha_s$ . . . . .	27
1.26 Determination of effective coupling strength in the model of Coleman-Smith. . . . .	28
1.27 Calculation by Coleman-Smith of dijet asymmetry $A_J$ for leading jets with $E_T > 20$ GeV as the medium temperature is varied and as the jet cone radius is varied at fixed temperature . . . . .	29
1.28 Calculations by Qin et al. of dijet $A_J$ for $E_{T,1} > 20$ GeV and $E_{T,2} > 5$ GeV for $R = 0.2, 0.4$ jets . . . . .	29
1.29 Calculations from Qin et al. of jet $R_{AA}$ for central and mid-central collisions for $R = 0.2, 0.4$ jets . . . . .	30
1.30 $A_J$ distributions in MARTINI+MUSIC and in the model of Qin et al. at LHC and RHIC energies . . . . .	31
1.31 Calculations by Vitev et al. for the inclusive jet $R_{AA}$ vs jet energy and radius . . . . .	32
1.32 Calculations of jet $R_{AA}$ vs $p_T$ for central collisions at the LHC and at RHIC using the hybrid strong coupling approach of Casalderrey-Solana et al . . . . .	32
1.33 Compilation of results for jet and hadron observables at RHIC and the LHC using the JEWEL parton shower Monte Carlo . . . . .	34
1.34 Calculations by Vitev et al. of the vacuum and medium modified distribution for direct photon triggered reconstructed jet events at LHC and RHIC energies . . . . .	35
1.35 Calculations by Vitev et al. of the jet $R_{AA}$ opposite to a tagged direct photon in Au+Au collisions at 200 GeV and Pb+Pb collisions at 2.76 TeV . . . . .	36



1.36	Q-PYTHIA simulation with quenching parameter $\hat{q} = 0$ and $\hat{q} = 10 \text{ GeV}/c^2$ for the fragmentation function of light quark and gluon jets as a function of $z$ . . . . .	36
1.37	The modified fragmentation function for $p_T > 100 \text{ GeV}$ jets in central Pb+Pb collisions vs $z$ from ATLAS and vs $\zeta$ from CMS . . . . .	37
1.38	Comparison of the fraction of quark and gluon jets from leading order pQCD calculations for RHIC and LHC energies. . . . .	38
1.39	The muon stopping power in copper . . . . .	38
1.40	FONLL calculations of heavy flavor jets, fragmentation hadrons, and decay electrons vs $p_T$ . . . . .	39
1.41	CUJET calculations of $R_{AA}$ in central Au+Au collisions at RHIC and in Pb+Pb collisions at the LHC, with light, charm and beauty hadrons and electrons shown as separate curves. . . . .	40
1.42	Calculations by Vitev et al. of beauty tagged jets showing the sensitivity to radiative and collisional energy loss contributions . . . . .	41
1.43	$D$ meson fragmentation function in PYTHIA and Q-PYTHIA for anti- $k_T$ jets with $R = 0.4$ and $E_T^{\text{jet}} > 20 \text{ GeV}$ as a function of $z$ . . . . .	42
1.44	Fraction of inclusive $b$ -jets, as a function of jet $p_T$ , originating from the pair creation, flavor excitation and gluon splitting modes in $\sqrt{s} = 200 \text{ GeV}$ PYTHIA events . . . . .	42
1.45	Comparison of nuclear modification measured by PHENIX and ALICE, showing that suppression is much stronger at the lower energy . . . . .	44
1.46	Hydrodynamic simulations by Habich et al. of temperature vs time in Au+Au and Al+Al collisions at 200 GeV and Pb+Pb collisions at 2.76 TeV . . . . .	45
1.47	Calculations for Upsilon state suppression at RHIC and LHC energies vs collision centrality . . . . .	45
1.48	Comparison of $\psi'$ nuclear modification measured by PHENIX and ALICE, showing very similar suppression at RHIC and LHC energies. . . . .	47
1.49	Jet, photon and $\pi^0$ rates for $ \eta  < 1.0$ from NLO pQCD calculations scaled to Au+Au central collisions for $\sqrt{s_{NN}} = 200 \text{ GeV}$ . . . . .	49
1.50	NLO pQCD calculations of direct photons and $\pi^0$ for RHIC and LHC, compared to PHENIX measurements of direct $\gamma$ to $\pi^0$ ratio in $p+p$ (Au+Au or Pb+Pb) collisions . . . . .	50
1.51	Statistical projections of $R_{AA}$ for hard probes in central Au+Au events with the sPHENIX detector after two years of data-taking, and kinematic reach of various jet quenching observables from previous and future RHIC and LHC data-taking . . . . .	51
2.1	End view of the sPHENIX detector with its component subdetectors . . . . .	53

2.2	Pseudorapidity distribution of PYTHIA jets reconstructed with the FASTJET anti- $k_T$ and the fraction of events in which the leading and subleading jet are in the specified acceptance . . . . .	56
2.3	Acceptance increase for various processes for the proposed sPHENIX barrel detector compared with the current PHENIX central arm spectrometers . . . . .	56
3.1	Engineering drawing of sPHENIX, showing the superconducting solenoid containing the electromagnetic calorimeter and surrounded by the hadronic calorimeter, with a model of the associated support structure . . . . .	61
3.2	The BaBar solenoid in its transfer frame for shipping at SLAC in May, 2013. . . . .	63
3.3	Calculation of the magnetic field from the solenoid with the flux returned by the hadronic calorimeter. . . . .	64
3.4	View of a prototype electromagnetic calorimeter module with fibers embedded before light guides are installed . . . . .	65
3.5	Energy resolution achieved in beam tests of a prototype electromagnetic calorimeter compared with GEANT4 simulation . . . . .	66
3.6	Average fractional energy contained in a block of iron vs block thickness . . . . .	67
3.7	Cross section of sPHENIX. The outer hadronic calorimeter surrounds the solenoid cryostat. . . . .	68
3.8	Scintillating tiles in the sampling gap of sPHENIX hadronic calorimeter, showing the transverse segmentation into elements 0.1 units of pseudorapidity wide. . . . .	68
3.9	Grooved scintillating tiles for inner HCal section, showing the path of the fiber and the uniform thickness of the tiles. This was the design of the tile used in the prototype. . . . .	69
3.10	Measurement of uniformity of light collection in an sPHENIX prototype tile measured with a $^{90}\text{Sr}$ source at the University of Colorado. . . . .	70
3.11	GEANT4 event display showing the fiber matrix and an electron shower development in the calorimeter. . . . .	72
3.12	Transverse view of a 10 GeV/ $c$ electron in sPHENIX, showing it showering mainly in the EMCal . . . . .	72
3.13	Distribution of energy deposited in the electromagnetic calorimeter for single towers and in $3 \times 3$ arrays of towers in central HIJING events . . . . .	73
3.14	Transverse view of a 10 GeV/ $c$ $\pi^-$ in sPHENIX. It penetrates the EMCAL and magnet and showers in the first segment of the HCal. . . . .	73
3.15	Energy occupancy distribution for the inner and outer hadronic calorimeter sections in 10% central Au+Au HIJING events run through the full GEANT4 simulation. . . . .	74

3.16	Energy deposited in the three longitudinal segments of the calorimetry by 32 GeV/ $c$ charged pions, showing the good containment and Gaussian response of the calorimeter . . . . .	75
3.17	Energy resolution and linearity of the full calorimeter as a function of incident hadron energy . . . . .	75
3.18	Block diagram of a temperature compensating circuit for SiPMs . . . . .	77
3.19	SPICE simulation of a prototype temperature compensating circuit for SiPM readout of the sPHENIX EMCal and HCal. . . . .	78
3.20	Block diagram of read out electronics based on electronics designed for the HBD. . .	79
3.21	Block diagram of 64 channel ADC board based on design of the HBD system. . . . .	80
3.22	Current-day and reconfigured arrangement of silicon tracking layers in the PHENIX VTX . . . . .	81
3.23	Full GEANT4 simulation and track model evaluation of single pion $p_T$ resolution . .	83
3.24	Fraction of primary tracks producing hits in all seven tracking layers that are reconstructed and fraction of reconstructed tracks whose reconstructed momentum lies within $3\sigma$ of the truth momentum of the associated GEANT4 track . . . . .	84
3.25	DCA distributions in three $p_T$ bins from reconstruction of 5000 central HIJING events. .	84
3.26	DCA resolution versus $p_T$ from simulations with pions embedded in central HIJING events. . . . .	85
3.27	Electron ID efficiency versus pion rejection near central rapidity ( $ \eta  < 0.2$ ) based on a GEANT4 simulation of single particles . . . . .	86
3.28	Electron ID efficiency versus pion rejection near central rapidity ( $ \eta  < 0.2$ ) based on a GEANT4 simulation of single particles embedded in 0–10% central HIJING events . .	87
3.29	C-AD projections of instantaneous luminosity vs time in store and average luminosity as a function of the integration range around the nominal interaction point for Au+Au at 200 GeV . . . . .	88
3.30	Trigger efficiency for jets using GEANT4 simulated calorimeter-based triggers as a function of $R = 0.4$ truth-level jet $E_T$ , with results for quark- and gluon-initiated jets shown separately . . . . .	90
3.31	Rejection factor for minimum bias $p+p$ events using GEANT4 simulated calorimeter-based triggers, as a function of the minimum $E_T$ trigger requirement . . . . .	91
3.32	Rejection factor and efficiency for an electron trigger requiring a minimum amount of energy in a region of the electromagnetic calorimeter ( $\Sigma E$ ) . . . . .	92
3.33	HIJING and GEANT4 calculated EMCal trigger patch $4 \times 4$ rejections for central and mid-central events ( $b = 4$ and $b = 8$ fm) as a function of threshold energy. . . . .	93

3.34	(Left) HIJING and GEANT4 calculated EMCAL trigger patch $4 \times 4$ rejections for $p$ +Au minimum bias collisions. (Right) HIJING and GEANT4 calculated full calorimeter jet patch trigger rejections for $p$ +Au minimum bias collisions. . . . .	93
3.35	Full HIJING and GEANT4 calculated calorimeter (EMCAL and HCal) trigger patch rejections for central and mid-central events ( $b=4$ and $b=8$ fm) as a function of threshold energy . . . . .	94
3.36	Illustration of sPHENIX underlying structural support, support equipment, overall assembly and maintenance concepts with and without endcaps. . . . .	95
3.37	Closeup view of EMCAL and HCal with the solenoid cryostat and services. . . . .	98
3.38	Pictures of the HCal prototype under construction and of the calorimeters in the MWest beamline of the Fermilab Test Beam Facility . . . . .	99
4.1	GEANT4 event display of PYTHIA dijet events with indicating clusters found in the calorimeter and reconstructed charged tracks . . . . .	104
4.2	GEANT4 simulations with PYTHIA dijet events and the resulting jet energy resolution for anti- $k_T$ and $R = 0.4$ with input calorimeter towers and clusters, and comparison of the jet energy resolution with pure calorimetric cluster input and particle flow jet algorithm . . . . .	105
4.3	The GEANT4 calculated energy resolution of single jets in $p+p$ collisions reconstructed with the FASTJET anti- $k_T$ algorithm with $R = 0.2$ and $R = 0.4$ . . . . .	106
4.4	GEANT4 calculated energy resolution of single jets in $p+p$ collisions separated into quark and gluon jets, and the PYTHIA calculated fragmentation function of quark and gluon jets separately . . . . .	107
4.5	Unfolding the effect of finite detector resolution on jet reconstruction in $p+p$ events	108
4.6	Dijet asymmetry, $A_J$ , in $p+p$ collisions . . . . .	109
4.7	The GEANT4 calculated energy resolution of PYTHIA jets embedded in a Au+Au HIJING event, reconstructed using the anti- $k_T$ algorithm with $R = 0.2$ and $R = 0.4$ .	110
4.8	Schematic diagram for the jet reconstruction algorithm. . . . .	111
4.9	Event displays of true and reconstructed jets shown overlaid on background subtracted calorimeter towers from fast simulation . . . . .	112
4.10	The true/fake composition of the jet spectrum in central 0–10% Au+Au based on 750M HIJING events . . . . .	113
4.11	The true/fake composition of the jet spectra in central 0–10% Au+Au based on 750 million HIJING events for $R = 0.3$ and $R = 0.4$ jets. . . . .	114
4.12	The efficiency for finding jets in central Au+Au collisions as a function of true jet energy and for $R = 0.2, 0.3$ and $0.4$ . . . . .	114
4.13	The jet energy scale and energy resolution of reconstructed jets in Au+Au collisions	115

4.14	Jet purity ( $S/(S+B)$ ) in 0–10% Au+Au collisions from HIJING. The purity values are for a ideal detector smeared by the GEANT4 parametrized EMCal and HCal resolutions . . . . .	115
4.15	Total transverse energy in $\Delta\eta \times \Delta\phi = 0.5 \times 0.5$ regions ( $\Sigma E_T^{0.5 \times 0.5}$ ) in HIJING Au+Au $\sqrt{s_{NN}} = 200$ GeV events with $b = 4$ fm and $b = 8$ fm . . . . .	117
4.16	Mean and RMS of the total transverse energy in finite-sized regions ( $\Sigma E_T$ ), in HIJING Au+Au $\sqrt{s_{NN}} = 200$ GeV events . . . . .	118
4.17	The charged background energy density, $\rho_{ch}$ , and the distribution of $\delta p_T$ for $R = 0.2$ jets with a $p_T$ constituent cut of 150 MeV/ $c$ for tracks and 350 MeV for clusters, determined using random cones and embedded tracks methods . . . . .	119
4.18	STAR preliminary result showing how jet candidates are found using the unmodified information in the event . . . . .	119
4.19	Effect of smearing the inclusive jet spectrum in Au+Au collisions . . . . .	120
4.20	Single inclusive jet $R_{AA}$ with $R = 0.2$ for Au+Au central events from the unfolding of the $p+p$ and Au+Au spectra with an estimated systematic uncertainty as a multiplicative factor of approximately $\pm 10\%$ . . . . .	121
4.21	The effect of smearing on $A_J$ for $R = 0.3$ jets . . . . .	122
4.22	Purity results for $R = 0.2, 0.3, 0.4, 0.5$ anti- $k_T$ calorimetric reconstructed jets in 0–10% central Au+Au HIJING events . . . . .	123
4.23	STAR result for $A_J$ for $R = 0.2$ and $R = 0.4$ jets, triggered on a high $E_T$ electromagnetic calorimeter tower . . . . .	124
4.24	sPHENIX capabilities for measuring the inclusive jet fragmentation function, $D(z)$ , for $p_T > 40$ GeV/ $c$ jets . . . . .	125
4.25	Modified fragmentation function $D(z)$ in the medium expressed as the ratio of the modified $D(z)$ to that assuming vacuum fragmentation . . . . .	126
4.26	Photon-jet capability in sPHENIX, derived from a full GEANT4 simulation of PYTHIA events with a $> 20$ GeV photon embedded into central Au+Au HIJING events. . . . .	127
4.27	Effect of smearing on the energy ratio $E_{jet}/E_\gamma$ for $R = 0.3$ jets . . . . .	128
4.28	NLO pQCD calculation for the subprocess contributions as a function of jet transverse energy at midrapidity in $p+p$ collisions at 200 GeV . . . . .	129
4.29	Full GEANT4 simulations of PYTHIA dijets embedded in central Au+Au HIJING events with reconstruction of trigger and away-side jets, showing high purity even for large $R$ . . . . .	130
4.30	Illustration of a technique for ensemble mixing as developed by the STAR Collaboration. . . . .	131

4.31	JEWEL jet quenching Monte Carlo calculations in Au+Au 0-10% central collisions triggering on an anti- $k_T$ jet with $R = 0.2$ with $E_T > 30$ GeV and measuring the modification of away-side correlated jet yields ( $I_{AA}$ ) . . . . .	131
4.32	Distribution of the DCA significance $S$ for the highest- $S$ track (left panel) and second highest- $S$ track (right panel) in $p_T = 20$ GeV jets. Each panel shows the per-jet distribution for light (black), charm (red) and bottom (blue) jets. . . . .	133
4.33	Performance of $b$ -jet tagging algorithms for $p_T = 20$ GeV jets based on requiring at least one, two or three tracks in the jet to have a 2-D DCA significance above some minimum value . . . . .	134
4.34	Performance of $b$ -jet tagging algorithms for $p_T = 20$ GeV jets based on requiring at least two tracks in the jet to have a 2-D DCA significance above some minimum value	135
4.35	Performance of $b$ -jet tagging algorithms for $p_T = 20$ GeV jets requiring at least two tracks in the jet to have a 2-D DCA significance above some minimum value . . . . .	136
4.36	Projected statistical uncertainties on the $R_{AA}$ for $b$ -jets in 0–20% Au+Au events, assuming an overall suppression of $R_{AA} = 0.6$ , a $b$ -jet tagging efficiency of 50%, $\mathcal{L} = 630 \text{ pb}^{-1}$ of $p+p$ events and $0.6 \times 10^{12}$ sampled minimum bias Au+Au events . . . . .	137
4.37	Reconstructed $D$ meson signal to background in 0-10% central Au+Au collisions. . . . .	138
4.38	Projected statistical uncertainties on the $R_{pAu}$ for charged pions inclusive jets and $b$ -jets for minimum bias $p+Au$ events corresponding to 10 weeks of minimum bias $p+Au$ and $p+p$ running. . . . .	140
4.39	$R_{pPb}$ for mid-rapidity charged particles vs $p_T$ as measured by CMS, and for inclusive full jets vs jet $p_T$ as measured by ATLAS . . . . .	141
4.40	$R_{CP}$ for inclusive jets vs approximate total jet energy $p = p_T \times \cosh(y^*)$ , for forward and mid-rapidity regions, as measured by ATLAS, and for inclusive jets at mid-rapidity as a function of the detector-level jet $p_T$ as measured by PHENIX . . . . .	141
4.41	Temperature profile vs time from a full dynamical calculation for various collision species and energies, and results for the transverse flow velocity profile at time $\tau = 2 \text{ fm}/c$ . . . . .	143
4.42	Jet, photon and $\pi^0$ rates with $ \eta  < 1.0$ from NLO pQCD . . . . .	144
4.43	Projected statistical uncertainties on $R_{AA}$ for inclusive photons, $b$ -jets, inclusive jets and charged hadrons . . . . .	145
4.44	The mass spectrum for reconstructed electron decay tracks from the three Upsilon states, corresponding to 10 weeks of $p+p$ running, including the effects of electron identification efficiency and trigger efficiency. . . . .	147
4.45	The signal plus background in the Upsilon mass region for ten billion 0–10% central Au+Au events, assuming a pion rejection of 90:1 and an electron pair identification efficiency of 49% . . . . .	148

4.46	Estimate of the statistical precision of a measurement of the $Y$ states in Au+Au collisions using sPHENIX, assuming that the measured $R_{AA}$ is equal to the results of a recent theory calculation . . . . .	149
4.47	Estimate of the yields expected for the three $Y$ states as a function of $p_T$ from a 10 week $p+p$ run. . . . .	150
4.48	Estimate of the statistical precision of a measurement of $R_{AA}$ versus $p_T$ for the $Y$ states using sPHENIX, for the most central 0–10% of events . . . . .	150
4.49	Estimate of the statistical precision of a measurement of $R_{pAu}$ for the $Y$ states using sPHENIX, in four centrality bins . . . . .	151
A.1	Event display for a central HIJING $p+A$ collision at $\sqrt{s} = 200$ GeV. This detector concept adds calorimetrically instrumented endcaps to the sPHENIX barrel tracking and calorimetry. . . . .	154
A.2	The GEANT4 simulated jet resolution of single jets for energy (top row), $\phi$ (middle row) and $\eta$ (bottom row) in $p+p$ (open markers) and $p+A$ (closed markers) collisions reconstructed with the FASTJET anti- $k_T$ algorithm with $R = 0.4$ (blue) and $R = 0.6$ (red). . . . .	156
A.3	(Left) Efficiency for direct photons and two-pairs from neutral pion decay as a function of $p_T$ for different EMCAL and Preshower cuts. (Right) The corresponding enhancement in the direct photon S/B as a function of $p_T$ . Note that no isolation cuts are applied. . . . .	158
B.1	The evolution of the sPHENIX into a detector for eRHIC physics, with additional capabilities supporting its focus on $e+p$ and $e+A$ collisions . . . . .	161
B.2	Kinematic coverage of ePHENIX for two beam energy configurations, $10 \times 250$ GeV and $5 \times 50$ GeV, which show the range of eRHIC capabilities . . . . .	164
B.3	The projected reduction in the uncertainty on the gluon longitudinal spin distribution based on simulated PYTHIA events corresponding to an integrated luminosity of $10 \text{ fb}^{-1}$ at the $10 \text{ GeV} \times 250 \text{ GeV}$ beam energy configuration . . . . .	165
B.4	The transverse-momentum distribution of an up quark with $x = 0.1$ in a transversely polarized proton and the transverse-momentum profile of the up quark Siverts function accessible at eRHIC . . . . .	166
B.5	The virtuality $Q^2$ and $\nu$ coverage for ePHENIX (EIC) measurements with collisions of 5 GeV electrons on 100 GeV/nucleon heavy nuclei, data from HERMES on the modified fragmentation from xenon targets ( $R_{Xe}$ ) . . . . .	168
B.6	Coverage in $x$ and $Q^2$ for the EIC and the ePHENIX detector for 10 GeV electrons on 100 GeV/nucleon nuclei, and the kinematic coverage by previous experiments in $e+A$ and $\nu+A$ DIS and Drell-Yan measurements . . . . .	170
B.7	Ratio of diffractive-to-total cross-section for $e+Au$ normalized to $e+p$ plotted as a function of the squared mass of the hadronic final state, $M_X^2$ . . . . .	171

B.8	The distribution of scattered electrons in pseudorapidity and energy from PYTHIA DIS simulations for $e+p$ collisions with $10 \text{ GeV} \times 250 \text{ GeV}$ beam energies . . . . .	174
B.9	Momentum spectra for scattered electrons, charged pions and photons for the $10 \text{ GeV} \times 250 \text{ GeV}$ beam energy configuration . . . . .	175
B.10	For $10 \text{ GeV} \times 250 \text{ GeV}$ beam energy configuration: fraction of charged particles from DIS electrons before and after electron identification with the EMCAL response and E/p matching . . . . .	175
B.11	For $10 \text{ GeV} \times 250 \text{ GeV}$ beam energy configuration: the fraction of events in $(x, Q^2)$ space surviving after a $> 2 \text{ GeV}$ energy cut on the DIS scattered electron . . . . .	176
B.12	For $10 \text{ GeV} \times 250 \text{ GeV}$ beam energy configuration: the relative resolution for $Q^2$ and $x$ as a function of $(x, Q^2)$ . . . . .	177
B.13	For $10 \text{ GeV} \times 250 \text{ GeV}$ beam energy configuration: Statistics survivability in $(x, Q^2)$ bins. . . . .	178
B.14	Distribution of hadrons from DIS events in $e+p$ as a function of momentum and pseudorapidity, based on PYTHIA simulations of the $10 \text{ GeV} \times 250 \text{ GeV}$ beam energy configuration . . . . .	179
B.15	$x$ and $Q^2$ distribution of events with kaons which can be identified with the ePHENIX PID detectors in expected binning at (left) low and (right) high $z$ . . . . .	180
B.16	Efficiency as a function of $x$ and $Q^2$ of kaon identification when comparing to baseline ePHENIX design with a DIRC, RICH and Aerogel when one of these subsystems is removed. The top three plots are for low $z$ ( $0.3 < z < 0.35$ ) and the bottom three are for high $z$ ( $0.7 < z < 0.75$ ). Also shown are lines indicating different values of $y$ . . . . .	181
B.17	For the $10 \text{ GeV} \times 250 \text{ GeV}$ beam energy configuration: DVCS photon energy vs pseudorapidity distribution; the $z$ -axis scale shows the relative distribution of events from the MILOU event generator. . . . .	182
B.18	For $10 \text{ GeV} \times 250 \text{ GeV}$ beam energy configuration: $x$ - $Q^2$ coverage for DVCS events with photon detected in the electron-going direction, $\eta < -1$ (left), or central rapidities, $ \eta  < 1$ (middle) and hadron-going direction, $\eta > 1$ (right). The $z$ -axis scale shows relative distribution of events from the MILOU event generator. . . . .	183
B.19	For the $10 \text{ GeV} \times 100 \text{ GeV}$ beam energy configuration: Top: Pseudorapidity distribution for the most forward going particle in DIS events (black) and in diffractive events (blue); Bottom: Efficiency (dashed) and purity (solid) for diffractive event identification as a function of pseudorapidity cut defining the rapidity gap, for different detector acceptance: $ \eta  < 5$ (left), $ \eta  < 4$ (middle), $ \eta  < 3$ (right). Obtained using the RAPGAP generator developed at HERA and tuned to H1 and ZEUS data. . . . .	184
B.20	Engineering rendering of ePHENIX in the PHENIX experimental hall. The drawing shows the location of the final eRHIC focusing quadrupoles as well as the electron bypass beamline behind the detector. . . . .	185



- B.21 A cross section through the top-half of the ePHENIX detector concept, showing the location of the superconducting solenoid, the barrel calorimeter system, the EMCal in the electron-going direction and the system of tracking, particle identification detectors and calorimeters in the hadron-going direction. Forward detectors are also shown along the outgoing hadron beamline. The magenta curves are contour lines of magnetic field potential as determined using the 2D magnetic field solver, POISSON. 186
- B.22 The response of the ePHENIX detector to a single event, as determined using GEANT4. The field map in this simulation was determined using the 2D magnetic field solver OPERA. These same OPERA calculations were used to verify and validate the calculations underlying the magnetic field lines shown in Figure B.21. . . . . 187
- B.23 Momentum resolution over the full pseudorapidity coverage of the planned tracking system in the high momentum limit. Multiple scattering contribution to the relative momentum resolution (not shown on the plot) was studied with GEANT4 simulation, and found to vary from below 1% at low pseudorapidity to  $\sim 3\%$  at  $|\eta|=3$ . . . . . 188
- B.24 PANDA Crystal Endcap Calorimeter [212]. The PWO crystal modules are shown in green color, which is projective towards the target. . . . . 191
- B.25 Čerenkov angle versus momentum for various particle species. . . . . 193
- B.26 The cross-section of the gas-based RICH detector in the  $r$ - $z$  plane that crosses the mirror center. The interaction point is centered at  $(0,0)$ . The geometric center of the mirror is shown as the blue dot at  $(r, z) = (40 \text{ cm}, 100 \text{ cm})$ . The mirror and RICH entrance window are shown by the solid and dashed blue curves, respectively. Several example tracks and the central axis of their Čerenkov light cone are illustrated by the black lines. The Čerenkov photons are reflected by the mirror to the focal plane, shown in red. . . . . 193
- B.27 Azimuthal angular dispersion of gas-based RICH ring due to fringe magnetic field for a  $p = 10 \text{ GeV}/c$  track. It is compared to the maximum RICH ring angle as shown on the right vertical axis. . . . . 194
- B.28 Reconstructed mass distribution via  $m(p, \theta_{Crk})$  at  $\eta = 4$  for reconstructed momenta 30  $\text{GeV}/c$  (left), 50  $\text{GeV}/c$  (middle) and 70  $\text{GeV}/c$  (right), for pions (red), kaons (green) and protons (blue), with the parent momentum and particle abundances from the PYTHIA generator. Vertical lines indicate the symmetric mass cuts corresponding to 90% efficiency. Note that particle true momentum is on the average smaller than reconstructed momentum, see Figure B.29. . . . . 196
- B.29  $\pi, K, p$  purities at pseudorapidity 4.0 as a function of reconstructed momentum, based on symmetric cut on reconstructed mass corresponding to 90% efficiency (solid lines), and asymmetric cut with stricter selection on the kaons with efficiency 65% (dashed line); Also indicated in angle brackets are the values of the average true momentum at each reconstructed momentum, which are different due to momentum smearing and sharply falling momentum spectra. . . . . 196
- B.30 Approximate focusing method using two (left) and three (right) layers of aerogel with slightly different indices of refraction proposed by Belle II [215] . . . . . 197

B.31 BaBar DIRC geometry [213]. All dimensions are given in mm. . . . .	198
B.32 Simulated PID Efficiency matrix and its uncertainty for $1.0 < \eta < 1.4$ region, utilizing combined information of the BaBar DIRC and $dE/dx$ measured in the tracking detector [213]. Note that the off-diagonal efficiency values are scaled by a factor of 10. . . . .	199
B.33 Floor plan showing the locations of ZDC, Roman Pots, and IR magnets . . . . .	200

# Bibliography

- [1] C. N. Bo et al. Extracting jet transport coefficients from jet quenching at RHIC and the LHC. 2013. URL: <https://sites.google.com/a/lbl.gov/jetwiki/documents-1/report-on-status-of-qhat>. (document), 1.2, 1.7
- [2] The PHENIX Collaboration. Future opportunities in  $p+p$  and  $p+A$  collisions at RHIC with the forward sPHENIX detector, 2014. URL: [http://www.phenix.bnl.gov/phenix/WWW/publish/dave/sPHENIX/pp\\_pA\\_whitepaper.pdf](http://www.phenix.bnl.gov/phenix/WWW/publish/dave/sPHENIX/pp_pA_whitepaper.pdf). (document), A, A.1
- [3] A. Bazavov, T. Bhattacharya, M. Cheng, N. H. Christ, C. DeTar, S. Ejiri, S. Gottlieb, R. Gupta, U. M. Heller, K. Huebner, C. Jung, F. Karsch, E. Laermann, L. Levkova, C. Miao, R. D. Mawhinney, P. Petreczky, C. Schmidt, R. A. Soltz, W. Soeldner, R. Sugar, D. Toussaint, and P. Vranas. Equation of state and qcd transition at finite temperature. *Phys. Rev. D*, 80:014504, Jul 2009. URL: <http://link.aps.org/doi/10.1103/PhysRevD.80.014504>, doi: 10.1103/PhysRevD.80.014504. 1, 1.1
- [4] A. Adare et al. Enhanced production of direct photons in Au+Au collisions at  $\sqrt{s_{NN}} = 200$  GeV and implications for the initial temperature. *Phys. Rev. Lett.*, 104:132301, 2010. arXiv:0804.4168, doi:10.1103/PhysRevLett.104.132301. 1
- [5] M. Luzum and P. Romatschke. Viscous hydrodynamic predictions for nuclear collisions at the LHC. *Phys. Rev. Lett.*, 103:262302, 2009. arXiv:0901.4588, doi:10.1103/PhysRevLett.103.262302. 1
- [6] A. Adams, L. D. Carr, T. Schaefer, P. Steinberg, and J. E. Thomas. Strongly correlated quantum fluids: ultracold quantum gases, quantum chromodynamic plasmas, and holographic duality. 2012. arXiv:1205.5180. 1
- [7] S. S. Gubser. Using string theory to study the quark-gluon plasma: Progress and perils. *Nucl. Phys.*, A830:657C–664C, 2009. arXiv:0907.4808. 1
- [8] S. S. Gubser, I. R. Klebanov, and A. W. Peet. Entropy and temperature of black 3-branes. *Phys. Rev.*, D54:3915–3919, 1996. arXiv:hep-th/9602135, doi:10.1103/PhysRevD.54.3915. 1
- [9] U. A. Wiedemann. Stepping outside the neighborhood of  $T(c)$  at LHC. *Nucl. Phys.*, A830:74C–80C, 2009. arXiv:0908.2294. 1
- [10] G. Aad et al. Measurement of the Azimuthal Angle Dependence of Inclusive Jet Yields in Pb+Pb Collisions at  $\sqrt{s_{NN}} = 2.76$  TeV with the ATLAS detector. 2013. arXiv:1306.6469. 1

- [11] G. Aad et al. Measurement of the jet radius and transverse momentum dependence of inclusive jet suppression in lead-lead collisions at  $\sqrt{s_{NN}} = 2.76$  TeV with the ATLAS detector. *Phys. Lett.*, B719:220–241, 2013. arXiv:1208.1967, doi:10.1016/j.physletb.2013.01.024. 1, 4.4.1, 4.5
- [12] K. Adcox et al. Formation of dense partonic matter in relativistic nucleus-nucleus collisions at RHIC: Experimental evaluation by the PHENIX collaboration. *Nucl. Phys.*, A757:184–283, 2005. arXiv:nucl-ex/0410003, doi:10.1016/j.nuclphysa.2005.03.086. 1.1
- [13] M. Luzum and P. Romatschke. Conformal relativistic viscous hydrodynamics: Applications to RHIC results at  $\sqrt{s_{NN}} = 200$  GeV. *Phys. Rev.*, C78:034915, 2008. arXiv:0804.4015, doi:10.1103/PhysRevC.78.034915. 1.1
- [14] P. Danielewicz and M. Gyulassy. Dissipative phenomena in quark gluon plasmas. *Phys. Rev.*, D31:53–62, 1985. doi:10.1103/PhysRevD.31.53. 1.1
- [15] P. Kovtun, D. Son, and A. Starinets. Viscosity in strongly interacting quantum field theories from black hole physics. *Phys. Rev. Lett.*, 94:111601, 2005. arXiv:hep-th/0405231, doi:10.1103/PhysRevLett.94.111601. 1.1, 1.2
- [16] H. Song and U. W. Heinz. Causal viscous hydrodynamics in 2+1 dimensions for relativistic heavy-ion collisions. *Phys. Rev.*, C77:064901, 2008. arXiv:0712.3715, doi:10.1103/PhysRevC.77.064901. 1.1
- [17] B. Alver, C. Gombeaud, M. Luzum, and J.-Y. Ollitrault. Triangular flow in hydrodynamics and transport theory. *Phys. Rev.*, C82:034913, 2010. arXiv:1007.5469, doi:10.1103/PhysRevC.82.034913. 1.1
- [18] D. A. Teaney. Viscous Hydrodynamics and the Quark Gluon Plasma. 2009. arXiv:0905.2433. 1.1
- [19] B. Schenke, S. Jeon, and C. Gale. Elliptic and triangular flows in 3 + 1D viscous hydrodynamics with fluctuating initial conditions. *J. Phys. G*, G38:124169, 2011. 1.1
- [20] A. Adare et al. Measurements of higher-order flow harmonics in Au+Au collisions at  $\sqrt{s_{NN}} = 200$  GeV. arXiv:1105.3928 [hep-ex] (2011). 1.1
- [21] A. Adare et al. Energy loss and flow of heavy quarks in Au+Au collisions at  $\sqrt{s_{NN}} = 200$  GeV. *Phys. Rev. Lett.*, 98:172301, 2007. arXiv:nucl-ex/0611018, doi:10.1103/PhysRevLett.98.172301. 1.1
- [22] A. Majumder, B. Muller, and X.-N. Wang. Small shear viscosity of a quark-gluon plasma implies strong jet quenching. *Phys. Rev. Lett.*, 99:192301, 2007. arXiv:hep-ph/0703082, doi:10.1103/PhysRevLett.99.192301. 1.2, 1.1, 1.2
- [23] H. Liu, K. Rajagopal, and U. Wiedemann. Calculating the jet quenching parameter from AdS/CFT. *Phys. Rev. Lett.*, 97:182301, 2006. arXiv:hep-ph/0605178, doi:10.1103/PhysRevLett.97.182301. 1.1, 1.2
- [24] L. Csernai, J. Kapusta, and L. McLerran. On the strongly-interacting low-viscosity matter created in relativistic nuclear collisions. *Phys. Rev. Lett.*, 97:152303, 2006. arXiv:nucl-th/0604032, doi:10.1103/PhysRevLett.97.152303. 1.2

- [25] P. B. Arnold, G. D. Moore, and L. G. Yaffe. Transport coefficients in high temperature gauge theories. 2. Beyond leading log. *JHEP*, 0305:051, 2003. arXiv:hep-ph/0302165. 1.2
- [26] M. Prakash, M. Prakash, R. Venugopalan, and G. Welke. Nonequilibrium properties of hadronic mixtures. *Phys. Rept.*, 227:321–366, 1993. doi:10.1016/0370-1573(93)90092-R. 1.2
- [27] N. Demir and S. A. Bass. Shear-viscosity to entropy-density ratio of a relativistic hadron gas. *Phys. Rev. Lett.*, 102:172302, 2009. arXiv:0812.2422, doi:10.1103/PhysRevLett.102.172302. 1.2
- [28] H. B. Meyer. A calculation of the shear viscosity in SU(3) gluodynamics. *Phys. Rev.*, D76:101701, 2007. arXiv:0704.1801, doi:10.1103/PhysRevD.76.101701. 1.2
- [29] Y. Hidaka and R. D. Pisarski. Small shear viscosity in the semi quark gluon plasma. *Phys. Rev.*, D81:076002, 2010. arXiv:0912.0940, doi:10.1103/PhysRevD.81.076002. 1.2
- [30] P. K. Srivastava and C. P. Singh. Critical Point on the QCD Deconfining Phase Boundary. 2012. 15 pages, 4 figures. arXiv:1201.0445. 1.2
- [31] P. Kovtun, G. D. Moore, and P. Romatschke. The stickiness of sound: An absolute lower limit on viscosity and the breakdown of second order relativistic hydrodynamics. *Phys. Rev.*, D84:025006, 2011. arXiv:1104.1586, doi:10.1103/PhysRevD.84.025006. 1.2
- [32] Charles Gale, Sangyong Jeon, Bjorn Schenke, Prithwish Tribedy, and Raju Venugopalan. Event-by-event anisotropic flow in heavy-ion collisions from combined Yang-Mills and viscous fluid dynamics. *Phys. Rev. Lett.*, 110:012302, 2013. arXiv:1209.6330, doi:10.1103/PhysRevLett.110.012302. 1.2
- [33] H. Song, S. A. Bass, and U. Heinz. Elliptic flow in 200 A GeV Au+Au collisions and 2.76 A TeV Pb+Pb collisions: insights from viscous hydrodynamics + hadron cascade hybrid model. *Phys. Rev.*, C83:054912, 2011. arXiv:1103.2380, doi:10.1103/PhysRevC.83.054912. 1.2
- [34] J. L. Nagle, I. G. Bearden, and W. A. Zajc. Quark-gluon plasma at RHIC and the LHC: perfect fluid too perfect? *New J. Phys.*, 13:075004, 2011. arXiv:1102.0680, doi:10.1088/1367-2630/13/7/075004. 1.2
- [35] H. Niemi, G. S. Denicol, P. Huovinen, E. Molnar, and D. H. Rischke. Influence of the shear viscosity of the quark-gluon plasma on elliptic flow in ultrarelativistic heavy-ion collisions. *Phys. Rev. Lett.*, 106:212302, 2011. arXiv:1101.2442, doi:10.1103/PhysRevLett.106.212302. 1.2
- [36] N. Armesto, B. Cole, C. Gale, W. A. Horowitz, P. Jacobs, et al. Comparison of Jet Quenching Formalisms for a Quark-Gluon Plasma ‘Brick’. 2011. arXiv:1106.1106. 1.2
- [37] P. B. Arnold, G. D. Moore, and L. G. Yaffe. Transport coefficients in high temperature gauge theories. 1. Leading log results. *JHEP*, 0011:001, 2000. arXiv:hep-ph/0010177. 1.2
- [38] S. Chatrchyan et al. Study of high-pT charged particle suppression in PbPb compared to pp collisions at  $\sqrt{s_{NN}} = 2.76$  TeV. *Eur. Phys. J.*, C72:1945, 2012. arXiv:1202.2554, doi:10.1140/epjc/s10052-012-1945-x. 1.2, 1.16

- [39] Thorsten Renk. On the sensitivity of jet quenching to near  $T_C$  enhancement of the medium opacity. *Phys. Rev.*, C89:067901, 2014. arXiv:1402.5798, doi:10.1103/PhysRevC.89.067901. 1.2, 1.7
- [40] J. Liao and E. Shuryak. Angular Dependence of Jet Quenching Indicates Its Strong Enhancement Near the QCD Phase Transition. *Phys. Rev. Lett.*, 102:202302, 2009. arXiv:0810.4116, doi:10.1103/PhysRevLett.102.202302. 1.2, 1.3
- [41] Jiechen Xu, Jinfeng Liao, and Miklos Gyulassy. Anisotropic Jet Quenching in semi-Quark-Gluon Plasmas with Magnetic Monopoles in Ultrarelativistic Heavy Ion Collisions. 2014. arXiv:1411.3673. 1.2, 1.8
- [42] W. A. Horowitz and M. Gyulassy. The Surprising Transparency of the sQGP at LHC. *Nucl. Phys.*, A872:265–285, 2011. arXiv:1104.4958. 1.2
- [43] K. Aamodt and C. A. Loizides. Suppression of charged particle production at large transverse momentum in central Pb–Pb collisions at  $\sqrt{s_{NN}} = 2.76$  TeV. *Phys. Lett.*, B696:30–39, 2011. arXiv:1012.1004. 1.2
- [44] X.-F. Chen, T. Hirano, E. Wang, X.-N. Wang, and H. Zhang. Suppression of high  $p_T$  hadrons in  $Pb + Pb$  Collisions at LHC. *Phys. Rev.*, C84:034902, 2011. arXiv:1102.5614, doi:10.1103/PhysRevC.84.034902. 1.2
- [45] B. G. Zakharov. Variation of jet quenching from RHIC to LHC and thermal suppression of QCD coupling constant. *JETP Lett.*, 93:683–687, 2011. arXiv:1105.2028, doi:10.1134/S0021364011120162. 1.2
- [46] A. Buzzatti and M. Gyulassy. Jet Flavor Tomography of Quark Gluon Plasmas at RHIC and LHC. *Phys. Rev. Lett.*, 108:022301, 2012. 4 pages, 3 eps figures. arXiv:1106.3061, doi:10.1103/PhysRevLett.108.022301. 1.2
- [47] A. Buzzatti and M. Gyulassy. A running coupling explanation of the surprising transparency of the QGP at LHC. *Nucl. Phys.*A904-905, 2013:779c–782c, 2013. arXiv:1210.6417, doi:10.1016/j.nuclphysa.2013.02.133. 1.2
- [48] A. Adare et al. Evolution of  $\pi^0$  suppression in Au+Au collisions from  $\sqrt{s_{NN}} = 39$  to 200 GeV. *Phys. Rev. Lett.*, 109:152301, 2012. arXiv:1204.1526, doi:10.1103/PhysRevLett.109.152301. 1.2
- [49] Alexander Schmah. The beam energy scan at RHIC: Recent results from STAR. *J. Phys. Conf. Ser.*, 426:012007, 2013. doi:10.1088/1742-6596/426/1/012007. 1.2
- [50] A. Adare et al. Azimuthal anisotropy of  $\pi^0$  production in Au+Au collisions at  $\sqrt{s_{NN}} = 200$  GeV: path-length dependence of jet quenching and the role of initial geometry. *Phys. Rev. Lett.*, 105:142301, 2010. arXiv:1006.3740, doi:10.1103/PhysRevLett.105.142301. 1.2, 1.9
- [51] C. Marquet and T. Renk. Jet quenching in the strongly-interacting quark-gluon plasma. *Phys. Lett.*, B685:270–276, 2010. arXiv:0908.0880, doi:10.1016/j.physletb.2010.01.076. 1.2

- [52] J. Casalderrey-Solana, Doga Can Gulhan, Jose Guilherme Milhano, Daniel Pablos, and Krishna Rajagopal. Jet quenching within a hybrid strong/weak coupling approach. *Nucl. Phys., A*, 2014. arXiv:1408.5616. 1.2, 1.6, 1.32
- [53] Jorge Casalderrey-Solana, Doga Can Gulhan, Guilherme, Daniel Pablos, and Krishna Rajagopal. A Hybrid Strong/Weak Coupling Approach to Jet Quenching. *JHEP*, 1410:19, 2014. arXiv:1405.3864, doi:10.1007/JHEP10(2014)019. 1.2, 1.6, 1.32
- [54] S. Bass et al. Systematic comparison of jet energy-loss schemes in a realistic hydrodynamic medium. *Phys. Rev., C*79:024901, 2009. arXiv:0808.0908, doi:10.1103/PhysRevC.79.024901. 1.9, 1.5
- [55] S. Wicks, W. Horowitz, M. Djordjevic, and M. Gyulassy. Elastic, inelastic, and path length fluctuations in jet tomography. *Nucl. Phys., A*784:426–442, 2007. arXiv:nucl-th/0512076, doi:10.1016/j.nuclphysa.2006.12.048. 1.9
- [56] K. Rajagopal. International Quark Matter presentation (2011). URL: <http://qm2011.in2p3.fr/node/12>. 1.3
- [57] C. E. Coleman-Smith, G.-Y. Qin, S. A. Bass, and B. Muller. Jet modification in a brick of QGP matter. 2011. arXiv:1108.5662. 1.3, 1.6, 1.25
- [58] C. E. Coleman-Smith, S. A. Bass, and D. K. Srivastava. Implementing the LPM effect in a parton cascade model. *Nucl. Phys., A*862-863:275–278, 2011. arXiv:1101.4895, doi:10.1016/j.nuclphysa.2011.05.071. 1.3, 1.6, 1.6, 1.6
- [59] C. E. Coleman-Smith and B. Muller. What can we learn from Dijet suppression at RHIC? 2012. arXiv:1205.6781. 1.3, 1.13, 1.25, 1.27
- [60] Y. He, I. Vitev, and B.-W. Zhang. Next-to-leading order analysis of inclusive jet and di-jet production in heavy ion reactions at the Large Hadron Collider. 2011. arXiv:1105.2566. 1.3, 1.14, 1.6, 4.20
- [61] R. B. Neufeld and I. Vitev. Parton showers as sources of energy-momentum deposition in the QGP and their implication for shockwave formation at RHIC and at the LHC. 2011. 8 pages, 4 figures. arXiv:1105.2067. 1.3, 1.14, 1.6, 4.20
- [62] I. Vitev and B.-W. Zhang. Jet tomography of high-energy nucleus-nucleus collisions at next-to-leading order. *Phys. Rev. Lett.*, 104:132001, 2010. arXiv:0910.1090, doi:10.1103/PhysRevLett.104.132001. 1.3, 1.14, 1.6, 4.20
- [63] B. Muller. "Talk given at RHIC/AGS Users Meeting, June 2011". 1.4, 1.15
- [64] B. Muller. Parton energy loss in strongly coupled AdS/CFT. *Nucl. Phys., A*855:74–82, 2011. arXiv:1010.4258, doi:10.1016/j.nuclphysa.2011.02.022. 1.4
- [65] Thorsten Renk. Physics probed by the  $P_T$  dependence of the nuclear suppression factor. *Phys. Rev., C*88(1):014905, 2013. arXiv:1302.3710, doi:10.1103/PhysRevC.88.014905. 1.4
- [66] A. Majumder and C. Shen. Suppression of the High  $p_T$  Charged Hadron  $R_{AA}$  at the LHC. *Phys. Rev. Lett.*, 109:202301, 2012. arXiv:1103.0809, doi:10.1103/PhysRevLett.109.202301. 1.4

- [67] A. Majumder and J. Putschke. Mass depletion: a new parameter for quantitative jet modification. 2014. arXiv:1408.3403. 1.4
- [68] Korinna C. Zapp. JEWEL 2.0.0: directions for use. *Eur. Phys. J.*, C74:2762, 2014. arXiv:1311.0048, doi:10.1140/epjc/s10052-014-2762-1. 1.4, 1.6, 1.33
- [69] M. Habich, J.L. Nagle, and P. Romatschke. Particle spectra and HBT radii for simulated central nuclear collisions of C+C, Al+Al, Cu+Cu, Au+Au, and Pb+Pb from  $\sqrt{s}=62.4-2760$  GeV. 2014. arXiv:1409.0040. 1.4, 1.9, 1.46, 4.41, 4.9
- [70] K. Adcox et al. Suppression of hadrons with large transverse momentum in central Au+Au collisions at  $\sqrt{s_{NN}} = 130$  GeV. *Phys. Rev. Lett.*, 88:022301, 2002. arXiv:nucl-ex/0109003, doi:10.1103/PhysRevLett.88.022301. 1.5
- [71] C. Adler et al. Centrality dependence of high  $p_T$  hadron suppression in Au+Au collisions at  $\sqrt{s_{NN}} = 130$  GeV. *Phys. Rev. Lett.*, 89:202301, 2002. arXiv:nucl-ex/0206011. 1.5
- [72] A. Adare et al. Quantitative constraints on the transport properties of hot partonic matter from semi-inclusive single high transverse momentum pion suppression in Au+Au collisions at  $\sqrt{s_{NN}} = 200$  GeV. *Phys. Rev. C*, 77:064907, 2008. arXiv:0801.1665, doi:10.1103/PhysRevC.77.064907. 1.5
- [73] A. Adare et al. Transition in yield and azimuthal shape modification in dihadron correlations in relativistic heavy ion collisions. *Phys. Rev. Lett.*, 104:252301, 2010. arXiv:1002.1077, doi:10.1103/PhysRevLett.104.252301. 1.5
- [74] A. Adare et al. Suppression of away-side jet fragments with respect to the reaction plane in Au+Au collisions at  $\sqrt{s_{NN}} = 200$  GeV. *Phys. Rev. C*, 2010. arXiv:1010.1521. 1.5
- [75] J. Adams et al. Distributions of charged hadrons associated with high transverse momentum particles in  $p+p$  and Au+Au collisions at  $\sqrt{s_{NN}} = 200$  GeV. *Phys. Rev. Lett.*, 95:152301, 2005. arXiv:nucl-ex/0501016. 1.5
- [76] J. L. Nagle. Ridge, bulk, and medium response: how to kill models and learn something in the process. *Nucl. Phys.*, A830:147C–154C, 2009. arXiv:0907.2707. 1.5
- [77] G. Aad et al. Observation of a centrality-dependent dijet asymmetry in lead-lead collisions at  $\sqrt{s_{NN}} = 2.76$  TeV with the ATLAS detector at the LHC. *Phys. Rev. Lett.*, 105:252303, 2010. Accepted for publication at Physical Review Letters. arXiv:1011.6182, doi:10.1103/PhysRevLett.105.252303. 1.5, 1.19, 4.2, 4.3.2
- [78] S. Chatrchyan et al. Observation and studies of jet quenching in PbPb collisions at nucleon-nucleon center-of-mass energy = 2.76 TeV. *Phys. Rev.*, C84:024906, 2011. arXiv:1102.1957, doi:10.1103/PhysRevC.84.024906. 1.5, 1.5, 1.20, 1.6, 4.3.2, 4.6
- [79] X.-N. Wang, Z. Huang, and I. Sarcevic. Jet quenching in the opposite direction of a tagged photon in high-energy heavy ion collisions. *Phys. Rev. Lett.*, 77:231–234, 1996. arXiv:hep-ph/9605213, doi:10.1103/PhysRevLett.77.231. 1.5, 1.7
- [80] S. Chatrchyan et al. Studies of jet quenching using isolated-photon+jet correlations in PbPb and pp collisions at  $\sqrt{s_{NN}} = 2.76$  TeV. 2012. Submitted to Physics Letters B. arXiv:1205.0206. 1.5



- [81] S. Chatrchyan et al. Jet momentum dependence of jet quenching in PbPb collisions at  $\sqrt{s_{NN}} = 2.76$  TeV. 2012. arXiv:1202.5022. 1.5, 4.2
- [82] P. Steinberg. Recent Heavy Ion Results with the ATLAS Detector at the LHC. 2011. arXiv:1110.3352. 1.5
- [83] H. Caines. Jets and jet-like Correlations at RHIC. 2011. arXiv:1110.1878. 1.5
- [84] J. Putschke. STAR: Jet reconstruction, direct gamma and multi-hadron correlations: Hard probes of the initial and final state. *Nucl. Phys.*, A855:83–91, 2011. 1.5
- [85] J. Putschke. First fragmentation function measurements from full jet reconstruction in heavy-ion collisions at  $\sqrt{s_{NN}} = 200$  GeV by STAR. *Eur. Phys. J.*, C61:629–635, 2009. arXiv:0809.1419. 1.5
- [86] P. M. Jacobs. Background fluctuations in heavy ion jet reconstruction. 2010. arXiv:1012.2406. 1.5
- [87] Y.-S. Lai. Direct jet reconstruction in  $p+p$  and Cu+Cu collisions at PHENIX. *Nucl. Phys.*, A855:295–298, 2011. 1.5
- [88] Y.-S. Lai. Probing medium-induced energy loss with direct jet reconstruction in  $p+p$  and Cu+Cu collisions at PHENIX. *Nucl. Phys.*, A830:251C–254C, 2009. arXiv:0907.4725. 1.5
- [89] L. Adamczyk et al. Jet-Hadron Correlations in  $\sqrt{s_{NN}} = 200$  GeV Au+Au and  $p+p$  Collisions. 2013. arXiv:1302.6184. 1.5, 1.22, 4.5, 4.6
- [90] J. Casalderrey-Solana, J. G. Milhano, and U. Wiedemann. Jet quenching via jet collimation. *J. Phys. G*, G38:124086, 2011. arXiv:1107.1964. 1.6
- [91] T. Renk. Energy dependence of the dijet imbalance in Pb-Pb collisions at 2.76 ATeV. 2012. arXiv:1204.5572. 1.6
- [92] T. Renk. Jets in medium: What RHIC and LHC measurements of  $R_{AA}$  and  $I_{AA}$  can teach about the parton-medium interaction. 2011. arXiv:1111.0769. 1.6
- [93] JET Topical Collaboration. URL: <http://jet.lbl.gov>. 1.6
- [94] K. C. Zapp, J. Stachel, and U. Wiedemann. LPM-effect in Monte Carlo models of radiative energy loss. *Nucl. Phys.*, A830:171C–174C, 2009. arXiv:0907.4304. 1.6, 1.6
- [95] T. Renk. YaJEM: a Monte Carlo code for in-medium shower evolution. *Int. J. Mod. Phys.*, E20:1594–1599, 2011. arXiv:1009.3740, doi:10.1142/S0218301311019933. 1.6, 1.6
- [96] C. Young, S. Jeon, C. Gale, and B. Schenke. Monte-Carlo simulation of jets in heavy-ion collisions. 2011. arXiv:1109.5992. 1.6, 1.6, 1.6
- [97] I. P. Lokhtin, A. V. Belyaev, and A. M. Snigirev. Jet quenching pattern at LHC in PYQUEN model. *Eur. Phys. J.*, C71:1650, 2011. arXiv:1103.1853, doi:10.1140/epjc/s10052-011-1650-1. 1.6, 1.6
- [98] N. Armesto, L. Cunqueiro, and C. A. Salgado. Monte Carlo for jet showers in the medium. *Nucl. Phys.*, A830:271C–274C, 2009. arXiv:0907.4706. 1.6, 1.6

- [99] T. Renk. Biased Showers — a common conceptual framework for the interpretation of High  $p_T$  observables in heavy-ion collisions. 2012. arXiv:1212.0646. 1.6, 1.24, 4.5
- [100] K. Geiger and B. Muller. Dynamics of parton cascades in highly relativistic nuclear collisions. *Nucl. Phys.*, B369:600–654, 1992. doi:10.1016/0550-3213(92)90280-0. 1.6
- [101] C. Wesp, A. El, F. Reining, Z. Xu, I. Bouras, et al. Calculation of shear viscosity using Green-Kubo relations within a parton cascade. *Phys. Rev.*, C84:054911, 2011. arXiv:1106.4306, doi:10.1103/PhysRevC.84.054911. 1.6
- [102] G.-Y. Qin and B. Muller. private communication. 1.28, 1.6, 1.29, 1.30, 4.4.3, 4.20
- [103] G.-Y. Qin and B. Muller. Explanation of Di-jet asymmetry in Pb+Pb collisions at the Large Hadron Collider. *Phys. Rev. Lett.*, 106:162302, 2011. 4 pages, 3 figures, made corrections for numerical inaccuracies, qualitative conclusions unaffected. arXiv:1012.5280, doi:10.1103/PhysRevLett.106.162302. 1.6, 1.6
- [104] B. Schenke, C. Gale, and S. Jeon. MARTINI: Monte Carlo simulation of jet evolution. *Acta Phys. Polon. Supp.*, 3:765–770, 2010. arXiv:0911.4470. 1.6
- [105] B. Schenke, S. Jeon, and C. Gale. (3+1)D hydrodynamic simulation of relativistic heavy-ion collisions. *Phys. Rev.*, C82:014903, 2010. arXiv:1004.1408, doi:10.1103/PhysRevC.82.014903. 1.6
- [106] C. Young, B. Schenke, S. Jeon, and C. Gale. Dijet asymmetry at the energies available at the CERN Large Hadron Collider. *Phys. Rev.*, C84:024907, 2011. arXiv:1103.5769, doi:10.1103/PhysRevC.84.024907. 1.6
- [107] C. Young and B. Schenke. private communication. 1.30
- [108] Korinna Zapp, Gunnar Ingelman, Johan Rathsman, Johanna Stachel, and Urs Achim Wiedemann. A Monte Carlo Model for 'Jet Quenching'. *Eur. Phys. J.*, C60:617–632, 2009. arXiv:0804.3568, doi:10.1140/epjc/s10052-009-0941-2. 1.33
- [109] Wei Dai, Ivan Vitev, and Ben-Wei Zhang. Momentum imbalance of isolated photon-tagged jet production at RHIC and LHC. *Phys. Rev. Lett.*, 110:142001, 2013. arXiv:1207.5177, doi:10.1103/PhysRevLett.110.142001. 1.7, 1.34, 1.35
- [110] G. Aad et al. Measurement of inclusive jet charged-particle fragmentation functions in Pb+Pb collisions at  $\sqrt{s_{NN}} = 2.76$  TeV with the ATLAS detector. 2014. arXiv:1406.2979. 1.37
- [111] Serguei Chatrchyan et al. Measurement of jet fragmentation in PbPb and  $pp$  collisions at  $\sqrt{s_{NN}} = 2.76$  TeV. *Phys. Rev.*, C90:024908, 2014. arXiv:1406.0932, doi:10.1103/PhysRevC.90.024908. 1.37
- [112] W. Horowitz and M. Gyulassy. Heavy quark jet tomography of Pb+Pb at LHC: AdS/CFT drag or pQCD energy loss? *Phys. Lett.*, B666:320–323, 2008. arXiv:0706.2336, doi:10.1016/j.physletb.2008.04.065. 1.8
- [113] Y. Dokshitzer and D. Kharzeev. Heavy quark colorimetry of QCD matter. *Phys. Lett.*, B519:199–206, 2001. arXiv:hep-ph/0106202, doi:10.1016/S0370-2693(01)01130-3. 1.8

- [114] M. Cacciari. private communication. 1.8, 1.40
- [115] Jiechen Xu, Alessandro Buzzatti, and Miklos Gyulassy. Azimuthal jet flavor tomography with CUJET2.0 of nuclear collisions at RHIC and LHC. *JHEP*, 1408:063, 2014. arXiv:1402.2956, doi:10.1007/JHEP08(2014)063. 1.8, 1.41
- [116] Jinrui Huang, Zhong-Bo Kang, and Ivan Vitev. Inclusive b-jet production in heavy ion collisions at the LHC. *Phys. Lett.*, B726:251–256, 2013. arXiv:1306.0909, doi:10.1016/j.physletb.2013.08.009. 1.8, 1.42, 1.8
- [117] A. Adil and I. Vitev. Collisional dissociation of heavy mesons in dense QCD matter. *Phys. Lett.*, B649:139–146, 2007. arXiv:hep-ph/0611109, doi:10.1016/j.physletb.2007.03.050. 1.8
- [118] R. Sharma, I. Vitev, and B.-W. Zhang. Light-cone wave function approach to open heavy flavor dynamics in QCD matter. *Phys. Rev.*, C80:054902, 2009. arXiv:0904.0032, doi:10.1103/PhysRevC.80.054902. 1.8
- [119] V. Abazov et al. *b*-Jet Identification in the D0 Experiment. *Nucl. Instrum. Meth.*, A620:490–517, 2010. arXiv:1002.4224, doi:10.1016/j.nima.2010.03.118. 1.8
- [120] X. Zhao and R. Rapp. Medium Modifications and Production of Charmonia at LHC. *Nucl. Phys.*, A859:114–125, 2011. 7 pages, 9 eps figures. arXiv:1102.2194, doi:10.1016/j.nuclphysa.2011.05.001. 1.9
- [121] R. Arnaldi.  $J/\psi$  production in  $p+A$  and  $A+A$  collisions at fixed target experiments. *Nucl. Phys.*, A830:345c–352c, 2009. arXiv:0907.5004, doi:10.1016/j.nuclphysa.2009.10.030. 1.9
- [122] N. Brambilla, S. Eidelman, B. K. Heltsley, R. Vogt, G. T. Bodwin, et al. Heavy quarkonium: progress, puzzles, and opportunities. 2010. arXiv:arXiv:1010.5827. 1.9, 1.9, 1.10
- [123] B. Abelev et al.  $J/\psi$  production at low transverse momentum in Pb-Pb collisions at  $\sqrt{s_{NN}} = 2.76$  TeV. 2012. arXiv:1202.1383. 1.9, 1.45
- [124] Serguei Chatrchyan et al. Observation of sequential Upsilon suppression in PbPb collisions. *Phys. Rev. Lett.*, 109:222301, 2012. arXiv:1208.2826, doi:10.1103/PhysRevLett.109.222301. 1.9
- [125] Betty Bezverkhny Abelev et al. Suppression of  $Y(1S)$  at forward rapidity in Pb-Pb collisions at  $\sqrt{s_{NN}} = 2.76$  TeV. 2014. arXiv:1405.4493. 1.9
- [126] Betty Bezverkhny Abelev et al. Production of inclusive  $Y(1S)$  and  $Y(2S)$  in p-Pb collisions at  $\sqrt{s_{NN}} = 5.02$  TeV. 2014. arXiv:1410.2234. 1.9
- [127] A. Adare et al. Measurement of  $Y(1S+2S+3S)$  production in  $p+p$  and Au+Au collisions at  $\sqrt{s_{NN}} = 200$  GeV. 2014. arXiv:1404.2246. 1.9, 4.11
- [128] L. Adamczyk et al. Suppression of Upsilon Production in d+Au and Au+Au Collisions at  $\sqrt{s_{NN}} = 200$  GeV. *Phys. Lett.*, B735:127, 2014. arXiv:1312.3675, doi:10.1016/j.physletb.2014.06.028. 1.9

- [129] B. Muller, J. Schukraft, and B. Wyslouch. First results from Pb+Pb collisions at the LHC. 2012. [arXiv:1202.3233](#). 1.9
- [130] A. Emerick, X. Zhao, and R. Rapp. Bottomonia in the quark-gluon plasma and their production at RHIC and LHC. 2011. [arXiv:1111.6537](#). 1.9
- [131] L. Ruan, G. Lin, Z. Xu, K. Asselta, H. F. Chen, et al. Perspectives of a midrapidity dimuon program at RHIC: a novel and compact muon telescope detector. *J. Phys. G*, G36:095001, 2009. [arXiv:0904.3774](#), [doi:10.1088/0954-3899/36/9/095001](#). 1.9
- [132] K. Eskola, H. Paukkunen, and C. Salgado. EPS09: a new generation of NLO and LO nuclear parton distribution functions. *JHEP*, 04:065, 2009. [arXiv:0902.4154](#), [doi:10.1088/1126-6708/2009/04/065](#). 1.10
- [133] F. Arleo, P.B. Gossiaux, T. Gousset, and J. Aichelin. Charmonium suppression in p-A collisions. *Phys. Rev.*, C61:054906, 2000. 1.10
- [134] D.C. McGlinchey, A.D. Frawley, and R. Vogt. Impact parameter dependence of the nuclear modification of  $J/\psi$  production in  $d+Au$  collisions at  $\sqrt{s_{NN}} = 200$  GeV. *Phys. Rev.*, C87(5):054910, 2013. 1.10
- [135] F. Arleo and S. Peigne. Heavy-quarkonium suppression in p-A collisions from parton energy loss in cold QCD matter. *JHEP*, 1303:122, 2013. [arXiv:1212.0434](#), [doi:10.1007/JHEP03\(2013\)122](#). 1.10
- [136] Betty Abelev et al. Long-range angular correlations on the near and away side in  $p$ -Pb collisions at  $\sqrt{s_{NN}} = 5.02$  TeV. *Phys. Lett.*, B719:29–41, 2013. 1.10
- [137] Georges Aad et al. Measurement with the ATLAS detector of multi-particle azimuthal correlations in p+Pb collisions at  $\sqrt{s_{NN}}=5.02$  TeV. *Phys. Lett.*, B725:60–78, 2013. 1.10
- [138] Serguei Chatrchyan et al. Multiplicity and transverse momentum dependence of two- and four-particle correlations in pPb and PbPb collisions. *Phys. Lett.*, B724:213–240, 2013. 1.10
- [139] A. Adare et al. Quadrupole Anisotropy in Dihadron Azimuthal Correlations in Central  $d+Au$  Collisions at  $\sqrt{s_{NN}}=200$  GeV. *Phys. Rev. Lett.*, 111:212301, 2013. 1.10
- [140] A. Adare et al. Nuclear modification of  $\psi'$ ,  $\chi_c$  and  $J/\psi$  production in  $d+Au$  collisions at  $\sqrt{s_{NN}} = 200$  GeV. *Phys. Rev. Lett.*, 111:202301, 2013. 1.10
- [141] E.G. Ferreira, F. Fleuret, J.P. Lansberg, and A. Rakotozafindrabe.  $J/\psi$  and  $\psi'$  production in proton(deuteron)-nucleus collisions: lessons from RHIC for the proton-lead LHC run. *J. Phys. Conf. Ser.*, 422:012018, 2013. [arXiv:1211.4749](#), [doi:10.1088/1742-6596/422/1/012018](#). 1.10
- [142] A. Capella, A. Kaidalov, A. Kouider Akil, and C. Gerschel.  $J/\psi$  and  $\psi'$  suppression in heavy ion collisions. *Phys. Lett.*, B393:431–436, 1997. 1.10
- [143] W. Vogelsang. private communication. 1.11, 1.49, 4.42
- [144] W. Fischer. RHIC Luminosity Upgrade Program. *Conf. Proc.*, C100523:TUXMH01, 2010. 1.11

- [145] RHIC Beam Projections [online]. URL: <http://www.rhichome.bnl.gov/RHIC/Runs/RhicProjections.pdf>. 1.11, 3.8
- [146] S. Afanasiev et al. Measurement of Direct Photons in Au+Au Collisions at  $\sqrt{s_{NN}} = 200$  GeV. 2012. arXiv:1205.5759. 1.50
- [147] A. Adare et al. Direct-Photon Production in  $p + p$  Collisions at  $\sqrt{s} = 200$  GeV at Midrapidity. 2012. arXiv:1205.5533. 1.50
- [148] O.D. Tsai, L.E. Dunkelberger, C.A. Gagliardi, S. Heppelmann, H.Z. Huang, et al. Results of & on a new construction technique for W/ScFi Calorimeters. *J. Phys. Conf. Ser.*, 404:012023, 2012. doi:10.1088/1742-6596/404/1/012023. 3.2.1
- [149] Tungsten Heavy Powder. URL: <http://www.tungstenheavypowder.com>. 3.2.1
- [150] R. Wigmans. Calorimetry: Energy measurement in particle physics. *Int. Ser. Monogr. Phys.*, 107:1-726, 2000. 3.6
- [151] Inc. Saint-Gobain Ceramics & Plastics. Scintillating optical fibers. 3.3
- [152] Kuraray Co. Ltd. Scintillation materials catalogue. 3.3
- [153] A. Izmaylov, S. Aoki, J. Blocki, J. Brinson, A. Dabrowska, et al. Scintillator counters with WLS fiber/MPPC readout for the side muon range detector (SMRD) of the T2K experiment. *Nucl. Instrum. Meth.*, A623:382-384, 2010. arXiv:0904.4545, doi:10.1016/j.nima.2010.03.009. 3.3
- [154] O. Mineev, A. Afanasjev, G. Bondarenko, V. Golovin, E. Gushchin, et al. Scintillator counters with multi-pixel avalanche photodiode readout for the ND280 detector of the T2K experiment. *Nucl. Instrum. Meth.*, A577:540-551, 2007. arXiv:physics/0606037, doi:10.1016/j.nima.2007.04.161. 3.3
- [155] S. Agostinelli et al. GEANT4: A Simulation toolkit. *Nucl. Instrum. Meth.*, A506:250-303, 2003. doi:10.1016/S0168-9002(03)01368-8. 3.4, 4.1
- [156] M. Allen et al. PHENIX inner detectors. *Nucl. Instrum. Meth.*, A499:549-559, 2003. doi:10.1016/S0168-9002(02)01956-3. 3.9
- [157] T. Sjostrand, P. Eden, C. Friberg, L. Lonnblad, G. Miu, et al. High-energy physics event generation with PYTHIA 6.1. *Comput. Phys. Commun.*, 135:238-259, 2001. arXiv:hep-ph/0010017, doi:10.1016/S0010-4655(00)00236-8. 4.1, 4.3.1
- [158] M. Gyulassy and X. Wang. HIJING 1.0: A Monte Carlo program for parton and particle production in high-energy hadronic and nuclear collisions. *Comput. Phys. Commun.*, 83:307, 1994. arXiv:nucl-th/9502021, doi:10.1016/0010-4655(94)90057-4. 4.1
- [159] M. Cacciari and G. P. Salam. Dispelling the  $N^3$  myth for the  $k_t$  jet-finder. *Phys. Lett.*, B641:57-61, 2006. arXiv:hep-ph/0512210, doi:10.1016/j.physletb.2006.08.037. 4.1, 4.2, A.1
- [160] I. P. Lokhtin and A. M. Snigirev. A Model of jet quenching in ultrarelativistic heavy ion collisions and high-p(T) hadron spectra at RHIC. *Eur. Phys. J.*, C45:211-217, 2006. arXiv:hep-ph/0506189, doi:10.1140/epjc/s2005-02426-3. 4.1, 4.4.4

- [161] J.A. Hanks, A.M. Sickles, B.A. Cole, A. Franz, M.P. McCumber, et al. Method for separating jets and the underlying event in heavy ion collisions at the BNL Relativistic Heavy Ion Collider. *Phys. Rev.*, C86:024908, 2012. arXiv:1203.1353, doi:10.1103/PhysRevC.86.024908. 4.1, 4.4.1
- [162] M. Cacciari, G. Salam, and G. Soyez. The anti- $k_t$  jet clustering algorithm. *JHEP*, 0804:063, 2008. arXiv:0802.1189, doi:10.1088/1126-6708/2008/04/063. 4.2
- [163] Florian Beaudette. The CMS Particle Flow Algorithm. pages 295–304, 2014. arXiv:1401.8155. 4.2
- [164] Particle-Flow Event Reconstruction in CMS and Performance for Jets, Taus, and MET. Technical Report CMS-PAS-PFT-09-001, CERN, 2009. Geneva, Apr 2009. 4.2
- [165] Matthew Nguyen. Jet Reconstruction with Particle Flow in Heavy-Ion Collisions with CMS. *J. Phys.*, G38:124151, 2011. arXiv:1107.0179, doi:10.1088/0954-3899/38/12/124151. 4.2
- [166] Jet Performance in pp Collisions at 7 TeV. URL: <http://cdsweb.cern.ch/record/1279362>. 4.3
- [167] T. Auye. Unfolding algorithms and tests using RooUnfold. 2011. arXiv:1105.1160. 4.3.1
- [168] B. A. Cole. Jet probes of  $\sqrt{s_{NN}} = 2.76$  TeV Pb+Pb collisions with the ATLAS detector. *J. Phys. G*, G38:124021, 2011. 4.4.1
- [169] Nestor Armesto, Leticia Cunqueiro, Carlos A. Salgado, and Wen-Chang Xiang. Medium-evolved fragmentation functions. *JHEP*, 0802:048, 2008. arXiv:0710.3073, doi:10.1088/1126-6708/2008/02/048. 4.25, 4.6
- [170] Impact parameter-based b-tagging algorithms in the 7 TeV collision data with the ATLAS detector: the TrackCounting and JetProb algorithms. 2010. 4.7
- [171] Performance of Impact Parameter-Based b-tagging Algorithms with the ATLAS Detector using Proton-Proton Collisions at  $\sqrt{s} = 7$  TeV. 2010. 4.7
- [172] Commissioning of b-jet identification with pp collisions at  $\sqrt{s} = 7$  TeV. 2010. 4.7
- [173] Serguei Chatrchyan et al. Identification of b-quark jets with the CMS experiment. *JINST*, 8:P04013, 2013. arXiv:1211.4462, doi:10.1088/1748-0221/8/04/P04013. 4.7
- [174] G. Brandenburg et al. Charged track multiplicity in B meson decay. *Phys. Rev.*, D61:072002, 2000. arXiv:hep-ex/9907057, doi:10.1103/PhysRevD.61.072002. 4.7
- [175] Georges Aad et al. Measurement of the flavour composition of dijet events in pp collisions at  $\sqrt{s} = 7$  TeV with the ATLAS detector. *Eur. Phys. J.*, C73:2301, 2013. arXiv:1210.0441, doi:10.1140/epjc/s10052-013-2301-5. 4.7
- [176] Soft muon tagging and Dstar/mu correlations in 7 TeV collisions with ATLAS. 2010. 4.7
- [177] Serguei Chatrchyan et al. Evidence of b-jet quenching in PbPb collisions at  $\sqrt{s_{NN}} = 2.76$  TeV. *Phys. Rev. Lett.*, 113:132301, 2014. arXiv:1312.4198, doi:10.1103/PhysRevLett.113.132301. 4.7

- [178] Performance of the ATLAS Secondary Vertex b-tagging Algorithm in 7 TeV Collision Data. 2010. 4.7
- [179] D. Buskulic et al. A Precise measurement of Gamma ( $Z \rightarrow b\bar{b}$ ) / Gamma ( $Z \rightarrow$  hadrons). *Phys.Lett.*, B313:535–548, 1993. doi:10.1016/0370-2693(93)90028-G. 4.7
- [180] CMS Collaboration. Charged particle nuclear modification factor and pseudorapidity asymmetry in pPb collisions at  $\sqrt{s_{NN}}=5.02$  TeV with CMS. 2013. 4.8, 4.39
- [181] The ATLAS collaboration. Centrality and rapidity dependence of inclusive jet production in  $\sqrt{s_{NN}} = 5.02$  TeV proton–lead collisions with the ATLAS detector. 2014. 4.8, 4.8, 4.39, 4.40
- [182] The ATLAS collaboration. Charged hadron production in p+Pb collisions at  $\sqrt{s_{NN}} = 5.02$  TeV measured at high transverse momentum by the ATLAS experiment. 2014. 4.8
- [183] Dennis V. Perepelitsa. Exploring cold nuclear matter effects in d+Au with high- $p_T$  reconstructed jets at PHENIX. *Nucl. Phys.*, A904-905:1003c–1006c, 2013. doi:10.1016/j.nuclphysa.2013.02.184. 4.8, 4.40
- [184] Serguei Chatrchyan et al. Studies of dijet transverse momentum balance and pseudorapidity distributions in pPb collisions at  $\sqrt{s_{NN}} = 5.02$  TeV. *Eur. Phys. J.*, C74:2951, 2014. arXiv:1401.4433, doi:10.1140/epjc/s10052-014-2951-y. 4.8
- [185] CMS Collaboration. Nuclear Modification Factor  $R_{pA}$  of b jets in pPb collisions. 2014. 4.8
- [186] D. Acosta et al. Y production and polarization in  $p\bar{p}$  collisions at  $\sqrt{s} = 1.8$  TeV. *Phys. Rev. Lett.*, 88:161802, 2002. doi:10.1103/PhysRevLett.88.161802. 4.11
- [187] J. Gaiser. Charmonium Spectroscopy From Radiative Decays of the  $J/\psi$  and  $\psi'$ . SLAC-0255, UMI-83-14449-MC, SLAC-R-0255, SLAC-R-255, 1982. 4.11
- [188] M. Strickland and D. Bazow. Thermal bottomonium suppression at RHIC and LHC. *Nucl. Phys.*, A879:25–58, 2012. arXiv:1112.2761, doi:10.1016/j.nuclphysa.2012.02.003. 4.46, 4.11, 4.11, 4.48
- [189] PHENIX Collaboration. The PHENIX Decadal Plan, 2010. URL: [http://www.phenix.bnl.gov/phenix/WWW/docs/decadal/2010/phenix\\_decadal10\\_full\\_refs.pdf](http://www.phenix.bnl.gov/phenix/WWW/docs/decadal/2010/phenix_decadal10_full_refs.pdf). B
- [190] A. Accardi et al. Electron Ion Collider: The Next QCD Frontier - Understanding the glue that binds us all. 2012. arXiv:1212.1701. B, B.1, B.1.1, B.2, B.3, B.4, B.3, B.3, B.7, B.4, B.5.6
- [191] 2007 Long Range Plan: The Frontiers of Nuclear Science, 2007. URL: <http://science.energy.gov/~media/np/nsac/pdf/docs/NuclearScienceHighRes.pdf>. B.1
- [192] D. de Florian, R. Sassot, M. Stratmann, and W. Vogelsang. Extraction of Spin-Dependent Parton Densities and Their Uncertainties. *Phys. Rev.*, D80:034030, 2009. arXiv:0904.3821, doi:10.1103/PhysRevD.80.034030. B.3
- [193] M. Anselmino et al. Transversity and Collins functions from SIDIS and  $e^+e^-$  data. *Phys. Rev.*, D75:054032, 2007. arXiv:hep-ph/0701006, doi:10.1103/PhysRevD.75.054032. B.3
- [194] X.-D. Ji. Gauge invariant decomposition of nucleon spin and its spin - off. *Phys. Rev. Lett.*, 78:610–613, 1997. arXiv:hep-ph/9603249, doi:10.1103/PhysRevLett.78.610. B.3

- [195] A. Airapetian et al. Hadronization in semi-inclusive deep-inelastic scattering on nuclei. *Nucl. Phys.*, B780:1–27, 2007. arXiv:0704.3270, doi:10.1016/j.nuclphysb.2007.06.004. B.3, B.5
- [196] D. Boer et al. Gluons and the quark sea at high energies: Distributions, polarization, tomography. 2011. arXiv:1108.1713. B.3, B.4
- [197] A. Daniel et al. Measurement of the nuclear multiplicity ratio for  $K_s^0$  hadronization at CLAS. *Phys. Lett.*, B706:26–31, 2011. arXiv:1111.2573, doi:10.1016/j.physletb.2011.10.071. B.5
- [198] E. Iancu, K. Itakura, and L. McLerran. Geometric scaling above the saturation scale. *Nucl. Phys.*, A708:327–352, 2002. arXiv:hep-ph/0203137, doi:10.1016/S0375-9474(02)01010-2. B.6
- [199] C. Aidala et al. sPHENIX: An Upgrade Concept from the PHENIX Collaboration. 2012. arXiv:1207.6378. B.5
- [200] F. Sauli. GEM: A new concept for electron amplification in gas detectors. *Nucl. Instrum. Meth.*, A386:531–534, 1997. doi:10.1016/S0168-9002(96)01172-2. B.5
- [201] P. Abbon et al. The COMPASS experiment at CERN. *Nucl. Instrum. Meth.*, A577:455–518, 2007. arXiv:hep-ex/0703049, doi:10.1016/j.nima.2007.03.026. B.5
- [202] R. Bell et al. The BaBar superconducting coil: Design, construction and test. *Nucl. Phys. Proc. Suppl.*, 78:559–564, 1999. doi:10.1016/S0920-5632(99)00603-9. B.5.1, B.2, B.5.6
- [203] S. An et al. A 20-ps timing device: A Multigap Resistive Plate Chamber with 24 gas gaps. *Nucl. Instrum. Meth.*, A594:39–43, 2008. doi:10.1016/j.nima.2008.06.013. B.5.2
- [204] B. Adams et al. Measurements of the Gain, Time Resolution, and Spatial Resolution of a 20x20cm MCP-based Picosecond Photo-Detector. *Proceedings of the Vienna Conference on Instrumentation*, 2013. URL: <http://psec.uchicago.edu/library/doclib/documents/222/sendit>. B.5.2, B.5.5
- [205] B. Yu et al. A gem based tpc for the legs experiment. In *Nuclear Science Symposium Conference Record, 2005 IEEE*, volume 2, pages 924–928, 2005. doi:10.1109/NSSMIC.2005.1596405. B.5.2
- [206] L. Musa et al. Letter of intent for the upgrade of the alice experiment. Technical Report LHCC-I-022, CERN, 2012. B.5.2
- [207] B. Ketzer. A Time Projection Chamber for High-Rate Experiments: Towards an Upgrade of the ALICE TPC. 2013. arXiv:1303.6694. B.5.2
- [208] T. Abe et al. The International Large Detector: Letter of Intent. 2010. arXiv:1006.3396. B.5.2
- [209] P. Schade and J. Kaminski. A large TPC prototype for a linear collider detector. *Nucl. Instrum. Meth.*, A628:128–132, 2011. doi:10.1016/j.nima.2010.06.300. B.5.2



- [210] C. Woody. Future Applications of GEM Detectors at BNL. Technical report, 2013. Talk on RD51 Collaboration Meeting. B.5.2, B.5.2
- [211] D. Abbaneo et al. Technical Proposal A GEM Detector System for an Upgrade of the CMS Muon Endcaps. Technical report, 2012. B.5.2
- [212] Technical Design Report for PANDA Electromagnetic Calorimeter (EMC). 2008. arXiv:0810.1216. B.24, B.5.3, B.5.6
- [213] I. Adam et al. The DIRC particle identification system for the BaBar experiment. *Nucl. Instrum. Meth.*, A538:281–357, 2005. doi:10.1016/j.nima.2004.08.129. B.5.5, B.25b, B.31, B.5.5, B.32, B.5.6
- [214] W. Anderson et al. Design, Construction, Operation and Performance of a Hadron Blind Detector for the PHENIX Experiment. *Nucl. Instrum. Meth.*, A646:35–58, 2011. arXiv:1103.4277, doi:10.1016/j.nima.2011.04.015. B.5.5
- [215] T. Iijima et al. A Novel type of proximity focusing RICH counter with multiple refractive index aerogel radiator. *Nucl. Instrum. Meth.*, A548:383–390, 2005. arXiv:physics/0504220, doi:10.1016/j.nima.2005.05.030. B.5.5, B.30, B.5.6
- [216] E. Grauges et al. SuperB Progress Reports – Detector. 2010. arXiv:1007.4241. B.5.5
- [217] D. Trbojevic, 2013. Private communication. B.33
- [218] C. Adler et al. The RHIC zero degree calorimeter. *Nucl. Instrum. Meth.*, A470:488–499, 2001. arXiv:nucl-ex/0008005, doi:10.1016/S0168-9002(01)00627-1. B.5.6
- [219] L. Adamczyk et al. Single Spin Asymmetry  $A_N$  in Polarized Proton-Proton Elastic Scattering at  $\sqrt{s} = 200$  GeV. *Phys. Lett.*, B719:62–69, 2013. arXiv:1206.1928, doi:10.1016/j.physletb.2013.01.014. B.5.6